Keck Institute for Space Studies

Postdoctoral Fellowship Final Report

BY

Dr. Siddhartha Pathak

October, 2012

Acknowledgements

I am grateful to the W. M. Keck Institute of Space Studies (KISS) Postdoctoral Fellowship program for their support for the last two years (2010-2012) of my postdoctoral research at California Institute of Technology (Caltech). I would like to specially thank Prof Thomas A. Prince for allowing me the opportunity to be a part of this select group of people with the KISS fellowship at Caltech, and to Ms Michelle A Judd for the awesome support she provided during the years of my fellowship program. I am honored to be a part of this great group of people in the KISS community and hope that this is just the beginning of a long-lasting relationship.

Special thanks are due to Prof. Julia R Greer, my mentor at Caltech, who guided me through the potential pitfalls as I embarked on my postdoctoral research. The work on carbon nanotube (CNT) samples was the result of a very successful collaboration with Prof. Chiara Daraio and Dr. Jordan R. Raney, whose expertise in the CNT synthesis techniques was invaluable for my work.

I would like to acknowledge the help and support I received from the Greer group members on my various projects, especially Dr. Shelby Hutchens, Dr. SeokWoo Lee, Ms. Nisha Mohan, Ms. EeJane Lim and Ms. Elizabeth Decolvenaere on the CNT projects, and Ms. Allison Kunz and Mr. Zachary H. Aitken on the grain boundary projects. Finally thanks also to all of my other friends at Caltech for making my stay such a memorable one.

Summary

This report is composed of several papers and a book chapter that describe the key results of my research on nanomechanical investigations of two different material systems – grain boundaries in metals and mechanical behavior of vertically aligned carbon nanotube (VACNT) brushes or arrays..

Grain boundaries – the interfaces between two grains, or crystallites, in a polycrystalline material – play an important role in the mechanical response of polycrystalline metals, and understanding their deformation behavior is key to their successful use in various applications, including outer space. In this report I detail our investigations on this topic using two different approaches. In Chapter 1, we explore the mechanical behavior of grain boundaries in aluminum using micro and nano-pillars under uniaxial compression, while in Chapter 2 the mechanical response of interfaces in Fe-3%Si steel is explored using spherical indentation. In particular the paper discussed in Chapter 2 entitled "Studying Grain Boundary Regions in Polycrystalline Materials Using Spherical Nano-Indentation and Orientation Imaging Microscopy" deserves special mention as a finalist nominee for the Journal of Materials Science Robert W. Cahn Best Paper Prize for 2012 (the "Cahn Prize").

Similarly VACNT forests are prime candidates for use in micro-electro-mechanical systems (MEMS) as well as energy dissipative systems such as viscoelastic rubbers and foams. VACNTs are complex, hierarchical structures of intertwined tubes arrayed in a nominally vertical alignment due to their perpendicular growth from a stiff substrate. They are a unique class of materials having many of the desirable thermal, electrical, and mechanical properties of individual carbon nanotubes, while exhibiting these properties through the collective interaction of thousands of tubes on a macroscopic scale. In addition to their distinctive buckling behavior and their ability to recover from large deformations, VACNTs have also been reported to demonstrate examples of extreme mechanical performance – a unique viscoelastic response that spans a truly wide temperature range from -196^{o}C to 1000^{o}C – something no other material has shown so far. Such properties earmark them for applications in extreme environments, such as in NASA's planned future planetary missions to Titan, Europa and Venus. A proper

understanding of the collective mechanical behavior of these structures, especially instabilities leading to buckling and inhomogeneities which weaken mechanical performance, is thus of great importance for their design and success in their current and future applications.

Chapters 3 to 7 in this report detail my various projects on VACNTs. We start in Chapter 3 – the chapter published in Encyclopedia of Nanotechnology (Springer) 2012, which provide a broad overview of VACNTs in general. Chapters 4 and 5 explore the response of VACNTs under uniaxial compression, while Chapters 6 and 7 look at their deformation under flat punch indentation.

Publications

1. Siddhartha Pathak□, Seok-Woo Lee, Julia R. Greer. Deformation of carbon nanotube pillars at cryogenic temperatures: an *in-situ* study. In preparation
2. Siddhartha Pathak□, Nisha Mohan, Elizabeth Decolvenaere, Alan Needleman, Mostafa Bedewy, Anastasios John Hart, Julia R. Greer. Effect of density gradients on the deformation of carbon nanotube pillars: an *in-situ* study. submitted
3. S Pathak, N Mohan, P PSS Abadi, S Graham, B A Cola, JR Greer. Compressive Response of Vertically Aligned Carbon Nanotube Films via In-Situ Flat Punch Indentations, *Journal of Materials Research*, 2012 – DOI: 10.1557/jmr.2012.366
4. S Pathak, J R Raney, C Daraio. Effect of morphology on the strain recovery of vertically aligned carbon nanotube arrays: an in situ study. 2012 – submitted
5. S Pathak, Ee J. Lim, Parisa P.S.S. Abadi, S Graham, Baratunde A. Cola, Julia R. Greer. Higher Recovery and Better Energy Dissipation at Faster Strain Rates in Carbon Nanotube Bundles: an in-situ Study. *ACS Nano*, (2012); 6(3): 2189-97.
6. S Pathak, J Michler, K Wasmer and SR Kalidindi. Studying Grain Boundary Regions in Polycrystalline Materials Using Spherical Nano-Indentation and Orientation Imaging Microscopy, *J. Materials Science* Volume 47, Issue 2 (2012), Page 815-823. Nominated as **finalist** for the *Journal of Materials Science* Robert W. Cahn Best Paper Prize for 2012 (the **"Cahn Prize"**).
7. SB Hutchens, E Decolvenaere, S Pathak, JR Greer. Nanoshearing. *Materials Today*, Volume 15, Issue 3, March 2012, Page 127
8. A. Kunz , S Pathak, J. R. Greer. Size effects in Al nanopillars: single crystalline versus bicrystalline. *Acta Materialia* (2011) 59(11): p. 4416-4424.

Book Chapter

9. S Hutchens, S Pathak. Vertically Aligned Carbon Nanotubes, Collective Mechanical Behavior. *Encyclopedia of Nanotechnology* (Springer) 2012, Part 22, 2809-2818, DOI: 10.1007/978-90-481-9751-4_387

Research Fellowships and Awards

- 2012 Director's Postdoctoral Fellow, Los Alamos National Laboratory, Los Alamos, NM
- 2011 ThinkSwiss Research Scholar – this scholarship provides funding for a research stay in Switzerland (20 scholarships are awarded every year in this nationwide program)
- Work on carbon nanotubes (CNT) selected as the cover image for 2012 for Materials Today through an international level competition.
- First prize in the NanoArt 2011 International Online Competition http://www.nanotech-now.com/columns/?article=550
- Work featured as a slide show on Discovery Channel news Nov 2011 http://news.discovery.com/tech/scientists-artists-nanoart-exhibition-111109.html
- CNT work featured in Advanced Materials & Processes magazine, Feb 2011

Invited Presentations

1) S Pathak (presenter), ZG Cambaz, Y Gogotsi, W Mook, J Michler. Viscoelasticity and High Buckling Stress of Dense Carbon Nanotube Brushes. MS&T Annual meeting, Columbus, Ohio, Oct 2011
2) S Pathak (presenter), SR Kalidindi. Studying the Mechanical Response of Regions within Grains and Near Grain Boundaries using Spherical Nanoindentation. TMS Annual meeting, San Diego, Feb-March 2011

Conference Presentations

3) S Pathak (presenter), Nisha Mohan, Elizabeth Decolvenaere, Alan Needleman, Mostafa Bedewy, Anastasios John Hart, Julia R. Greer. Effect of density gradients on the deformation of carbon nanotube pillars: an *in-situ* study. 2012 MRS Fall meeting, Boston, Nov-Dec 2012
4) S Pathak (presenter), N Mohan, Ee J. Lim , PPSS Abadi , S Graham, BA Cola, JR Greer. "Insights into Energy Absorption Mechanisms in Hierarchical Carbon Nanotube Forests." 2012 MRS Spring Meeting, San Francisco, 9-13 April USA.

5) S Pathak (presenter), SR Kalidindi. Studying the Mechanical Response of Regions within Grains and Near Grain Boundaries using Spherical Nanoindentation. ICOTOM annual meeting, IIT Bombay, India, Dec 2011
6) S Pathak (presenter), ZG Cambaz, Y Gogotsi, W Mook, J Michler. Viscoelasticity and High Buckling Stress of Dense Carbon Nanotube Brushes. TMS Annual meeting, San Diego, Feb-March 2011
7) S Pathak (presenter), SR Kalidindi, R Raghavan, J Michler. Stress-strain response from spherical nano-indentation and micro-pillar compression experiments: A comparative study. TMS Annual meeting, San Diego, Feb-March 2011
8) S Pathak (presenter), JL Riesterer, SJ Vachhani, K Wasmer, J Michler, SR Kalidindi. "On the Sequence of Events during Pop-ins in Spherical Nanoindentation"; MRS Fall meeting, Boston, Nov-Dec 2010

Poster Presentations

9) S Pathak, N Mohan, Ee J. Lim , PPSS Abadi , S Graham, BA Cola, JR Greer. "Insights into Energy Absorption Mechanisms in Hierarchical Carbon Nanotube Forests." 2012 ICB Army-Industry Collaboration Conference and Comprehensive Review, Santa Barbara, CA, USA
10) S Pathak, W Mook, ZG Cambaz, Y Gogotsi, J Michler. "In-situ SEM Micro-compression of Dense Carbon Nanotube Brushes"; MRS Fall Meeting, Boston, 2010

Science Saturdays – Caltech Public Science lecture series

11) "Hyperspeed" – Discussion leader for Caltech outreach program (audience of 500), Feb 12, 2011

Table of Contents:

Selected Publications

CHAPTER 1: A Kunz , S Pathak, J R Greer. Size effects in Al nanopillars: single crystalline versus bicrystalline. *Acta Materialia* (2011) 59(11): p. 4416-4424.

CHAPTER 2: S Pathak, J Michler, K Wasmer and SR Kalidindi. Studying Grain Boundary Regions in Polycrystalline Materials Using Spherical Nano-Indentation and Orientation Imaging Microscopy, *J. Materials Science* Volume 47, Issue 2 (2012), Page 815-823. Nominated as **finalist** for the *Journal of Materials Science* Robert W. Cahn Best Paper Prize for 2012 (the **"Cahn Prize"**).

CHAPTER 3: S Hutchens, S Pathak. Vertically Aligned Carbon Nanotubes, Collective Mechanical Behavior. *Encyclopedia of Nanotechnology* (Springer) 2012, Part 22, 2809-2818, DOI: 10.1007/978-90-481-9751-4_387

CHAPTER 4: S Pathak, Ee J. Lim, Parisa P.S.S. Abadi, S Graham, Baratunde A. Cola, Julia R. Greer. Higher Recovery and Better Energy Dissipation at Faster Strain Rates in Carbon Nanotube Bundles: an in-situ Study. *ACS Nano*, (2012); 6(3): 2189-97.

Supporting information for Chapter 4.

CHAPTER 5: Siddhartha Pathak, Nisha Mohan, Elizabeth Decolvenaere, Alan Needleman, Mostafa Bedewy, Anastasios John Hart, Julia R. Greer. Effect of density gradients on the deformation of carbon nanotube pillars: an *in-situ* study. 2012 – in preparation.

Supporting information for Chapter 5.

CHAPTER 6: S Pathak, N Mohan, P PSS Abadi, S Graham, B A Cola, JR Greer. Compressive Response of Vertically Aligned Carbon Nanotube Films via In-Situ Flat Punch Indentations, *Journal of Materials Research*, 2012 – DOI: 10.1557/jmr.2012.366

CHAPTER 7: S Pathak, J R Raney, C Daraio. Effect of morphology on the strain recovery of vertically aligned carbon nanotube arrays: an in situ study. 2012 – submitted

Available online at www.sciencedirect.com
ScienceDirect
Acta Materialia 59 (2011) 4416–4424
Acta MATERIALIA
www.elsevier.com/locate/actamat

Size effects in Al nanopillars: Single crystalline vs. bicrystalline

Allison Kunz, Siddhartha Pathak, Julia R. Greer *

Division of Engineering and Applied Sciences, California Institute of Technology, 1200 East California Boulevard, MC 309-81, Pasadena, CA 91125-8100, USA

Received 31 January 2011; received in revised form 25 March 2011; accepted 25 March 2011
Available online 22 April 2011

Abstract

The mechanical behavior of bicrystalline aluminum nano-pillars under uniaxial compression reveals size effects, a stochastic stress–strain signature, and strain hardening. Pillar diameters range from 400 nm to 2 μm and contain a single, non-sigma high angle grain boundary oriented parallel to the pillar axes. Our results indicate that these bicrystalline pillars are characterized by intermittent strain bursts and exhibit an identical size effect to their single crystalline counterparts. Further, we find that the presence of this particular grain boundary generally decreases the degree of work hardening relative to the single crystalline samples. These findings, along with transmission electron microscopy analysis, show that nano-pillar plasticity in the presence of a grain boundary is also characterized by dislocation avalanches, likely resulting from dislocation nucleation-controlled mechanisms, and that at these small length scales this grain boundary may serve as a dislocation sink rather than a dislocation source.

Keywords: Compression test; Nanoindentation; Electron backscatter diffraction; Interfaces; Aluminum

1. Introduction

The development of uniaxial micro-mechanical testing has led to a renaissance of research in mechanical metallurgy. The original work by Uchic et al. [1] demonstrated that cylindrical Ni pillars with micron scale diameters, fabricated using the focused ion beam (FIB) technique, exhibited an entirely new behavioral regime: discrete strain "bursts", low hardening rates even for large strains, and a power law relationship between flow stress and pillar diameter [2]. A large number of subsequent nano- and micro-pillar studies revealed similar stress–strain curves and identical size effects for a number of fcc metals [3–8]. Remarkably, the power-law size effect proved to be consistent for all fcc metals, generally of the form $\sigma_f \propto D^n$, where D is the pillar diameter and n is of the order of -0.6. While the origins of this size effect are a matter of intense debate, it is generally agreed that the higher stresses attained during mechanical deformation of small scale crystals are a result of nucleation-governed plasticity. Mobile dislocations inside these pillars are attracted to the free surface in response to the image forces, and new dislocations have to be nucleated either in the bulk of the pillar or on its surface in order to accommodate further deformation. Deep in the sub-micron regime it has been shown that the strained fcc pillars experience "hardening by dislocation starvation", whereby mobile dislocations exit the pillar at the free surface at a faster rate than they multiply [3,9]. A convincing example of this concept is the "mechanical annealing" of nickel in an in situ transmission electron microscopy (TEM) compression study by Shan et al. [10].

Since 2005 nano-mechanical testing of pillars has quickly evolved and expanded. New fabrication methods and custom built in situ mechanical equipment allow uniaxial tension experiments in addition to compression tests [11–16]. As first shown by Kiener et al., samples with heads suitable for tension testing and corresponding nano-indenter "grippers" can be made using FIB technology [17,18]. Electroplating methods have also produced

* Corresponding author.
E-mail address: jrgreer@caltech.edu (J.R. Greer).

1359-6454/$36.00
doi:10.1016/j.actamat.2011.03.065

Cu pillars for both uniaxial tension and compression testing, with the additional capability of creating pillars with diameters below 100 nm [19,20]. Beyond fcc, the effect of size on strength for a variety of crystal structures has been investigated, including bcc [21–29] and hcp [30–32]. Computational techniques like molecular dynamics (MD) [33–35] and dislocation dynamics (DD) [36,37] have also been widely utilized to shed light on the underlying defect mechanisms leading to this size-dependent strengthening. For example, MD simulations of fcc and bcc nano-pillars by Weinberger et al. demonstrate dislocation starvation in the former and dislocation multiplication in the latter [38,39]. DD simulations generally reveal the operation of truncated Frank–Read sources, or so-called "single-arm sources" [40]. The experimental and computational findings on mostly micron sized fcc pillars in compression up to 2008 can be found in a thorough review by Uchic et al. [41], while a recent review by Greer and de Hosson [42] offers a discussion on subsequent size effects studies spanning other materials and sub-micron sizes.

While so far most groups have focused on studying size effects in monolith systems such as single crystals, several researchers have looked at more complex microstructures, such as nano-crystalline [43], nano-twinned [44,45], nano-laminate [46,47], and alloyed materials [48,49], to name a few. For example, Jang et al. found a "smaller is weaker" phenomenon in nanocrystalline Ni–W pillars with an average grain size of 60 nm [50], while Mara et al. found that the presence of closely spaced Cu–Nb nano-laminates overrides the size effect, with the strength being a function of the laminate spacing rather than the sample dimensions [46]. Several computational studies investigating deformation of small scale interface-containing metallic systems have also been published and were summarized in a recent review by Zhu and Li [51]. In many cases the presence of internal boundaries has an effect on the size-dependent strength. These results are especially relevant for industrial applications, since most engineering materials are usually polycrystalline or multiphase rather than perfect single crystals. However, most reported literature on the mechanical properties of such materials reveals the aggregate effects of many interfaces rather than the role of individual interfaces. Therefore, the fundamental questions about the effects of individual interfaces, for example the relative influences of different types of interfaces (homogeneous vs. heterogeneous, coherent vs. incoherent, internal vs. free surface, etc.) on dislocation motion and overall sample plasticity, remain elusive.

This work compares the uniaxial compression results of single crystalline and bicrystalline aluminum pillars with diameters between ~400 nm and 2 μm. The bicrystalline pillars contain a single grain boundary vertically oriented along the pillar axis. We report the emergence of an identical size effect regardless of the presence of a boundary, and discuss their deformation in the framework of nucleation-controlled plasticity.

2. Experiments

Commercially available high purity aluminum (5 N purity, ESPI Metals) was annealed under vacuum at 350 °C overnight and then electropolished by Able Electropolishing Co. Grain orientation maps were obtained by automatic indexing of electron backscatter diffraction (EBSD) patterns using a Zeiss1550 VP field emission scanning electron microscope equipped with an EBSD system from Oxford Instruments, as shown in Fig. 1a. Once a high angle grain boundary of suitable length had been located, nanopillar samples containing this boundary close to the center of each sample were fabricated using a FEI Nova 200 scanning electron microscope with a focused ion beam (FIB) according to the procedure outlined in Greer et al. [2]. All nano-pillars had height to width ratios between 3:1 and 4:1, as well as less than 2° of vertical taper, with diameters ranging from roughly 400 to 2000 nm. Bicrystalline pillars contained the grain boundary oriented lengthwise, along the pillar or loading axis. A scanning electron microscopy (SEM) image of a representative bicrystalline pillar with overlaid EBSD pattern is shown in Fig. 1b. Single crystalline nanopillars were made using the same methodology in the two grains adjacent to the high angle boundary.

Uniaxial compression tests were conducted using a Nanoindenter G200 (Agilent Technologies). Using the dynamic contact module (DCM) with a 7 μm diameter flat punch we were able to simultaneously measure load, displacement, and harmonic contact stiffness during the tests. The tests were performed under displacement rate control via a feedback loop to attain a constant 0.001 s^{-1} strain rate until 15% strain. True stress and true strain, including the Sneddon correction, were calculated using the method also outlined in Greer et al. [2]. For each test the harmonic contact stiffness data were compared with the theoretical stiffness to ensure accurate effective pillar dimensions. SEM images of a bicrystalline pillar before and after uniaxial compression are given in Fig. 1c and d, respectively.

In order to determine the oxygen content in the aluminum sample and, hence, the extent of the native oxide layer on the sample surface, quantitative energy-dispersive X-ray spectroscopy (EDS) measurements (Oxford Instruments INCA 4.08) were performed using the same electron microscope as for the EBSD study. The results for the aluminum sample were compared with those for gold, tungsten, niobium, titanium and Fe–3% Si steel, all analyzed during the same session at 5 keV and a working distance of 10 mm. The process was repeated on a second day for consistency. The wt.% (wt.% = apparent concentration/intensity correction) of the element was calculated from the EDS spectrum after correcting for inter-element effects using the XPP matrix correction scheme built-in in the INCA software. The at.% (at.% = wt.%/atomic weight) was calculated from the measured wt.% values for each element, with the sum of atomic weights of all elements in the sample being normalized to 100%.

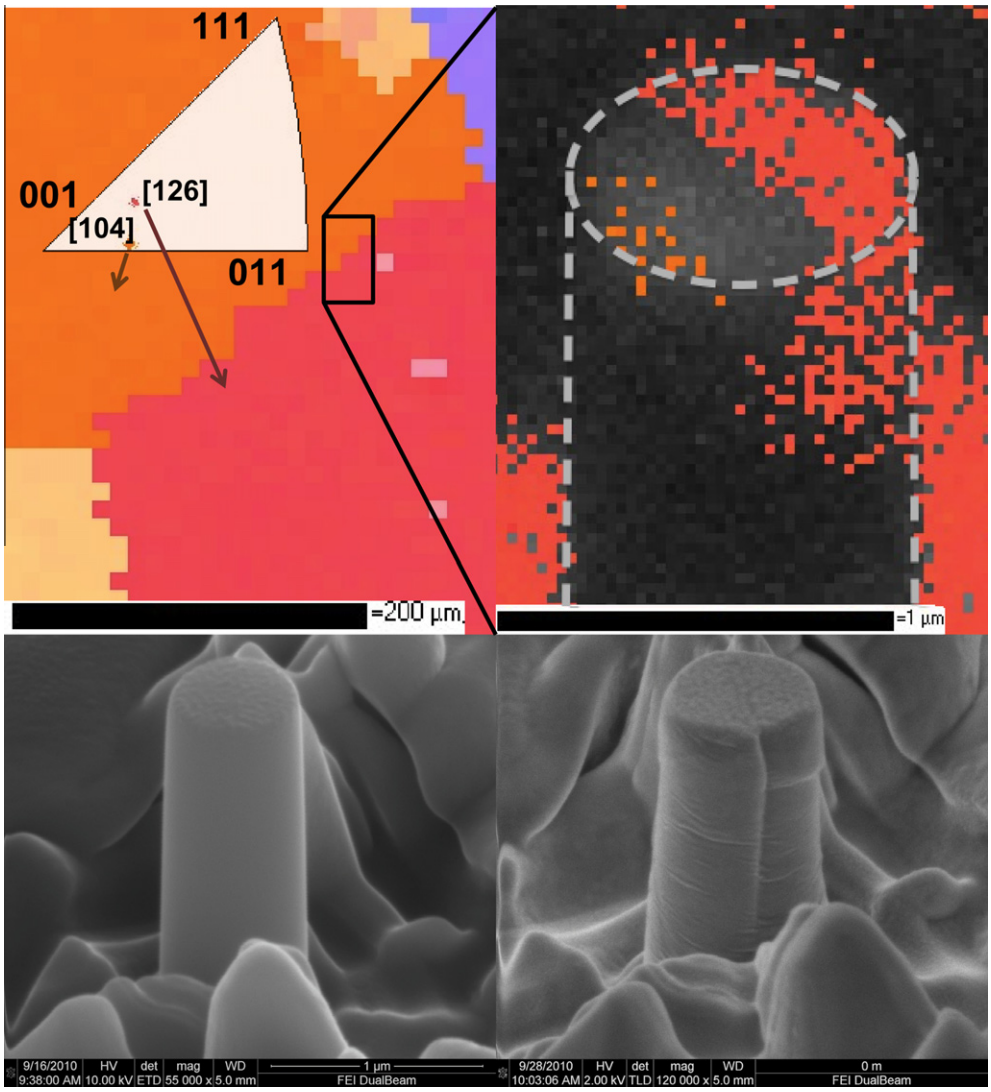

Fig. 1. (a) Crystallographic orientation map of a polycrystalline aluminum sample. (Inset) The inverse pole figure. (b) EBSD image of a typical grain boundary in a pillar. SEM images of the pillars (c) before and (d) after compression to 15% strain.

Transmission electron microscopy (TEM) of a representative post-compression bicrystalline nano-pillar was conducted using an FEI Tecnai F-20 microscope. To prepare the TEM sample a micron thick protective coating of tungsten was deposited on the nanopillar using the Nova 200, and a segment containing the coated pillar on a coupon of the underlying parent material was milled out. A micromanipulator (Omniprobe) was used to lift out the segment, which was then glued to a copper TEM lamella with additional tungsten deposition. FIB cleaning of cross-sections at very low currents of 10 pA and 30 kV was used to thin the pillar-containing segment of aluminum down to less than 100 nm thick.

3. Results

Representative compressive stress–strain curves for single crystalline nano-pillars from each grain and for bicrystalline aluminum nano-pillars are presented in Fig. 2. All of the curves exhibit the discrete stochastic bursts that are characteristic of small scale fcc deformation. The orientation information provided by EBSD was used to calculate the anisotropic Young's modulus $E_{[hkl]}$ and maximum Schmid factors for each orientation. To calculate the modulus of the bicrystalline pillars we assumed an isostrain model with equal volume fractions for both grains. Since aluminum is fairly isotropic (the theoretical values for $E_{[126]}$ and $E_{[104]}$ differ by only 2.7%), any uncertainty about the exact volume fraction of each grain did not have a significant effect on the bicrystalline data analysis. The average slopes of the unloading curves matched their respective theoretical Young's moduli $E_{[hkl]}$ to within 5%. Table 1 provides the Euler angles, Young's moduli, both calculated and measured, and the Schmid factors for the first available slip system for each type of pillar.

The flow stresses at 7.5% strain for single crystalline and bicrystalline samples, resolved by their respective Schmid factors, are plotted as a function of pillar diameter in

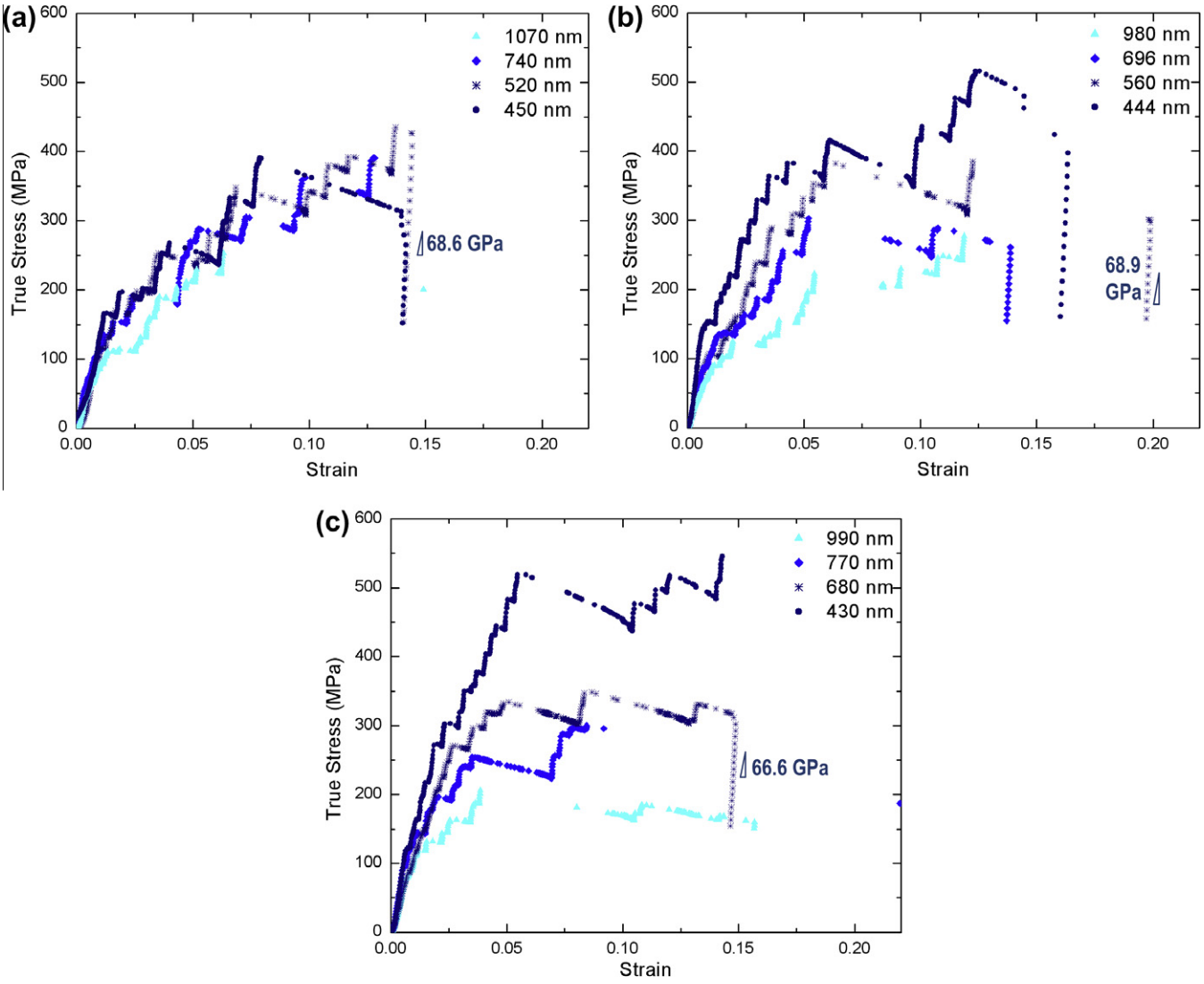

Fig. 2. Representative stress–strain curves for single crystalline pillars oriented with Z in the (a) [1 0 4] and (b) [1 2 6] directions, as well as (c) bicrystalline pillars created at the boundary between two grains.

Table 1
Summary of the crystallographic data and size effects.

Pillar type	Euler angle	$E_{[hkl]}$(GPa)		Schmid factor	Slip systems	Power law coefficient n	R^2
		Calculated	Measured				
Single-crystalline						−0.625	0.656
[126]-oriented	19.2, 18.4, 28.1	65.72	68.63	0.4879	(1 −1 −1) [−1 0 −1]	−0.629	0.788
[104]-oriented	269.1, 15.5, 85.5	67.50	68.87	0.4803	(1 1 1) [0 1 −1], (−1 1 −1) [0 1 1]	−0.578	0.689
Bicrystalline		66.61	64.85	0.4841		−0.590	0.715

Fig. 3a and b. Note that the highly stochastic nature of the nano-pillar deformation, combined with possible uncertainty at initial loading between the pillar and the punch, make an unambiguous determination of the yield (elastic to plastic transition) very difficult. Calculating the flow stress at 7.5% strain, on the other hand, removes this ambiguity, since this particular strain level is after full contact has been established, but before the stochastic nature of the bursts obscures precise determination of flow stress.

The data for the single crystalline pillars (Fig. 3a) reproduces the expected power law relationship between the resolved shear flow stress and pillar diameter with a slope of −0.625, nearly identical to that observed for most non-pristine fcc metals [41]. Fig. 3b compares the single

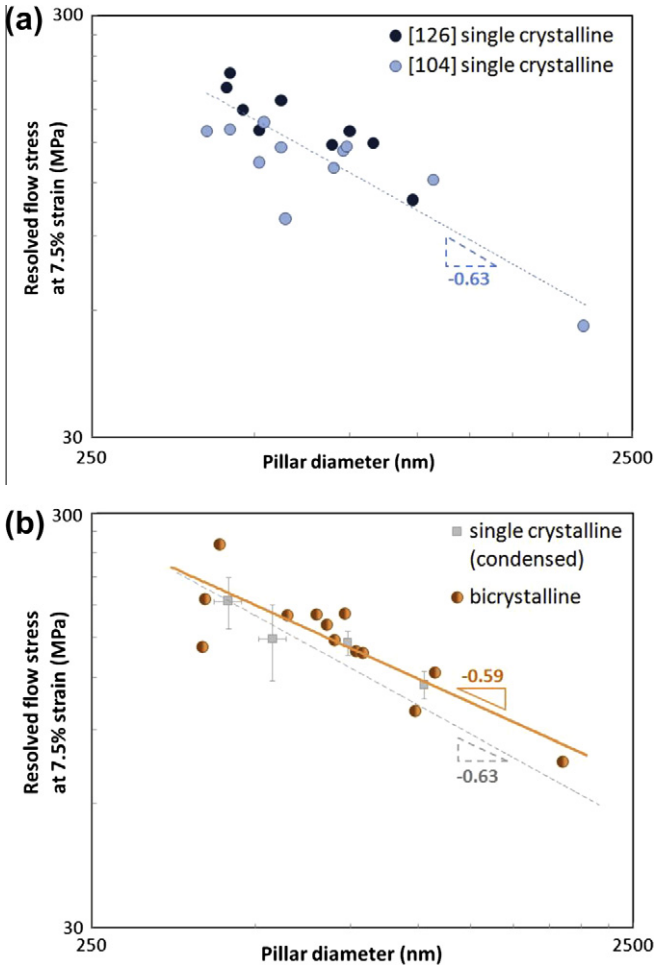

Fig. 3. Size effect plots showing the power law relationship between pillar diameter and flow stress for (a) single crystalline and (b) single crystalline (condensed) vs. bicrystalline pillars. The error bars reflect the standard deviation.

crystalline data shown in Fig. 3a, condensed into fewer points with error bars reflecting the standard deviations for clarity, with the bicrystalline results. Interestingly, we find that the size effect exhibited by the bicrystalline samples is nearly equivalent to the single crystalline ones: the pillars containing grain boundaries give a slope of −0.590, which is only a 5.6% difference from the single crystalline case. Another interesting observation that can be made based on this data is that the bicrystalline pillars and [104]-oriented single crystalline pillars show a significantly larger spread in flow stresses after 5% strain than the tightly distributed [126]-oriented single crystalline pillars. We ascribe this to the fact that the [104] direction is favorably oriented for bi-slip, with two slip systems sharing the highest Schmid factor values, while [126] is oriented for single slip only. Table 1 shows a summary of the primary slip systems for each orientation, as well as their Schmid factors and elastic moduli. The power law coefficients n and their R^2 values are also included in Table 1.

We also investigate the amount of flow stress increase with increasing strain for each pillar type. Since the deformation of these nano-structures is characterized by intermittent strain bursts, the conventional definition of strain hardening is ill suited here. Instead, we define our hardening figure of merit as the angle calculated from the slope of the region between full flat punch–pillar contact and the beginning of unloading on the stress–strain curves. This slope is normalized to the flow stress at 7.5% strain in order to deconvolute any pillar size effect from the hardening data. We note, however, that these behavioral regimes are evident even without normalization of the hardening slope with the flow stress. The point of full contact was determined by the strain at which the measured harmonic contact stiffness matched the theoretical stiffness calculated from the effective pillar dimensions. A schematic outlining this procedure on a representative stress–strain curve, as well as the corresponding stiffness plot, are shown in Fig. 4. Due to the uncertainty in the measurements immediately following a strain burst, when the indenter lags behind the pillar deformation, only peak values in the loading direction of each burst were used to represent the applied stress. These hardening angles normalized to the 7.5% flow stresses are plotted as a function of pillar diameter in Fig. 5. Only samples for which the hardening angles could be reliably calculated, i.e. with enough burst peaks to obtain a reliable average slope, are included in the figure. Note also that the constraints imposed by the experimental set-up are known to affect pillar hardening, as studied by Dehm et al. [52], and thus only tests conducted using the same set-up can be directly compared with each other. As can be seen from Fig. 5, the pillars containing grain boundaries exhibit lower average angles compared with their single crystalline counterparts, forming two adjacent behavioral regimes.

4. Discussion

Although the size effect here appears to remain unchanged despite the presence of this particular grain boundary, the stress–strain curves of single crystalline vs. bicrystalline samples exhibit distinct characteristics. First, we compare the data for single crystalline pillars fabricated from the two adjacent grains with each other. Figs. 2a and b and 3a show that the [104]-oriented single crystalline pillars exhibit a shorter average burst size and less pronounced size effect. In order to understand the mechanisms behind these different characteristics we return to the EBSD analysis of the grain orientations. The inverse pole figure in Fig. 1a indicates that the [126] orientation corresponds to single slip, while the [104] orientation is likely to experience double slip. Previous work by Ng and Ngan [53] has shown the collapse of Schmid's law during uniaxial compression of aluminum sub-micron pillars: this research found that as the volume of the pillar decreases the probability that a dislocation exists in the theoretically favored slip orientation (maximum Schmid factor) also decreases. Thus, in smaller pillars the dislocations residing in the slip planes less favored for slip

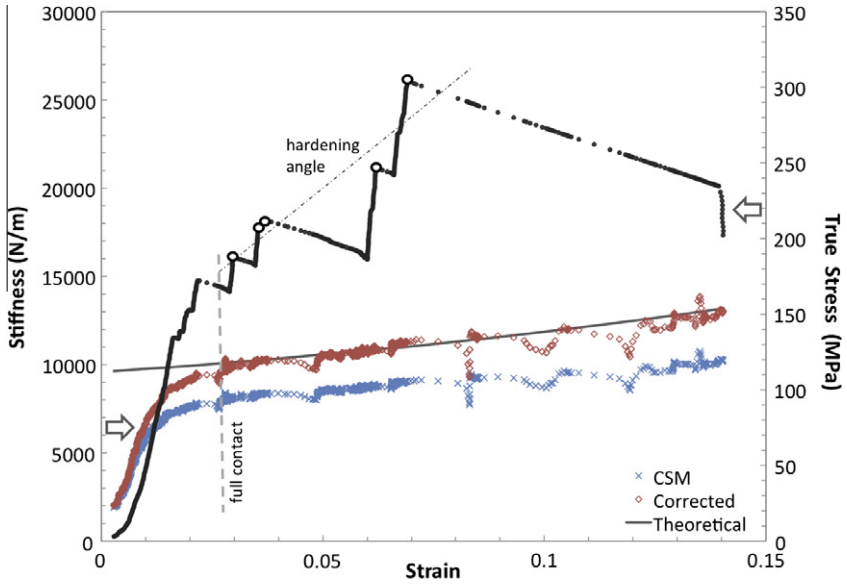

Fig. 4. Compression data analysis. Both the instrument contact stiffness measurements (CSM) and data adjusted with the Sneddon correction from Greer et al. [2], are plotted, along with the theoretical stiffness. The stress–strain curve from the same pillar is also given, with peak values following full contact in bold and their hardening angle indicated by the black dashed line.

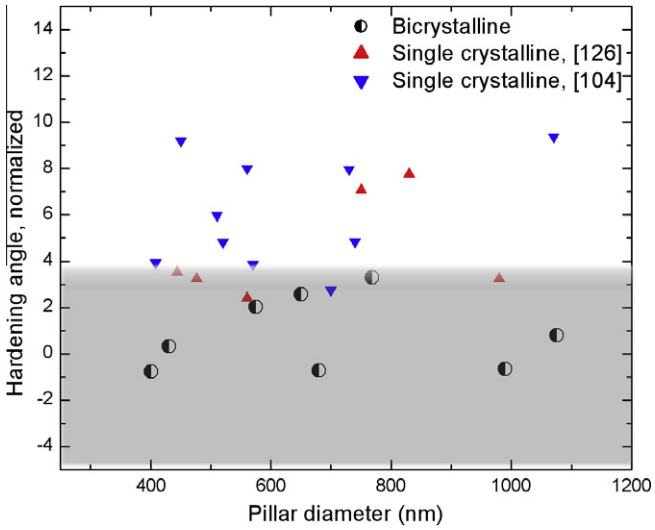

Fig. 5. Plot of hardening angle vs. pillar diameter for the three sets of pillars. The shaded area emphasizes the lower average hardening angle for bicrystalline pillars relative to single crystalline ones.

may possibly be the ones available for slip, thereby requiring higher resolved shear stresses for their activation. Multiple slip provides a greater number of equivalent slip systems, which increases hardening through shortening the dislocation mean free path, manifesting itself as a shorter average burst size. Deforming pillars with an imperfect double slip orientation, meaning that some nominally double slip oriented pillars deform via symmetrical slip, others via single slip, would lead to a greater variability in yield stresses and hardening behavior. All of these characteristics are consistent with our data for [104]-oriented samples. On the other hand, the [126]-oriented samples show consistent hardening and a well-defined size effect. The behavior of the bicrystalline samples resembles more closely that of the [126] pillars oriented for single slip than the [104]-oriented samples oriented for double slip. This similarity is likely due to the slightly higher Schmid factor for the [126] crystal orientation, which would therefore be more likely to yield first. However, there is much less hardening in the bicrystalline samples compared with single crystalline ones in both orientations.

The relatively large average burst sizes (Fig. 2c) and the much lower hardening angles (Fig. 5) in the bicrystalline samples may imply one of three scenarios. In the first two cases either the dislocations travel unimpeded over appreciable distances causing little or no dislocation storage, or the dislocations pile up at obstacles (such as a boundary) and are collectively emitted in relatively large bursts. These two observations might suggest that this particular grain boundary serves as a sink rather than a source of dislocations under applied uniaxial compressive loads. These results agree well with the classical work of Dollar and Gleiter [54], who showed that random high angle boundaries in an irradiated Au foil act as perfect dislocation sinks. Recent nanoindentation studies by Pathak et al. [55] and EBSD measurements by Sun et al. [56] have also demonstrated the ability of high angle grain boundaries to act as efficient dislocation sinks as a function of applied strain.

The third possibility is that the grain boundary itself undergoes some kind of localized breakdown and compatibility loss. Such a scenario was discussed in the work of Ng and Ngan [57], in which the authors noted intense shear of the grain boundary during uniaxial compression of ~6 μm diameter bicrystalline aluminum micro-pillars. As discussed later, TEM micrographs of our bicrystalline pillars

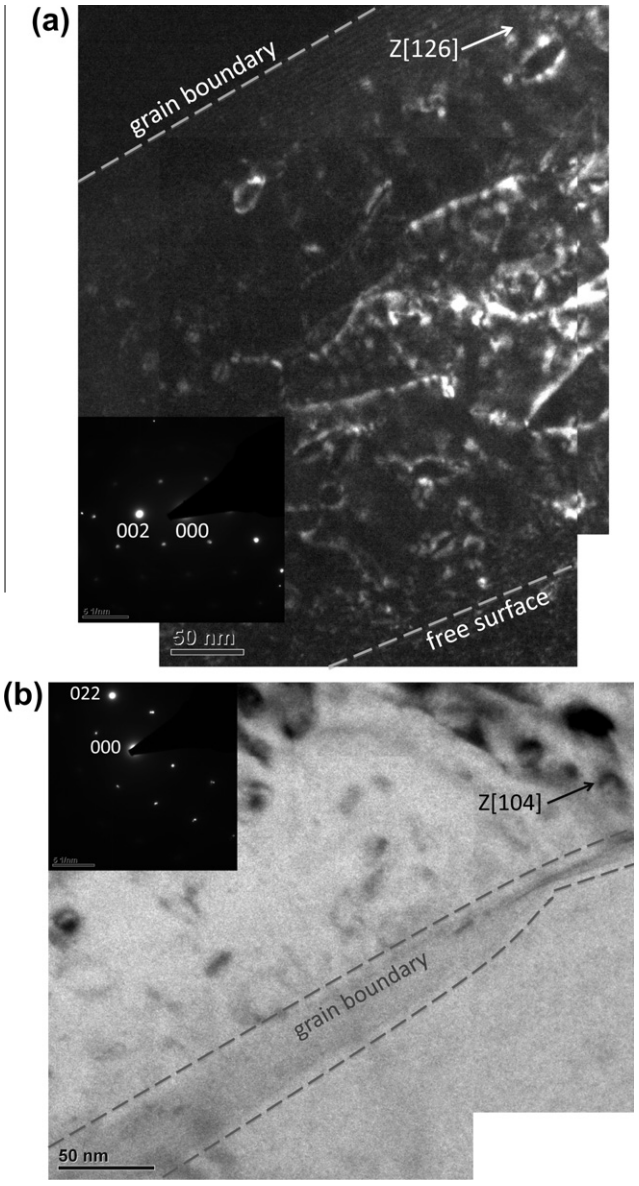

Fig. 6. (a) Dark field TEM image of the [126]-oriented half and (b) bright field TEM image of the [104]-oriented half of the same bicrystalline pillar after uniaxial compression to 15% strain. FIB damage, in the form of dislocation loops, is evident in both sets of images.

(Fig. 6) corroborate this possibility, as it is evident that the boundary itself was altered in the course of compression. Thus, when exposed to sufficiently high stresses, such as those experienced by our nano-pillars, such grain boundary relief (or breakdown) mechanisms could also potentially trigger the significantly larger bursts in our bicrystalline pillars shown in Fig. 2c. Note that such large bursts were not observed in the work of Ng and Ngan [57], probably because the micron sized pillars used in their study experienced roughly an order of magnitude lower stresses than our nanoscale bicrystalline pillars. The exact nature and possibility of the grain boundary breakdown mechanism still remains to be explored in detail, and efforts addressing this aspect are currently underway.

Interestingly, continuum-based crystalline plasticity simulations accounting for the discrete behavior of the dislocation bursts have also noted a larger first burst during compression of bicrystalline, as well as single crystalline, Al pillars [58]. This is explained by simultaneous competition by multiple slip systems for accommodation of the shear stress prior to the first burst. Additionally, one localized slip will only be accommodated if the neighboring region, still free of defects, can also accommodate slip propagation. The presence of a boundary could potentially accentuate this first burst, and efforts are currently underway to conduct a statistical analysis comparing such burst distributions between single and bicrystalline samples, which will be disseminated in a separate manuscript.

Of note is the exact opposite effect seen by Ng and Ngan [57], whose bicrystalline aluminum micro-pillars displayed larger hardening angles compared with their single crystal counterparts by a factor of nearly 2.5. However, the grain boundaries in their study had completely different grain boundary characteristics in terms of crystallographic orientations and boundary misorientations. Also, their boundaries were not positioned lengthwise down the pillar, parallel to the loading axis, but instead at a large angle to the loading axis, with one end exiting the pillar through the cylinder wall. These differences indicate the importance of understanding the grain boundary characteristics and orientation when analyzing such cases. Also, the size of their samples was nearly an order of magnitude larger than ours, allowing enough space to form an intertwined dislocation sub-structure.

To further understand microstructural evolution in the bicrystalline pillars we performed TEM analyses on a representative post-mortem sample, shown in Fig. 6, which reveals no evidence of dislocations piling up at the grain boundary. Fig. 6a provides dark field images with

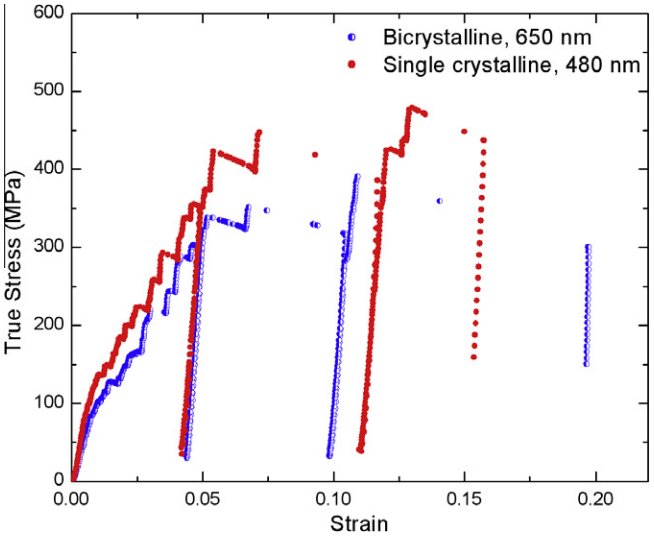

Fig. 7. Stress–strain curves from representative single and bicrystalline pillars subjected to cyclic uniaxial compression testing, showing no Bauschinger effect.

Table 2
Quantitative EDS analysis results.

	Gold	Aluminum	Tungsten	Niobium	Titanium	Fe–3% Si steel
wt.%	O K: 0 Au M: 100	O K: 2.04 ± 0.34 Al K: 97.96 ± 0.34	O K: 1.38 ± 0.26 W M: 98.62 ± 0.26	O K: 4.97 ± 0.43 Nb L: 95.03 ± 0.43	O K: 0.83 ± 0.37 Ti K: 99.17 ± 0.37	O K: 2.07 ± 0.29 Si K: 2.7 ± 0.29 Fe L: 95.46 ± 0.41
at.%	O K: 0 Au M: 100	O K: 3.42 Al K: 96.58	O K: 13.93 W M: 86.07	O K: 23.17 Nb L: 76.83	O K: 2.45 Ti K: 97.55	O K: 6.69 Si K: 4.46 Fe L: 88.85

$g = 002$ near the [1 1 0] zone axis for the [126]-oriented half of the pillar; the sample tilt resulted in a brightness gradient across the images. Dislocations are clearly visible, with the smaller, looped dislocations probably being the result of FIB damage and the longer dislocation segments probably associated with pillar deformation. The FIB damage appears to have an even distribution across the entire surface, a common effect observed by several groups [59–61], while the dislocations associated with deformation appear to be concentrated in the center of the half-pillar, as opposed to near the free surface or the grain boundary. Fig. 6b is a representative higher magnification bright field image with $g = 022$ near the [1 0 0] zone axis for the [104]-oriented half of the same pillar, where again we see evidence of FIB damage, but not of dislocations associated with deformation. It is especially compelling that the regions next to the grain boundary in both grains are relatively defect free. This lack of evidence of dislocation pile-ups at the grain boundary and the presence of a so-called "denuded zone" [54], a region free of defect agglomerates near an interface, is consistent with our hypothesis that this boundary serves as a dislocation sink. A distinct rotation of the grain boundary is also observed in the bright field image (Fig. 6b), suggesting that the grain boundary itself is deforming, although the mechanism remains to be further investigated.

The presence of a native oxide film on the sample surfaces may be a concern in our experiments, as it may trap the dislocations inside the pillar, generate dislocation pile-ups against the pillar–oxide interface, and require higher deformation stresses. Previous work on single crystalline aluminum micro-pillars by Ng and Ngan [62] illustrated that a nanocrystalline tungsten coating both increased the yield stresses and suppressed the discrete nature of the stress–strain curves. Simulations by Deshpande et al. [63] and thin film experiments by Nicola et al. [64] also showed that surface passivation results in significantly more pronounced work hardening and a clear Bauschinger effect. Aluminum is known to generate a 5–10 nm oxide layer on its surface, and in order to test its effect on our pillar compression experiments we ran intentional loading–unloading segments during the compression tests on both single and bicrystalline nano-pillar samples, the results of which are shown in Fig. 7. As seen from this plot, neither stress–strain curve indicates strong hardening or a Bauschinger effect, indicating that the native oxide layer does not serve as a passivation layer, and, therefore, probably does not play a significant role in plastic deformation at this length scale. Similarly, the EDS results shown in Table 2 indicate that the weight percentage of oxygen in aluminum (~2 wt.%) is comparable with that of W, Nb, Ti and Fe–3% Si steel, metals whose size effects have been reported by multiple groups [22,27,57]. Note that the EDS data is limited to only a weight estimation of the oxygen content; it does not provide any information on the mechanical strength of the oxide itself. Table 2 also indicates that, other than noble metals such as gold, all of the other metals tested have a layer of native oxide on their surface which has not been shown to affect their mechanical behavior at submicron length scales [21,22]. The low oxygen weight percentages in Al, when combined with the lack of a Bauschinger effect shown in Fig. 7, may indicate that the surface aluminum oxide is unlikely to contribute greatly to the mechanical strength of the aluminum nano-pillars in compression experiments.

5. Conclusions

We have examined the effect of a vertical, non-sigma, high angle grain boundary on the mechanical properties and deformation behavior of sub-micron Al pillars subjected to uniaxial compression. We observe similar stress–strain signatures, containing numerous discrete displacement bursts, as well as an identical power law "smaller is stronger" size effect in these bicrystalline samples as compared with their single crystalline counterparts. We also observe lower hardening angles and larger burst extents in the bicrystalline pillars, implying little or no dislocation storage and suggesting that this grain boundary may act as a dislocation sink. TEM analysis confirms this hypothesis, as the near boundary regions appear to be defect free, with no evidence of dislocation pile-ups. Since similar work on larger sized bicrystalline aluminum pillars with a different type of grain boundary exhibited the opposite effect: smaller burst sizes and increased hardening, this study reveals that the character of the boundary and sample size appear to play a significant role in the deformation behavior. Efforts are currently underway at comparing the effects of grain boundaries with very different characters on deformation behavior.

Acknowledgements

S.P. gratefully acknowledges the support from the W.M. Keck Institute for Space Studies Postdoctoral Fellowship

program. J.R.G. gratefully acknowledges financial support from an NSF Career award (DMR-0748267). The authors also thank Andrew T. Jennings and Carol Garland for TEM assistance and A. Fernandez, A. Jerusalem, and C. Weinberger for useful discussions.

References

[1] Uchic MD, Dimiduk DM, Florando JN, Nix WD. Science 2004;305:986.
[2] Greer JR, Oliver WC, Nix WD. Acta Mater 2005;53:1821.
[3] Greer JR, Nix WD. Phys Rev B 2006;73:245410.
[4] Volkert CA, Lilleodden ET. Phil Mag 2006;86:5567.
[5] Ng KS, Ngan AHW. Acta Mater 2008;56:1712.
[6] Dimiduk DM, Uchic MD, Parthasarathy TA. Acta Mater 2005;53:4065.
[7] Budiman A, Han S, Greer JR, Tamura N, Patel J, Nix WD. Acta Mater 2007;56:602.
[8] Kiener D, Motz C, Schoberl T, Jenko M, Dehm G. Adv Eng Mater 2006;8:1119.
[9] Zheng H, Cao A, Weinberger CR, Huang JY, Du K, Wang J. Nat Commun 2010;1:144.
[10] Shan ZW, Mishra R, Syed SA, Warren OL, Minor AM. Nat Mater 2008:7.
[11] Greer JR, Kim J-Y, Burek MJ. J Mater 2009;61:19.
[12] Kiener D, Grosinger W, Dehm G. Scripta Mater 2009;60:148.
[13] Dehm G. Prog Mater Sci 2009;54:664.
[14] Legros M, Gianola DS, Motz C. MRS Bull 2010:35.
[15] Richter G, Hillerich K, Gianola DS, Monig R, Kraft O, Volkert CA. Nano Lett 2009;9:3048.
[16] Zhang D, Breguet J-M, Clavel R, Phillippe L, Utke I, Michler J. Nanotechnology 2009;20:365706.
[17] Kiener D, Grosinger W, Dehm G, Pippan R. Acta Mater 2008;56:580.
[18] Kim J-Y, Greer JR. Acta Mater 2009:57.
[19] Jennings AT, Greer JR. Philos Mag A 2010;DOI:10.
[20] Jennings AT, Burek MJ, Greer JR. Phys Rev Lett 2010:104.
[21] Kim J-Y, Jang D, Greer JR. Scripta Mater 2009;61:300.
[22] Kim J-Y, Jang D, Greer JR. Acta Mater 2010;58:2355.
[23] Han SM, Bozorg-Grayeli T, Groves JR, Nix WD. Scripta Mater 2010;63:1153.
[24] Bei H, Shim S, George EP, Miller MK, Herbert EG, Pharr GM. Scripta Mater 2007;57:397.
[25] Bei H, Shim S, Pharr GM, George EP. Acta Mater 2008;56:4762.
[26] Schneider AS, Kaufmann D, Clark BG, Frick CP, Gruber PA, Monig R, et al. Phys Rev Lett 2009:103.
[27] Schneider AS, Clark BG, Frick CP, Gruber PA, Arzt E. Mater Sci Eng A 2009;508:241.
[28] Zaiser M, Schwerdtfeger J, Schneider AS, Frick CP, Clark BG, Gruber PA, et al. Phil Mag 2008;88:3861.
[29] Lowry MB, Kiener D, LeBlanc MM, Chisholm C, Florando JN, Morris JWJ, et al. Acta Mater 2010;58:5160.
[30] Lilleodden E. Scripta Mater 2010;62:532.
[31] Byer CM, Li B, Cao B, Ramesh KT. Scripta Mater 2010;62:536.
[32] Yu Q, Shan Z-W, Li J, Huang X, Xiao L, Sun J, et al. Nature 2010;463:335.
[33] Cao A, Wei Y, Ma E. Phys Rev B 2008;77:195429.
[34] Deng C, Sansoz F. Acta Mater 2009;57:6090.
[35] Jin Z-H, Gumbsch P, Albe K, Ma E, Lu K, Gleiter H, et al. Acta Mater 2008;56:1126.
[36] Senger J, Weygand D, Gumbsch P, Kraft O. Scripta Mater 2008;58:587.
[37] Weygand D, Poignant M, Gumbsch P, Kraft O. Mater Sci Eng A 2008;483–484:188.
[38] Weinberger C, Cai W. Proc Nat Acad Sci USA 2008;105:14304.
[39] Greer JR, Weinberger C, Cai W. Mater Sci Eng A 2008;493:21.
[40] Lee S, Nix W. Mater Sci Eng A 2010;527:1903.
[41] Uchic MD, Shade PA, Dimiduk DM. Annu Rev Mater Res 2009:39.
[42] Greer JR, de Hosson JTM. Prog Mater Sci 2011. doi:10.1016/j.pmatsci.2011.01.005.
[43] Rinaldi A, Peralta P, Friesen C, Sieradzki K. Acta Mater 2008;56:511.
[44] Konstantin AA, Sansoz F. Nano Lett 2007;7:2056.
[45] Deng C, Sansoz F. Appl Phys Lett 2009;95:091914.
[46] Mara NA, Bhattacharyya D, Dickerson P, Hoagland RG, Misra A. Appl Phys Lett 2008;92:231901.
[47] Mara NA, Bhattacharyya D, Hirth JP, Dickerson P, Misra A. Appl Phys Lett 2010:97.
[48] San Juan JM, Nó ML, Schuh CA. Adv Mater 2008;20:272.
[49] Clark BG, Gianola DS, Kraft O, Frick CP. Adv Eng Mater 2010;12:808.
[50] Jang D, Greer JR. Scripta Mater 2011;64:77.
[51] Zhu T, Li J. Prog Mater Sci 2010;55:710.
[52] Kiener D, Motz C, Dehm G. Mater Sci Eng A 2009;505:79.
[53] Ng KS, Ngan AHW. Scripta Mater 2008;59:796.
[54] Dollar M, Gleiter H. Scr Metall 1985;19:481.
[55] Pathak S, Michler J, Wasmer K, Kalidindi S. Submitted for publication. 2011.
[56] Sun S, Adams BL, Shet C, Saigal S, King W. Scripta Mater 1998;39:501.
[57] Ng KS, Ngan AHW. Phil Mag 2009;89:3013.
[58] Jerusalem A. Private communications.
[59] Kiener D, Motz C, Rester M, Jenko M, Dehm G. Mater Sci Eng A 2006;459:262.
[60] Shim S, Bei H, Miller MK, Pharr GM, George EP. Acta Mater 2009;57:503.
[61] Kiener D, Motz C, Dehm G, Pippan R. Int J Mater Res 2009;100:1074.
[62] Ng KS, Ngan AHW. Acta Mater 2009;57:4902.
[63] Deshpande VS, Needleman A, Van der Giessen E. J Mech Phys Solids 2005;53:2661.
[64] Nicola L, Xiang Y, Vlassak JJ, Van der Giessen E, Needleman A. J Mech Phys Solids 2006:54 2089.

Studying grain boundary regions in polycrystalline materials using spherical nano-indentation and orientation imaging microscopy

Siddhartha Pathak, Johann Michler, Kilian Wasmer & Surya R. Kalidindi

Journal of Materials Science
Full Set - Includes `Journal of Materials Science Letters'

ISSN 0022-2461
Volume 47
Number 2

J Mater Sci (2012) 47:815-823
DOI 10.1007/s10853-011-5859-z

Springer

J Mater Sci (2012) 47:815–823
DOI 10.1007/s10853-011-5859-z

Studying grain boundary regions in polycrystalline materials using spherical nano-indentation and orientation imaging microscopy

Siddhartha Pathak · Johann Michler · Kilian Wasmer · Surya R. Kalidindi

Received: 24 June 2011 / Accepted: 6 August 2011 / Published online: 18 August 2011

Abstract In this article, we report on the application of our spherical nanoindentation data analysis protocols to study the mechanical response of grain boundary regions in as-cast and 30% deformed polycrystalline Fe–3%Si steel. In particular, we demonstrate that it is possible to investigate the role of grain boundaries in the mechanical deformation of polycrystalline samples by systematically studying the changes in the indentation stress–strain curves as a function of the distance from the grain boundary. Such datasets, when combined with the local crystal lattice orientation information obtained using orientation imaging microscopy, open new avenues for characterizing the mechanical behavior of grain boundaries based on their misorientation angle, dislocation density content near the boundary, and their propensity for dislocation source/sink behavior.

S. Pathak · J. Michler · K. Wasmer
EMPA, Swiss Federal Laboratory for Materials Science and Technology, Feuerwerkerstrasse 39, 3602 Thun, Switzerland

S. Pathak (✉) · S. R. Kalidindi
Department of Materials Science and Engineering, Drexel University, Philadelphia, PA 19104, USA
e-mail: pathak@caltech.edu; siddharthapathak@gmail.com

Present Address:
S. Pathak
Materials Science, California Institute of Technology (Caltech), 1200 E. California Blvd., MC 309-81, Pasadena, CA 91125-8100, USA

S. R. Kalidindi
Department of Mechanical Engineering and Mechanics, Drexel University, Philadelphia, PA 19104, USA

Introduction

Grain boundaries play an important role in the mechanical response of polycrystalline metals. The well-known Hall–Petch effect [1, 2] relates the increase in yield strength to a decrease in the average grain size in the sample through a power-law expression. Although the effect is clearly established, its physical origins are a matter of debate in literature [3, 4]. The physical explanations for the Hall–Petch effect generally assume either dislocation pile-ups [1, 2] or higher dislocation densities in the grain boundary regions [5]. The dislocation pile-up model implicitly assumes that the grain boundaries are not effective as dislocation sinks. On the other hand, the models that invoke higher dislocation densities in the grain boundary regions (compared to the bulk of the grain) rely on grain boundaries serving as effective sources of dislocations [6]. In this article, we outline a new methodology for studying these effects across individual grain boundaries using spherical nanoindentation stress–strain curves.

Mechanical studies involving grain boundaries have traditionally been conducted on macroscopic specimens containing multi-grained microstructures, and only recently researchers have started to interrogate the mechanical response of materials at the scale of individual grain boundaries. Among the experimental techniques available at these length scales, nanoindentation, with its high resolution load and depth sensing capabilities, shows the greatest promise due to its ease of experimentation and versatility [7, 8]. In particular, using spherical indenters, our recent work [9–11] has demonstrated the feasibility of transforming the raw load–displacement data into meaningful indentation stress–strain curves. These indentation data analyses methods have captured successfully the local loading and unloading elastic moduli, the local indentation

yield strengths, and certain aspects of post-yield strain hardening behavior in various polycrystalline metal samples. More specifically, the use of these indentation stress–strain curves makes it possible to analyze the initial loading segments of spherical indentation; before the indentation itself imposes additional local plastic deformation and alters the local microstructure and its properties. This has enabled the measurement of the local indentation yield strengths in individual grains of deformed polycrystalline metallic samples, which in turn can be related to percentage increases in the local slip resistances from their fully annealed conditions [12]. In this paper, we apply these methods to indentations across grain boundaries showing their potential in investigating the role of grain boundaries in the mechanical response of polycrystalline samples.

Other than nanoindentation certain other techniques of testing miniaturized samples, such as compression testing of micro-pillars containing grain boundaries produced by removing material around a selected region of interest using a focused-ion beam (FIB), have also shown promise in examining the mechanical behavior of grain boundaries [13]. However, these techniques typically require tremendous resources in terms of sample preparation, test conditions and operator time, which make their large scale use uneconomical.

Prior attempts to study the mechanical response of grain boundary regions using indentation have been mostly limited to measuring the hardness and modulus using sharp (Vickers, Berkovich, cube corner) indenters. However, most studies have found hardness to be a poor indicator for measuring grain boundary strengthening effects [14, 15]. Only one study [16] has reported a significant change of hardness close to grain boundary, but these results could not be reproduced by others [17]. It is interesting to note that the few studies which have reported a weak dependence of hardness on the distance from the grain boundary have all used very low maximum loads for their hardness measurements [18–23]. This was studied systematically in the work of Eliash et al. [24] who noted that the width of their grain boundary-affected zone in molybdenum decreased with increasing maximum indentation loads, and for indentation loads exceeding 10 mN (using a Berkovich indenter), the trend vanishes. These studies point to the importance of calculating the contact stresses at or close to yield in indentation experiments.

The focus of the above mentioned studies has been primarily on measuring the resistance offered by grain boundaries to dislocation transmission across them. In these studies, the sharp indenters introduced substantial amount of plastic deformation in the sample before the dislocations were pushed to the grain boundaries and impeded by them. Therefore, the plastic deformation introduced by indentation in those experiments is likely to influence strongly the mechanical property being measured. The approach taken in this study is fundamentally different. The use of spherical indentation and our indentation data analyses protocols allow us to estimate the local indentation yield strength from the initial loading segment. In this way, the characterized property (the initial indentation yield point from the loading segment) corresponds to the intact material at the indentation site, and can be used to differentiate between inherent differences in the local material structure at the indentation site. Using Orientation Imaging Microscopy (OIM) [25, 26], which is based on automated indexing of back-scattered electron diffraction patterns, the structure information at the indentation site is then correlated with the mechanical data obtained from nanoindentation. In particular, in this study we demonstrate the capability of our techniques to measure the differences in indentation modulus and yield stresses across grain boundaries both as a function of the grain boundary character (high versus low angle grain boundary measured using OIM), and imposed cold work on the sample.

In addition, our investigations also revealed a new method for characterizing the dislocation source/sink behavior of grain boundaries by monitoring the (lack of) pop-ins in the vicinity of some (but not all) grain boundaries. The pop-in or strain burst being referred to here is the first pop-in in the sample under the indenter at lower loads [27], and should not be confused with the grain boundary induced pop-ins that occurs at much higher indentation loads and depths (hundreds of nanometers) [15, 22, 28]. As discussed in this article, the decrease in the propensity of pop-ins in the near-grain boundary regions in annealed samples could be used to quantify their potency as effective dislocation sources.

Materials and methods

Polycrystalline as-cast samples of Fe–3%Si steel, sectioned from the chill zone of a directionally solidified electrical steel ingot, were used in this study. We selected these particular samples since we have already established a number of the experimental protocols and the orientation dependence of indentation yield strength in annealed crystals in this material [12, 27]. These samples exhibited extremely large grains (of the order of few millimeters in effective grain size). One sample was given a 30% reduction in simple compression at room temperature to produce a moderately deformed microstructure.

Surface preparation is known to influence the extraction of indentation stress–strain curves from spherical nanoindentation on metal samples, as discussed in detail in our earlier report [27]. Following the procedure outlined in [27], the samples (as-cast as well as 30% deformed) were

prepared for indentation using a Buehler grinding and polishing machine. After grinding with SiC papers, 3 and 1 μm diamond suspensions were used for polishing the samples in conjunction with several intermediate etches by Nital (5% volume mixture of nitric acid in ethanol). The samples were subsequently polished using 0.05 μm colloidal silica. Two approaches were followed for removing the disturbed surface layer caused by mechanical polishing. For one set of both the as-cast and 30% deformed samples, the final step included vibratory polishing with 0.02 μm colloidal silica on a Buehler vibratory polisher for several (2–4) days. Another sample set was electropolished at room temperature using a mixture of 95% acetic acid and 5% perchloric acid at a voltage of 60–90 V and a current of 0.5–1 A.

OIM scans on the samples (as-cast as well as deformed) were already obtained in a previous study [12]. Based on the OIM scans, three grains in the as-cast sample (labelled 1, 2, and 3) and two grains in the 30% deformed sample (labelled 4 and 5) were chosen for this study. In particular, the boundaries between Grains 1 and 2 (high mis-orientation angle in annealed condition), 2 and 3 (low mis-orientation angle in annealed condition), and 4 and 5 (high mis-orientation angle in the deformed condition) were studied by nanoindentation. The processing history of these samples (as described before) is such that the boundaries of the large (millimetre–range) grains studied here are expected to be nominally perpendicular to the sample surface. This was also verified by cutting ~10 μm deep trenches across the boundaries using FIB sections.

Nanoindentations were carried out using two different nanoindenters—the MTS XP® system maintained and operated by the Centralized Research Facilities in the College of Engineering at Drexel University, Philadelphia, USA, and the Agilent G200® system located at the Paul Scherrer Institut (PSI), Villigen, Switzerland. Both systems were equipped with the continuous stiffness measurement (CSM) attachment. Three different spherical diamond tips with radii of 1, 10, and 13.5 μm, respectively, were used in this study. The different radii of the indenters allow us to explore the influence of indentation length scales on the measurements. The indentations were performed on a line inclined at a shallow angle to the grain boundary, so as to allow more indents close to the grain boundary. The large grain sizes in our samples allowed us to perform between three to five lines of indents, with each line containing 20 indents spaced 10 μm apart, across each grain boundary for each indenter size. This resulted in at least 100 indents across every grain boundary. The rather larger number of indentations used in this study allows us to ensure that the mechanical trends across the grain boundaries can be clearly distinguished from the inherent experimental scatter present in nanoindentation measurements. The perpendicular distance from the center of the indent to the grain boundary line was calculated as the distance of the respective indent from the boundary. The indentation contact radius at maximum load for the smaller 1 μm indenter was around 400 nm for the samples studied here; for the larger 10 and 13.5 μm indenters, the indentation contact radius was around 1 μm. So the 10 μm spacing between indents should be sufficient to prevent any interference between neighboring indents.

The measured load–displacement data in spherical nanoindentation was converted into indentation stress–strain curves to allow a better analysis of the local mechanical response. The data analysis protocols are detailed in Ref. [9] and can be briefly summarized as a two-step procedure. The first step in the analysis process is an accurate estimation of the point of effective initial contact in the given data set, i.e., a clear identification of a zero-point that makes the measurements in the initial elastic loading segment consistent with the predictions of Hertz's theory [29–31]. As shown in Ref. [9], the zero point can be conveniently determined using the following equation for the initial elastic segment in a frictionless, spherical indentation:

$$S = \frac{3P}{2h_e} = \frac{3\left(\tilde{P} - P*\right)}{2\left(\tilde{h}_e - h*\right)} \tag{1}$$

where $\tilde{P}$, $\tilde{h_e}$, and S are the measured load signal, the measured displacement signal, and the continuous stiffness measurement (CSM) signal in the initial elastic loading segment from the machine, respectively, and $P*$ and $h*$ denote the values of the load and displacement values at the point of effective initial contact. Rearrangement of Eq. 1 reveals that a plot of $\tilde{P} - \frac{2}{3}S\tilde{h}_e$ against S will produce a linear relationship whose slope is equal to $-\frac{2}{3}h*$and the y-intercept is equal to P^*. A linear regression analysis can then be performed to identify the point of the effective initial contact (P^* and h^*) very accurately.

In the second step, the values of indentation stress and strain can be calculated by recasting Hertz theory for frictionless, elastic, spherical indentation as

$$\sigma_{\text{ind}} = E_{\text{eff}}\varepsilon_{\text{ind}},\ \sigma_{\text{ind}} = \frac{P}{\pi a^2},\ \varepsilon_{\text{ind}} = \frac{4}{3\pi}\frac{h_e}{a} \approx \frac{h_e}{2.4a},$$
$$a = \frac{S}{2E_{\text{eff}}},\ \frac{1}{E_{\text{eff}}} = \frac{1-\nu_s^2}{E_s} + \frac{1-\nu_i^2}{E_i},\ \frac{1}{R_{\text{eff}}} = \frac{1}{R_i} + \frac{1}{R_s}, \tag{2}$$

where σ_{ind} and ε_{ind} are the indentation stress and indentation strain, a is the radius of the contact boundary at the indentation load P, h_e is the elastic indentation depth, S (=dP/dh_e) is the elastic stiffness described earlier, R_{eff} and E_{eff} are the effective radius and the effective stiffness of the indenter and the specimen system, ν and E are the

Poisson's ratio and the Young's modulus, and the subscripts s and i refer to the specimen and the indenter, respectively.

Results and discussion

Effects of surface preparation and indenter size on pop-ins

Pop-ins or displacement bursts are a common feature in indentation measurements on samples with low dislocation densities. These are attributed to the fact that the indentation zone size in these experiments at the point of initiation of plastic strain under the indenter is comparable or smaller than the dislocation-network length scales in the sample (e.g., spacing of dislocations, dislocation cell size). The occurrence of the pop-ins can therefore be correlated to the difficulty of activating a dislocation source in the primary indentation zone. As expected, the propensity for pop-ins decreases with an increase in the indentation zone size (larger indenter radius), as well as with an increase in the dislocation density of the sample (e.g., in a deformed material) [27].

It is well-known that metal samples typically have a 5–10 nm-thick native oxide layer on their surfaces, and the breakup of such an oxide film could also result in pop-in events. However, no such pop-in events were found to occur in the 30% deformed Fe–3%Si samples (shown later in Fig. 4). Since the oxide layer thickness is expected to be identical in both samples (as-cast and deformed), the pop-ins seen in this study are not thought be due to the oxide layer breakup. This issue has been discussed in significant detail in our previous publication [27] as well.

Pop-ins, which appear as displacement bursts in a load versus displacement plot, manifest as strain bursts in indentation stress–strain curves. As seen in Fig. 1, an indentation stress–strain plot with an initial pop-in often exhibits a large discontinuity. This makes it difficult to accurately estimate the indentation yield strength (Y_{ind}) from such a plot. As-cast samples prepared using electropolishing are highly susceptible to this problem, as shown in Fig. 1a. In this study, we have vibro-polished one set of the as-cast samples with the hope of avoiding the pop-ins without significantly affecting the indentation yield strength. Representative indentation load–displacement curves and stress–strain curves obtained from the same grain in the as-cast sample with an electro-polished surface and a vibro-polished surface are compared to each other in Fig. 1a. The excellent agreement between the back-extrapolated Y_{ind} obtained on the electro-polished surface (with the pop-in) and the Y_{ind} measured on the vibro-polished surface (without

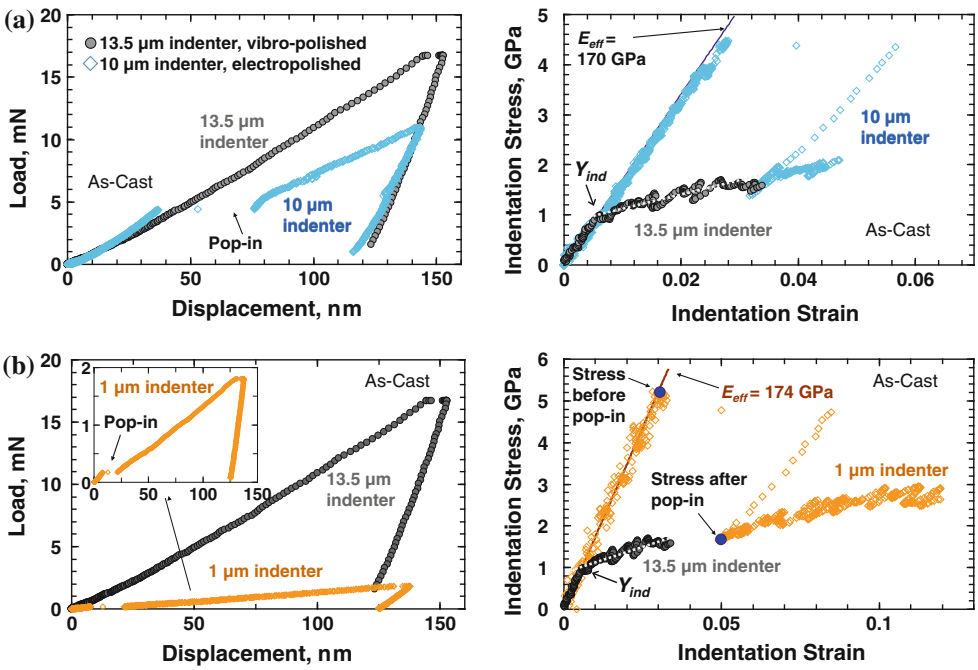

Fig. 1 **a** Effect of final surface finish: vibro-polish versus electro-polish. Indentations on the as-cast Fe–3%Si steel's electro-polished surface almost always result in a large pop-in. Pop-ins are usually suppressed on the vibro-polished surfaces when using the large 13.5 μm indenter. **b** Effect of indenter size: indents with the small 1 μm indenter show consistent pop-ins on the vibro-polished surface. The good agreements between the indentation stress–strain curves from different surface finishes and different indenter radii provide additional validation of the data analysis protocols used. The ratio of the stress before and after pop-in is used as an indicator of the ease of establishing a dislocation source in the indentation zone

the pop-in) was confirmed in numerous measurements on the sample. These measurements indicate that the vibro-polishing method introduces only a small number of dislocations into the sample surface, which are enough to suppress the pop-ins for the larger indenter sizes (10 and 13.5 μm radii) but do not appear to influence the measured Y_{ind} on the as-cast samples.

Figure 1b provides a comparison of the indentation stress–strain curves obtained in the same grain using the 1 and 13.5 μm indenters, both on vibro-polished surfaces. It is seen that the 1 μm indenter produces a large pop-in confirming that the amount of dislocations introduced during vibro-polishing is not large enough to suppress pop-ins at the small (1 μm radius) indenter sizes. The good agreement between the back-extrapolated Y_{ind} from the indentation stress–strain curve with the pop-in and the Y_{ind} from the indentation stress–strain curve without the pop-in, despite the big difference in the indenter radii, is quite reassuring. All of these observations indicate that it is viable to extract a value of the Y_{ind} on the vibro-polished surfaces of the as-cast samples.

Following the observations above, vibro-polishing was chosen as the final sample surface preparation step for the as-cast samples studied here. Vibro-polishing also reduces the possibility of developing a significant groove at the grain boundary that often results from electropolishing [19, 24]. Thus, for the present sample set, the smaller 1 μm radius indenter is ideal for studying the pop-in behavior in the grain boundary regions, while the larger 10 and 13.5 μm radii indenters, which seldom exhibit pop-ins, are ideally suited for estimating the Y_{ind} values in the same regions. The 30% deformed Fe–3%Si sample has a significantly larger dislocation density and hence no pop-ins are observed on this material irrespective of the indenter radius size and/or surface finish technique used [27].

Grain boundaries as dislocation sources

In order to examine the potential role of grain boundaries as dislocation sources, we examined the ratio of indentation stresses before and after the pop-in as a function of the distance from the grain boundary. As an example, the indentation stresses before and after pop-in on the indentation stress–strain curve are identified in Fig. 1b. It is suggested here that the ratio of these stresses can be used as a measure of the difficulty of establishing a dislocation source in the sample. In the limiting case where the pop-in disappears completely, this ratio becomes one and suggests that there was no difficulty in establishing a dislocation source.

As mentioned earlier, the pop-in behavior across grain boundaries was studied using the smaller 1 μm radius spherical indenter. In order to allow for more measurements, the indentations were performed on a line inclined at a shallow angle to the grain boundary as shown in Fig. 2. This approach allowed us to get many more measurements at varying distances from the grain boundary while ensuring that the indentations were sufficiently spaced to avoid any interference from each other.

Figure 2 shows two representative measurements on two different grain boundaries with two substantially different

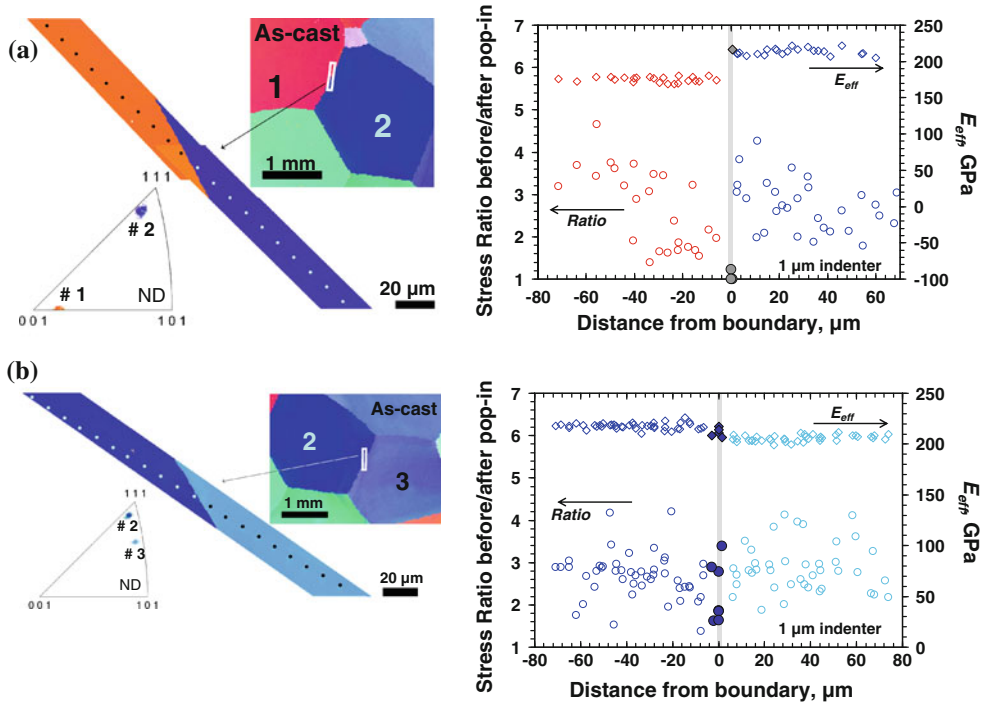

Fig. 2 Effective modulus (E_{eff}) and ratio of stresses before and after pop-ins across **a** a high angle grain boundary between Grains 1 and 2 and **b** a low angle grain boundary between Grains 2 and 3 in vibro-polished as-cast Fe–3%Si steel. The OIM maps show the location of a representative row of indents with respect to the corresponding boundaries

lattice misorientation angles. The OIM scans in Fig. 2 are color-coded to reflect the positions of the orientations in the inverse pole figure map using the standard convention (i.e., grains colored red, green, and blue have (001), (101), and (111) crystallographic planes parallel to the sample surface, respectively). In the indentation stress-ratio plots shown in Fig. 2, the grain boundary has been marked as a vertical line with a finite thickness. The thickness of this line reflects the region in which the primary indentation zone size at Y_{ind} includes the grain boundary. In other words, any indentation performed within the thickness of the vertical line shown as the grain boundary is expected to apply substantial stress on the grain boundary. The thickness of the line representing the grain boundary is calculated as $3a_{Y_{ind}}$, where $a_{Y_{ind}}$ is the contact radius at the indentation yield stress (following Ref. [9]).

Figure 2 shows the variance of the ratio of the indentation stress before and after pop-in with the distance from the grain boundary for the two boundaries depicted in the figure. It is seen that the grain boundary between Grains 1 and 2 is quite effective as a dislocation source (Fig. 2a), because the pop-ins essentially disappear in the indentations conducted at the grain boundary (reflected by the observation that the ratio of indentation stress before and after the pop-in goes to one). Note also the higher effective modulus (E_{eff}) for the near-(111) oriented Grain 2 as compared to the near-(001) oriented Grain 1 in Fig. 2a, denoting the high mismatch in stiffness between the two grains. Figure 2b also indicates that the other (low angle) grain boundary between Grains 2 and 3 is not as effective in suppressing the pop-ins, because the indentation stress ratio at the grain boundary has not changed significantly from the bulk of the grains. It is therefore clear from Fig. 2 that different grain boundaries exhibit different levels of potency in serving as dislocation sources in the deformation of polycrystalline materials, and the experimental protocols suggested here are capable of quantifying their effectiveness. Similar decrease and/or disappearance of the nanoindentation pop-ins in the vicinity of some (but not all) grain boundaries have been noted by other researchers as well [14, 19, 21, 22, 24, 28]. Obviously, it is important to repeat these measurements on a much larger number of grain boundaries to quantify the misorientation dependence of the grain boundary potency in serving as dislocation sources.

Grain boundaries regions in as-cast samples

As noted earlier, pop-ins can be suppressed using a larger indenter (see Figs. 1b, 3b). Therefore, we studied the changes in indentation moduli and yield strengths in the grain boundary regions in the as-cast samples using a larger 13.5 μm radius spherical indenter using the protocols

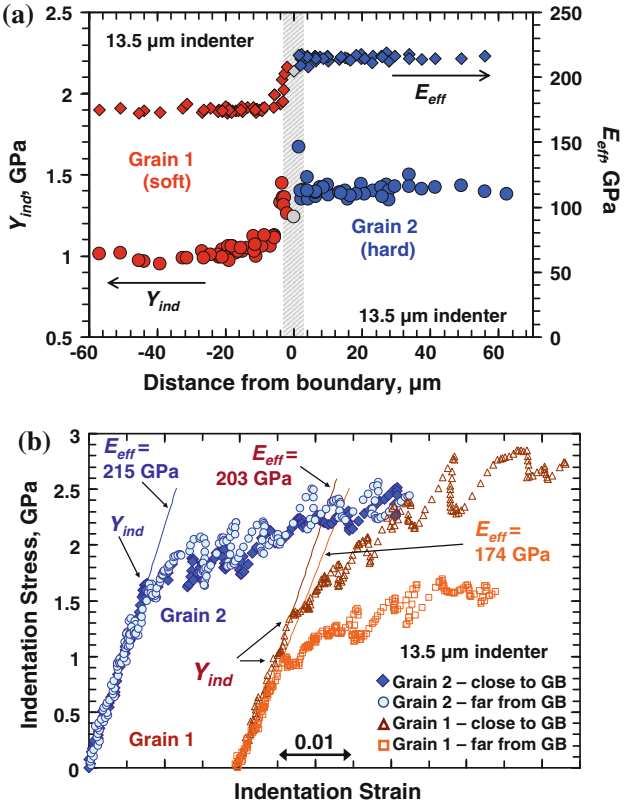

Fig. 3 **a** Measure of E_{eff} and Y_{ind} across the same high angle grain boundary shown in Fig. 2a. **b** Representative indentation stress–strain curves from the two grains showing the differences in mechanical responses between near grain boundary regions versus grain interiors

described earlier. The effective indentation modulus (E_{eff}) and the indentation yield strength (Y_{ind}) extracted from these measurements on the boundary between Grains 1 and 2 are plotted in Fig. 3a as a function of the distance from the grain boundary. The grains are labeled as 'soft' and 'hard' in a relative sense based on their indentation yield strengths. Note that the same grain boundary region in Fig. 3a is marked as a much wider region compared to Fig. 2 because of the larger indenter tip size in Fig. 3. Figure 3b shows representative indentation stress–strain curves in each grain for regions close to the grain boundary (that is indents placed within the thickness of the vertical line shown as the grain boundary in Fig. 3a), and far from the grain boundary.

Figure 3a provides strong validation for our protocols. The as-cast samples are not expected to have any excess dislocation storage at the grain boundaries. Therefore, both E_{eff} and Y_{ind} are fairly uniform in each grain and there is almost a step transition at the grain boundary. As expected, the indentation stress–strain curves in the regions adjacent to the grain boundary on the side of the soft grain show a composite effect with increases in both the indentation

modulus and the indentation yield strength reflecting contributions from both grains (see Fig. 3b).

Grain boundaries regions in deformed samples

Next, we studied selected grain boundary regions in the 30% compressed samples using the same protocols. As reported in our previous studies [12, 27], pop-ins do not appear in deformed samples where it is relatively easy to set up a dislocation source using the existing network of forest dislocations in the sample. Therefore, we investigated the grain boundary regions in the deformed samples using both small and large indenters, as well as both vibro-polished and electro-polished surfaces. A representative set of results from this study are presented in Fig. 4. Figure 4b shows representative indentation stress strain curves in each grain for regions close to and far from the grain boundary, while the summary of the E_{eff} and Y_{ind} values are shown in Fig. 4c.

As in the as-cast sample, the values of E_{eff} were fairly uniform in each grain of the 30% deformed sample as well and show a step like transition at the grain boundary. However, the variation of Y_{ind} indicated a substantial transition zone on one side of the grain boundary. The measurements are also remarkably consistent from all three indenters used in the study, despite the large range in the indenter tip radii. This level of consistency in the measurements provides additional validation for the protocols used in this study. No effects of the final surface polishing step (vibro-polish versus electro-polish) were observed.

In order to better understand the measurements of Y_{ind} shown in Fig. 4c, we have computed the percentage increases in the yield strength from the as-cast condition as a function of the distance from the grain boundary, as shown in Fig. 4d. As demonstrated in our recent study [12], it is possible to experimentally map the orientation dependence of the indentation yield strength for a given sample and to use this map for normalizing the indentation yield strength. This form of normalization accounts for the orientation dependence of the indentation measurements, and thus the percentage increase in the Y_{ind} can be interpreted as the percentage increase in the local slip resistance at the indentation site. This in turn can be interpreted as an indicator of the local dislocation density at the indentation site.

The Taylor factors in simple compression for Grains 4 and 5 were estimated using standard crystal plasticity models [32] to be 2.01 and 3.15, respectively. This suggests that Grain 5 should show more hardening as a result of the 30% compression compared to Grain 4. The measurements shown in Fig. 4d away from the grain boundary are in complete accord with this expectation.

However, it is seen from Fig. 4d that the grain boundary region on the side of Grain 5 accumulated much less dislocation density in the immediate vicinity of the grain boundary than far away from the boundary. Furthermore, it is seen that the dislocation density very near the grain boundary on the side of Grain 5 is also somewhat lower

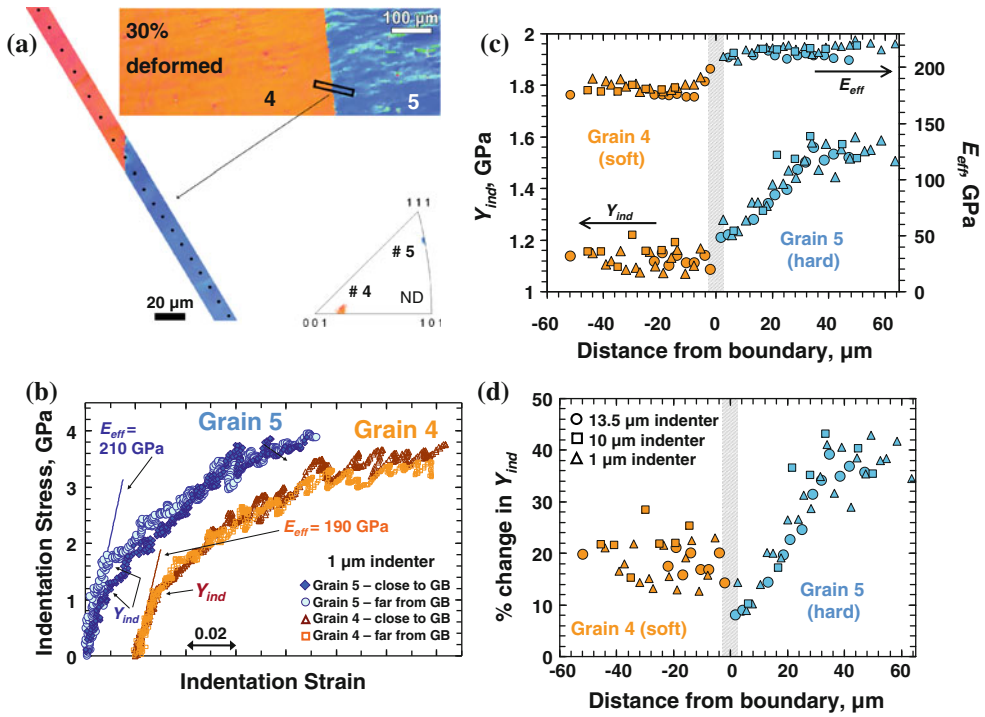

Fig. 4 **a** OIM maps of the 30% deformed Fe–3%Si steel sample showing the location of the indents with respect to the grain boundary. **b** Representative indentation stress–strain curves from the two grains showing the differences in mechanical responses between near grain boundary regions versus grain interiors. **c** Measure of E_{eff} and Y_{ind} across the grain boundary between Grains 4 and 5. **d** Estimate of the percentage change in Y_{ind} from the annealed condition following Ref. [12]

than the dislocation density in the grain boundary region on the side of Grain 4. These observations suggest that the nature of the grain boundary or the grain boundary character on both sides of a grain boundary can be substantially different from each other. In the example shown in Fig. 4, it is seen that the grain boundary on the side of Grain 5 acts as an efficient dislocation sink by absorbing the dislocations from the grain boundary region on the side of Grain 5.

We note here again that these samples were sectioned from a directionally solidified electrical steel ingot, and as such the grain boundaries explored in this study are expected be nominally vertical to the indentation surface. This was also verified by ~ 10 μm deep FIB cuts across the boundaries. Thus, any possibility of an inclined geometry of the boundaries below the surface is very remote. It is also noteworthy that these observations are consistent with previously reported observations in aluminum bicrystals based on high resolution measurements of orientation gradients on the sample surface [33–35].

Hardness across grain boundaries

It is emphasized here that insights obtained about the grain boundary regions from Figs. 3 and 4 are largely made possible by the use of our spherical nanoindentation data analyses protocols. In particular, computing the local indentation yield stress from the initial loading segment allows us to estimate the changes in the dislocation content at the indentation site, before the additional plastic strain induced by the indentation itself. This is in contrast to traditional hardness measurements using nanoindentation, where the contact stress at a specified load is typically measured after the material has experienced significant plastic strain. As a result, the conventional hardness measurements in the grain boundary regions fail to reveal meaningful trends. This is demonstrated in Fig. 5, where the variation of the local hardness is plotted as a function of the distance from the grain boundary. The hardness values in this case was estimated as the contact stress at 14 mN of load using the 13.5 μm indenter for the same grain boundary regions that are shown in Figs. 3 and 4. The hardness data shown in Fig. 5 does not reveal any discernable or useful trends. This observation was also reported by other researchers who have used indentation hardness to measure the mechanical response of grain boundaries [14, 15, 24]. The above discussion suggests that the initial indentation yield stress calculated from the loading segments of spherical indentation is a more reliable measure of the changes in the local dislocation density in the sample, and can potentially provide valuable new insights into the mechanical response of grain boundary regions.

Effect of indenter size

As noted earlier, indenter size strongly influenced the occurrence of pop-ins in the as-cast grains. In the experiments on deformed grains where there were no pop-ins, it was observed that the indenter size also strongly influenced the strain hardening rates observed in the indentation stress–strain curves. As an example, the indentation stress–strain curves obtained in the deformed Grain 5 using two different indenter sizes (1 and 10 μm radii) are shown in Fig. 6a. Although there is excellent agreement in the values of the indentation yield strength in the two indentation stress–strain curves, the post yield behaviors are substantially different.

In order to understand the differences in the post-yield behaviors for the different indenter sizes, we present in Fig. 6b the evolution of the contact radius corresponding to the two indentation stress–strain curves in Fig. 6a. It is seen that the contact radius for the smaller indenter is only about 100 nm at indentation yield. The indentation zone size can be estimated to be of the order of 2–3 times the contact radius [9]. In general dislocation cells sizes in most metals are reported to be of the order of 1 μm. Therefore, the length scale of the indentation zone for the small indenter may not be adequate to set up the dislocation structures needed to efficiently produce forest dislocations needed for strain hardening. As the indentation strain increases, the contact radius gradually increases and the strain hardening rate

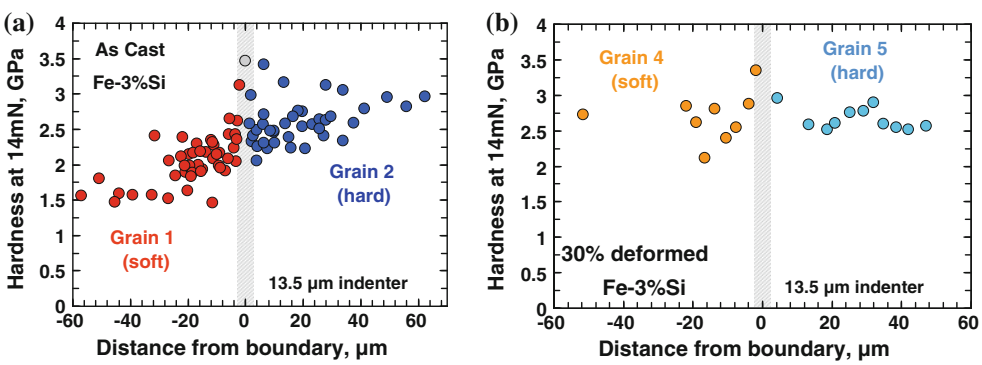

Fig. 5 Hardness profiles, calculated as the contact stress at 14 mN load for the 13.5 μm indenter, across **a** Grains 1 and 2 for the as-cast Fe–3%Si sample and **b** Grains 4 and 5 for the 30% deformed Fe–3%Si sample

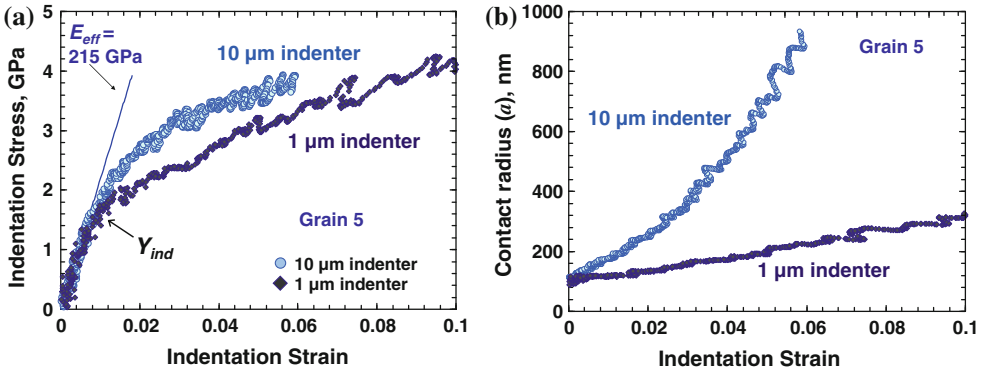

Fig. 6 Effect of indenter size on the indentation stress–strain curves from deformed samples. **a** While the indentation stress–strain curves obtained using two different indenter radii show a similar Y_{ind} value, the bigger 10 μm indenter shows larger strain hardening than the smaller 1 μm indenter. **b** Changes in contact radius a with indentation strain for the two different indenter sizes

appears to pick up. On the other hand, the contact radius increases much faster for the larger indenter. This appears to correspond well with the increased strain hardening rates obtained with the larger indenter.

Conclusions

In summary, we have demonstrated a novel way of characterizing the mechanical behavior of grain boundary regions in polycrystalline materials using spherical nanoindentation. This has been made possible by the combined use of OIM and our data analysis procedures for spherical nanoindentation which allow us to analyze the initial loading portion of the indentation stress–strain response. In this study, our analysis techniques have been able to characterize the indentation yield strengths of near grain boundaries regions in both as-cast and deformed samples, and estimate the percentage increases in local slip resistances. Analysis of the pop-in behavior across grain boundaries was also found to be a useful indicator of the boundary's potency as a dislocation source. Use of these new protocols over a larger number of different kinds of boundaries is expected to be very useful for correlating the structures of the grain boundaries with their mechanical response.

Acknowledgements Authors acknowledge funding from ARO grant W911NF-10-1-0409, Dr. Dejan Stojakovic's help in sample preparation, and many insightful discussions with Prof. Roger Doherty (Drexel University) in preparation of this manuscript. The authors thank Dr. Manuel Pouchon for allowing the use of the Agilent G200® nanoindentation system located at the Paul Scherrer Institut, Villigen, Switzerland, while the MTS XP® System used in this study is maintained and operated by the Centralized Research Facilities in the College of Engineering at Drexel University.

References

1. Hall EO (1951) Proc Phys Soc 64:747
2. Petch NJ (1953) Iron Steel Inst J 174:25
3. Lasalmonie A, Strudel JL (1986) J Mater Sci 21:1837. doi: 10.1007/BF00547918
4. Meyers M, Chawla K (2007) In: Mechanical Behavior Of Materials, Prentice-Hall, Upper Saddle River
5. Meyers MA, Ashworth E (1982) Philos Mag A 46:737
6. Li JCM (1963) Trans Metall Soc AIME 227:239
7. Bucaille JL, Stauss S, Felder E, Michler J (2003) Acta Mater 51: 1663
8. Stauss S, Schwaller P, Bucaille JL, Rabe R, Rohr L, Michler J, Blank E (2003) Microelectron Eng 67–68:818
9. Kalidindi SR, Pathak S (2008) Acta Mater 56:3523
10. Pathak S, Kalidindi SR, Klemenz C, Orlovskaya N (2008) J Eur Ceramic Soc 28:2213
11. Pathak S, Shaffer J, Kalidindi SR (2009) Scr Mater 60:439
12. Pathak S, Stojakovic D, Kalidindi SR (2009) Acta Mater 57:3020
13. Kunz A, Pathak S, Greer JR (2011) Acta Mater 59:4416
14. Ohmura T, Tsuzaki K, Fuxing Y (2005) Mater Trans 46:2026
15. Wang MG, Ngan AHW (2004) J Mater Res 19:2478
16. Lee CS, Han GW, Smallman RE, Feng D, Lai JKL (1999) Acta Mater 47:1823
17. Wo PC, Ngan AHW (2004) J Mater Res 19:189
18. Soifer YM, Verdyan A, Kazakevich M, Rabkin E (2002) Scr Mater 47:799
19. Ohmura T, Tsuzaki K (2008) J Phys D 41:074015
20. Goken M, Kempf M, Bordenet M, Vehoff H (1999) Surface Interface Anal 27:302
21. Ohmura T, Tsuzaki K (2007) J Mater Sci 42:1728. doi: 10.1007/s10853-006-0885-y
22. Soer WA, Aifantis KE, De Hosson JTM (2005) Acta Mater 53:4665
23. Soer WA, De Hosson JTM (2005) Mater Lett 59:3192
24. Eliash T, Kazakevich M, Semenov VN, Rabkin E (2008) Acta Mater 56:5640
25. Adams BL (1997) Ultramicroscopy 67:11
26. Adams BL, Wright SI, Kunze K (1993) Metall Trans A 24A:819
27. Pathak S, Stojakovic D, Doherty R, Kalidindi SR (2009) J Mater Res 24:1142
28. Britton TB, Randman D, Wilkinson AJ (2009) J Mater Res 24:607
29. Hertz H (1896) Miscellaneous Papers. MacMillan and Co. Ltd., New York
30. Johnson KL (1987) Contact Mechanics: Cambridge University Press, Cambridge
31. Sneddon IN (1965) Int J Eng Sci 3:47
32. Kalidindi SR, Bhattacharyya A, Doherty RD (2004) In: Proceedings of the Royal Society of London, Series A (Mathematical, Physical and Engineering Sciences) 460: 1935
33. Sun S, Adams BL, King WE (2000) Philos Mag A 80:9
34. Sun S, Adams BL, Shet C, Saigal S, King W (1998) Scr Mater 39:501
35. Zaefferer S, Kuo JC, Zhao Z, Winning M, Raabe D (2003) On the influence of the grain boundary misorientation on the plastic deformation of aluminum bicrystals. Acta Mater 51:4719

V

Vertically Aligned Carbon Nanotubes

► Chemical Vapor Deposition (CVD)

Vertically Aligned Carbon Nanotubes, Collective Mechanical Behavior

Shelby B. Hutchens and Siddhartha Pathak
California Institute of Technology MC 309-81, Pasadena, CA, USA

Synonyms

CNT arrays; CNT brushes; CNT bundles; CNT foams; CNT forests; CNT mats; CNT turfs

Definition

Vertically aligned carbon nanotubes are complex, hierarchical structures of intertwined tubes arrayed in a nominally vertical alignment due to their perpendicular growth from a stiff substrate. They are a unique class of materials having many of the desirable thermal, electrical, and mechanical properties of individual carbon nanotubes, while exhibiting these properties through the collective interaction of thousands of tubes on a macroscopic scale.

Introduction

While individual CNTs have been announced as the strongest material known and have shown extremely high strength and Young's modulus in tensile tests (► Carbon Nanotubes), VACNTs are more likely to find use in applications requiring large compliance and deformability. Examples of these include microelectromechanical systems (MEMS) and impact mitigation/energy absorption, where they are promising candidates for their multifunctional nature, wide ranging thermal stability, and relative ease of manufacture. A proper understanding of the collective mechanical behavior of these structures, especially instabilities leading to buckling and inhomogeneities which weaken mechanical performance, is thus of great importance for their design and success in these and other future applications.

Several features set VACNTs apart from other CNT structures. First, the tubes that make up the material grow perpendicularly to the support substrate, making them *nominally* vertically aligned. An important characteristic all VACNTs share is that the tubes themselves are long enough to become intertwined with each other during the growth process, making the structure into a kind of fibrous mat. This is in contrast to arrays of vertically aligned CNTs that are short and/or sparse enough that each CNT stands alone. Because of the nominal alignment, VACNTs exhibit a marked anisotropy in structure which is most apparent at magnifications of 1,000 × (see Fig. 1, left). Magnifying one hundred times more reveals their highly interconnected, foam-like structure and the network

B. Bhushan (ed.), *Encyclopedia of Nanotechnology*, DOI 10.1007/978-90-481-9751-4,

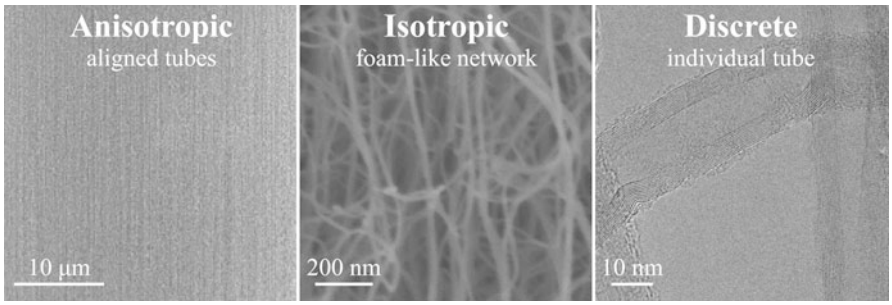

Vertically Aligned Carbon Nanotubes, Collective Mechanical Behavior, Fig. 1 A series of micrographs illustrating the hierarchical nature of the VACNTs. The *left* and *center* images are taken with a scanning electron microscope (SEM). The *right* image is a transmission electron micrograph (TEM)

of CNTs begins to appear nearly isotropic. Magnifying another hundred times, one obtains a view of the individual CNTs themselves. As evidenced by the micrographs in Fig. 1, in the as-grown state, certain segments of the CNT forest may be pre-buckled/pre-bent, with the resulting bending strain energy being balanced by the favorable contact energy between the tubes [1].

The method by which these structures are synthesized is the primary factor affecting their complex, hierarchical morphology. This microstructure, in turn, affects their mechanical behavior, in particular the modulus, buckling strength, and recoverability. Synthesis techniques for VACNTs can be divided into two main categories: the Chemical Vapor Deposition (CVD) synthesis method, and the Carbide-Derived Carbon (CDC) synthesis method. In the CVD process, the VACNT film is coated onto an existing substrate. This is accomplished by depositing a thin layer of catalyst (e.g., Fe) on the substrate (typically Si or Quartz) and flowing a carbon source (e.g., ethylene) over the substrate at atmospheric pressure and temperatures typically around 750°C. In the CDC method [2], on the other hand, carbon is formed by selective extraction of the metal or metalloid atoms in the carbide (e.g., silicon carbide) at high temperatures (>1,600°C), transforming the carbide structure into pure carbon. Since the CNT layer is formed by inward growth, this usually retains the original shape and volume of the precursor.

VACNTs grown by these different techniques demonstrate very different structure and mechanical properties. Even within materials grown via CVD, control of the growth conditions, such as the atmosphere, catalyst activity, and pressure, are known to significantly affect the repeatability of the VACNT's morphology and hence the consistency of mechanical properties [3]. Differences in the growth processes used are revealed in the widely varying VACNT information reported in literature, as seen in the large range of properties in Table 1, not to mention variations in tube diameter (from 2–3 [4] to 20–50 nm [5], to greater than 100 nm [6]), number of walls in the CNT structure, and degree of tube alignment; properties which are sometimes neither measured nor reported. Further, the different stages of the CNT growth process can result in a height-dependent inhomogeneity [7]. This manifests as a gradient in both the density and the alignment of the tubes within the same VACNT structure. As discussed later in this entry, such a structure gradient may lead to a corresponding strength and stiffness gradient along the VACNT height. As an extreme example of the microstructure–property relationship, CDC-VACNTs are known to have a considerably higher average density (roughly 10 times higher than typical VACNTs), due to the conformal transformation of the carbide into carbon. This in turn leads to significantly larger values for the elastic modulus and yield stress in CDC-VACNTs [4] (see Table 1). These promising characteristics, however, are unavailable for applications requiring macroscopic films as currently only VACNTs grown via CVD can reach macroscopic heights (∼mm). Growth of CDC-VACNTs remains limited to only a few micrometers in height.

Another marked difference in material behavior is the ability of some microstructures to recover from large deformations, while others deform plastically. Within those materials grown via CVD, several groups have observed excellent recoverability [8–10] in their VACNT samples, seeing less than 15% deformation after thousands of cycles of strain to 85%. Other

Vertically Aligned Carbon Nanotubes, Collective Mechanical Behavior, Table 1 Summary of reported VACNT elastic modulus values

Synthesis technique	Density	Measurement method	E (MPa)	Yield/ buckling strength (MPa)	Reference
CVD	87% porosity	Uniaxial compression	50	12	Cao et al. [8]
	97% porosity	Uniaxial compression	818	14.1	Deck et al. [14]
	NG[d]	DMA[e]	~50	NA[f]	Mesarovic et al. [1]
	NG	Uniaxial compression	<2	NA	Suhr et al. [9]
	10^{10} tubes/cm^{2}[a]	Uniaxial compression	0.22–0.25	NA	Tong et al. [15]
	NG	Nanoindentation – Berkovich uniaxial compression	15	0.2–4.3	Zbib et al. [11]
	NG	Nanoindentation – Berkovich	58	NA	Zhang et al. [12]
	NG	Nanoindentation – Berkovich	50 ± 25[b]	NA	Qiu et al. [16]
	0.018 g/cm^3 0.114[c] g/cm^3	Uniaxial compression	NG	0.12 5.5 [c]	Bradford et al. [13]
CDC	0.95 g/cm^3	Nanoindentation – spherical	18,000	90–590	Pathak et al. [4]

NG not given, *DMA* dynamic mechanical analysis, *NA* not applicable
[a]Density in tubes per unit area. Tubes were 20–30 nm in diameter
[b]Reported as reduced modulus. Indentation was performed with a diamond tip, so difference from sample modulus is small
[c]After post-growth CVD treatment

groups, however, observe that the materials remain plastically deformed [5, 11, 12]. Energy can be dissipated in the former as they behave like viscoelastic rubbers (discussed in a later section), whereas energy can be absorbed in the latter. Both appear to deform via the same structural mechanism (localized buckles) intrinsic to the complex microstructure of these systems. It is still largely unclear what is responsible for a VACNT material displaying plastic versus recoverable behavior. Since individual CNTs are known to recover from large bending angles, the plasticity must be due to their collective interactions. Possible interactions include entanglement, tube-to-tube adhesion through attractive interactions (e.g., van der Waals), or the fracture of the tubes themselves. However, fracture is unlikely as experimental observations of quasi-static mechanical loading have shown no evidence of individual tube failure, most notably in Ref. [5]. Two promising clues arise from recent work by Bradford et al. [13]. They find that VACNTs can be converted from irrecoverable to viscoelastic (recoverable) by a second CVD treatment that increases tube diameter and surface roughness, suggesting either may play a role in determining recoverability.

Instrumented indentation, using a variety of tip geometries such as flat punch, spherical, Berkovich, and cube corner, has been the most common method for studying mechanical properties of VACNTs [6]. Each geometry has its own strengths and weaknesses. While maintaining parallel contact between the indenter and the sample is a major concern for flat punch indentation, it does allow for loading in a direction largely normal to tube growth. Because of the marked anisotropy of VACNTs, the sharper Berkovich or cube corner geometries can cause the CNTs to bend away from the indenter in shorter samples, which results in testing a slightly different mode of behavior by applying more load in the direction perpendicular to growth. In both cases, modulus and hardness are measured from the unloading portion of the test. On the other hand, spherical indentation is advantageous in that it allows indentation stress–strain curves to be extracted from the raw load–displacement data, which enables resolution of the evolution of the mechanical response in the VACNT array: from initial elasticity, to the initiation of buckling, to post-buckling behavior at finite strains [4]. Though indentation is a relatively simple test to perform, analyses of the results, especially nonlinear elastic behavior is difficult due to their highly localized stress fields. It is also limited in total strain.

Another testing geometry, that of uniaxial compression, eliminates these localized, applied stress fields

and reveals the existence of a localized deformation mechanism in VACNTs. In these tests, the samples are either large (~1 mm tall) bulk films and compressed between two platens or they are microscale cylinders and compressed using a flat punch indenter. These tests, especially when performed in situ (load–displacement data gathered simultaneously with micrographs in a SEM) can offer valuable insights on the morphological evolution in the VACNTs during deformation [5] and are discussed in detail in the next section.

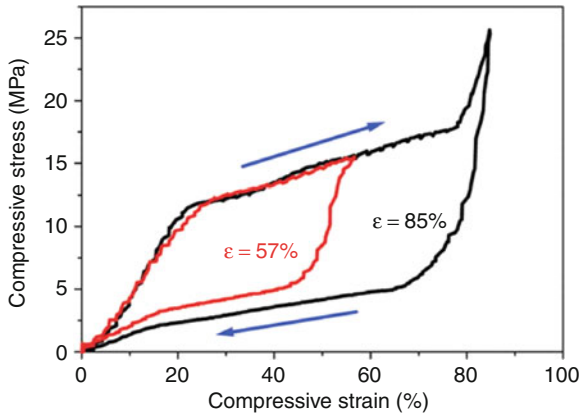

Vertically Aligned Carbon Nanotubes, Collective Mechanical Behavior, Fig. 2 Nominal stress–strain response from the uniaxial compression of a macroscale VACNT sample illustrating the overall embodiment of foam-like elastic-plateau-densification regimes [8] (Reprinted from [8] with permission from AAAS (American Association for the Advancement of Science))

Deformation Under Large Strain

The deformation of VACNTs is governed by their hierarchical microstructure, collective intertube interactions, and inherent property gradient. Taken as a whole, their highly porous nature gives them an overall foam-like response. The idealized stress–strain response of traditional foams is characterized by three distinct loading regimes: an initial elastic loading at low strain, followed by a plateau in the stress during which the supporting struts bend and buckle, and finally a densification regime in which the space between struts has been nearly eliminated and the material begins to approach behavior intrinsic to the struts themselves. For such a response, it is the intermediate plateau regime that is responsible for the bulk of energy absorption in the material, since the area under this region of the stress–strain curve, corresponding to the work done on the material, is largest. This foam-like response of a bulk VACNT film is apparent in the three distinctly differently sloped regions of the stress–strain response shown in Fig. 2. Locally, however, the response of VACNTs is quite unlike that of traditional foams. In VACNTs, the accommodation of strain during uniaxial compression is accomplished entirely through the formation of folds or buckles of small regions of the structure while the remaining portion remains nearly undeformed. This superposition of an overall foam-like response with localized strain accommodation is the key characteristic of VACNT deformation.

Experimental characterization of this buckle formation yields several interesting qualitative results. In their early study, Cao et al. [8] compressed relatively large structures (area: 0.5–2 cm^2, height: 860 μm–1.2 mm) and observed that the buckles formed near the bottom of the structure (the end from which the CNTs grow perpendicularly to the substrate) are more deformed that those that formed near the top (Fig. 3a). Motivated by this observation, they hypothesized that the bottom buckles form first. A reversal of the loading direction, by flipping the sample upside down, resulted in the same deformed morphology, with the tightest buckles forming at what was the end of the sample attached to the growth substrate. These observations point to the idea of an inherent, axial property gradient being responsible for the sequential nature of the buckling. Note that each individual buckle is on the order of 12–25 μm in size (depending on sample height) so that several tens of buckles form during deformation. The sequential, localized buckling phenomenon was later observed in much smaller samples, by Zbib et al. [11] and Hutchens et al. [5] (Fig. 3b, c) illustrating the universality of this response in VACNTs. Buckles in these microscopic studies were 12 and 7 μm in wavelength (measured from the unbuckled conformation) for cylindrical samples with diameters of 30–300 and 50 μm, respectively. The bottom-first buckling mechanism was visually verified by Hutchens et al. [5] through in situ experiments that further revealed the mechanism by which a single, localized buckle evolves. As shown in their study, each individual buckle does not form all at once, but rather nucleates at one point and then propagates laterally

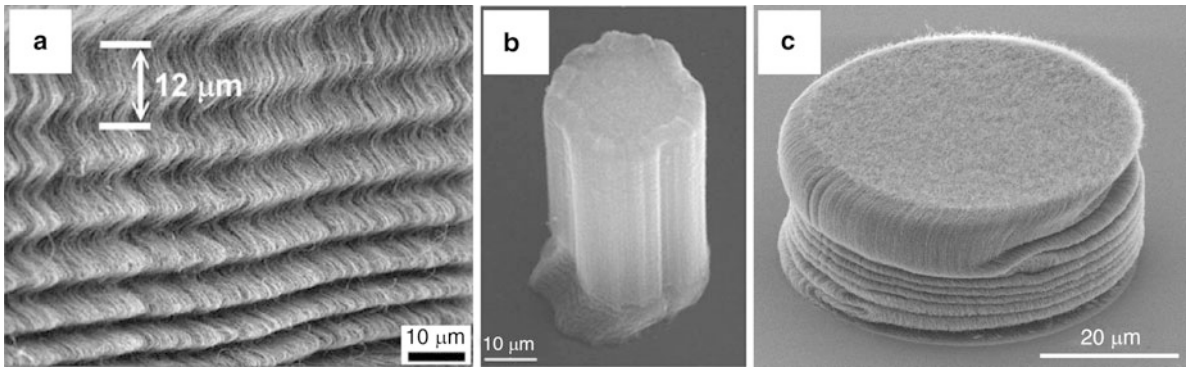

Vertically Aligned Carbon Nanotubes, Collective Mechanical Behavior, Fig. 3 Examples of local buckling in VACNTs. (**a**) Close-up of the wavelike deformation observed after nominal strains of 0.85 over 1,000 cycles from Cao et al. [8] (Reprinted from [8] with permission from AAAS). On the *right*, *bottom*-first localized buckles observed after the uniaxial microcompression of VACNT pillars by (**b**) Zbib et al. [11] (Copyright IOP Publishing Ltd. Reproduced with permission), and (**c**) Hutchens et al. [5] (Copyright Wiley-VCH Verlag GmbH & Co. KGaA. Reproduced with permission)

across the cylindrical sample until completion [5]. In addition, each subsequent buckle begins only after the previous buckle has completely formed, that is, the crease has spread across the entire cylinder. Figure 4 illustrates the evolution and localization of deformation for a uniaxially loaded VACNT cylinder. Cross correlation of the in situ images with the accompanying stress–strain data reveals that the localized buckle formation and propagation correspond to undulations in the nominal stress–strain curve. Specifically, softening corresponds to the first appearance of the buckle and the subsequent hardening coincides with the lateral propagation of the buckle. This localized response overlays the aforementioned overall foam-like behavior seen in these materials.

Notable differences between the classic foam-like stress–strain behavior and the overall response of VACNTs in uniaxial compression studies of VACNT structures have also been observed in both macroscopic [8, 9, 15] and microscopic [5, 11] samples. First, the plateau regime is highly sloped. In typical foams, a sloped plateau indicates some homogeneous variation in strut buckling stress due either to random strut alignment, a distribution of strut sizes (aspect ratio, diameter, etc.), or both. While both kinds of inhomogeneities exist in VACNTs, the plateau regime is too highly sloped to be explained by these small fluctuations and the nonlocal nature of the buckling points to another cause. In fact, the sloped plateau regime actually points toward evidence of an axial property gradient in VACNTs. As discussed previously, a gradient in tube density arises in VACNTs as a result of the CVD growth process. This gradient can be such that there is a lower tube density at the bottom of the structure (i.e., the point at which the substrate attaches) than the top. It follows that such a tube density gradient would result in a corresponding strength and stiffness gradient. This property gradient is evident in the stress–strain response from Fig. 4 in the progressive increase in peak stress values for undulations in the plateau region. Throughout this plateau, buckles are known to form sequentially, bottom-to-top, and therefore each subsequent buckle forms at a higher (and more dense) location within the cylinder than the previous buckle, requiring a larger stress in order to form a new fold. Such property dependence has been modeled by Hutchens et al. [5] in a viscoplastic finite element framework which showed a direct correspondence between the presence and extent of an applied property gradient and the amount of hardening within the plateau. Details of this and other efforts to capture VACNT deformation mechanisms through modeling are summarized in the next section.

Modeling of VACNT Deformation

Only a few preliminary models exist to describe the mechanical deformation of VACNTs. Motivated by both the morphology of the VACNTs (a series of nominally vertical struts) as well as the observed buckling behavior, many researchers utilize an Euler buckling framework to mechanistically describe their findings. In Euler buckling, an ideal column

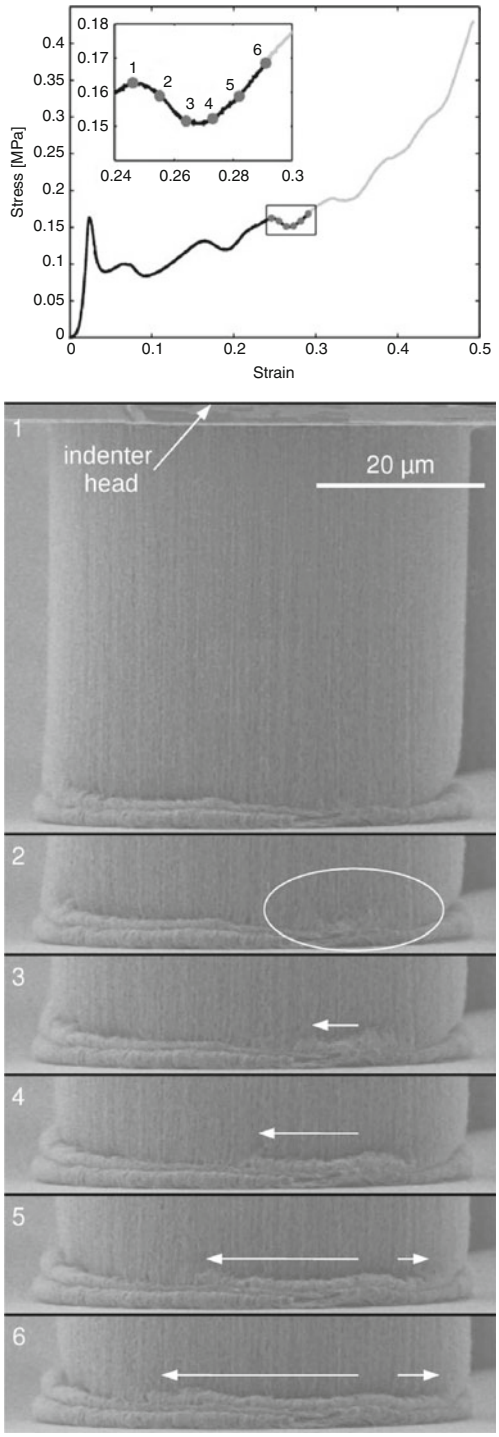

Vertically Aligned Carbon Nanotubes, Collective Mechanical Behavior, Fig. 4 In situ video micrographs and accompanying nominal stress–strain data illustrating bottom-first buckling and buckle initiation and propagation events [5] (Copyright Wiley-VCH Verlag GmbH & Co. KGaA. Reproduced with permission)

(perfectly straight, homogeneous, and free from initial stress) is determined to buckle when the applied load reaches some critical value that causes the column to be in a state of unstable equilibrium. Up to the point of buckling, the column is assumed to be perfectly elastic. Scaling calculations by Cao et al. [8] utilize this critical stress to estimate the transition stress value for departure from linear elastic behavior, that is, the buckling stress, given a reasonable estimate of the tube number density. Similarly, Mesarovic et al. [1] include an additional intertube contact energy to account for favorable van der Waals interactions between tubes in their energetic treatment of VACNTs. Another Euler-based model by Zbib et al. [11], motivated by the formation of buckles they observed, proposes piecewise buckling that assumes the top of the pillar deforms via simple shear while the bottom undergoes collapse. Using this framework, they predict the buckling stress increases asymptotically with decreasing pillar height (for similar aspect ratio pillars). Notably, however, none of these models make predictions concerning the length-scale of the buckles formed or their dependence on material parameters such as density, stiffness, tube alignment, or diameter.

Another subset of mechanical analyses utilizes an alternating hardening-softening-hardening local constitutive relation and are the only theories that attempt to capture material response beyond the initial buckling event. The hardening-softening-hardening behavior is motivated by the anticipated behavior of the individual CNT struts. Locally, the material is expected to transition from elastic loading (hardening) to buckling during which the load carrying capacity of the tubes decreases (softening). Eventually, the material densifies, corresponding to a return to hardening behavior. The first of the analyses to use this general behavior, a hierarchical bistable spring model, captures the *quantitative* stress–strain response of VACNTs in compression [17]. The second, a finite element, viscoplastic solid, captures the *qualitative*, sequential, periodic buckle morphology [18]. The bistable spring model consists of mesoscale elements characterized by elastic-plateau-densification and, most importantly, hysteresis in the unloading curve. These mesoscale elements are the limiting case of infinitely many bistable spring elements in series. Briefly, a bistable spring consists of two thermodynamically stable elastic loading sections (hardening)

separated by an unstable, negative stiffness region (softening) of the stress–strain curve across which the material snaps, similar to a phase transition. When placed in series, these mesoscale elements closely capture the hysteretic unloading response seen by Cao et al. [8]. Thus, this model can be utilized to characterize the energy dissipation in VACNTs. In the finite element model, Hutchens et al. [18] postulate a positive–negative–positive sloped stress–strain relation reminiscent of a bistable spring, but rather than being elastic, it is used as a plastic hardening function governing the local deformation of an element post-elastic loading. These latter analyses find that this constitutive relation is capable of producing sequential, periodic buckles in an axisymmetric, circular cylindrical mesh with fixed boundary conditions at the base (similar to VACNTs). In addition, an axial gradient in the strength is not necessary to initiate the bottom-first buckling seen in experiments; rather, the fixed boundary conditions are sufficient for a uniform property distribution. However, a reversal of buckle initiation, top-to-bottom, can be achieved for a sufficient inverse axial gradient (having lower strength at the top of the pillar than the bottom). Both of these analyses capture essential elements of VACNT deformation, but do so for two very different sets of experimental observations: recoverable deformation and plastic deformation, respectively.

Viscoelasticity

In addition to their distinctive buckling behavior and their ability to recover from large deformations, VACNTs have also been reported to demonstrate another case of extreme mechanical performance – a unique viscoelastic response that spans a truly wide temperature range from −196°C to 1,000°C – something no other material has shown so far. Viscoelastic materials exhibit both viscous and elastic characteristics when subjected to load. Thus, a viscoelastic material is able to both dissipate energy through viscous behavior (as in honey), while storing energy though elasticity (as in rubber band). The stress–strain response of viscoelastic materials is typified by hysteresis in the loading-unloading cycle.

Viscoelastic behavior in a material is generally characterized in terms of its loss (E'') or storage modulus (E') (or by the ratio, known as $\tan\delta = E''/E'$, of these two moduli). E'' relates to the amount of energy dissipated while E' represents the stored energy in the material. The angle, δ, is the phase lag between the oscillatory load and displacement responses under sinusoidal loading. In a typical experiment, the material is loaded to a predetermined strain and the mechanical probe is oscillated across a range of frequencies. By measuring the resultant load amplitude, displacement amplitude, and the phase lag during the test, the values of loss modulus, storage modulus, and tan δ can be determined. Similarly, viscoelasticity can also be quantified by the memory or hysteresis effects during load-unload cycles under deformation, where the energy dissipated is given by the area of the hysteresis loop. These viscoelastic effects have recently been documented in the highly intertwined random networks of VACNTs. Viscoelasticity in CVD-VACNTs has been demonstrated by Hutchens et al. [5], where both storage and loss stiffnesses were studied in a frequency range from 1 to 45 Hz at different strain levels (Fig. 5a). Note that these stiffness values are proportional to moduli given a known Poisson's ratio, which is lacking for VACNTs. The elastic response is clearly frequency independent, indicating the VACNT's elastic deformation is likely due to the same mechanism (likely tube bending) over the range of timescales tested. As shown in Fig. 5a, more energy is dissipated (higher values of loss stiffnesses) at larger strain levels when a higher fraction of the VACNT pillar has buckled. Interestingly, for the more dense CDC-VACNTs the opposite seems to be true (Fig. 5b). For the highly dense CDC-VACNTs, Pathak et al. [4] have shown a significant drop in the tan δ values of the CNTs after buckling, that is, when the material was highly compacted. These observations indicate that while an increase in density can significantly increase the viscoelastic behavior of CNTs, there appears to be a cutoff beyond which the contacting CNTs became increasingly bundled resulting in a decrease in their ability to dissipate energy.

A recent report by Xu et al. [10] also suggests a rubber-like viscoelastic behavior in a random network of long, interconnected, and tangled CNTs, similar in many ways to VACNTs but significantly less aligned, over a very wide temperature range – from −196°C to 1,000 °C, with a possibility of extending this behavior beyond 1,500 °C. While the oxidizing nature of carbon may limit the application of these materials to only vacuum or protective

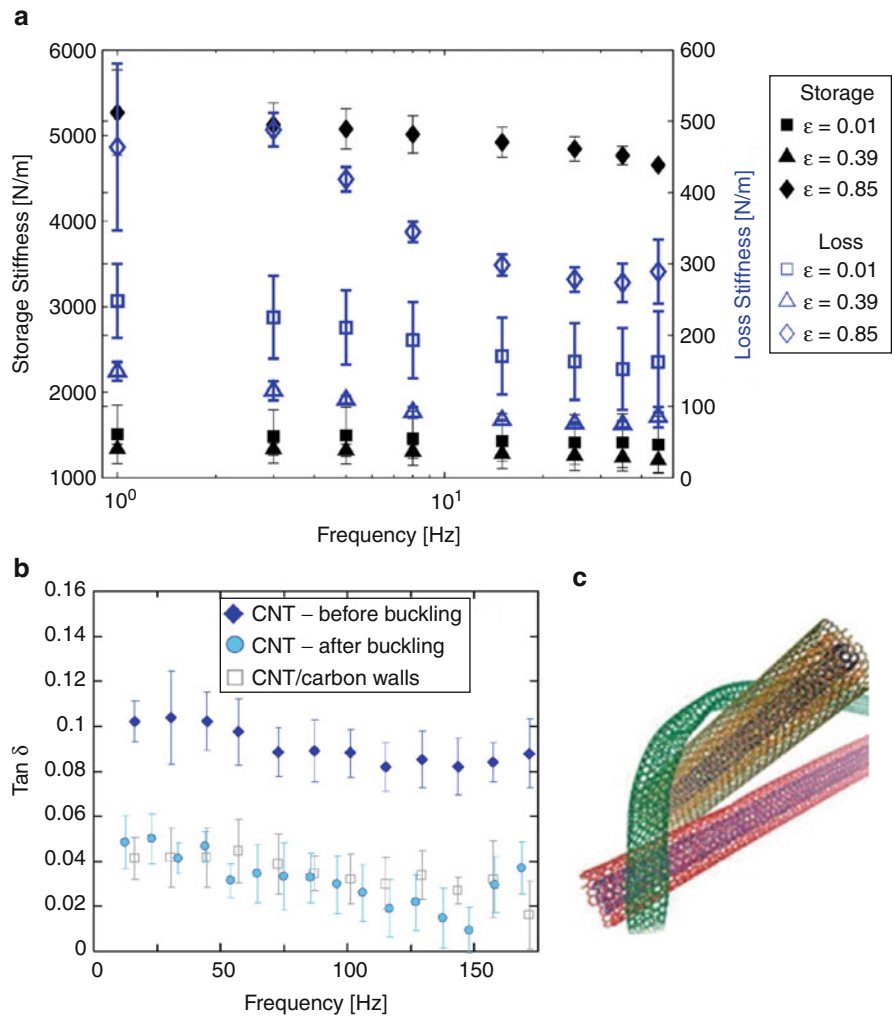

Vertically Aligned Carbon Nanotubes, Collective Mechanical Behavior, Fig. 5 Viscoelastic behavior as seen in: (**a**) CVD-VACNTs showing an increase in the loss stiffness with increasing strains [5] (Copyright Wiley-VCH Verlag GmbH & Co. KGaA. Reproduced with permission) (**b**) CDC-VACNTs showing a significantly decrease in values of tan δ after buckling (Reproduced from [4] with permission from Elsevier) (**c**) Atomistic modeling image of a possible entangled arrangement of single, double, and triple-walled CNTs leading to their rubber-like viscoelastic behavior (Reprinted from [19] [8] with permission from AAAS)

(reducing) environments, CNTs are nevertheless the only known solids to demonstrate such behavior at extremely low or very high temperatures. The authors attribute the reversible dissipation of energy in CNTs over this remarkable range to the zipping and unzipping of the CNTs upon contact (see Fig. 5c) caused by the van der Waals interactions. In this instance, "reversible" means that beyond a critical strain the zipping/unzipping process was no longer possible everywhere as more and more tubes become permanently entangled at higher strain. This would lead to a loss in their viscoelasticity, similar to the observations in the highly dense CDC-VACNTs (Fig. 5b).

The unique combination of superior mechanical properties and the ability to dissipate energy during deformation is expected to have significant impact in damping applications utilizing VACNTs. These, combined with the wide temperature range of its viscoelastic behavior, make VACNT-based materials a promising choice for use in mechanical applications under extreme temperatures or temperature gradients. Possible environments range from the cold of interstellar space to down-to-earth viscoelastic applications, such as MEMS devices to high temperature vacuum furnaces.

Applications

As described in detail in (► Carbon-Nanotubes) multiwall carbon nanotubes are well known for a variety of exceptional properties. These include a high tensile modulus, on the order of 1 TPa, high

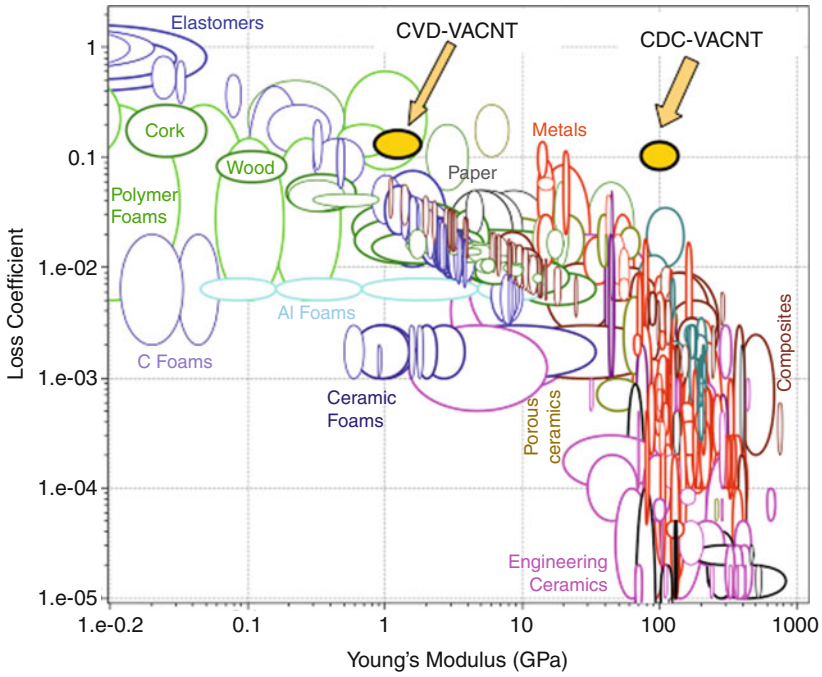

Vertically Aligned Carbon Nanotubes, Collective Mechanical Behavior, Fig. 6 An Ashby plot of loss coefficient (energy dissipated in a stress–strain cycle) versus modulus illustrating the relation of VACNTs to other damping materials

strength, on the order of tens of GPa, high thermal conductivity, recoverability after large bending angle deformation, and a range of electrical properties depending on the chirality of the graphene walls. For these reasons they are currently the subject of a wide range of research (see Function follows shape: Examples from Carbon Nanotubes Research). In the form of VACNTs, these individual tube properties may be significantly altered by the collective interaction of thousands of tubes. Several applications of VACNT structures currently under study rely on the mechanical behavior described earlier in this entry. A remarkable, but incomplete list includes: components of highly compliant thermal contacts for microelectromechanical systems (MEMS) and microelectronics [3, 11] (see Carbon Nanotubes Integrated with MEMS), dry adhesives (see ▶ Gecko Adhesion), thermally robust energy dissipating rubber [10, 19], and energy absorption or impact mitigation [20]. Other applications, such as optical coatings and cold cathode arrays, may rely less on the mechanical properties for optimization and design, but understanding is still necessary for evaluation of robustness and in-use lifetime analysis.

We go through each application briefly to highlight the VACNT-specific mechanical behavior of interest. First, thermal contacts for delicate electronics devices have two requirements. They must be highly thermally conductive and make conformal contact (to increase heat transfer) while avoiding damage to the components they are transferring heat to and from. CNT foams are ideal for this application due to the high compliance that comes from the reduced load capacity of the CNT struts as they buckle. Dry adhesive applications of VACNTs take advantage of the hierarchical structure which can, as desired in MEMS switches, make conformal contact to surfaces at a variety of roughness length scales, thereby increasing the attractive interactions between the tubes and the surface. Third, energy dissipating and absorbing applications require more in-depth knowledge of the deformation mechanism. As mentioned in the previous section, energy dissipation is currently thought to be due to tube zipping/unzipping or tube-to-tube sliding and rearrangement [1, 4, 9, 10, 19], while energy absorption is certainly maximized during buckle formation. Future applications may be able to take advantage of yet undiscovered traits of the incompletely characterized VACNTs.

Summary and Outlook

Although the mechanisms governing VACNTs collective mechanical behavior are still largely

uncharacterized, the special properties of multiwall carbon nanotubes combined with the complex interactions that arise between them in the hierarchical VACNT microstructure have generated significant research interest. Their wide range of properties, mechanical, electrical, and thermal, make them ideal candidates as multifunctional materials, particularly for applications in which soft materials (such as polymers) have traditionally dominated. Notably, VACNTs occupy a unique niche among engineering materials as shown in the Ashby property chart in Fig. 6 with the ability to span a wide range of properties given a tunable microstructure. The authors believe that there are two major hurdles to rationally designing VACNTs for any application: control of the CNT growth process and understanding of the relationship between the microstructure and mechanical response. These hurdles are interrelated through the fact that the design space cannot be systematically probed until the microstructure can be systematically controlled. Mastery of these unknowns will not only further VACNTs place as novel materials in the current applications under study, but may reveal previously undiscovered behaviors in microstructures yet to be created or characterized.

Cross-References

- ▶ Carbon-Nanotubes
- ▶ Gecko Adhesion

References

1. Mesarovic, S.D., McCarter, C.M., Bahr, D.F., Radhakrishnan, H., Richards, R.F., Richards, C.D., McClain, D., Jiao, J.: Mechanical behavior of a carbon nanotube turf. Scr. Mater. **56**, 157–160 (2007)
2. Presser, V., Heon, M., Gogotsi, Y.: Carbide-derived carbons – from porous networks to nanotubes and graphene. Adv. Funct. Mater. **21**, 810–833 (2011)
3. McCarter, C.M., Richards, R.F., Mesarovic, S.D., Richards, C.D., Bahr, D.F., McClain, D., Jiao, J.: Mechanical compliance of photolithographically defined vertically aligned carbon nanotube turf. J. Mater. Sci. **41**, 7872–7878 (2006)
4. Pathak, S., Cambaz, Z.G., Kalidindi, S.R., Swadener, J.G., Gogotsi, Y.: Viscoelasticity and high buckling stress of dense carbon nanotube brushes. Carbon **47**, 1969–1976 (2009)
5. Hutchens, S.B., Hall, L.J., Greer, J.R.: In situ mechanical testing reveals periodic buckle nucleation and propagation in carbon nanotube bundles. Adv. Funct. Mater. **20**, 2338–2346 (2010)
6. Qi, H.J., Teo, K.B.K., Lau, K.K.S., Boyce, M.C., Milne, W.I., Robertson, J., Gleason, K.K.: Determination of mechanical properties of carbon nanotubes and vertically aligned carbon nanotube forests using nanoindentation. J. Mech. Phys. Solids **51**, 2213–2237 (2003)
7. Bedewy, M., Meshot, E.R., Guo, H.C., Verploegen, E.A., Lu, W., Hart, A.J.: Collective mechanism for the evolution and self-termination of vertically aligned carbon nanotube growth. J. Phys. Chem. C **113**, 20576–20582 (2009)
8. Cao, A.Y., Dickrell, P.L., Sawyer, W.G., Ghasemi-Nejhad, M.N., Ajayan, P.M.: Super-compressible foamlike carbon nanotube films. Science **310**, 1307–1310 (2005)
9. Suhr, J., Victor, P., Sreekala, L.C.S., Zhang, X., Nalamasu, O., Ajayan, P.M.: Fatigue resistance of aligned carbon nanotube arrays under cyclic compression. Nat. Nanotechnol. **2**, 417–421 (2007)
10. Xu, M., Futaba, D.N., Yamada, T., Yumura, M., Hata, K.: Carbon nanotubes with temperature-invariant viscoelasticity from-196° to 1000°C. Science **330**, 1364–1368 (2010)
11. Zbib, A.A., Mesarovic, S.D., Lilleodden, E.T., McClain, D., Jiao, J., Bahr, D.F.: The coordinated buckling of carbon nanotube turfs under uniform compression. Nanotechnology **19**, 175704 (2008)
12. Zhang, Q., Lu, Y.C., Du, F., Dai, L., Baur, J., Foster, D.C.: Viscoelastic creep of vertically aligned carbon nanotubes. J. Phys. D: Appl. Phys. **43**, 315401 (2010)
13. Bradford, P.D., Wang, X., Zhao, H., Zhu, Y.T.: Tuning the compressive mechanical properties of carbon nanotube foam. Carbon **49**, 2834–2841 (2011)
14. Deck, C.P., Flowers, J., McKee, G.S.B., Vecchio, K.: Mechanical behavior of ultralong multiwalled carbon nanotube mats. J. Appl. Phys. 101:23512-23511-23519 (2007)
15. Tong, T., Zhao, Y., Delzeit, L., Kashani, A., Meyyappan, M., Majumdar, A.: Height independent compressive modulus of vertically aligned carbon nanotube arrays. Nano Lett. **8**, 511–515 (2008)
16. Qiu, A., Bahr, D.F., Zbib, A.A., Bellou, A., Mesarovic, S.D., McClain, D., Hudson, W., Jiao, J., Kiener, D., Cordill, M.J.: Local and non-local behavior and coordinated buckling of CNT turfs. Carbon **49**, 1430–1438 (2011)
17. Fraternali, F., Blesgen, T., Amendola, A., Daraio, C.: Multiscale mass-spring models of carbon nanotube foams. J. Mech. Phys. Solids **59**, 89–102 (2011)
18. Hutchens, S.B., Needleman, A., Greer, J.R.: Analysis of uniaxial compression of vertically aligned carbon nanotubes. J. Mech. Phys. Solids **59**, 2227–2237 (2011)
19. Gogotsi, Y.: High-temperature rubber made from carbon nanotubes. Science **330**, 1332–1333 (2010)
20. Misra, A.A.G., Greer, J.R., Daraio, C.: Strain rate effects in the mechanical response of polymer-anchored carbon nanotube foams. Adv. Mater. **20**, 1–5 (2008)

Vibration Assisted Machining

► Ultrasonic Machining

Viscosity

► Interfacial Investigation of Protein Films Using Acoustic Waves

Visual Prosthesis

► Artificial Retina: Focus on Clinical and Fabrication Considerations

Visual Servoing for SEM

► Robot-Based Automation on the Nanoscale

Higher Recovery and Better Energy Dissipation at Faster Strain Rates in Carbon Nanotube Bundles: An *in-Situ* Study

Siddhartha Pathak,[†,*] Ee J. Lim,[†] Parisa Pour Shahid Saeed Abadi,[‡] Samuel Graham,[‡,§] Baratunde A. Cola,[‡,§] and Julia R. Greer[†]

[†]Materials Science, California Institute of Technology (Caltech), Pasadena, California, United States and [‡]George W. Woodruff School of Mechanical Engineering, and [§]School of Materials Science and Engineering, Georgia Institute of Technology, Atlanta, Georgia, United States

ABSTRACT

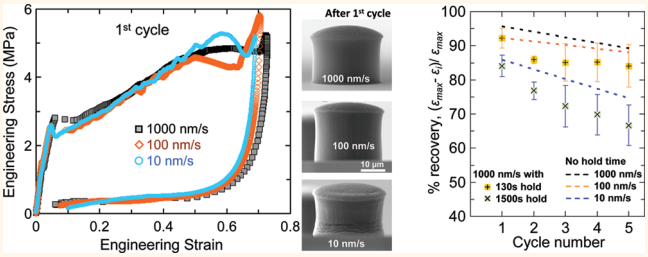

We report mechanical behavior and strain rate dependence of recoverability and energy dissipation in vertically aligned carbon nanotube (VACNT) bundles subjected to quasi-static uniaxial compression. We observe three distinct regimes in their stress—strain curves for all explored strain rates from 4×10^{-2} down to 4×10^{-4} /sec: (1) a short initial elastic section followed by (2) a sloped plateau with characteristic wavy features corresponding to buckle formation and (3) densification characterized by rapid stress increase. Load—unload cycles reveal a stiffer response and virtually 100% recoverability at faster strain rates of 0.04/sec, while the response is more compliant at slower rates, characterized by permanent localized buckling and significantly reduced recoverability. We propose that it is the kinetics of attractive adhesive interactions between the individual carbon nanotubes within the VACNT matrix that governs morphology evolution and ensuing recoverability. In addition, we report a 6-fold increase in elastic modulus and gradual decrease in recoverability (down to 50%) when VACNT bundles are unloaded from postdensification stage as compared with predensification. Finally, we demonstrate energy dissipation capability, as revealed by hysteresis in load—unload cycles. These findings, together with high thermal and electrical conductivities, position VACNTs in the "unattained-as-of-to-date-space" in the material property landscape.

KEYWORDS: vertically aligned carbon nanotubes · compression · mechanical properties · energy storage · recovery

Resilience, or a material's ability to recover back to its original dimensions after deformation, is a key criterion in assessing lifetime reliability of material systems. If a material exhibits time-dependent deformation, that is, viscoelasticity, like vertically aligned carbon nanotube (VACNT) bundles,[1,2] it is common for its stress—strain behavior to exhibit a hysteresis loop upon cyclical loading, thus dissipating energy in every cycle.[3] Here we show that both recoverability and energy dissipation in VACNTs are strongly dependent on strain-rate, attaining their maxima by loading at faster rates. Specifically, we find that when compressed at the faster strain rates of 4×10^{-2}/sec, the VACNT bundles recover virtually back to their original dimensions, while at the slower deformation rates of 4×10^{-4}/sec, they remain permanently deformed (<86% recovery), as evidenced by their post-mortem morphology containing localized buckles. The resilience of the VACNT samples is further compromised when they are loaded to beyond densification threshold strains of $\varepsilon \geq 0.65-0.7$ for all strain rates.

It has been shown previously that compressive behavior of VACNT bundles is strongly affected by variations in their complex hierarchical morphology, collective intertube interactions, and inherent property gradients, which in turn are controlled by the synthesis techniques.[4] In part, this is evidenced by the wide range of mechanical properties reported for VACNTs, such as variations in modulus and buckling strength that range anywhere from sub-MPa[1,5] to tens of MPa[6−8] to GPa[9,10] levels. Another marked difference among existing reports is the ability (or lack thereof) of some VACNT microstructures to recover from large deformations; with some exhibiting superior creep recovery,[1−3,11] while others deform permanently even at modest strains.[8,12−14] The ability of VACNT bundles to dissipate energy while maintaining their dimensional stability with >80% recovery has suggested their future use for energy storage applications such as viscoelastic rubbers and foams.[2,15]

In this work ~30 μm × 30 μm (height × diameter) cylindrical pillars of VACNTs were grown by atmospheric pressure chemical

* Address correspondence to pathak@caltech.edu, siddharthapathak@gmail.com.

Received for review October 24, 2011 and accepted February 14, 2012.

Published online 10.1021/nn300376j

vapor deposition (APCVD) and tested both in air and in an *in situ* nanomechanical instrument inside of a scanning electron microscope (SEM) under compressive cyclic loading (up to five load–unload cycles) at three different displacement rates of 10, 100, and 1000 nm/s, which correspond to strain rates of 0.0004, 0.004, and 0.04/sec, respectively (see Methods). The stress–strain responses of VACNTs were measured using quasi-static uniaxial compression experiments on these cylindrical specimens[1,3,12] as in this configuration the deformation occurs under a relatively homogeneous stress field, which is in contrast to quasi-static nanoindentation[10,16,17] or dynamic impact testing methods[18–20] where the presence of strong strain gradients obscure stress–strain calculations. The *in situ* observations in SEM during the experiments allow for simultaneous correlation between morphological evolution in VACNTs and their stress–strain behavior.[12,21]

As shown in the representative stress–strain curve at 100 nm/sec in Figure 1, these pillars exhibit remarkable resilience (>90% recovery), with virtually no discernible changes from their original morphology (compare Figures 1b and 1f) even after cycling to relatively high strains of 70–80%. Furthermore, their load-unload trajectories are characterized by a considerable hysteresis loop, implying energy dissipation during deformation.

It has been proposed that some of the factors leading to nearly full recovery and energy dissipation in VACNT bundles can be attributed to their hierarchical microstructure[1,2,12] (Figure 1b). At the lowest magnification (bottom SEM image Figure 1b) the VACNT pillar has a distinctive muffin-like shape, with a bulbous top caused by the particular APCVD growth process (see Methods). APCVD VACNT pillars of such short heights also tend to have a lower density (and hence, a more compliant structure) at the bottom closer to the substrate compared to taller APCVD forests.[22] This is evident in the darker hue in the bottom $\sim 2\ \mu$m of the pillar in Figure 1b. Not surprisingly, upon compression the first buckling instability forms at this location (Figure 1c). Compared to other CNT structures, VACNT bundles are characterized by a significant number (~millions) of CNTs arrayed in a nominally vertical alignment growing perpendicularly to the support substrate, as seen at higher (micrometer level) magnifications (Figure 1b, second image from bottom). However the long strands of individual CNTs intertwine in the course of their growth, which becomes apparent at higher magnifications (Figure 1b, third image from bottom). Upon careful examination, in their as-grown states some tubes appear prebuckled and/or prebent, and the favorable contact energy between the tubes is thought to balance the bending strain energy of their arrangement, resulting in a more stable low energy configuration.[6] This is in contrast to arrays of VACNTs that are short and/or sparse enough that each individual CNT stands alone.[23] At still higher magnifications (nanometer length scales, see top TEM image in Figure 1b), individual, discrete CNTs dominate the mechanical performance with details like CNT diameter, number of walls *etc*. governing their deformation.

Despite their complex, hierarchical microstructure, the general compressive behavior of VACNTs is akin to that of typical open-cell foams,[24] as evident from Figure 1a. In the spirit of the overall open foam-like response, the stress–strain curves of VACNTs are characterized by 3 distinct regimes: (1) initial linear elastic region, followed by (2) an oscillatory plateau region, where each undulation is associated with localized buckling events, extending to the strains of ~65–70%, beyond which the stress steeply increases due to (3) densification. At the scale of its constituents, however, the response of VACNTs is quite different from that of traditional foams. In VACNT bundles, the postelastic compressive strain is accommodated entirely *via* the formation of lateral folds or buckles usually close to the bottom of the bundle, while the remaining portion remains virtually unscathed.[12] This is in contrast to traditional foams, where cell-edge bending and cell collapse are primarily responsible for the elastic–plastic foam response.[24,25] In our VACNT samples (Figure 1c), the formation of the first buckle at the bottom signals the transition from elastic to plateau regime. The postelastic plateau region in the stress–strain curve also shows marked differences from that of an open cell foam response, as evidenced by its nonzero positive slope and wave-like shape, where each undulation can be traced to subsequent buckling events (videos S1, S2 and S3 in the Supporting Information). The positive slope of the plateau region has been attributed to the presence of a vertical property gradient in the VACNT pillars.[3,12] The plateau region continues to slope upward until ~50% strain, where a pronounced kink forms approximately at the midheight of the pillar, leading to softening. This kink formation marks the end of the plateau, after which the stress–strain behavior shifts into the densification regime characterized by a steep stress increase over a very small strain.

The initial portion of the "elastic" regime (at very low strains $\varepsilon \leq 0.05$ shown in Figure 1a) is often affected by experimental artifacts like the small initial misalignment between the indenter head and the micropillar, as well as top surface imperfections. Here, the deformation of the entire bulbous top of the VACNT pillars is fully contained within this elastic region, rendering quantitative analysis of this section of the stress–strain impractical. Therefore, we focus our analysis on the postelastic deformation only (see Methods).

Figure 1a also shows the effect of load-unload cycling on the mechanical behavior of VACNT micropillars compressed at 100 nm/s. It is evident that the first cycle is distinctly different from all subsequent

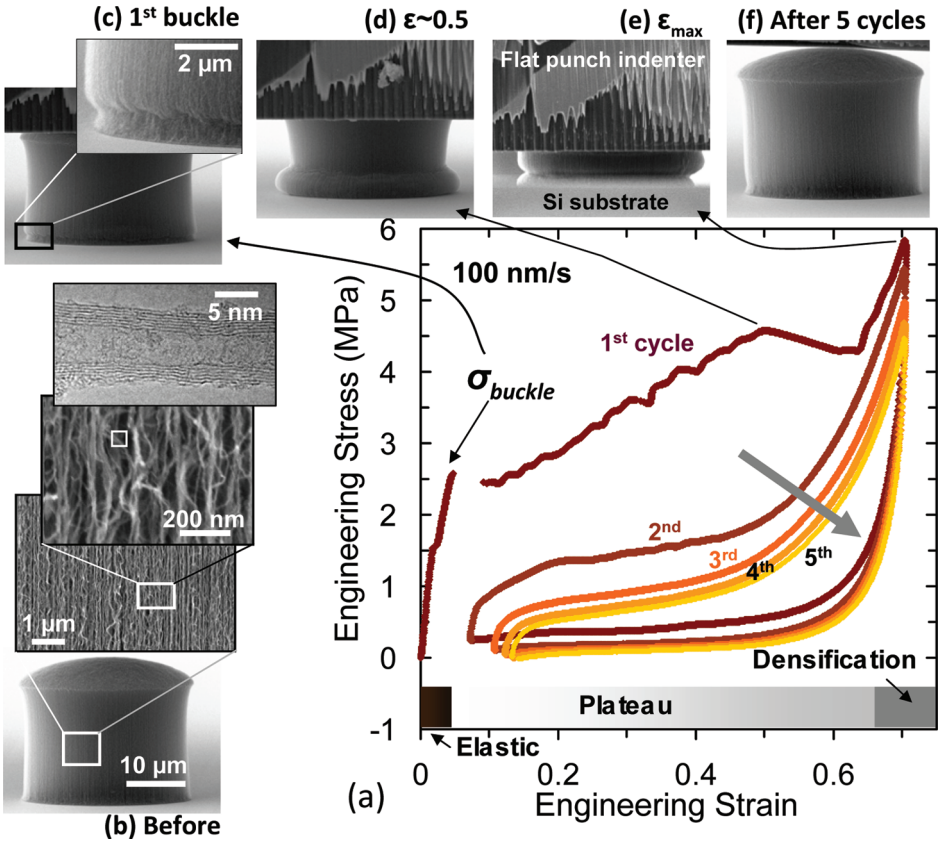

Figure 1. (a) 5 load−unload cycles in compression of a VACNT micro-muffin by a flat punch diamond indenter at 100 nm/s showing 3 distinct regimes; elastic, plateau, and densification. The first buckling instability, formed at the bottom of the pillar shown in (c), marks the start of the sloped plateau region where buckles form progressively. Densification typically starts after the large buckle at $\varepsilon \sim 0.5$ (d) and continues till ε_{max} (e). Successive load−unload cycles to the same strain in (a) also reveal a gradual drop in stress and recovery every cycle, suggesting progressive damage accumulation in the material. Micrographs in (b) reveal the hierarchical morphology of VACNTs, which consist of nominally vertical aligned CNTs at low magnification, and a complex intertwined network at higher magnification. Individual multiwalled CNTs are visible in the TEM image. SEM pictures are taken at a 86 deg tilt angle.

loading cycles, which are self-consistent. For example the buckling stress as well as the plateau stress for the first loading are much higher than those in the latter cycles. It is also apparent that both the amount of hysteresis, corresponding to the energy dissipated every cycle, and the recovered strain after unloading decrease with increasing cycle number.

Under varying displacement rates (Figure 2), further differences in the amount of recovery come to light. As seen from the first unloading segment, recoverability appears to increase at higher strain rates when unloaded from the same nominal maximum strain. This is also evident from the post-mortem SEM images, which clearly show permanent deformation and remnants of buckles in the samples compressed at the slowest 10 nm/s displacement rate, while samples compressed at higher rates appear identical to their initial state, that is, lacking any evidence of deformation. Note also that the plateau region in the samples deformed at the slowest rate shows more pronounced undulations, corresponding to more buckling events occurring at this rate (compare Supporting Information videos S1, S2, and S3). All of this suggests a strong dependence

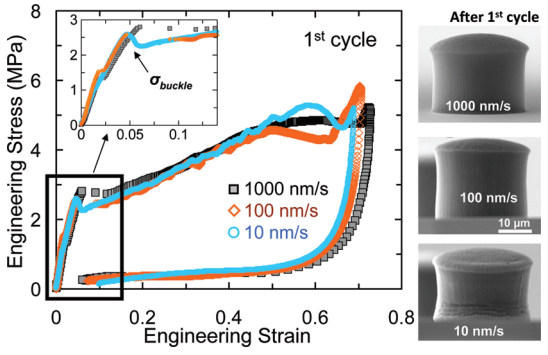

Figure 2. Tests at different displacement rates showing more pronounced buckling signatures and lesser recovery at the lower rates. SEM images in the figure are taken at a 86° tilt angle.

of deformation commencement on strain rate. Further, our demonstration of nearly full recovery and a lack of morphological damage in VACNTs deformed at the highest tested strain rates may have significant implications for its use as protective materials.

Stiffness changes, measured as the elastic modulus calculated from the initial unloading slope in the

stress−strain curves, as a function of displacement rate and maximum strain, are shown in Figure 3. For a particular displacement rate (for example 100 nm/s, orange diamonds in Figure 3a), the moduli obtained in such a way change considerably depending on the maximum strains attained before unloading. Thus while the moduli in the plateau regime start at a low value (around 120 MPa at $\varepsilon = 0.1$ for 100 nm/s), they increase steadily to ~175 MPa up to the strain of $\varepsilon \sim 0.5$. This evolution in the modulus mirrors the trends shown in the shape of the stress−strain curve for the first load−unload cycle shown in Figures 1 and 2. As seen from Figure 1a and 1d, the strain at $\varepsilon \approx 0.5$ is associated with the formation of a large buckle in the middle of the pillar, and is followed by a decrease in the slope of the stress−strain curve. Following a similar trend, the modulus also drops to 145 MPa at strains higher than 0.5. Once the densification threshold strain is reached ($\varepsilon \geq 0.65-0.7$), the modulus increases rapidly with strain to values of up to 2−4 times than that in the predensification regime.

The variations in the modulus between the different regimes are also revealed in Figure 3b, where the results from the pre- and postdensification regimes are summarized separately. The considerably higher moduli in the densification regime, for example, increasing by more than a factor of 2 from 177 ± 11 MPa to 385.1 ± 149 MPa in the first cycle for the fastest 1000 nm/s displacement rate, are likely the effect of the significant increase in density due to compaction of the sample. In addition both pre- and postdensification regimes in Figure 3b show an increasing trend in the stiffness with faster rates, a behavior considered typical for viscoelastic solids.[26] Thus the fastest deformation rate of 1000 nm/s consistently results in the higher moduli in both regimes. Repeated cycling further exacerbates the localization of deformation into folds, leading to stiffness degradation (Figure 3b).

The % recovery shows a similar correlation with both the displacement rate and the maximum attained strains (Figure 4). Figure 4a shows recovery to be virtually 100% when unloaded from elastic regime, >90% when unloaded from the plateau regime, and only 50−80% when unloaded from strains in the densification segment ($\varepsilon \geq 0.65-0.7$). The recovery in the postdensification regime is seen to decrease gradually from >80% to ~50% with increasing strain levels. Similar to the modulus, samples deformed at the slowest 10 nm/s rate are most permanently deformed (*i.e.*, least recovered, with 86.9 ± 2% recovery for the first cycle), while those compressed at the fastest (1000 nm/s) rate show a high 95.6 ± 3% recovery. While the recovery prior to densification decreases gradually with cycling, after densification the recovery drops sharply in the second cycle and then stabilizes to a relatively lower value (Figure 4b). We find that the error bars in the data within the postdensification regime (right image in Figure 4b) are

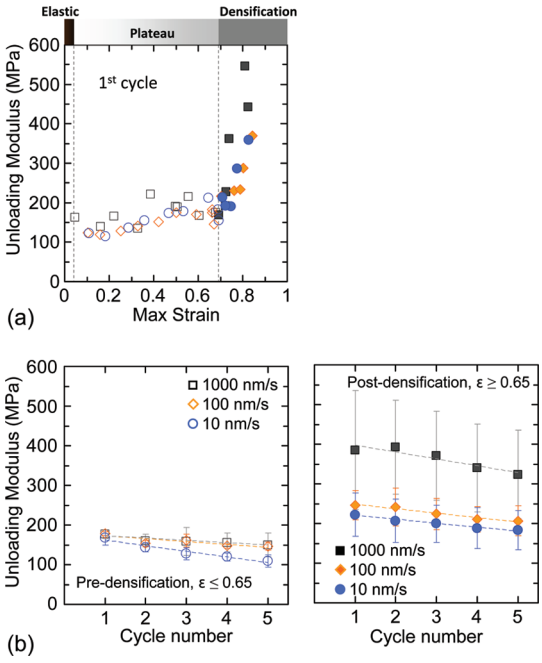

Figure 3. (a) Changes in the unloading modulus as a function of the maximum strains attained before unloading showing a response similar to the material's stress−strain behavior. (b) Modulus values (average ± standard deviation) at different load−unload cycles as a function of their displacement rates in the predensification (open symbols) and postdensification (filled symbols) regimes.

significantly larger than those before densification, likely a result of the % recovery being a strong function of the unloading strain in this regime. Also since the VACNT pillars compressed at the fastest rate of 1000 nm/s were subjected to higher strains (Figure 4a), they recovered less than the ones compressed at the slower 100 nm/s rate in the postdensified regime (Figure 4b).

Our viscoelastic analysis (see Figure S1 in the Supporting Information) indicates that the time constant associated with the recovery of the VACNTs is very short, on the order of ~0.1 s (see also ref 12), and significantly below the deformation rates studied in our work. We also verified the same by loading the VACNTs *in situ* in SEMentor at various displacement rates (of 10, 100, and 1000 nm/s) and then quickly unloading the indenter head, which confirmed that VACNT recovery occurs very rapidly; at the frame capture rate of 30 frames/sec the entire recovery was completed within a single frame at unloading.

Interestingly, relative recovery, defined as recovery compared with the previous, as opposed to initial, cycle (Figure 4c), shows an identical trend for pre and postdensified regimes. By the third cycle, data across all three rates shows ~100% relative recovery. This suggests that in spite of the differences in their absolute values, the recovery in the VACNTs follows a deterministic (rather than stochastic) mechanism for all deformation rates.

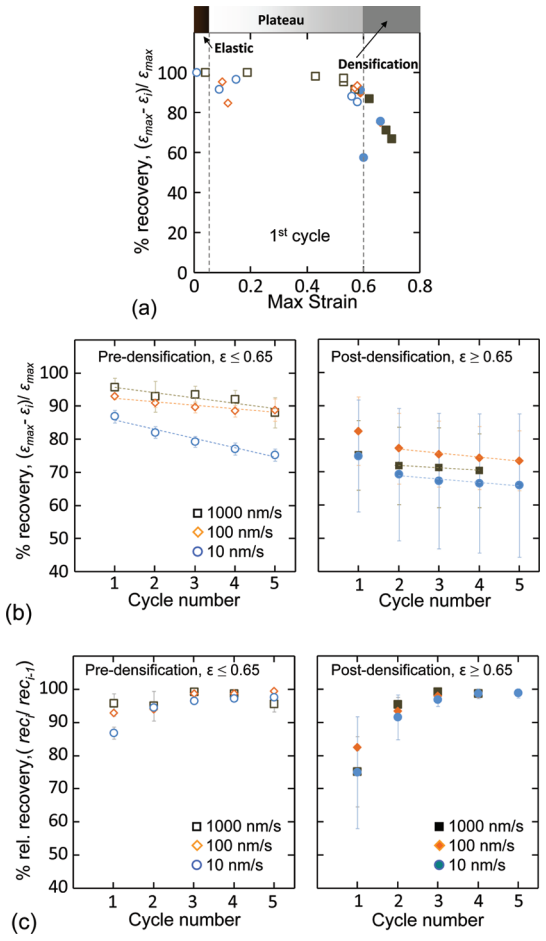

Figure 4. (a) Percent recovery as a function of maximum strain attained before unloading showing higher recovery in the predensification regime (open symbols) while the recovery progressively decreases beyond densification (filled symbols). This is shown more clearly in panels (b) where recovery is higher at faster rates. (c) Similarity of changes in relative recovery values suggest that the process of mechanical damage accumulation is consistent among different rates. Note that tests in the postdensification regime for the 1000 nm/s rate in (b) and (c) had only four load–unload cycles.

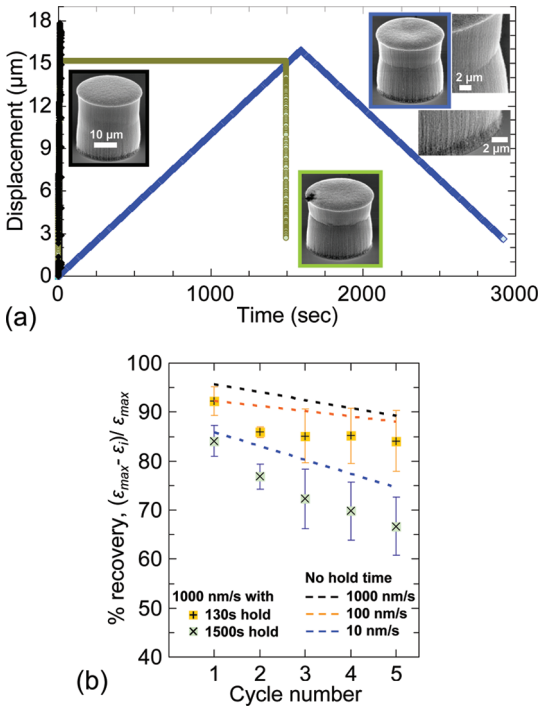

Figure 5. (a) Schematic of test designs showing displacement–time plots for three different cases: a fast load-unload test at 1000 nm/s (black curve), a slow load-unload test at 10 nm/s (blue), and a fast load-unload test at 1000 nm/s with a 1500 s hold time at maximum displacement (green). All samples were loaded to a nominal maximum strain of $\varepsilon \approx 0.6$. Inset micrographs show the postcompression images of the VACNT micropillars taken at a 60 deg tilt angle after 5 such load–unload cycles. (b) Percent recovery as a function of cycle number for tests with and without hold times. The trend lines for the tests without hold time is reproduced from the data in Figure 4b of the manuscript.

While a robust mathematical description of the time dependence of VACNT recovery is beyond the scope of this work, the basic phenomenological process may be understood as follows. When compressed at the lower deformation rates, the individual CNT struts rearrange themselves by twisting, bending, *etc.*, in response to the applied compressive load, thereby coming into close contact with one another. This type of individual strut reconfiguration is not unreasonable in a high-entropy deformation process (*i.e.*, many different configurations are available at each time step). Several groups have now shown that VACNTs deform similarly to foams[3,12,24] likely due to their open cell structure created by interwoven and intertwined tubes, which act as supporting struts.[3,12] In addition, CNTs are inherently "sticky," experiencing an adhesive driving force due to van der Waals interactions.[27] Therefore, in the course of compression at the slower rates, an ever-increasing number of individual struts coalesce by coming into close proximity of one another, thereby forming localized densified regions (*i.e.*, buckles). Importantly, the adhesion process appears to be largely irreversible; that is, the adhesion driving force overrides the stored elastic energy upon unloading. This implies that after unloading the buckles remain even while undergoing elastic recovery. This all is in contrast to the deformation at higher rates, where the entire structure recovers completely, with no evidence of the buckles' presence upon unloading (see Figures 1, 2, and 5). We believe that this behavior stems from an insufficient interaction time between individual tubes to come in contact with one another. This results in a significantly reduced contact intertubular area as compared with the slowly deformed case, and hence leads to much lower adhesion. Compression at higher rates is likely a lower-entropy process since there are fewer configurations available during each time step, and therefore less intertubular contact occurs, leading to the lack of localized "zipped-up" densified buckles.[2,11,15,16]

Thus, it stands to reason that if different VACNT micropillars were allowed similar amounts of time for

the reconfiguration to occur, they should exhibit similar percent recovery for all loading rates. This is shown schematically in Figure 5a, where loading the sample to $\varepsilon \approx 0.6$ (predensification regime) at the fast rate of 1000 nm/s and then holding it at the max load for ~1500 s (green curve) ensures that it spends an equivalent amount of time before unload as the sample deformed at 10 nm/s test (blue curve). Figure 5b clearly shows that a hold time of ~130 s decreases the recovery for the 1000 nm/s displacement rate tests from 96 to 92% in the first cycle, while a longer hold time of ~1500 s brings it down even further to 86%. Note that these reduced percent recovery values are similar to those for the slower 100 and 10 nm/s rates, respectively (see also Figure 4b). Pillars subjected to the additional hold times at maximum strain show a steeper decrease in their recovery in cycles after the second load–unload (Figure 5b), implying that the longer time spent at a high strain is more detrimental to recovery than a gradual increase in strain to a maximum value over the entire time period. The above results suggest that it is the time spent by the VACNTs under high strains, rather than the loading history, that determines the permanence of their deformation.

The postcompression images in Figure 5a also demonstrate a similar signature: while a VACNT micropillar deformed at 1000 nm/s with no hold is virtually indistinguishable from its original configuration (left inset micrograph bordered in black), those micropillars deformed for longer periods of time have accordion-like morphologies, with vertically stacked folds along their heights (inset micrograph in the middle and right, bordered in green and blue, respectively), for both slow and fast loading rates.

The combination of recoverability and viscoelasticity in VACNTs results in their path-dependent load–unload behavior upon cycling, manifested as hysteresis loops shown in Figure 1a. The fraction of energy dissipated during the process can be calculated as the loss coefficient η (see Methods), shown in Figure 6a as a function of cycling. From this figure it is apparent that the loss coefficient is significantly higher for the first load–unload cycle (η = 0.13–0.15) after which η drops sharply (to values of 0.07 and lower). Subsequent load-unload cycles cause the amount of energy dissipated to decrease steadily with increased cycling. η also appears to be strain dependent, and is maximized at the fastest 1000 nm/sec rate, similar to the trends noted for modulus and recovery. No particular differences were noticed between the pre- and postdensification regimes in terms of the loss coefficient values. These results match well with the tan δ measurements (see Figure S1 in Supporting Information)

The strain rate dependence of the recovery and energy dissipation in the VACNTs appears to follow a strong correlation with their increased stiffness at the faster rates. Higher stiffness at faster rates leads to a corresponding

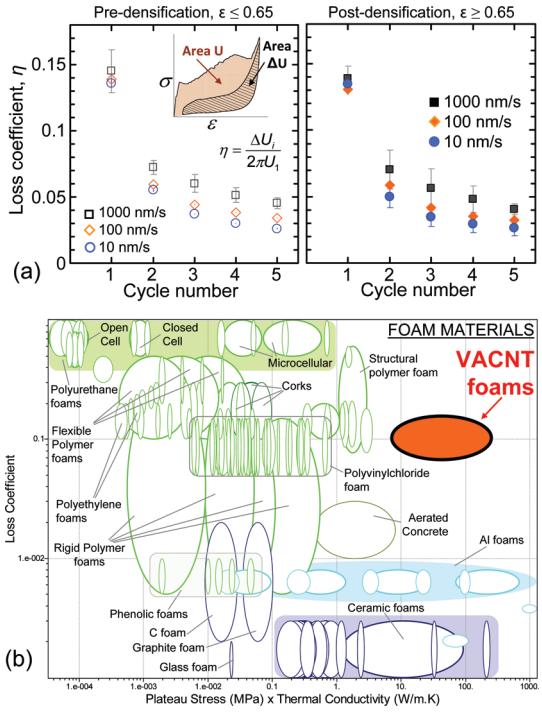

Figure 6. (a) The loss coefficient values as a function of load–unload cycles showing better energy dissipation at higher rates. (b) Ashby chart of loss coefficient (energy dissipation) *vs* plateau stress (signifying the foam strength) multiplied by thermal conductivity of foam materials showing the VACNT system as an ideal candidate for combining the advantages of both metallic and polymeric foams. Using electrical conductivity instead of thermal also generates a very similar plot.

increase in the buckling stress (Figures 1 and 2), which increases from 2.43 ± 0.16 MPa at 10 nm/s to 2.55 ± 0.2 MPa at 100 nm/s to 2.69 ± 0.12 MPa at 1000 nm/s (average ± standard deviation of 10 or more measurements). Usually, the buckling stress defines the beginning of the plateau region, and since the plateau region accounts for the largest fraction of the area under the stress–strain curve, a higher buckling stress corresponds to greater energy absorption in the material and the ability to sustain higher stresses during the extended deformability in this plateau region. Energy dissipation in VACNT bundles, on the other hand, is achieved upon unloading when the VACNTs transform back to their nearly original alignment (unbuckle) by dissipating the excess energy. Since energy dissipated is calculated as a function of the area under the load–unload curve, this value is inherently linked to the amount of recovery of the unloading curve. Hence the rate-dependent damping behavior of the VACNTs can also be explained by a similar line of reasoning as the VACNT recovery described earlier.

CONCLUSION

In summary, we demonstrate that VACNT cylindrical bundles grown by CVD technique exhibit unique deformation properties, namely resilience, deformability, and energy dissipation, all of which increase at faster strain

rates. We hypothesize that it is the inability of individual CNTs in the VACNT matrix to reconfigure and come into contact with one another, promoting adhesion and localized buckle formation, which governs recoverability. Specifically, we find that the deformation at slower strain rates results in the formation of localized, permanent buckles along the pillar height, while faster strain rates render the individual struts' interaction times insufficient for adhesion, leading to nearly full recovery. As such, these materials appear to combine the best aspects of different foam characteristics, such as their ability to switch between various buckled morphologies which makes them capable of undergoing large strains of *ca.* 60−80% without generating damaging peak stresses (similar to metallic foams[25]), as well as their high resilience and close to 100% recovery upon load release leading to a higher energy dissipation (as in polymeric foams[24]). This combination of desirable properties suggests their potential use in protective applications. Even more importantly, their multifunctional nature, high electrical (comparable to copper) and thermal (similar to metals) conductivities,[28,29] and relative ease of manufacture identifies VACNT bundles as a completely new class of material systems entering the "white space" in the material property chart, as shown in Figure 6b.[30]

METHODS

CNT Pillar Growth. Nominally *ca.* 30 μm × 30 μm (height × diameter) size micropillars of VACNTs were grown using an atmospheric pressure chemical vapor deposition (APCVD) technique in a commercial (CVD) system (Black Magic Pro 4″, Aixtron SE).[22] Photolithography and a photoresist lift-off process were employed to pattern a trilayer catalyst of Ti (30 nm)/Al (10 nm)/Fe (3 nm) deposited by electron beam evaporation on Si substrates to seed the growth of micropillars. A gas mixture of 160/100/7500 sccm of $C_2H_2/H_2/N_2$ was used to maintain the chamber pressure at 750 mbar during growth, which occurred at ∼750 °C. Multiwall CNTs, with an average diameter of 8.8 ± 2.1 nm (average ± standard deviation), were produced by this process. The average mass density (CNT mass divided by volume) was measured to be ∼80 mg/cm^3. The muffin-like shape of the VACNT micropillars is an artifact of this APCVD growth process that remains unexplained. High magnification SEM shows that the bulb top is formed by the ends of nanotubes, suggesting that the particular bulb top shape was caused by lower CNT growth rates near the rim of the pillars. Transmission electron microscopy (TEM) images of the APCVD-VACNTs were taken in a JEOL 4000EX machine.

Compression Tests. Vertically oriented cylindrical pillars with an aspect ratio (height/diameter ≈ 30 μm/30 μm) were synthesized for cyclic compression tests. The compression experiments were performed using the XP module of Agilent's nanoindenter G200 with custom Testworks software control methods as described in ref 12. Compression tests were performed in air using a diamond flat punch of ∼120 μm diameter at different displacement rates: 10, 100, and 1000 nm/s, which correspond to strain rates of 0.0004, 0.004, and 0.04/sec, respectively. Typically five load−unload cycles were performed at each strain level. The maximum strains reached for the pillars were varied from 10 to 80%. A minimum of 10 tests were conducted at each compression rate.

As has been observed before by several research groups,[6,12] CNTs frequently adhere to the diamond indenter tip, which results in slightly negative values of load during the final stages of unloading in some cases (see Figure 1a). This effect is further intensified by the additional CNTs present in the protruded bulbous head of the pillar. To mitigate this effect each cycle was unloaded to only 10% of the max load in the previous cycle. In addition to maintaining a positive value of the load (and stress), this approach also helps to prevent loss of contact between the indenter tip and the pillar during loading and hence maintain the cyclic nature of the tests.

***In-Situ* SEM Experiments.** To capture the local deformation events occurring during compression, *in situ* tests were also conducted inside our custom built mechanical deformation system, SEMentor,[31] which is composed of a nanomechanical dynamic contact module (Agilent Corp.) inside a SEM (Quanta 200, FEI). Tests in the SEMentor were conducted with a ∼60 μm × 80 μm conductive diamond flat punch in a similar manner to the G200. The compression axis in the SEMentor is inclined by about 86° with respect to the electron beam, thus allowing continuous observation of the deformation morphology of the VACNT micropillar during the loading/unloading cycle, simultaneously with the acquisition of the load and displacement values. The SEM observations were recorded as a video file and later synchronized with the engineering stress−strain curve to provide a one-to-one correlation between each video frame and its corresponding position on the stress−strain curve (see videos S1, S2, and S3 in the Supporting Information). Testing parameters in the SEMentor were identical to that of the in-air G200 tests.

However, tests in the SEMentor differ from those in the G200 in some key aspects, such as the SEMentor tests are conducted in a vacuum environment with an electron beam focused on the pillar, and the VACNT micropillars are in a horizontal configuration (gravity acting perpendicular to the compression axis) inside the SEMentor. For this study, results from the SEMentor were used only for visualization purposes; all data analyses were performed on tests conducted in the G200 nanoindenter machine.

Data Analysis. Engineering stress (σ) and strain (ε) were calculated using the initial diameter (d_0) and height (h_0) of the VACNT micropillar, where h_0 = [total height of the pillar] − [height of the bulbous top], along with the corrected load (p_{corr}) and displacement (u_{corr}) following the procedure in ref 12. Frictional forces between the VACNT pillar and the indenter head were ignored.[32,33]

$$\sigma = \frac{p_{corr}}{\pi d_0^2/4'} \quad \varepsilon = \frac{u_{corr}}{h_0} \tag{1}$$

Note that eq 1 ignores the height of the bulbous top of the pillar when calculating engineering strain ε, thus assuming that the deformation of the protruded pillar top has little or no effect in the stress−strain response of the VACNT pillar. This assumption is motivated by evidence from the video files S1, S2 and S3 in the Supporting Information. As seen from these videos the deformation of the entire bulbous top of the pillar is concentrated entirely in the "elastic" portion of the loading response, while the rest of the pillar comes in full contact with the indenter head at the beginning of the "plateau" regime (see Figure 1a). We also verified this effect by monitoring the continuous stiffness measurement (CSM) signal during the test, which showed that the point of full contact of the pillar with the indenter head—and hence the entire deformation of the protruded head of the pillar—is within the initial "elastic" portion of the test. Additional validation of our approach is provided by the fact that the modulus (E) values measured as the slope of the initial 30% of the unloading stress−strain curve calculated using eq 1 (see Figure 3 in the manuscript) match closely with the values calculated from the viscoelastic tests

(Figure S1 in the Supporting Information). If h_0 is taken to be the total height of the pillar (rather than being corrected for the additional height of the bulb), the modulus values are overestimated by around 25%.

The percentage recovery (R) values in the VACNT micropillar samples were measured as amount of strain recovered at the end of every cycle with respect to the maximum applied strain; that is, $R = (\varepsilon_{max} - \varepsilon_{unload})/\varepsilon_{max}$, where ε_{max} is the maximum strain level at the end of loading and ε_{unload} is the strain after unloading to 10% of the max load in the respective cycle. Similarly the percentage relative recovery values were measured as the strain recovered in every cycle (i) compared to its previous one ($i-1$); that is, Relative Recovery $= R^i/R^{i-1} = (\varepsilon^i_{max} - \varepsilon^i_{unload})/(\varepsilon^{i-1}_{max} - \varepsilon^{i-1}_{unload})$ (Figure 4).

The loss coefficient, η (a dimensionless quantity), measures the degree to which a material dissipates energy and is calculated as[30]

$$\eta = \frac{\Delta U_i}{2\pi U_1}, \quad U = \int_0^{\sigma_{max}} \sigma \, d\varepsilon, \quad \Delta U = \oint \sigma \, d\varepsilon \qquad (2)$$

where U_1 is the elastic energy stored in the material when it is loaded elastically to a stress σ_{max} in the first cycle, and ΔU_i is the energy dissipated in the ith load−unload cycle (see Figure 6a). We point out that in eq 2 ΔU_i is normalized with respect to the area of the first loading cycle (*i.e.*, a constant value). Instead, normalizing the area of the hysteresis loop with respect to the area of the respective ith cycle can also provide useful information about the damping behavior of the VACNTs, as shown in the Supporting Information Figure S2.

A zero hold time at maximum load was used in all cases, except for the test shown in Figure 5. For the tests shown in Figure 5a three different test setups were used: the black curve denotes a VACNT micropillar loaded at a fast rate of 1000 nm/s up to a strain of ~0.6 (*i.e.*, in the predensification regime) and then unloaded at the same rate, the blue curve shows the same for a slow 10 nm/s loading−unloading rate, while the VACNT micropillar shown in the green curve was loaded at the fastest rate of 1000 nm/s to a maximum strain of $\varepsilon \approx 0.6$, held for 1500 s at that maximum strain level, and then unloaded again at 1000 nm/s. In other words, both VACNTs micropillars shown in green (fast 1000 nm/s loading rate) and blue (slow 10 nm/s loading rate) spent the same amount of time under compression before unload: $(\text{loading time} + \text{hold time})_{green,1000nm/s} = (\text{loading time})_{blue,10\ nm/s}$. Five such load−unload cycles were carried out for each pillar. In another similar set of experiments the VACNT micropillars were loaded at the fastest rate of 1000 nm/s, then held for 130 s at the maximum strain and subsequently unloaded, effectively bringing the time-spent-before-unload to the same level as in the case of a slower 100 nm/s load-unload test with no hold.

Conflict of Interest: The authors declare no competing financial interest.

Acknowledgment. The authors acknowledge S. Hutchens for helpful insights and guidance, N. Mohan for data analysis, financial support from the Georgia Institute of Technology Foundation through the Joseph Anderer Faculty Fellowship, and the Institute for Collaborative Biotechnologies (ICB) for financial support through Grant W911NF-09-0001 from the U.S. Army Research Office. The content of the information does not necessarily reflect the position or the policy of the Government, and no official endorsement should be inferred. S.P. gratefully acknowledges support from the W. M. Keck Institute for Space Studies Postdoctoral Fellowship program for this work. The authors acknowledge critical support and infrastructure provided for this work by the Kavli Nanoscience Institute at Caltech.

Supporting Information Available: Three *in situ* videos of the VACNT micropillar compressions, synchronized with their respective engineering stress−strain curves; video files S1, S2, and S3 illustrate the VACNT micropillar deformations at 10, 100, and 1000 nm/s which are shown at 100, 25, and 1 times their original speeds, respectively; viscoelastic characterization of the VACNT micropillars (Figure S1) and the details of the loss coefficient measurement (Figure S2). This material is available free of charge *via* the Internet at http://pubs.acs.org.

REFERENCES AND NOTES

1. Suhr, J.; Victor, P.; Sreekala, L. C. S.; Zhang, X.; Nalamasu, O.; Ajayan, P. M. Fatigue Resistance of Aligned Carbon Nanotube Arrays under Cyclic Compression. *Nat. Nanotechnol.* **2007**, *2*, 417–421.
2. Xu, M.; Futaba, D. N.; Yamada, T.; Yumura, M.; Hata, K. Carbon Nanotubes with Temperature-Invariant Viscoelasticity from −196 degrees to 1000 degrees C. *Science* **2010**, *330*, 1364–1368.
3. Cao, A. Y.; Dickrell, P. L.; Sawyer, W. G.; Ghasemi-Nejhad, M. N.; Ajayan, P. M. Super-Compressible Foamlike Carbon Nanotube Films. *Science* **2005**, *310*, 1307–1310.
4. Kumar, M.; Ando, Y. Chemical Vapor Deposition of Carbon Nanotubes: A Review on Growth Mechanism and Mass Production. *J. Nanosci. Nanotechnol.* **2010**, *10*, 3739–3758.
5. Tong, T.; Zhao, Y.; Delzeit, L.; Kashani, A.; Meyyappan, M.; Majumdar, A. Height Independent Compressive Modulus of Vertically Aligned Carbon Nanotube Arrays. *Nano Lett.* **2008**, *8*, 511–515.
6. Mesarovic, S. D.; McCarter, C. M.; Bahr, D. F.; Radhakrishnan, H.; Richards, R. F.; Richards, C. D.; McClain, D.; Jiao, J. Mechanical Behavior of a Carbon Nanotube Turf. *Scr. Mater.* **2007**, *56*, 157–160.
7. Qiu, A.; Bahr, D. F.; Zbib, A. A.; Bellou, A.; Mesarovic, S. D.; McClain, D.; Hudson, W.; Jiao, J.; Kiener, D.; Cordill, M. J. Local and Non-local Behavior and Coordinated Buckling of CNT Turfs. *Carbon* **2011**, *49*, 1430–1438.
8. Zhang, Q.; Lu, Y. C.; Du, F.; Dai, L.; Baur, J.; Foster, D. C. Viscoelastic Creep of Vertically Aligned Carbon Nanotubes. *J. Phys. D: Appl. Phys.* **2010**, *43*, 315401.
9. Deck, C. P.; Flowers, J.; McKee, G. S. B.; Vecchio, K. Mechanical Behavior of Ultralong Multiwalled Carbon Nanotube Mats. *J. Appl. Phys.* **2007**, *101*, 23512.
10. Pathak, S.; Cambaz, Z. G.; Kalidindi, S. R.; Swadener, J. G.; Gogotsi, Y. Viscoelasticity and High Buckling Stress of Dense Carbon Nanotube Brushes. *Carbon* **2009**, *47*, 1969–1976.
11. Xu, M.; Futaba, D. N.; Yumura, M.; Hata, K. Carbon Nanotubes with Temperature-Invariant Creep and Creep-Recovery from −190 to 970 °C. *Adv. Mater.* **2011**, *23*, 3686–3691.
12. Hutchens, S. B.; Hall, L. J.; Greer, J. R. *In Situ* Mechanical Testing Reveals Periodic Buckle Nucleation and Propagation in Carbon Nanotube Bundles. *Adv. Funct. Mater.* **2010**, *20*, 2338–2346.
13. Zbib, A. A.; Mesarovic, S. D.; Lilleodden, E. T.; McClain, D.; Jiao, J.; Bahr, D. F. The Coordinated Buckling of Carbon Nanotube Turfs under Uniform Compression. *Nanotechnol.* **2008**, *19*, 175704–1−7.
14. Cao, C.; Reiner, A.; Chung, C.; Chang, S.-H.; Kao, I.; Kukta, R. V.; Korach, C. S. Buckling Initiation and Displacement Dependence in Compression of Vertically Aligned Carbon Nanotube Arrays. *Carbon* **2011**, *49*, 3190–3199.
15. Gogotsi, Y. High-Temperature Rubber Made from Carbon Nanotubes. *Science* **2010**, *330*, 1332–1333.
16. Bradford, P. D.; Wang, X.; Zhao, H.; Zhu, Y. T. Tuning the Compressive Mechanical Properties of Carbon Nanotube Foam. *Carbon* **2011**, *49*, 2834–2841.
17. Maschmann, M. R.; Zhang, Q.; Wheeler, R.; Du, F.; Dai, L.; Baur, J. *In Situ* SEM Observation of Column-like and Foam-like CNT Array Nanoindentation. *ACS Appl. Mater. Interfaces* **2011**, *3*, 648–653.
18. Daraio, C.; Nesterenko, V. F.; Jin, S.; Wang, W.; Rao, A. M. Impact Response by a Foamlike Forest of Coiled Carbon Nanotubes. *J. Appl. Phys.* **2006**, *100*, 64309.
19. Misra, A.; Greer, J. R.; Daraio, C. Strain Rate Effects in the Mechanical Response of Polymer-Anchored Carbon Nanotube Foams. *Adv. Mater.* **2008**, *20*, 1–5.
20. Raney, J. R.; Fraternali, F.; Amendola, A.; Daraio, C. Modeling and *in Situ* Identification of Material Parameters for Layered Structures Based on Carbon Nanotube Arrays. *Compos. Struct.* **2011**, *93*, 3013–3018.
21. Yaglioglu, O. Carbon Nanotube Based Electromechanical Probes. Ph.D. Thesis, Massachusetts Institute of Technology, Cambridge, MA, 2007.

22. Abadi, P. P. S. S.; Hutchens, S.; Taphouse, J. H.; Greer, J. R.; Cola, B. A.; Graham, S. The Effect of Morphology on the Micro-compression Response of Carbon Nanotube Forests. *Carbon* **2011**submitted for publication.
23. Waters, J. F.; Riester, L.; Jouzi, M.; Guduru, P. R.; Xu, J. M. Buckling Instabilities in Multiwalled Carbon Nanotubes under Uniaxial Compression. *Appl. Phys. Lett.* **2004**, *85*, 1787–1789.
24. Gibson, L. J.; Ashby, M. F., *Cellular Solids: Structure and Properties*; Cambridge University Press: UK, 1999.
25. Gibson, L. J. Mechanical Behavior of Metallic Foams. *Annu. Rev. Mater. Sci.* **2000**, *30*, 191–227.
26. Lakes, R. S., *Viscoelastic Solids*; CRC Press, Boca Raton, FL, 1998.
27. Ruoff, R. S.; Tersoff, J.; Lorents, D. C.; Subramoney, S.; Chan, B. Radial Deformation of Carbon Nanotubes by van der Waals Forces. *Nature* **1993**, *364*, 514–516.
28. Baxendale, M. In *The Physics and Applications of Carbon Nanotubes*; 12th International School on Condensed Matter Physics: Contemporary Trends in Condensed Matter Physics and Technology, 1−6 Sept. 2002, USA, Kluwer Academic Publishers: Norwell, MA, 2003; pp 657−659.
29. Hu, X. J.; Padilla, A. A.; Xu, J.; Fisher, T. S.; Goodson, K. E. 3-Omega Measurements of Vertically Oriented Carbon Nanotubes on Silicon. *J. Heat Transfer* **2006**, *128*, 1109–1113.
30. Ashby, M. F. *Materials Selection in Mechanical Design*, 3rd ed.; Butterworth-Heinemann: Oxford, UK, 2005.
31. Kim, J.-Y.; Greer, J. R. Tensile and Compressive Behavior of Gold and Molybdenum Single Crystals at the Nano-Scale. *Acta Mater.* **2009**, *57*, 5245–5253.
32. Tu, J. P.; Jiang, C. X.; Guo, S. Y.; Fu, M. F. Micro-friction Characteristics of Aligned Carbon Nanotube Film on an Anodic Aluminum Oxide Template. *Mater. Lett.* **2004**, *58*, 1646–9.
33. Tu, J. P.; Zhu, L. P.; Hou, K.; Guo, S. Y. Synthesis and Frictional Properties of Array Film of Amorphous Carbon Nanofibers on Anodic Aluminum Oxide. *Carbon* **2003**, *41*, 1257–1263.

Supporting Online Material

Higher Recovery and Better Energy Dissipation at Faster Strain Rates in Carbon Nanotube Bundles: an *in-situ* Study.

Siddhartha Pathak [1*], Ee J. Lim [1], Parisa Pour Shahid Saeed Abadi [2], Samuel Graham [2,3], Baratunde A. Cola [2,3], Julia R. Greer [1]

[1] Materials Science, California Institute of Technology (Caltech), Pasadena, CA, USA
[2] George W. Woodruff School of Mechanical Engineering, Georgia Institute of Technology, Atlanta, GA, USA.
[3] School of Materials Science and Engineering, Georgia Institute of Technology, Atlanta, GA, USA.

[*] Contact author: - Materials Science, California Institute of Technology (Caltech), 1200 E. California Blvd., MC 309-81, Pasadena, CA 91125-8100, Phone: +1 (626) 395-8165, Fax: +1 (626) 395-8868, E-mail: pathak@caltech.edu, siddharthapathak@gmail.com

Viscoelastic Characterization

In addition to their distinctive buckling behavior and their ability to recover from large deformations, VACNTs have also been reported to demonstrate a unique viscoelastic response, which was reported by a subset of the current authors for two separate VACNT systems [1, 2]. The remarkable nature of the viscoelastic behavior of VACNTs was further demonstrated in [3], where the material was found to exhibit this behavior for a wide temperature range from -196°C to 1000°C – something no other material had shown previously. In the research conducted in our group viscoelastic behavior including storage and loss moduli over a range of frequencies was reported by Hutchens, et al [1]. Below we describe the results of our additional viscoelastic experiments performed on the described VACNT micro-pillars.

The viscoelastic properties of the VACNT film were measured using flat punch indentation following the procedure outlined in Ref [1]. In this method the indenter is loaded into the sample at a constant displacement rate of 10 nm/s up to a specified strain, where the indenter head is oscillated at ~8 nm amplitude across a range of frequencies from 1 to 50 Hz. This cut-off frequency (50 Hz) is an instrument limitation as detailed in Ref [1, 4]. The procedure was repeated at four different strains: ε = 0.18, 0.4, 0.62 and 0.84, which ensured visco-elastic characterization of the samples in both their pre and post-densification regimes.

Viscoelastic materials are commonly characterized by their storage (E') and loss (E'') moduli, where the former represents the stored energy or the elastic response, and the latter corresponds to the amount of energy dissipated or the viscous response, as well as their ratio – $\tan\delta$. Assuming linear viscoelastic behavior, these terms can be computed following the calculations described in Refs [4-7] as follows:

$$E' = k'\frac{\sqrt{\pi}}{2\beta}\frac{1-\nu_s^{\,2}}{\sqrt{A}},\ k' = \left|\frac{F_0}{u_0}\right|\cos\varphi - \left|\frac{F_0}{u_0}\right|_{air}\cos\varphi_{air},$$

$$E'' = k''\frac{\sqrt{\pi}}{2\beta}\frac{1-\nu_s^{\,2}}{\sqrt{A}},\ k'' = \left|\frac{F_0}{u_0}\right|\sin\varphi - \left|\frac{F_0}{u_0}\right|_{air}\sin\varphi_{air},$$

$$\tan\delta = \frac{E''}{E'} \qquad (1)$$

Here k' and k'' are the storage and loss stiffnesses of the sample, obtained by finding the real and complex parts, respectively, of the stiffness differences between oscillating the indenter head on the sample at a fixed displacement and in air at the same raw displacement, β is a constant (=1 for a flat punch indenter), F_0 and u_0 are the load and displacement oscillation amplitudes respectively, and φ is the phase angle between the load and displacement oscillations. The accuracy in the values of E' and E'' in Eq. (1) can be affected by a couple of factors: uncertainties in the value of the Poisson ratio (since the Poisson's ratio can also be frequency dependent), and accuracy in the value of the contact area, especially at lower indentation depth where full contact may not have been established. On the other hand, calculation of $\tan\delta$ is independent of these parameters, and thus is ideally suited as a measure of the viscoelasticity of the indented material [2, 8].

The viscoelastic indentation response of the VACNT film, in terms of the measured values of their storage modulus (E'), loss modulus (E'') and $\tan\delta$ values, is shown below (Figure S1). Similar to the % recovery results discussed in the main manuscript, two distinct responses are seen in this figure depending on if the indenter is oscillated at levels corresponding to the (i) pre-densification regime (open symbols in Figure S1) or (ii) post-densification regime (filled symbols). While both E' and E'' are seen to increase by around 2-3 times after densification (Figures S1a and b), there is no difference in the values of $\tan\delta$ between the pre- pand post-densification regimes (Figure S1c). This indicates that both the values of E' and E'' have increased in equal proportions after densification.

The storage modulus values were found to be frequency independent over the range of frequencies used in this work. On the other hand the loss modulus (and the $\tan\delta$) values are strongly affected by the frequency, and they generally increase with increasing frequency, although a couple of local minimas can be indentified at 30 and 50 Hz respectively. Unfortunately the cut-off frequency (50 Hz) of our instrument prevents further study of this behavior at higher frequencies.

As shown in the figures of the main manuscript (Figures 1 and 2), the VACNT microstructure starts getting densified at strain levels of $\varepsilon \geq 0.65$-0.7. Thus the higher values of E' obtained in the post-densification regime indicate that the material is capable of storing a higher amount of energy in this state, with the excess energy presumably being stored in the buckled/densified regions. A correspondingly higher proportion of energy is also dissipated in this regime, as indicated by a similar increase in the values of E'' . However, the overall visco-elastic response of the VACNT material still remains unaffected, as seen in Figure S1c. These results match well with the loss coefficient measurements shown in Figure 6 (main manuscript), which also show similar values of loss coefficient between the pre- and post densification regimes. An analogous response was also noted by Xu et al. over a much wider temperature range of -196°C to 1000°C [3]. In addition the unloading modulus values shown in Figure 3 (main manuscript) are also are also found to match well with that of E' in Figure S1a.

Characterization of Material Damping Response

The loss coefficient, η, (a dimensionless quantity) measures the degree to which a material dissipates energy and is calculated in two different ways as shown below [9]

$$\eta = \frac{\Delta U_i}{2\pi U_1} \ , \ U = \int_0^{\sigma_{max}} \sigma d\varepsilon \ , \ \Delta U = \oint \sigma d\varepsilon \qquad (2)$$

$$\eta = \frac{\Delta U_i}{2\pi U_i} \ , \ U = \int_0^{\sigma_{max}} \sigma d\varepsilon \ , \ \Delta U = \oint \sigma d\varepsilon \qquad (3)$$

where U_1 and U_i are the elastic energy stored in the material when it is loaded elastically to a stress σ_{max} in the 1st and the ith cycle respectively, and ΔU_i is the energy dissipated in the ith load-unload cycle (see Fig. S2). The main difference between the above two equations is that in Equation (2) the normalization is done with respect to the area of the 1st loading cycle, while in Equation (3) it is done w.r.t. the area of the ith cycle

respectively. In other words, the denominator in Equation (2) is a constant while that of Equation (3) changes with every cycle. Each definition shows a different trend in the values of η as shown in the figure below.

As seen from the figure below, use of Equation (2) results in sharp drop in the values of η after the 1st cycle (Figure S2a), but there is no such drop when using Equation (3). Note that the values of η for the 1st cycle are exactly the same in both figures (Figure S2a and S2b). After the 1st cycle, both figures show a similar drop in the values of η for increasing cycle number. In both cases, η also appears to be strain dependent, and is maximized at the fastest 1000 nm/sec rate, similar to the trends noted for modulus and recovery. As in the case of the tan δ values described earlier, no significant different difference is seen between the pre- and post-densification regimes.

1. Hutchens, S. B.; Hall, L. J.; Greer, J. R., In situ Mechanical Testing Reveals Periodic Buckle Nucleation and Propagation in Carbon Nanotube Bundles. *Advanced Functional Materials* 2010, 20, 2338-2346.
2. Pathak, S.; Cambaz, Z. G.; Kalidindi, S. R.; Swadener, J. G.; Gogotsi, Y., Viscoelasticity and high buckling stress of dense carbon nanotube brushes. *Carbon* 2009, 47, 1969-1976.
3. Xu, M.; Futaba, D. N.; Yamada, T.; Yumura, M.; Hata, K., Carbon Nanotubes with Temperature-Invariant Viscoelasticity from-196 degrees to 1000 degrees C. *Science* 2010, 330, 1364-1368.
4. Herbert, E. G.; Oliver, W. C.; Pharr, G. M., Nanoindentation and the dynamic characterization of viscoelastic solids. *Journal of Physics D: Applied Physics* 2008, 41, 074021-1.
5. Herbert, E. G.; Oliver, W. C.; Lumsdaine, A.; Pharr, G. M., Measuring the constitutive behavior of viscoelastic solids in the time and frequency domain using flat punch nanoindentation. *Journal of Materials Research* 2009, 24, 626-37.
6. Wright, W. J.; Maloney, A. R.; Nix, W. D., An improved analysis for viscoelastic damping in dynamic nanoindentation. *International Journal of Surface Science and Engineering* 2007, 1, 274-92.
7. Wright, W. J.; Nix, W. D. In *Storage and loss stiffnesses and moduli as determined by dynamic nanoindentation*, 506 Keystone Drive, Warrendale, PA 15086, United States, Materials Research Society: 506 Keystone Drive, Warrendale, PA 15086, United States, 2009; pp 863-871.
8. Pathak, S.; Gregory Swadener, J.; Kalidindi, S. R.; Courtland, H.-W.; Jepsen, K. J.; Goldman, H. M., Measuring the dynamic mechanical response of hydrated mouse bone by nanoindentation. *Journal of the Mechanical Behavior of Biomedical Materials* 2011, 4, 34-43.
9. Ashby, M. F., *Materials Selection in Mechanical Design*. Butterworth-Heinemann; : 2005 (3 ed.).

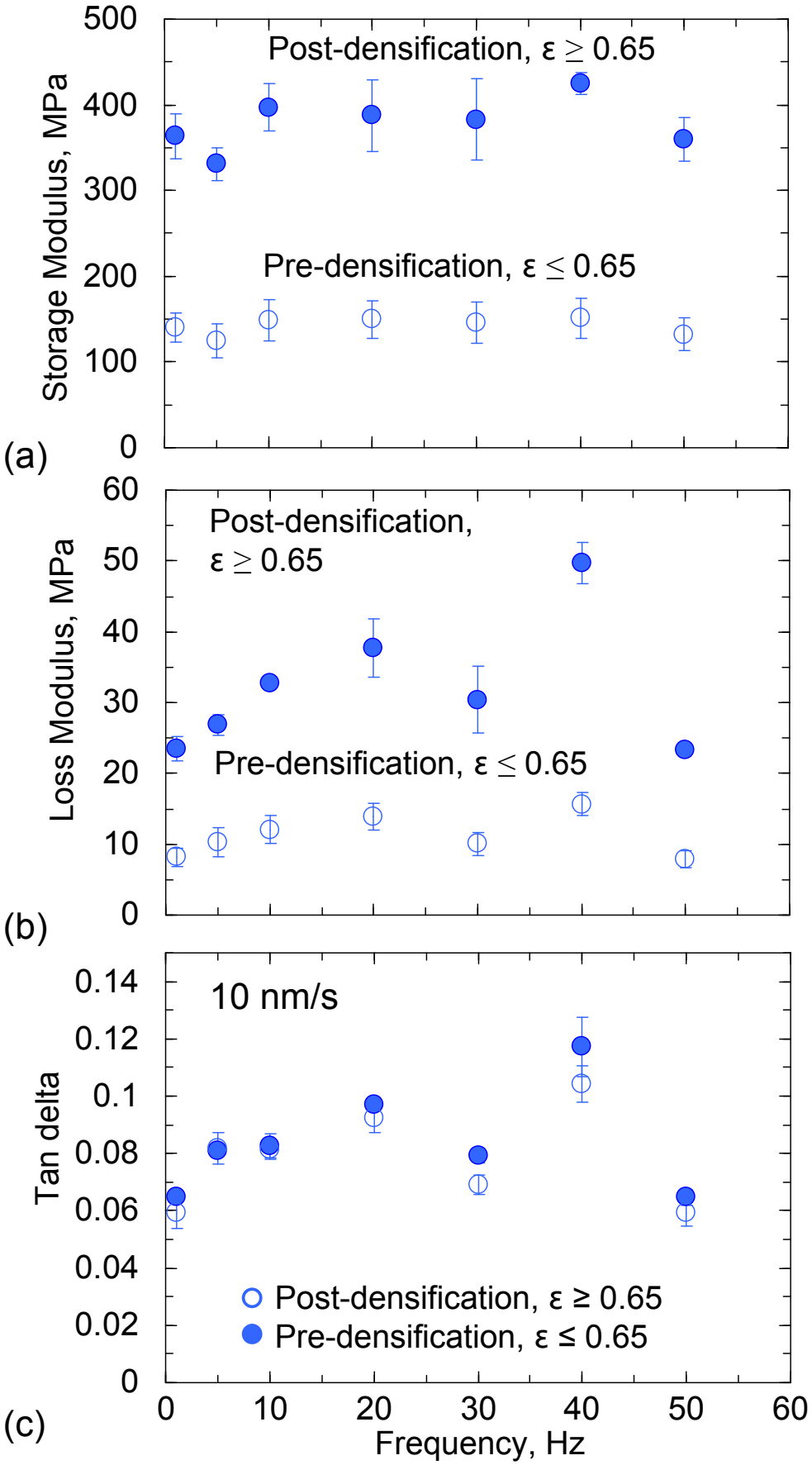

Figure S1 (Supporting online material). The viscoelastic indentation response of the VACNT micro-pillars loaded at a rate of 10 nm/s, in terms of the measured values (average ±standard deviation) of their (a) storage modulus, (b) loss modulus and (c) tan δ values, as a function of frequency.

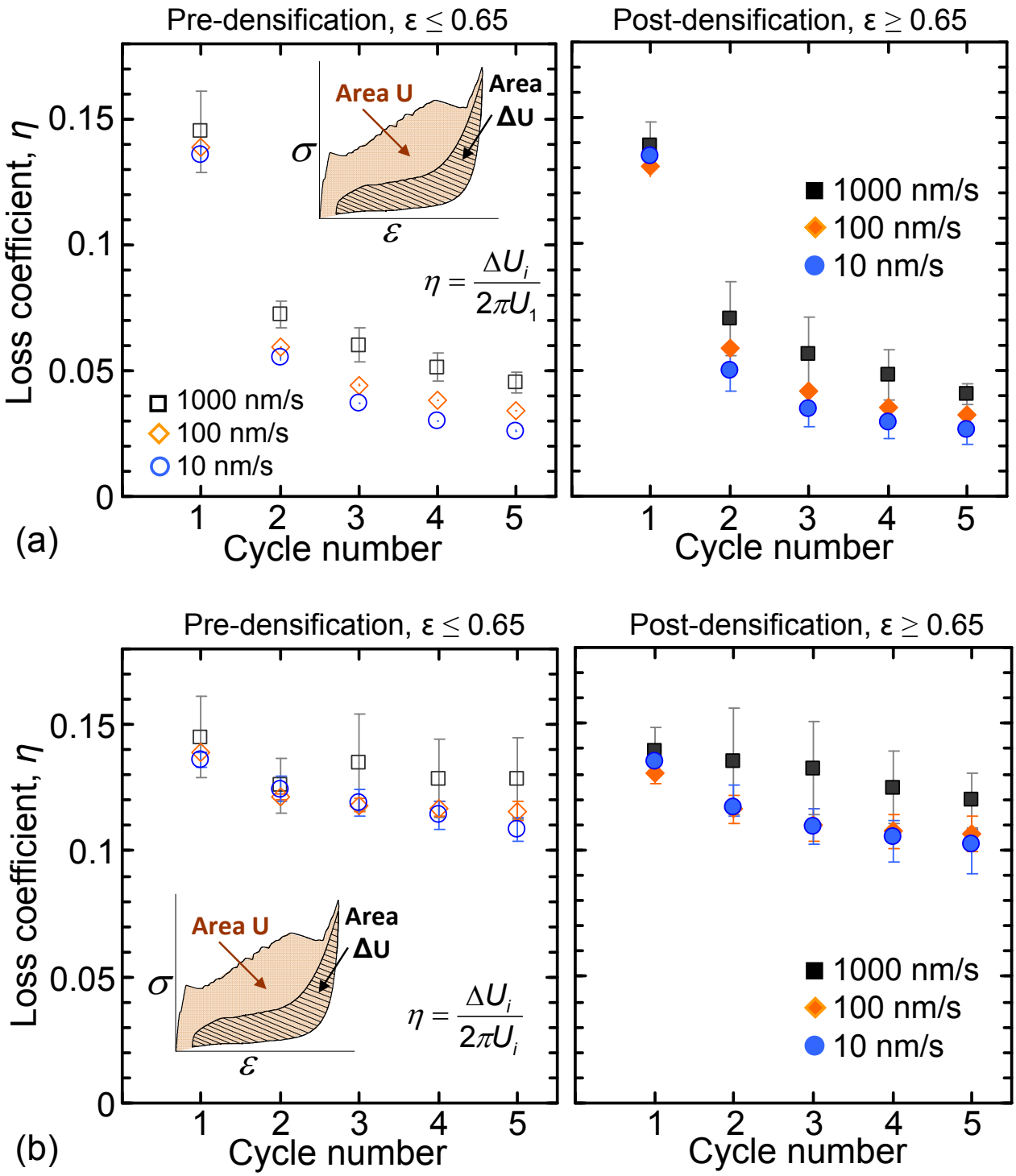

Figure S2 (Supporting online material). (a) The loss coefficient values calculated using Eq. (2) and (b) using Eq. (3) as a function of load-unload cycles showing better energy dissipation at higher rates.

Influence of density gradients on the stress-strain response of carbon nanotube micropillars

Siddhartha Pathak [1*], Nisha Mohan [1], Elizabeth Decolvenaere [1], Alan Needleman [2], Mostafa Bedewy [3], Anastasios John Hart [3], Julia R. Greer [1]

[1] Materials Science, California Institute of Technology (Caltech), Pasadena, CA, USA
[2] Department of Materials Science and Engineering, College of Engineering and Center for Advanced Scientific Computing and Modeling (CASCaM), University of North Texas, Denton, TX, USA.
[3] Mechanosynthesis Group, Department of Mechanical Engineering, University of Michigan, Ann Arbor, MI, USA.

Abstract

The combined results of *in-situ* micro-mechanical experiments, image analysis, and mechanics modeling revealed a linear correlation between the local number density of individual carbon nanotubes within vertically aligned carbon nanotubes (VACNT) forests, their microstructural deformation mechanism, and the hardening slope within their compressive stress-strain response. Both the stress-strain response and the commencement of localized buckling-like deformation were found to depend on the relative local density profile, which was quantified by edge-detection based image analysis. Those samples whose image analysis revealed a positive density gradient, i.e. where the density at the bottom of the forest was lower than that at the top, underwent a sequential bottom-to-top buckling and exhibited hardening in the stress-strain response. When the density gradient was insubstantial or slightly reversed, the bottom regions always buckled last and had a globally flat stress-strain response. These experimental findings were corroborated by the 2-dimensional, local material model based on a viscoplastic solid with plastic non-normality and with the effective stress – effective strain relation containing an initial peak, followed by softening and then hardening, originally reported by Hutchens, et al. [1,2] (Hutchens, S. B., Needleman, A. & Greer, J. R. Analysis of uniaxial compression of vertically aligned carbon nanotubes. Journal of the Mechanics and Physics of Solids 59, 2227-2237, 2011).

Keywords

Vertically aligned carbon nanotubes, compression, mechanical properties, energy storage, finite element simulation.

[*] Contact author: - Materials Science, California Institute of Technology (Caltech), 1200 E. California Blvd., MC 309-81, Pasadena, CA 91125-8100, Phone: +1 (626) 395-8165, Fax: +1 (626) 395-8868, E-mail: pathak@caltech.edu, siddharthapathak@gmail.com

1. Motivation and Background

Developing low-density materials for engineering applications requires knowing the relationships between their structural component geometries and the physical and mechanical properties of constituent materials, like density and strength. These relationships may be challenging to obtain, especially for the complex hierarchical and largely disordered cellular structures like vertically aligned carbon nanotubes (VACNT) forests. These materials represent examples of spatial hierarchy because the individual nanotubes have diameters on the order of tens of nanometers; the individual openings or inter-tube distances may range from a few to hundreds of nanometers, the heights of the individual nanotubes may be as high as hundreds of microns to several millimeters, and their lateral extent of the forests can have macroscopic dimensions. The complexity associated with this structural design, as well as the unique properties driven by the nanometer dimensions and the attractive van der Waals interactions among the individual tubes, render quantifying their physical properties like density, characteristic mean-free path, and cell size, which are usually trivial to measure in conventional foams, particularly challenging.

Further, one of the grand pursuits in materials sciences is to develop a quantitative, predictive relationship between the characteristic microstructure of a particular material and its mechanical properties. Such relationships are powerful because they enable the derivation of structurally relevant quantities like strength, fatigue resistance, and fracture toughness based on what is known about the material. For example, in a typical metal the well-known Hall-Petch effect [3,4] relates the increase in yield strength, σ, to a decrease in the average grain size, d, through a power-law: $\sigma \sim d^{1/2}$. In cellular materials [5], both the Young's modulus (E) and strength scale with density: $E, \sigma \sim \rho^2$. No analogous quantitative theory, which unambiguously predicts the mechanical response of carbon nanotube networks as a function of their local microstructural attributes like density, porosity, and/or tortuosity, exists. Establishing such a link will serve as the foundation for the development of reliability models, which will connect the characteristic intrinsic dimensions with the *deformation evolution mechanisms* and the *macroscale* mechanical properties. It is particularly important and relevant to establish such quantitative links between the VACNT microstructure and their mechanical properties because of their extensive use in technological applications, which range from micro-electro-mechanical systems (MEMS) to energy dissipative systems like viscoelastic rubbers and foams [6-11].

The details of the VACNT synthesis process, catalytic chemical vapor deposition, determines the diameter and quality of the individual CNTs, as well as the alignment and density of the forest. For example, using floating' vs. 'fixed' catalysts [12] in chemical vapor deposition (CVD) syntheses [13] and growing carbon nanotubes via the carbide-derived carbon (CDC) [14] methods have been shown to result in vastly different VACNT morphologies. Such variations are evident both at the individual tube level (such as variations in tube diameter from 2-3 nm [15], to 20-50 nm [16], to greater than 100 nm [17], number of walls in the CNT structure etc.) and at the collective matrix levels (such as density variations from 0.018 [18] to 0.95 gm/cm^3 [15]). In part, this is evidenced by the wide range of mechanical properties reported for the VACNTs grown by different methods. For example, the modulus and the compressive buckling strengths of VACNTs have been

reported to range anywhere from sub-MPa [11,19] to tens of MPa [20-22] to GPa [15,23] levels (Fig. S1a vs. S1b, c and d in Supplementary Information). An even more conspicuous example is that nominally identical VACNT samples have been found to substantially recover after large compressions [6,10,11,24,25] (Figs. S1a and b) or to deform permanently even at modest strains [16,22,26-28] (Figs. S1c and d).

Mechanical experiments like uniaxial compressions of VACNT samples with micrometer dimensions [6,12,16,25,29] and indentations into VACNT forests [15,30-32] have demonstrated the similarities in their mechanical deformation characteristics to those of typical open-cell foams [5]. In the spirit of such a foam-like response, the compressive stress-strain curves for VACNTs have been described by having 3 distinct regimes: (1) an initial linear elastic loading, followed by (2) an oscillatory plateau, where each undulation in the data corresponded to a localized buckle formation in the material, and (3) a densification, manifested by a rapid stress increase. In contrast to cellular foams, which typically deform by bending and collapsing of the cell walls[5,33], the post-elastic flow in VACNTs was accommodated entirely by the formation of localized folds or buckles of the entangled arrays, usually oriented orthogonally to the compression direction (Fig. S1) [6,12,19,26,27,30]. Most VACNT structures, including patterned micro-pillars, have also been reported to follow a particular bottom-to-top buckling sequence under uniaxial compression, where the first buckle nucleated close to the substrate, and each subsequent lateral collapse event initiated only after the preceding one was completed, thus sequentially collapsing the entire structure [6,12,16,25]. Another departure in the compressive behavior of VACNTs from that of typical open-cell foams is that the plateau region in their stress-strain curves has a positive global slope, which has been reported to range anywhere from 0.5 to 12 MPa [6,12,16,25]. In open-cell foams, this plateau region is virtually horizontal [5]. It has been speculated that the observed non-zero plateau slopes in VACNTs may be uniquely determined by a gradient in the material mechanical properties, like stiffness or yield strength, along the sample height [6,16]. This reasoning is motivated in part by the numerous observations during compressions which show the localized folds within CNT structures always forming first at locations close to the growth substrate, which in studies of the CNT growth process has been shown to be the location of lowest CNT number density [34,35]. The presence of fewer and wider separated individual tubes close to the growth substrate reduces the load-bearing capacity of the overall structure, which may drive the corresponding decrease in stiffness and yield stress at the base [6,26].

Recent models, which qualitatively captured the mechanics of VACNT deformation, have provided a physical foundation for the strengthening in the plateau region within the stress-strain VACNTs data [7,30]. Using a constitutive hardening-softening-hardening model with plastic non-normality, Hutchens et al. [1,2,36] showed that a linear variation in the input yield-like property along the sample height was correlated with the output slope of the plateau region in the stress-strain curve. A constant property along the sample height was shown to result in a flat plateau, while introducing a straight gradient in the input property caused a corresponding linear increase in the slope of the stress plateau. What remains unknown is the relationship between this yield-like mechanical property and the physical attributes of the material, which drive it. This is due, in part, by the difficulty of quantifying local microstructural characteristics of the VACNTs, as well as by the lack of experimental data, which demonstrates a flat plateau in the compressive stress-strain response of VACNTs.

The challenges associated with measuring the local CNT density within a VACNT forest have hampered the ability to develop experimentally-informed quantitative models of their deformation. During the early growth stages of a VACNT forest, the van der Waals attraction between CNTs causes them to self-organize into the aligned morphology after a threshold density is acheived. [32,35] Owing to CNT-CNT interactions, the resulting hierarchical forest is a highly intertwined porous 3-dimensional network structure. These morphological complexities result in several challenges when using scanning electron microscopes (SEM) to visualize the microstructure of VACNT forests: (1) ample adjustments in the imaging conditions like the depth of field, contrast, and brightness are required as the beam is rastered along the sample; (2) the interaction volume between the incident electrons and the secondary electrons in the SEM is ambiguous, which obscures the interpretation of a 2-dimensional image onto a 3-dimensional structure; and (3) sample-to-sample variation is substantial. Other methods have attempted to quantify the local morphology within VACNTs, for example small angle X-ray scattering (SAXS) and mass attenuation have been used to non-destructively quantify the alignment, diameter, and density of the CNTs. [32,35,37] However, a limitation is the X-ray beam size, which in recent studies was no smaller than 10 microns, [34,37] limiting the ability to characterize micro-scale density gradients as opposed to trends through millimeter-scale CNT forests.

Theoretical studies have also provided useful insights into the factors that may influence the mechanical properties of VACNTs. Astrom et al. modified the semi-theoretical version of the Cox shear-lag model [38] to describe the deformation of CNT mats and fibers by taking into account the statistical number of bundle–bundle contacts [39]. Their study suggested that the modulus of the CNT network was linearly related to the number of contact points. A similar result was obtained by Berhan and coworkers [40], who found that an increase in the waviness (tortuosity) of the nanotube ropes resulted in a significant reduction of their effective modulus [41]. Attempts have been made to explore these effects experimentally using a variety of techniques such as image analysis [32,42,43] and making analogies to the artificial neural networks [44], but no conclusive data was reported.

In this work, we used an edge detection technique based on the Canny algorithm [45] to the SEM images of VACNTs to calculate the relative differences in their 2-dimensional areal density as a function of spatial coordinates. SEM images were obtained by systematically adjusting the imaging parameters when visualizing two sets of VACNT samples, which exhibited substantially distinct mechanical behavior. The combination of such image analyses and *in-situ* micro-compression experiments revealed a quantifiable correlation between the relative density profiles, the microstructural deformation mechanism, and the mechanical stress-strain data. We then applied a 2-dimensional local material model based on a viscoplastic solid with plastic non-normality and with the effective stress – effective strain relation containing an initial peak, followed by softening and then hardening,[1] to quantify the mechanics of VACNT compressions. Reasoning that relative density was linearly related to the mechanical yield-like property at the same coordinates within the sample, we corroborated these experimental findings and revealed that the hardening slope of the plateau region in the stress-strain data was uniquely defined by the gradient in this property along the pillar height.

2. Materials and Methods

CNT Pillar Growth

VACNTs were synthesized by catalytic chemical vapor deposition (CVD) in a hot-walled reactor (Thermo-Fisher Mini-Mite, 22 mm inner diameter tube furnace with 12 in. heated length), from substrate-bound catalyst nanoparticles. Substrates were prepared by the physical vapor deposition of 1 nm of iron after 10nm of alumina on a thermally-oxidized (100) silicon wafer (0.5 mm thick). Micron-sized CNT pillars were prepared by photolithographic patterning of catalyst deposition (using SPR-220-3 photoresist). After lift-off of photoresist, millimeter-to-centimeter-sized silicon chips are loaded inside a quartz tube within the tube furnace. Before introducing the growth gas (ethylene) into the reactor, the multilayer thin film catalyst is heated in an atmosphere of hydrogen/helium to induce film dewetting into nanoscale particles. LabVIEW was used to interface and control all process variable, such as temperature and gas flow rates. After a five-minute helium (1000 sccm) purging step, hydrogen (400 sccm) and helium (100 sccm) are mixed and temperature is ramped up to 775 °C for 10 minutes and same temperature is maintained for another 10 minutes. Finally, ethylene (100 sccm) is introduced to the system for a maximum of 30 growth minutes. After growth, the tube is purged again with helium during cooling.

Ex-situ Compression Experiments

Two sets of stand-alone patterned VACNT samples, grown on the same Si substrate, were chosen for the compression tests (see Fig. 1). Both sample sets had the shape of micro-pillars, or columns, but differed in their cross-sectional geometry – one was a square with the sides of ~25 μm (hereafter referred to as "square pillars," Fig. 1c), and the other was a circle with the diameter of ~28 μm (hereafter referred to as "circular pillars," Fig. 1b). The heights of the square pillars were found to increase from 30 to 40.5 μm over the lateral distance of 2 mm on the Si substrate, and those of the circular pillars diminished from 42.6 to 38.7 μm over the same lateral extent. The compression experiments were performed in air, using the XP module of Agilent's nanoindenter G200 with a custom fabricated, ~120 μm diameter, diamond flat punch indenter tip. Tests were performed at constant displacement rates of 10 nm/s, 100 nm/s and 1000 nm/s using the Testworks software control methods described in Ref [16]. The maximum prescribed displacements ranged from 10% to 90% of the pillar heights, with multiple (up to 5) unload-reload cycles performed on the same pillar at discrete displacement intervals. During cyclical testing, the samples were unloaded to 10% of the maximum load in the previous cycle, and no constant-load holds were prescribed at the maximum loads before unloading. At least 5 tests were conducted at each compression rate.

In-situ Compression Experiments

In-situ uniaxial compression tests were conducted to capture the local microstructural evolution in the course of deformation. The *in-situ* testing was conducted in a custom built nanomechanical instrument, SEMentor, [46] which is comprised of a nano-mechanical dynamic contact module (Agilent Corp.) inside of a SEM (Quanta 200, FEI). The experimental methodology was nominally identical to the *ex-situ* experiments, with the exceptions of a vacuum environment and the flat punch dimensions of ~60 μm ×

80 μm in the SEMentor. The compression axis in the SEMentor is inclined by ~86^{o} with respect to the vertically-oriented electron beam, which allows for the unobstructed view of the deforming gauge section, while simultaneously acquiring the mechanical load and displacement data. The continuously captured image scans were recorded as a video file during the test and were synchronized with the mechanical data during post-processing to correlate each video frame with its corresponding position on the stress-strain curve (see video S1 in the SI). The CNT micro-pillars in the SEMentor were compressed horizontally, i.e. with the gravity acting perpendicular to the compression axis, while those in the G200 were conducted vertically. Although the effects of these differences are expected to be minor, the SEMentor-generated results were limited to visualization purposes, and all the data analyses were performed on tests conducted *ex-situ* in air in G200.

Data Analysis

Engineering stresses (σ) and strains (ε) were calculated using the initial dimensions of the VACNT micro-pillar along with the corrected load (p_{corr}) and displacement (u_{corr}) following the procedure in Ref [16]. Frictional forces between the VACNT pillar and the indenter head were not taken into account: [47-49]

$$\sigma = \frac{p_{corr}}{A_0} \ , \ \varepsilon = \frac{u_{corr}}{h_0} \qquad (1)$$

where $A_0 = w_0^2$ for the square pillars with the initial side width w_0 and $A_0 = \pi d_0^2/4$ for the circular pillars with the initial diameter d_0. The initial height of the pillars was h_0.

The percentage recovery (R) was defined as the strain recovered at the end of every cycle with respect to the total applied strain, $R = \frac{\varepsilon_{max} - \varepsilon_{unload}}{\varepsilon_{max}}$, where ε_{max} is the maximum strain at the end of loading and ε_{unload} is the strain after unloading to 10% of the max load in the previous cycle. Strain recovered in every cycle (i) was also compared to that in the previous cycle (i-1), to compute the relative recovery: $R_{relative} = \frac{R^i}{R^{i-1}} = \frac{\varepsilon_{max}^i - \varepsilon_{unload}^i}{\varepsilon_{max}^{i-1} - \varepsilon_{unload}^{i-1}}$

Image Analysis

The relative change in VACNT density along the heights of the samples was computed using an algorithmic image analysis technique centered on edge detection. During imaging, the samples were tilted to 30° with respect to the direction of the electron beam and imaged in a Zeiss 1550VP field emission SEM. The best imaging conditions were determined to be at 100 kX magnification, 10 kV accelerating voltage, at a working distance of 6 mm. These parameters captured a large enough representative area of the VACNT forest while maintaining an adequate resolution of the individual CNTs and bundles. To improve accuracy and to reduce variability in the interaction volume, the same SEM imaging conditions were maintained for each sample. 9-10 images at evenly spaced intervals were taken along the height of each pillar. The prescribed imaging contrast was set as constant along the entire height of every sample,

and only the brightness was adjusted to capture the full range of the intensity spectrum. To avoid any loss in resolution due to the 30° tilt of the samples, only the central 10% of each image was used for image analysis, as demonstrated in Fig. S2.

To estimate the number of CNTs in each image, the scans were first converted to grayscale, and the edges were identified and isolated using the Canny algorithm.[45] This method has been shown to be more accurate than the pure thresholding-based methods [43] because it preserves the overlapping tubes as individual entities. The Canny algorithm is deterministic, i.e. it always produces the same result for the same image, and it is not sensitive to the image brightness or its gradient. In the Canny algorithm, the image is first blurred using a Gaussian filter to remove the noise, with the pixel radius of the filter chosen specifically to minimize the background noise while preserving the necessary detail. In this work, a radius of 3 pixels, which corresponds to 1.8nm in the SEM images, was taken as the lower bound for the width of the tubes that were in best focus, i.e. likely located in the front of the sample. The partial derivatives of the intensities were taken along the horizontal and vertical directions in the image, and were subsequently inserted into analytical expressions to produce sets of angles and magnitudes of these partial derivatives at each point. A total of six discrete angles were evaluated at each point to minimize both computational time and the rate of false negatives. The resulting magnitudes were further filtered by the non-maximum suppression method, [51] which leaves only the image of the local maxima in the intensity gradient. The resulting image was thresholded based on these magnitudes, using hysteresis to preserve the neighboring lower intensity magnitudes that may belong to longer lines. Finally a black-and-white image was generated with a pixel intensity of 1 at the detected "edges", and 0 was assigned to all other locations. The resulting binary image was subsequently treated as a matrix and summed along the rows, producing a column vector of the number of edges.

Here, the number of tubes per unit width in each SEM image was calculated as half of the average of the column vectors. Although these values were found to be comparable across different samples captured with identical imaging conditions, the dependence of the Canny algorithm on the gradient means that the images had to be standardized for cross-comparison. This normalization required the images to be modified such that the mean became 0 and the standard deviation became 1. This was accomplished by defining the average relative tube number density, ζ, as

$$\zeta = \frac{x - \mu}{\sigma} \qquad (2)$$

where μ represents the mean number density of tubes in a set of images from a single pillar, and σ is the standard deviation of the mean number density of tubes in the same set. In Eq. 3, x is the pixel count transformed into a number density of tubes, i.e. $x = n/2 * (hw)$, where n is the pixel count in the central 10% of the image, and h and w are the number of rows and columns in that region, respectively. The factor of 2 is to account for both edges of each tube. A minimum of three pillars was used to generate the data of ζ versus vertical coordinate for a particular category of pillar morphology. The efficacy of ζ serving as a reliable figure-of-merit was crosschecked by a manual tube-counting procedure. A series of additional SEM images of the same samples was taken at a higher magnification of 200 kX and analyzed via the method above using a pixel radius of 6. These same images were overlaid with five horizontal lines, and the crossings between these lines and tubes in the images were manually counted. Similar trends were

identified when using the Canny algorithm vs. the manual counting technique, suggesting that the Canny method may represent an accurate approach to determine the relative local tube number density variation within the same sample.

Model Formulation

The mechanical behavior of the VACNT pillars with circular cross sections under compressive loading was modeled using a dynamic, axisymmetric finite element code following the procedure described in Ref. [1]. A compressible, isotropic elastic-viscoplastic constitutive relationship with plastic non-normality and a piecewise, linear hardening-softening-hardening type of flow strength function was used to model the material. This formulation has been reported to qualitatively capture some of the characteristics of the compression of VACNT micro-cylinders, such as the sequential formation of localized through-thickness folds oriented orthogonally to the compression direction and the oscillatory plateau region within the stress-strain curve, where each undulation corresponds to the formation and propagation of individual instabilities [36]. The global slope of the stress plateau region, θ, was reported to correlate with the mechanical yield-like property gradient along the sample height. Calculations of the plastic and elastic stress tensors (p and q) were carried out with the fixed plastic non-normality parameters α_p=0.2, β_p=0.28, where p and q are defined as follows: $=\tau-\beta_p(tr\tau)I$ and $q=\tau-\alpha_p(tr\tau)I$, where E/σ_o=100 (ratio of Youngs' Modulus to reference strength), γ_p=0.25 (plastic Poisson's ratio), m=0.02 (rate hardening exponent), H/r=3 (height to radius of pillar), ε_o=5000 (the reference strain rate). h_1=5.0, h_2=-1.5, h_3=1.5, ε_1=0.005, ε_2=0.1 (the hardening slopes and transition strains of the 'g' function) [36]. The 'g' function is the flow stress function used to simulate a rate-dependent solid and is defined over the plastic strain (ε_p) as follows (see also eqn. 10 in Needleman et. al, [36]):

$$g(\varepsilon_p)/\sigma_o = 1+ h_1(\varepsilon_p), \quad \varepsilon_p < \varepsilon_1;$$
$$= 1+ h_1(\varepsilon_1) + h_2(\varepsilon_p - \varepsilon_1), \quad \varepsilon_1<\varepsilon_p< \varepsilon_2;$$
$$= 1+ h_1(\varepsilon_1) + h_2(\varepsilon_2 - \varepsilon_1) + h_3(\varepsilon_p - \varepsilon_2), \quad \varepsilon_p> \varepsilon_2.$$

For further details on the complete formulation of the model, see Needleman et al. [36] In the model used in Ref. [36], this gradient was represented by the so-called strength multiplier, *SM*, which is a multiplier giving the the spatial variations of E (Young's modulus) and σ_o (reference strength) in the constitutive relation (see Fig. S3). In this work we further explored the effects of such a property gradient, focusing on 4 distinct cases: Case 1 – a flat SM function (*SM* is constant throughout the pillar height), Case 2 – a positive gradient in *SM* function (*SM* increases linearly with pillar height), Cas e3 – a negative gradient in *SM* function (*SM* decreases linearly towards the top of the sample), and Case 4 – a positive step function (*SM* has a sharp step-increase in the middle of the pillar height i.e. at z/H=0.5, where z and H are the variable and total heights of the pillar, respectively). The range of ΔSM (= $|SM_{top} - SM_{bottom}|$) was restricted to be between 0 to 40 % because sequential buckling disappeared outside of this range [36].

The computational results were analyzed in terms of (1) the normalized stress vs. strain, (2) the corresponding displacement contours of the outer edge of the sample, and (3) the strain rate contour plots, all as functions of deformation strain. As described in Ref[46], the true stress σ_t is calculated as $\sigma_t = P \Big/ \pi\left(R + u_r\left(R,H,t\right)\right)^2$, where P is the normal compressive force computed from the quasi-static principle of virtual work, and u_r is the

radial displacement of the cylinder as a function of its radius R, height H and the time step t.. This true stress is normalized by the reference yield stress σ_0. The true strain was computed by $\varepsilon_t = -ln(1+\varepsilon_n)$, with ε_n representing the nominal strain ($\varepsilon_n = \Delta H/H$), where ΔH is the top displacement, normalized by the initial height. The figures of merit for quantifying the output of the simulations were: (1) the transition strains (ε_1 and ε_2, Fig. 3d) and (2) the global hardening slope (θ) of the plateau region in the normalized stress-strain data. Cases 1, 2 and 3 required a single value of θ to define the entire plateau region, whereas in Case 4 (the *SM* step function), the plateau region had to be subdivided into two separate regions with the individual slopes of θ_1 and θ_2 (Fig. 3d). The evolution of the outer surface profiles was analyzed using the average amplitude (a) and wavelength (λ, Fig. 4a, right panel inset) of the resulting undulations at $\varepsilon_t = 40\%$ for each studied case. The strain rate contour plots (Fig. 4b), which are helpful for visualizing the sequential buckling process, are shown at the strains of $\varepsilon_t = 5\%$(initiation of the buckle-like fold), $\varepsilon_t = 10\%$ and 15% (propagation) and $\varepsilon_t = 20\%$ (densification) for the flat *SM* function (Case 1).

3. Results

Compression results

Experiments were performed on two sets of VACNT micropillars with square and circular cross sections, both grown by the same CVD process on the same substrate (Fig. 1), as described in the Methods section. The shape of the sample cross-sections did not appear to influence the deformation characteristics; rather it was their relative location on the substrate that likely played a key role in their resulting morphologies. The representative compressive mechanical response of each pillar type is shown in Fig. 1a. Stress-strain data for both pillar types exhibited 3 distinct regimes: (1) an initial linear elastic region, followed by (2) an oscillatory plateau region extending to the strains of ~75-80%, and (3) densification characterized by a steep stress increase upon further compression. While these features are commonly associated with the compressions of cellular solids such as open cell foams, [5] several important distinctions arise for the VACNTs. For example, the post-elastic stress plateau for both sets of pillars contained undulations, each of which corresponded to the consecutive buckling-like folding events (video S1 in the Supplementary Info). This is in contrast to traditional foams, where cell-edge bending and cell collapse mechanisms drive the stress plateau [5,52]. Several features were distinct between the two pillar types. The circular pillars had a nearly flat plateau (slope ~ 0.02 MPa) up to a strain of 75% (Fig. 1a). The plateau in the square pillars' data had two separate slopes: a relatively flat section up to 30% strain, followed by a steeper region, with the slope of 0.65 MPa to the unloading strain of 75% (Fig. 1b). The two pillar sets also differed in the amount of recovery after the first load-unload cycle: the circular pillars showed an almost 70% higher recovery than the square ones ($R \approx 42.6\%$).

In-situ uniaxial compressions tests were performed to identify whether any microstructural features and/or morphological attributes may have been associated with the distinctions in the mechanical response between the two sample types. These tests conveyed that the sequence in the formation of folds was consistently unique for each

sample type: for the square pillars the folds emanated from the bottom of the sample and propagated towards the top with increasing strain (Fig. 2a and video file S1); while the first instability in the circular pillars always formed somewhere at their mid-height (Fig. 2b, second panel from left),, and the buckle closest to the substrate was always the last one to form (Fig. 2b right-most panel). In the square pillars, the first buckling-like instability, which corresponded to the transition from the elastic segment to plateau in the stress-strain data, always formed at the bottom of the sample, immediately above the underlying Si substrate. After the initiation of the fold somewhere on the surface of the sample, the fold propagated laterally, spanning the entire pillar width. Consistent with the existing literature, the bottom-to-top buckling occurred in succession, with each subsequent buckle initiating only after the previous one, located below it, had completed [6,16]. Unloading the sample from the maximum compression of ~70% strain left the top third of the pillar virtually unscathed (Fig. 2a, third panel from left), and the buckle closest to the top was always the last one to form (Fig. 2a, right-most panel). In contrast, the SEM images of the post-compression circular pillars from the maximum strain of 70% showed that it was the *bottom* third of the pillar that remained undeformed (Fig. 2b, third panel from left). The central position of this set of pillars on the Si substrate prevented unobstructed observation of compression during the in-situ tests.

4. Discussion

4.1 Deformation mechanism as a function of local density variation.

Existing literature reports a wide range of mechanical properties of VACNTs, mainly due to the variations in their growth methods. Figure S1 highlights some examples, where VACNTs synthesized by different techniques were found to differ in their strengths (compare Fig. S1a vs. S1b, c and d), recoverability (full recovery, Figs. S1a and b vs . permanent deformation Figs. S1c and d), and the slope of the stress plateau in their stress-strain data (11, 5 and 0.6 MPa for Figs. S1a, c and d, respectively). To avoid such synthesis-induced variations, all the tested samples in this work were physically located on the same Si substrate and were synthesized using the same CVD process during the same run. The differences in their mechanical response, therefore, must stem from the variations in the specific details of their microstructure [10,11,16]. The hierarchy and complexity of the VACNT microstructure across multiple length scales are shown in Figs. 1c-e. At the lower magnifications of 4000X, the VACNT pillars appear either circular (Fig. 1b) or square (Fig. 1c). Increasing the magnification 10 times to 40,000X reveals the nominally vertical alignment of CNTs growing perpendicularly to the substrate within the overall VACNT network (Fig. 1d). A further five-fold increase in magnification to 200,000X reveals the isotropic CNT network with significant intertwining among the long, curved segments of the individual tubes that have a general vertical alignment [1,16,53]. As-grown, some tube segments within the CNT forest are bent to large angles, having formed contacts with one another as a result of the attractive van der Waals forces during growth. At the highest magnifications, which allow for the nanometer resolution in the TEM image shown in Fig. 1f, each nanotube is clearly visible. The overall properties of such a hierarchically composed material are expected to be a combination of the mechanical attributes of its constituents at each relevant length scale; from the individual nanotubes, whose properties are a function of their geometries,

the number of walls, and chirality – to the micron-sized "cell" dimensions - to the macroscopic, monolithic-like forests.

The compression results revealed that the two CNT micro-pillar shapes, which were grown on the same Si substrate, produced different deformation characteristics and different mechanical properties under compression. Specifically, the square pillars deformed by forming sequential folds, which progressed from the bottom of the sample towards its top (Fig. 2a). Alternatively, the first such instability in the circular pillars always formed somewhere along their heights and the last one – near the substrate. These deformation characteristics were reflected in the stress-strain data of each pillar type: the square pillars had steep slopes within their stress plateaus while the plateau region in the stress-strain data of the circular samples was globally flat. It is unlikely that the key reason for these differences was the square vs. circular cross-sectional shapes of the pillars, and hence using the axisymmetric pillar code to simulate both cases was reasonable. The key distinction between these two pillar types is in the local density and its variation along the pillar height. We hypothesize that the substantial differences in the deformation and mechanical properties between the two pillar types studied in this work were caused by the local density variation over the height of each pillar type.

4.2 Quantification of local density via image analysis.

Quantifying the absolute density while concurrently capturing the local fluctuations in such porous structures is challenging because the VACNTs do not have enough mass for the standard BET-type absorption techniques (see, for example [54-56], yet are too complicated for the typical image-based methods [57,58]. To overcome these difficulties, we chose to evaluate *relative* changes in the local VACNT density as a function of height rather than to attempt to compute the absolute densities. We utilized the edge detection techniques using the Canny algorithm[45] to systematically calculate the average relative number density, ζ, of tubes in each SEM image (see Materials and Methods). Image analysis revealed that the two types of samples exhibited mutually opposite trends with respect to the regions of highest relative density (Figure 2a,b). The square pillars had their highest ζ in the top 10 μm, and their density profiles resembled a step function, where $\zeta \approx 1$ for all locations above a pillar height of ~23 μm, and $\zeta \leq 0$ at all locales below. The maximum ζ in the circular pillars was located in the bottom ~10 μm, close to the substrate, and their relative density profiles were more or less random. Image analysis also revealed that the CNT number density dropped sharply in the midsection of all samples: at the height of ~ 23.7±3.5 μm in the 36 micron-tall the square pillars, and at ~16.3±1.5 μm in the 40 micron-tall circular ones.

Quantifying such relative density differences between the two sample sets is useful in understanding their deformation mechanism. For example, knowledge of the relative density profiles can be used to predict the location of the initial instability in a VACNT matrix. It is reasonable to expect the first folding event in compressed VACNTs originates close to the substrate because it is the region of the highest rigid constraint [26]. The square pillars in this study corroborate this idea (Fig. 2a). In contrast, the incipient localization in the circular pillars occurs somewhere in the middle of the pillar height because these locales correspond to the lowest relative CNT density along the pillar height. . In this case, the lower density trumps the constraining effects of the substrate in driving the instability. The final instabilities in both sets of pillars occurred in the regions

with the highest relative CNT densities: near the top in the square samples and near the bottom in the circular ones.

4.3 Linking density and strength

Beyond helping to explain and forecast the deformation mechanism, quantifying the local variations in density along the pillar heights may also be useful in predicting their compressive strengths as a function of deformation. Some of the features associated with the inelastic deformation of VACNTs under compression, such as the sequential buckle formation and the elastic-plateau-densification regimes in the stress-strain response, have been qualitatively captured using a finite deformation model of Hutchens et al [1,36]. This formulation uses a compressible elastic-viscoplastic constitutive relation with plastic non-normality and a linear hardening-softening-hardening flow strength function as described in the Materials and Methods section. The analyses in Ref. [1] also demonstrated the effect of an axial gradient in yield-like property over the height of the pillar on the stress-strain data and outer surface displacement.

To utilize this model in trying to link the microstructural detail like density to the mechanical stresses and strains, it is critical to first determine the relationship between the relative density and a mechanical property, which corresponds to the input function SM in the FE model. For example, the relationship between Young's modulus, E, scales with the square of the relative density for many low density materials such as open-cell foams, $E \sim \zeta^2$. [5] This relationship may not hold for the VACNTs, whose complex hierarchical make-up, as well as the friction and the van der Waals attraction among the individual nanotubes, elicit a unique stress-strain response. It is reasonable to expect that the stiffness or modulus of VACNT forests would depend on the number of intertube junctions in the matrix, as well as by the number of load-bearing members and their individual mechanical properties. To determine the dependence of Young's modulus on a morphology-governed figure of merit, Astrom et al. [39] applied a modified semi-theoretical version of the Cox shear-lag model [38] to CNT mats and fibers, while taking into account the statistical number of bundle–bundle contacts, which can be altered by chemical or irradiation-induced cross-linking. They confirmed that a critical issue in understanding elasticity of CNT networks is the lack of a quantifiable number of joints among crossing nanotubes. According to their model, the effective modulus of a single walled CNT mat is linearly related to the average number of bundle-bundle contacts per bundle. The number of fiber crossings also increased with the greater number of fibers,[41] and hence with the density, although this effect was not necessarily linear. This suggests that, to a first approximation, that the stiffness of VACNTs may be linearly related to its density, $E \sim \zeta$. Such a linear correlation was verified by Bradford et al [18] who used a post-growth CVD treatment on VACNT arrays to systematically vary their densities and then measured the compressive stresses as a function of compressive strain. The post-growth CVD treatment increased the individual CNT diameters through radial growth, which led to a higher global density, albeit the tube number density remained unchanged. A plot of the unloading elastic modulus as a function of density from the stress-strain data reported in [18] also shows a nearly linear dependence between the unloading modulus and density in VACNTs. Subsequent mechanical analysis is based on the assumption that the relationship between the stiffness and the relative density in VACNTs is linear.

4.4 Modeling stress vs. strain based on varying property gradients and constitutive relation

To uncover whether a quantifiable link between the relative density, a mechanical property gradient, and material strength could be established, we examined the output stress-strain data of the model with the input constitutive relation, which incorporated the same variation in the strength multiplier function, SM, as the variation in the relative CNT number density estimated from the image analysis. We assumed that the same spatial variation holds for Young's modulus E and for the reference flow strength σ_0. The absolute coefficient for the assumed linear correlation between the trends in density and the mechanical property will affect the linearly varying SM cases (Cases 1-3) but is not critical for the cases where the variation has the form of a step function case (Case 4). The strength gradients over the height in terms of *SM* function for all four cases considered are shown in Fig. 3(a, c), and the normalized stress-strain data for Cases 1-3 is shown in Fig. 3(b, d). These plots revealed a direct linear relationship between the global hardening slope, θ, of the stress-strain plateau and the strength multiplier range ΔSM ($\Delta SM = |SM_{top} - SM_{bot}| = 20\%$, shown as inset in Fig. 3a. Comparing Cases 2 and 3 revealed that a gradient of the same magnitude in either a forward or a reverse direction in SM, corresponding to the cases where density would vary from the bottom to the top vs. visa versa, led to the same slope in the hardening behavior in the normalized stress-strain curve. Such a lack of sensitivity to the sign of the gradient is likely due to the identical fixed boundary conditions in the axial direction (but not necessarily in the radial direction) at both ends of the pillar in the model. When the gradients of opposite signs are prescribed, the deformation would commence in the direction of weaker-to-stronger part of the pillar, i.e. in the opposing directions. No distinction between their stress-strain output would be expected because in both cases the stress is governed by the strain rate wave overcoming the progressively harder regions, regardless of their position within the pillar. For Case 4, where SM is represented as a step function along the sample height, and which matches the experiment most closely, a single value of slope was insufficient to characterize the stress-strain data. Rather, it was better described by two distinct slopes, θ_1 and θ_2, which were found to correlate with the relatively porous (weaker) bottom part and the more densely populated (stiffer) top segment. The normalized stress-strain curve for Case 4 (Fig. 3d, black curve) closely matched that for Case 1 (constant property, no gradient) until $\varepsilon_{1,}$. The second slope, θ_2, between the strains of ε_1 and ε_2 was significantly higher than θ_1 due to the abrupt shift to higher strengths in the middle of the pillar. In all cases, the slope(s) of the resulting stress-strain data qualitatively mimicked the shape of the input yield-like property gradient. It is reasonable, therefore, that a linear correlation between the two exists that can provide a quantifiable link between the measurable microstructural property, density, and the macroscopic mechanical response, stress as a function of strain. The hardening slope in Case 1, uniquely defined by a single value of $\theta_{,}$ is lower compared to the two linearly varying cases (Case 2 and 3), which suggests a linear relation between the output slope θ and the input property variation, ΔSM.

Table 1 provides a matrix of the input and output parameters for each studied case. The additional output figures of merit were amplitude, a, and the wavelength, λ, of the outer surface displacement undulations, whose definitions are schematically shown in Figure 4(d). Table 1 demonstrates a close-to-50% drop in the amplitude of the oscillations in Case 3 (negative property gradient) compared to Case 1 (no gradient) - likely due to the substrate-like hindrance from the fixed radial displacement boundary

condition at the bottom. As the instability progresses from the top towards the bottom of the sample, radial displacements are restricted, which lowers the buckle amplitude. No considerable effects are observed in the buckle wavelength because the axial boundary conditions at the top and bottom are similar. The presence of a step-form barrier in strength in Case 4 reduces the effective length of pillar to half of its real length, allowing only the lower half to undergo sequential folding, while the upper half has a single instability. In this case, both the amplitude and the wavelength of the outer surface displacements are lower than in all other cases.

The experimental results unambiguously revealed a correlation between the density gradient over the height of pillar and the hardening slope of the plateau region of stress-strain response. Assuming a linear correlation between the local density and yield-like strength at the same location (see Section 4.3 in Discussion), the strength variations in the simulated Cases 1 and 4 represent reasonable approximations to the density distributions gleaned from the uninformed image analysis for the two sets of pillars. Both the experimental and the simulated stress vs. strain relationships reflect the attributes of these input variations.

4.5 Effects of strain rate wave

Looking deeper into the mechanism of localized fold formation, we evaluated the effects of strain rate within the individual folding events. The instability appears to occur in two consecutive phases: initiation and propagation. As discussed in the previous section, the initiation of instabilities is uniquely defined by and is sensitive to the direction of the density gradient: the first buckling-like instability always nucleated at the weakest point over the height. This holds true in both the experiment (Fig. 2) and the simulations (Fig. 3). Case 4 in the simulations differs from all others because the sequential buckling propagated only in the relatively lower strength regions, in the bottom half of the pillar. The stress hardening slope from the initial loading to ε_1, θ_1, for Case 4 (step function) was virtually equivalent to that for Case 1 (uniform property), θ, which implies that the strain rate wave had not yet reached the strength barrier at that point. Figure 4(a-d) shows the outer surface displacements for each studied case at 4 progressively higher applied strains, and Fig. 4(e) shows the strain rate contour plots within the buckling phases for the no-gradient case (Case 1). These computational results revealed that in Case 1 (no gradient) the first fold initiated at the bottom with a high strain rate wave, which caused instability (leftmost panel in Fig. 4(e)). This high strain rate wave then propagated laterally to the right while concurrently climbing towards the top (Fig. 4, 2nd and 3rd panels). At each strain, only the part of pillar below the strain rate wave, became unstable and buckled, which led to the sequential formation of folds as the wave propagated through the structure. By the time the wave reached the top of the pillar, the entire sample became unstable, which shifted the deformation into the densification phase, indicated by the high strain rate dispersed over the entire sample (rightmost panel of Fig. 4) and the steep increase in the normalized stress at strains higher than ε_t =20% (Fig. 3).

4. Conclusion

This work presents the results of *in-situ* and *ex-situ* micro-mechanical experiments on stand-alone vertically aligned carbon nanotubes (VACNT) cylinders. Two distinct types of deformation mechanisms and ensuing mechanical data were uncovered for two sets of

pillars with different cross-sectional shapes: circular vs. square. All of these samples were physically grown on the same substrate and during the same synthesis instance. 2-dimensional edge detection algorithm applied to the systematically captured Scanning Electron Microscope (SEM) images along the height of each sample revealed distinct differences in the local density along the sample heights for each pillar type. We quantified the local density variations within each sample and postulate that these density profiles uniquely define both the deformation mechanism and the stress as a function of strain. Those samples whose image analysis revealed a positive density gradient, i.e. where the density at the bottom of the forest was lower than that at the top, underwent a sequential bottom-to-top buckling and exhibited hardening in the stress-strain response. When the density gradient was insubstantial or slightly reversed, the bottom regions always buckled last and had a globally flat stress-strain response. An axisymmetric finite element analysis using a size independent elastic-viscoplastic material model with plastic non-normality and with the effective stress - effective strain relation containing an initial peak, followed by abrupt softening and subsequent hardening, as described in Hutchens, et al.[31] was employed to quantify the relationship between the input flow strength gradient along the pillar height and the output mechanical response. The results of these simulations closely match those generated by the experiments, and both the experiments and the modeling provide a quantifiable relationship between the local number density of individual carbon strands within vertically aligned carbon nanotubes (VACNT) forests, their microstructural deformation mechanism, and the hardening slope within their compressive stress-strain response.

1 Hutchens, S. B., Needleman, A. & Greer, J. R. Analysis of uniaxial compression of vertically aligned carbon nanotubes. *Journal of the Mechanics and Physics of Solids* **59**, 2227-2237 (2011).

2 Hutchens, S. B., Needleman, A. & Greer, J. R. Erratum: Analysis of uniaxial compression of vertically aligned carbon nanotubes (Journal of the Mechanics and Physics of Solids (2011) 59 (2227-2237)). *Journal of the Mechanics and Physics of Solids* **60**, 1753-1756, doi:10.1016/j.jmps.2012.06.002 (2012).

3 Hall, E. O. The deformation and ageing of mild steel III. Discussion of results. *Proceedings of the Physical Society. Section B* **64**, 747-753, doi:04 002 (1951).

4 Petch, N. J. Cleavage strength of polycrystals. *Iron and Steel Institute -- Journal* **174**, 25-28, doi:04 003 (1953).

5 Gibson, L. J. & Ashby, M. F. *Cellular Solids: Structure and Properties*. (Cambridge University Press, 1999).

6 Cao, A. Y., Dickrell, P. L., Sawyer, W. G., Ghasemi-Nejhad, M. N. & Ajayan, P. M. Super-Compressible Foamlike Carbon Nanotube Films. *Science* **310**, 1307-1310, doi:10.1126/science.1118957 (2005).

7 Misra, A., Greer, J. R. & Daraio, C. Strain Rate Effects in the Mechanical Response of Polymer-Anchored Carbon Nanotube Foams. *Advanced Materials* **20**, 1-5 (2008).

8 Cho, J., Richards, C., Bahr, D., Jiao, J. & Richards, R. Evaluation of contacts for a MEMS thermal switch. *J. Micromech. Microeng.* **18**, doi:105012

10.1088/0960-1317/18/10/105012 (2008).
9 Cola, B. A., Xu, J. & Fisher, T. S. Contact mechanics and thermal conductance of carbon nanotube array interfaces. *International Journal of Heat and Mass Transfer* **52**, 3490-3503 (2009).
10 Xu, M., Futaba, D. N., Yamada, T., Yumura, M. & Hata, K. Carbon Nanotubes with Temperature-Invariant Viscoelasticity from-196 degrees to 1000 degrees C. *Science* **330**, 1364-1368, doi:10.1126/science.1194865 (2010).
11 Suhr, J. *et al.* Fatigue Resistance of Aligned Carbon Nanotube Arrays under Cyclic Compression. *Nature Nanotechnology* **2**, 417-421, doi:10.1038/nnano.2007.186 (2007).
12 Yaglioglu, O., Cao, A., Hart, A. J., Martens, R. & Slocum, A. H. Wide Range Control of Microstructure and Mechanical Properties of Carbon Nanotube Forests: A Comparison Between Fixed and Floating Catalyst CVD Techniques. *Advanced Functional Materials*, DOI: 10.1002/adfm.201200852, doi:10.1002/adfm.201200852 (2012).
13 Kumar, M. & Ando, Y. Chemical vapor deposition of carbon nanotubes: A review on growth mechanism and mass production. *Journal of Nanoscience and Nanotechnology* **10**, 3739-3758, doi:10.1166/jnn.2010.2939 (2010).
14 Presser, V., Heon, M. & Gogotsi, Y. Carbide-derived carbons - from porous networks to nanotubes and graphene. *Advanced Functional Materials* **21**, 810-833 (2011).
15 Pathak, S., Cambaz, Z. G., Kalidindi, S. R., Swadener, J. G. & Gogotsi, Y. Viscoelasticity and High Buckling Stress of Dense Carbon Nanotube Brushes. *Carbon* **47**, 1969-1976, doi:10.1016/j.carbon.2009.03.042 (2009).
16 Hutchens, S. B., Hall, L. J. & Greer, J. R. In situ Mechanical Testing Reveals Periodic Buckle Nucleation and Propagation in Carbon Nanotube Bundles. *Advanced Functional Materials* **20**, 2338-2346, doi:10.1002/adfm.201000305 (2010).
17 Qi, H. J. *et al.* Determination of mechanical properties of carbon nanotubes and vertically aligned carbon nanotube forests using nanoindentation. *Journal of the Mechanics and Physics of Solids* **51**, 2213-2237, doi:02 007 (2003).
18 Bradford, P. D., Wang, X., Zhao, H. & Zhu, Y. T. Tuning the Compressive Mechanical Properties of Carbon Nanotube Foam. *Carbon* **49**, 2834-2841 (2011).
19 Tong, T. *et al.* Height Independent Compressive Modulus of Vertically Aligned Carbon Nanotube Arrays. *Nano Letters* **8**, 511-515, doi:10.1021/nl072709a (2008).
20 Mesarovic, S. D. *et al.* Mechanical Behavior of a Carbon Nanotube Turf. *Scr. Mater.* **56**, 157-160, doi:10.1016/j.scriptamat.2006.09.021 (2007).
21 Qiu, A. *et al.* Local and Non-Local Behavior and Coordinated Buckling of CNT Turfs. *Carbon* **49**, 1430-1438, doi:10.1016/j.carbon.2010.12.011 (2011).
22 Zhang, Q. *et al.* Viscoelastic Creep of Vertically Aligned Carbon Nanotubes. *Journal of Physics D-Applied Physics* **43**, 315401-315401-315407, doi:315401 10.1088/0022-3727/43/31/315401 (2010).
23 Deck, C. P., Flowers, J., McKee, G. S. B. & Vecchio, K. Mechanical Behavior of Ultralong Multiwalled Carbon Nanotube Mats. *Journal of Applied Physics* **101**, 23512-23511-23519, doi:02 011 (2007).

24 Xu, M., Futaba, D. N., Yumura, M. & Hata, K. Carbon Nanotubes with Temperature-Invariant Creep and Creep-Recovery from −190 to 970 °C. *Advanced Materials* **23**, 3686-3691, doi:10.1002/adma.201101412 (2011).
25 Pathak, S. *et al.* Higher Recovery and Better Energy Dissipation at Faster Strain Rates in Carbon Nanotube Bundles: An in-Situ Study. *ACS Nano* **6**, 2189-2197, doi:10.1021/nn300376j (2012).
26 Zbib, A. A. *et al.* The Coordinated Buckling of Carbon Nanotube Turfs under Uniform Compression. *Nanotechnology* **19**, 175704-175701-175707, doi:175704 10.1088/0957-4484/19/17/175704 (2008).
27 Cao, C. *et al.* Buckling Initiation and Displacement Dependence in Compression of Vertically Aligned Carbon Nanotube Arrays. *Carbon* **49**, 3190-3199, doi:10.1016/j.carbon.2011.03.043 (2011).
28 Yaglioglu, O. *Carbon Nanotube Based Electromechanical Probes - PhD Thesis* PhD thesis, Massachusetts Institute of Technology, (2007).
29 Raney, J. R., Misra, A. & Daraio, C. Tailoring the microstructure and mechanical properties of arrays of aligned multiwall carbon nanotubes by utilizing different hydrogen concentrations during synthesis. *Carbon* **49**, 3631-3638 (2011).
30 Maschmann, M. R., Qiuhong, Z., Feng, D., Liming, D. & Baur, J. Length dependent foam-like mechanical response of axially indented vertically oriented carbon nanotube arrays. *Carbon* **49**, 386-397, doi:10.1016/j.carbon.2010.09.034 (2011).
31 Pathak, S. *et al.* Compressive Response of Vertically Aligned Carbon Nanotube Films via *In-Situ* Flat Punch Indentations. *Journal of Materials Research* (2012 (submitted)).
32 McCarter, C. M. *et al.* Mechanical compliance of photolithographically defined vertically aligned carbon nanotube turf. *Journal of Materials Science* **41**, 7872-7878, doi:10.1007/s10853-006-0870-5 (2006).
33 Maschmann, M. R. *et al.* Visualizing Strain Evolution and Coordinated Buckling within CNT Arrays by In Situ Digital Image Correlation. *Advanced Functional Materials* **22**, 4686-4695, doi:10.1002/adfm.201200676 (2012).
34 Bedewy, M. *et al.* Collective mechanism for the evolution and self-termination of vertically aligned carbon nanotube growth. *Journal of Physical Chemistry C* **113**, 20576-20582, doi:10.1021/jp904152v (2009).
35 Pour Shahid Saeed Abadi, P. *et al.* The Effect of Morphology on the Micro-Compression Response of Carbon Nanotube Forests. *Nanoscale* **4**, 3373-3380, doi:10.1039/c2nr30474k (2012).
36 Needleman, A., Hutchens, S. B., Mohan, N. & Greer, J. R. Deformation of plastically compressible hardening-softening-hardening solids. *Acta Mechanica Sinica* **28**, 1115-1124 (2012).
37 Wang, B. N., Bennett, R. D., Verploegen, E., Hart, A. J. & Cohen, R. E. Characterizing the Morphologies of Mechanically Manipulated Multiwall Carbon Nanotube Films by Small-Angle X-ray Scattering†. *The Journal of Physical Chemistry C* **111**, 17933-17940, doi:10.1021/jp071798c (2007).
38 Cox, H. L. Elasticity and strength of paper and other fibrous materials. *British Journal of Applied Physics* **3**, 72-79, doi:10.1088/0508-3443/3/3/302 (1952).

39 Astrom, J. A., Krasheninnikov, A. V. & Nordlund, K. Carbon nanotube mats and fibers with irradiation-improved mechanical characteristics: A theoretical model. *Phys. Rev. Lett.* **93**, 215503-215501-215503-215504, doi:10.1103/PhysRevLett.93.215503 (2004).

40 Berhan, L. *et al.* Mechanical properties of nanotube sheets: Alterations in joint morphology and achievable moduli in manufacturable materials. *Journal of Applied Physics* **95**, 4335-4345, doi:10.1063/1.1687995 (2004).

41 Berhan, L., Yi, Y. B. & Sastry, A. M. Effect of nanorope waviness on the effective moduli of nanotube sheets. *Journal of Applied Physics* **95**, 5027-5034, doi:10.1063/1.1687989 (2004).

42 Malik, H., Stephenson, K. J., Bahr, D. F. & Field, D. P. Quantitative characterization of carbon nanotube turf topology by SEM analysis. *Journal of Materials Science* **46**, 3119-3126, doi:10.1007/s10853-010-5192-y (2011).

43 Gao, Y. *et al.* Impact of nanotube density and alignment on the elastic modulus near the top and base surfaces of aligned multi-walled carbon nanotube films. *Carbon* **50**, 3789-3798, doi:10.1016/j.carbon.2012.04.004 (2012).

44 Al-Khedher, M. A., Pezeshki, C., McHale, J. L. & Knorr, F. J. Quality classification via Raman identification and SEM analysis of carbon nanotube bundles using artificial neural networks. *Nanotechnology* **18**, doi:10.1088/0957-4484/18/35/355703 (2007).

45 Canny, J. A computational approach to edge detection. *IEEE Transactions on Pattern Analysis and Machine Intelligence* **PAMI-8**, 679-698 (1986).

46 Kim, J.-Y. & Greer, J. R. Tensile and Compressive Behavior of Gold and Molybdenum Single Crystals at the Nano-Scale. *Acta Materialia* **57**, 5245-5253 (2009).

47 Tu, J. P., Jiang, C. X., Guo, S. Y. & Fu, M. F. Micro-Friction Characteristics of Aligned Carbon Nanotube Film on an Anodic Aluminum Oxide Template. *Materials Letters* **58**, 1646-1649 (2004).

48 Tu, J. P., Zhu, L. P., Hou, K. & Guo, S. Y. Synthesis and Frictional Properties of Array Film of Amorphous Carbon Nanofibers on Anodic Aluminum Oxide. *Carbon* **41**, 1257-1263 (2003).

49 Bhushan, B., Xing, L., Jungen, A. & Hierold, C. Adhesion and friction of a multiwalled carbon nanotube sliding against single-walled carbon nanotube. *Physical Review B (Condensed Matter and Materials Physics)* **77**, 165428-165421, doi:10.1103/PhysRevB.77.165428 (2008).

50 Ashby, M. F. *Materials Selection in Mechanical Design*. (Butterworth-Heinemann; , 2005 (3 ed.)).

51 Canny, J. F. *Finding Edges and Lines in Images* Master of Science thesis, Massachusetts Institute of Technology, (1983).

52 Gibson, L. J. Mechanical Behavior of Metallic Foams. *Annual Review of Materials Science* **30**, 191-227 (2000).

53 Deshpande, V. S. & Fleck, N. A. Isotropic constitutive models for metallic foams. *Journal of the Mechanics and Physics of Solids* **48**, 1253-1283, doi:10.1016/s0022-5096(99)00082-4 (2000).

54 Brunauer, S., Emmett, P. H. & Teller, E. Adsorption of gases in multimolecular layers. *Journal of the American Chemical Society* **60**, 309-319 (1938).

55 Błachnio, M., Staszczuk, P. & Grodzicka, G. Adsorption and porosity properties of pure and modified carbon nanotube surfaces. *J Therm Anal Calorim* **94**, 641-648, doi:10.1007/s10973-008-9371-x (2008).
56 Jagtoyen, M., Pardue, J., Rantell, T., Grulke, E. & Derbyshire, F. in *Pac. Basin Conf., Adsorpt. Sci. Technol.,.* (ed Duong D Do) 289-293 (World Scientific Publishing Co. Pte. Ltd., Singapore, Singapore).
57 Shaffer, M. S. P., Fan, X. & Windle, A. H. Dispersion and packing of carbon nanotubes. *Carbon* **36**, 1603-1612, doi:10.1016/s0008-6223(98)00130-4 (1998).
58 Ghasemi-Mobarakeh, L., Semnani, D. & Morshed, M. A novel method for porosity measurement of various surface layers of nanofibers mat using image analysis for tissue engineering applications. *Journal of Applied Polymer Science* **106**, 2536-2542, doi:10.1002/app.26949 (2007).

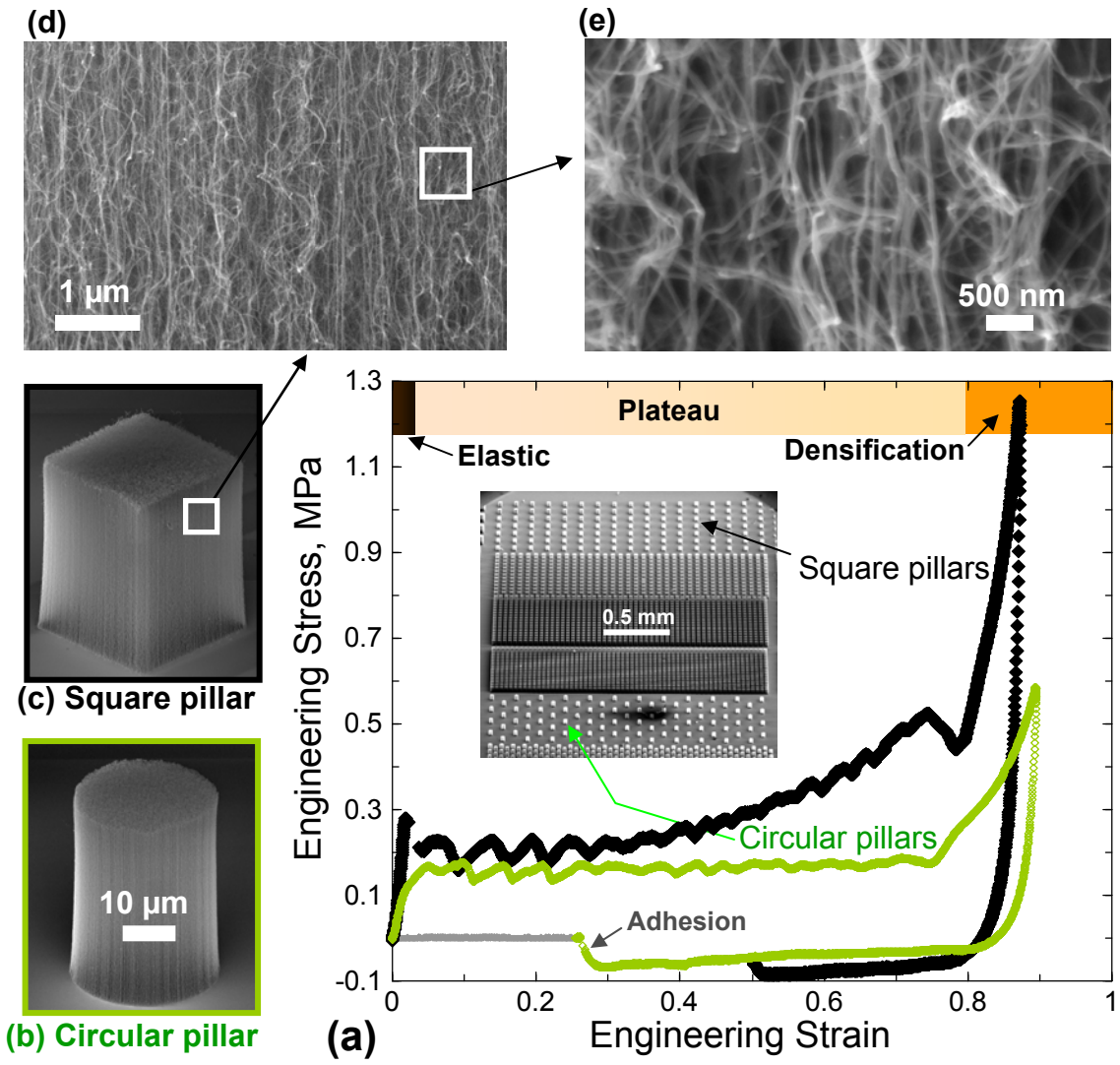

Figure 1. (a) Comparison of the stress-strain responses of two VACNT pillar systems grown on the same substrate; while the square pillars in (c) show a heavily sloped plateau region, the same for the circular pillars shown in (b) is almost flat (as in open-cell foams). The square pillars also show a lower recovery than the circular pillars.

Micrographs in (d) and (e) reveal the hierarchical morphology of VACNTs, which consist of nominally vertical aligned CNTs at low magnification, and a complex intertwined network at higher mag. SEM pictures are taken at a 60 deg tilt angle.

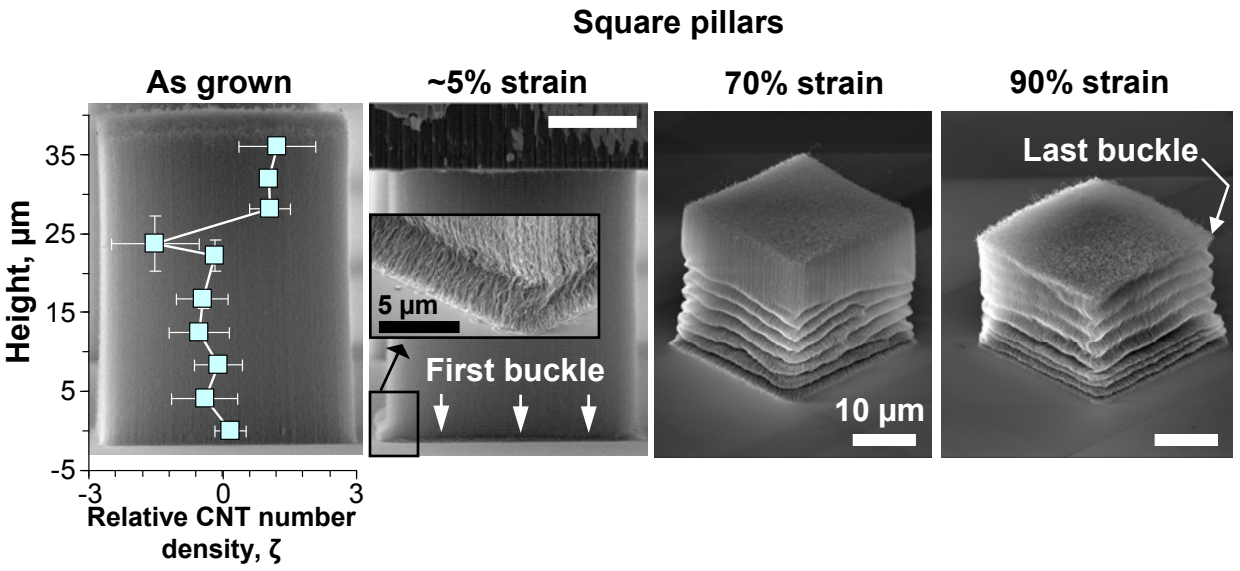

(a)

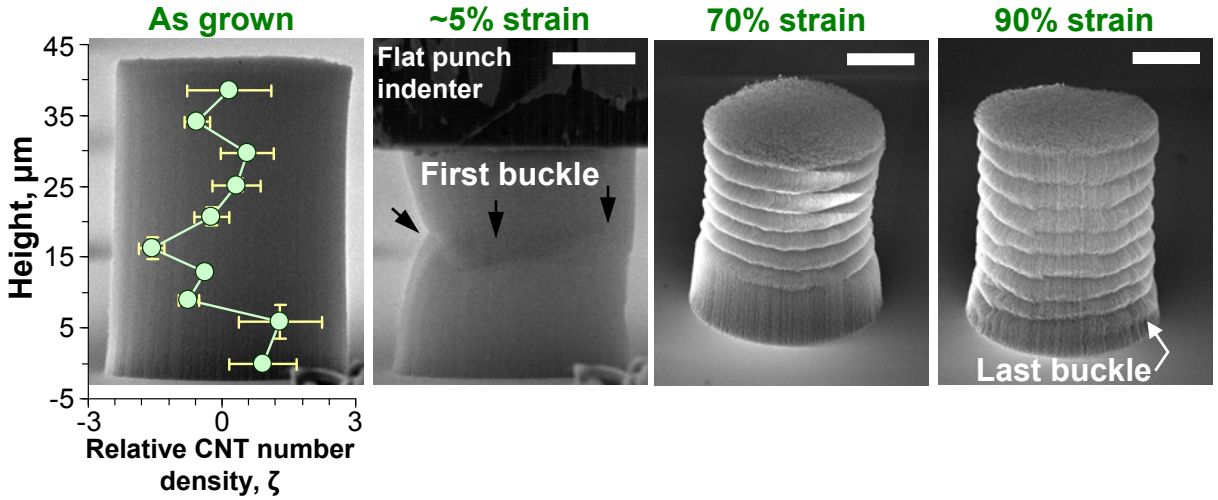

(b)

Circular pillars

Figure 2. Relationship between the relative tube number density ζ (Eq. XX) and the sequence of buckle-formation for the (a) square and (b) circular pillars.

In (a) the square pillars have a higher relative density ζ towards the top ~10 μm of the pillar, and buckles in this region of the pillar are the last to form. Buckling in these pillars follows a bottom-to-top sequence as shown by the SEM images. Thus the first buckle always forms at the bottom (indicated by white arrows), but the top half of the pillar is still undamaged when the sample is unloaded from a strain of ε ~ 0.7. The buckles in the region with the highest ζ values are the last to form.

On the other hand, in (b) the highest values of ζ are at the bottom ~10 μm of the circular pillars. Thus while the first buckle forms at the center of the circular pillars where the ζ value is low (indicated by the black arrows), the buckles at the bottom are the last ones to form at high strain levels ($\varepsilon \sim 0.9$), i.e. in the densification regime. At lower strains ($\varepsilon \sim 0.7$) the bottom section of the circular pillars are still free of buckles.

The two left SEM images in (a) and (b) were taken at a 86 deg tilt angle and have the same magnification, while the two right SEM pictures (of similar magnification) were taken at a 60 deg tilt angle. All scale-bars are of 10 μm length.

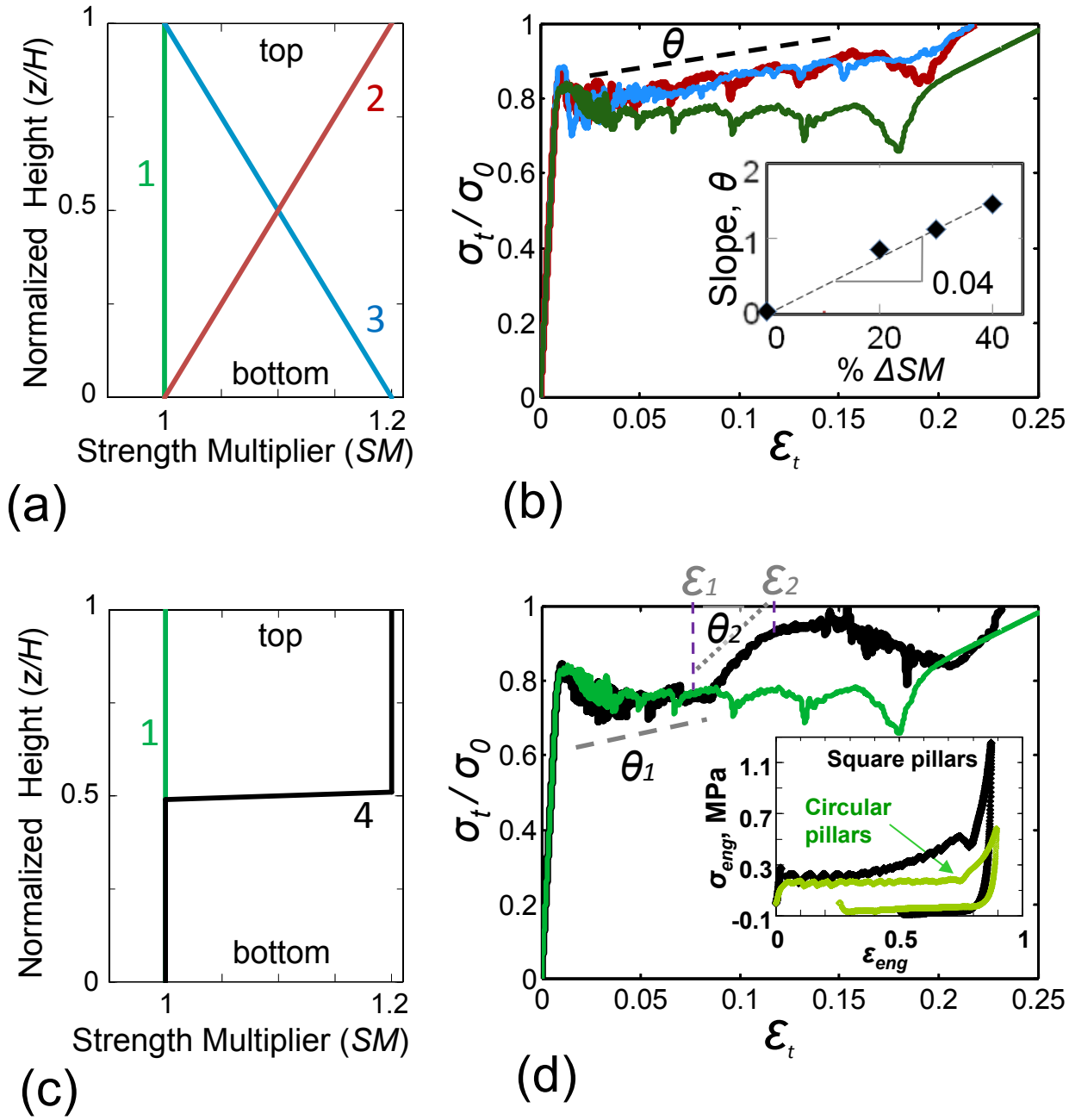

Fig 3. (a) Three variations of the *SM* function: Case 1: constant *SM* function, Case 2 and 3: linearly increasing and decreasing SM functions respectively. (b) Corresponding normalized stress-strain curves showing a linear elastic region, buckling perturbations in the plateau region and densification at ε_t ~20%. Inset: Plot of the hardening slope of the plateau region (θ) vs. % *ΔSM* over the height of the pillar, showing a linear relationship. (c) Comparison of Case 1 vs. Case 4 (step variation of the *SM* function over the pillar height). (d) Corresponding normalized stress-strain curves for these two cases. Note that the plateau region in case 4 can be further subdivided by two distinct slopes, θ_1 and θ_2. (d) Inset: Experimental uniaxial stress-strain curves responses of the square vs. circular pillars showing the similarity in their responses as compared to the two cases in (c).

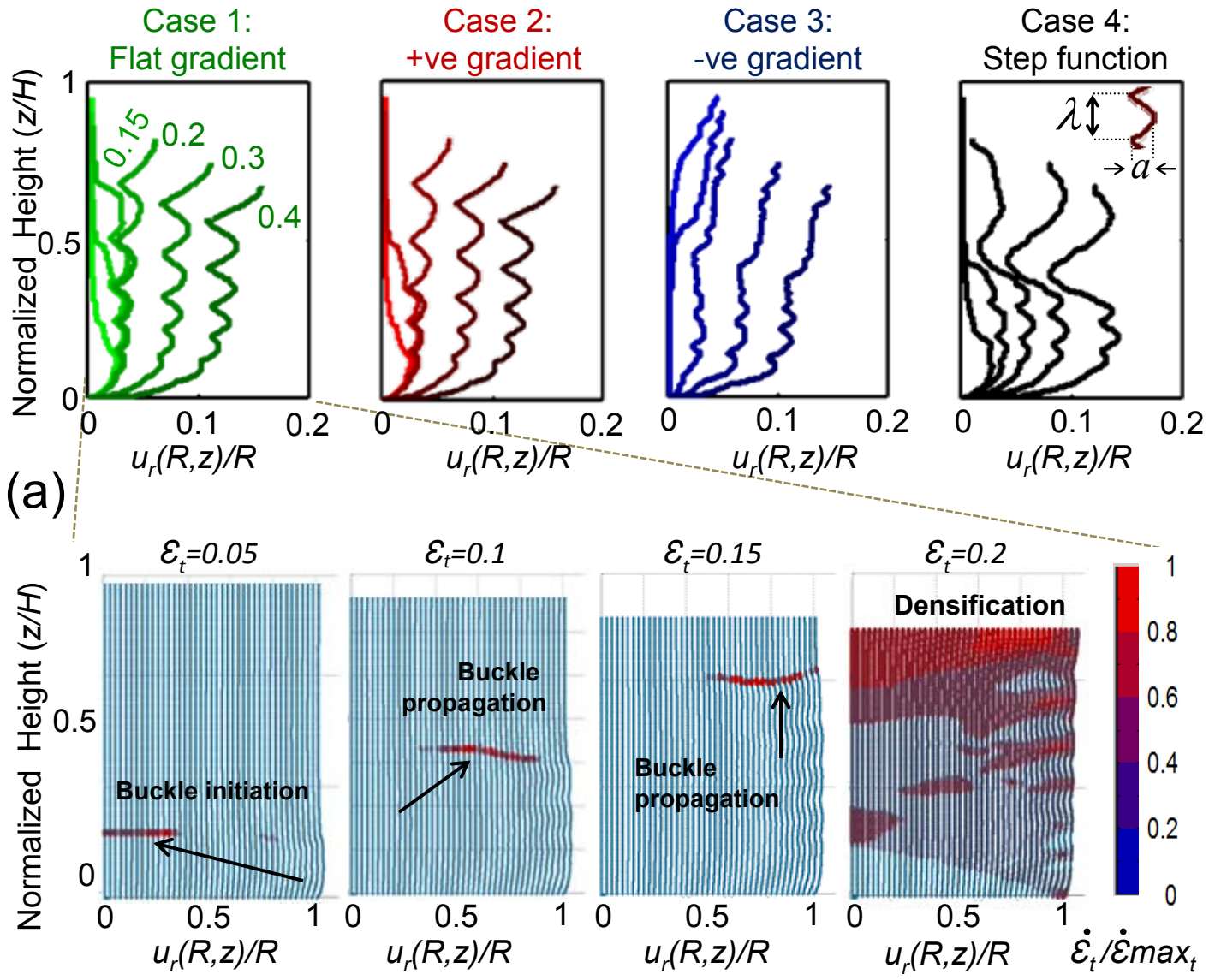

Figure 4. (a) Evolution of the outer deformation profiles corresponding to the four different SM functions shown in Fig. 3. The profiles are shown for strains of 5, 10, 20, 30 and 40%. Case 1 also shows an extra profile at 15% strain.
(b) Strain rate contour plots for Case 1 at four consecutive strains showing buckle initiation (ε_t= 0.05), propagation (ε_t= 0.1 and 0.15), and densification with high strain rate distribution (ε_t=0.2). The contour of high strain rate, which originates at the bottom right corner of the pillar due to restrictive boundary conditions, propagates sideways and also climbs the pillar height simultaneously. Further buckles initiate sequentially in the section below this wave front.

Table 1: Comparison of the deformation characteristics measured for the four variations of the SM function

Case #	Slope	Transition strain	Buckle amplitude (U_r/R)	Buckle wavelength (λ/R)
1	θ = 0.037	ε = 0.155	0.022	0.092
2	θ = 0.862	ε = 0.155	0.022	0.094
3	θ = 0.853	ε = 0.17	0.014	0.086
4	θ_1 = 0.025 θ_2 = 3.6	ε_1 = 0.089 ε_2 = 0.126	0.013	0.043

Supporting information for Chapter 5.

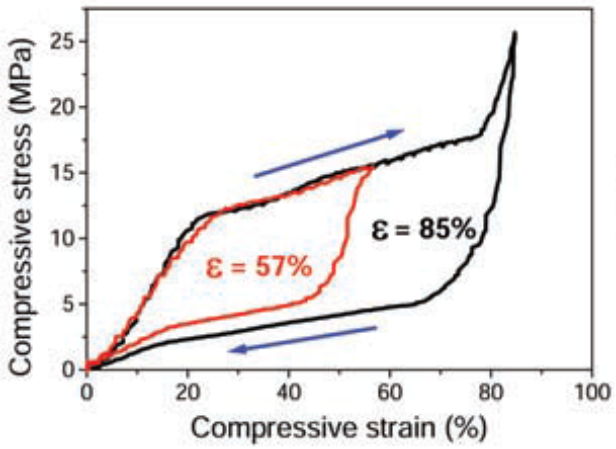

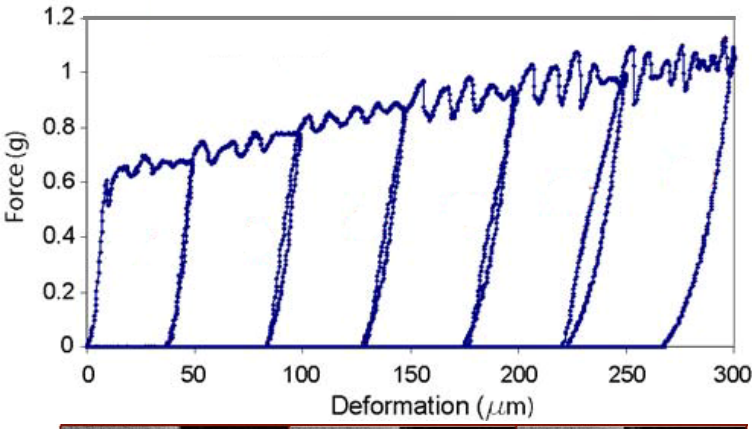

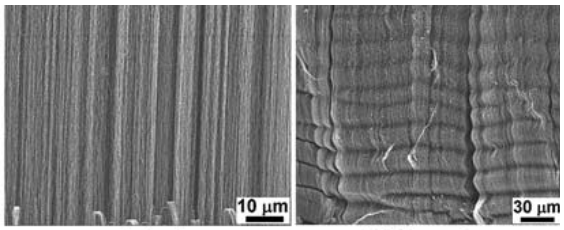

(a)

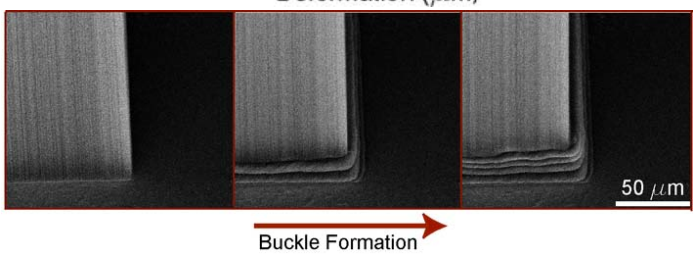

(b)

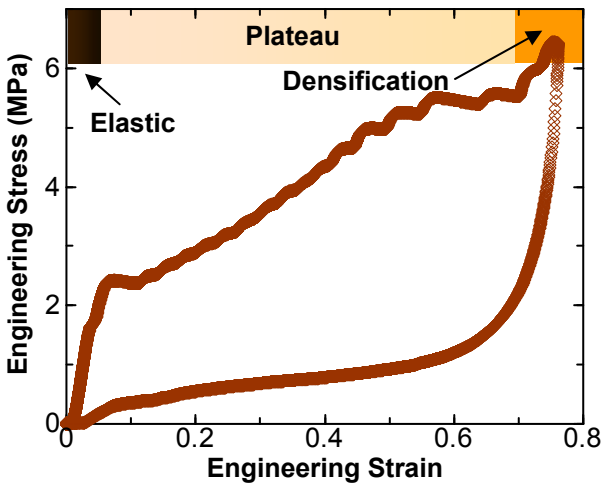

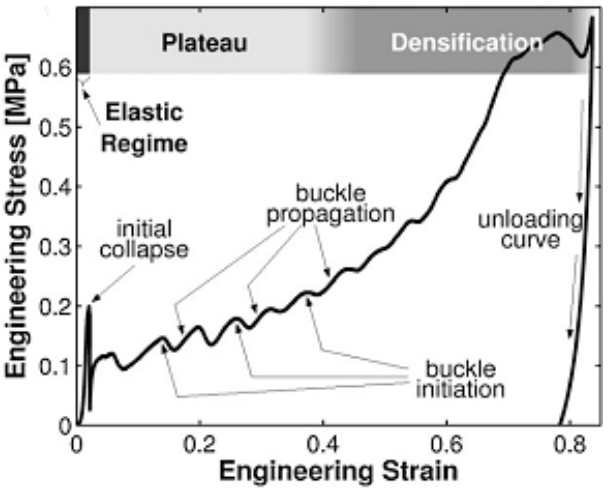

(c)

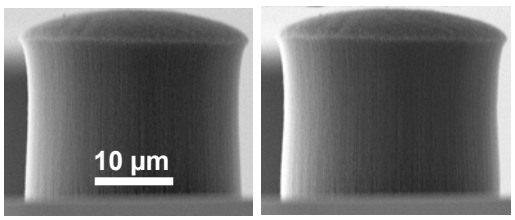

(d)

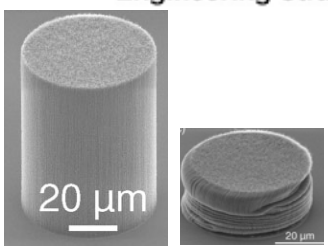

Figure S1. VACNT behavior under compression for (a) 860 μm thick VACNT array Ref Cao, (b) 400 μm diameter CNT column Ref Onnik (c) 30 μm × 30 μm (diameter × height) VACNT micro-pillar Ref Pathak and (d) 50 μm × 60 μm (diameter × height) VACNT micro-pillar Ref Hutchens. All of these VACNT systems show 3 distinct regimes in their stress-strain response – elastic, plateau and densification – similar to open-cell foams. Unlike foams the plateau region in the VACNTs generally has a strong positive slope. All VACNT systems also exhibit a bottom-first sequence of buckling.

However while both VACNT systems in (a) and (c) show remarkable recovery, even after multiple cycles, the VACNT systems in (b) and (d) does not exhibit any appreciable recovery.

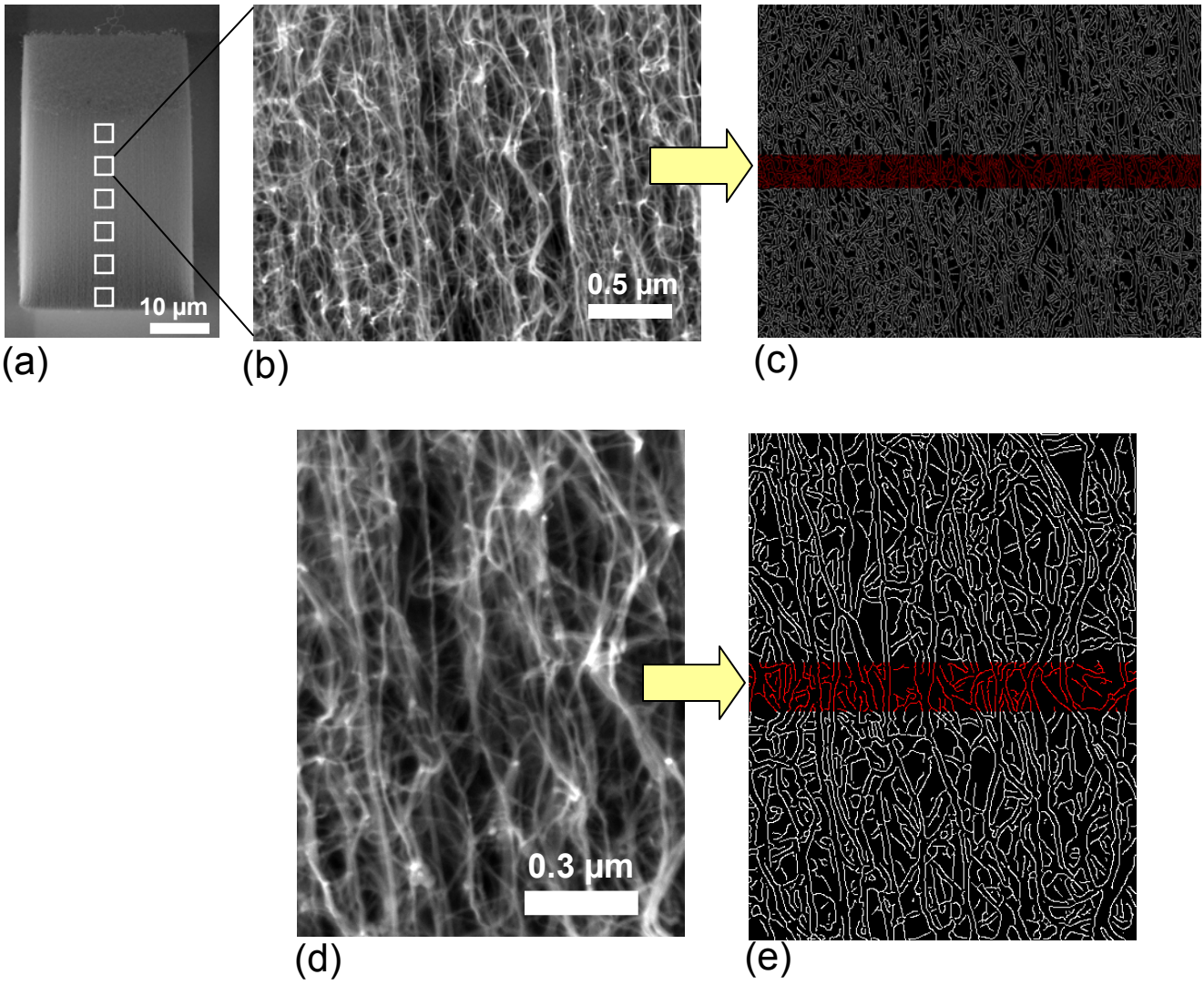

Figure S2. (a) For image analysis 9-10 images at evenly spaced intervals were taken along the height of each pillar, as shown in. To compute CNT number density, each captured image (b) was converted to grayscale, and the edges were isolated using the Canny algorithm (c). A magnified version is shown in (d) and (e)

To avoid any loss in resolution due to the 30° tilt of the samples, only the central 10% of each image was used for image analysis, as demonstrated by the red strips in (c) and (e).

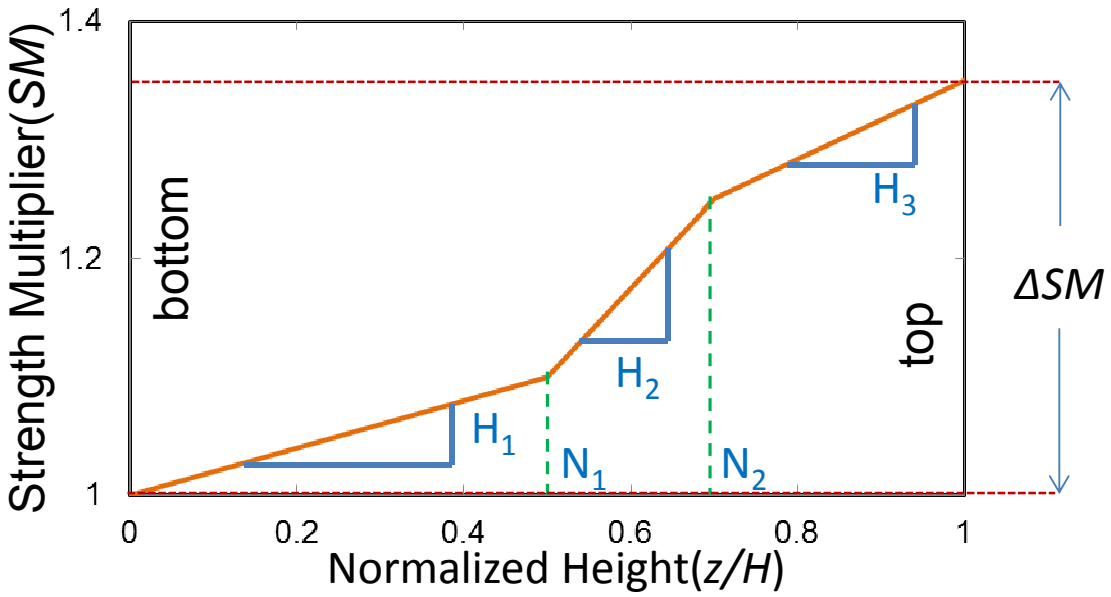

Figure S3. A three piecewise *SM* function was used along the pillar height to generate an axial gradient in property, applied on E and σ_0. The *SM* function can be defined using the three slopes H_1 , H_2 and H_3, the two transition strains N_1 and N_2 and the difference in strength between the top and bottom of the pillar, ΔSM.

Compressive response of vertically aligned carbon nanotube films gleaned from in situ flat-punch indentations

Siddhartha Pathak[a] and Nisha Mohan
Materials Science, California Institute of Technology (Caltech), Pasadena, California 91125

Parisa Pour Shahid Saeed Abadi
George W. Woodruff School of Mechanical Engineering, Georgia Institute of Technology, Atlanta, Georgia 30332

Samuel Graham and Baratunde A. Cola
George W. Woodruff School of Mechanical Engineering, Georgia Institute of Technology, Atlanta, Georgia 30332; and School of Materials Science and Engineering, Georgia Institute of Technology, Atlanta, Georgia 30332

Julia R. Greer
Materials Science, California Institute of Technology (Caltech), Pasadena, California 91125

(Received 31 March 2012; accepted 28 September 2012)

We report the mechanical behavior of vertically aligned carbon nanotube films, grown on Si substrates using atmospheric pressure chemical vapor deposition, subjected to in situ large displacement (up to 70 μm) flat-punch indentations. We observed three distinct regimes in their indentation stress–strain curves: (i) a short elastic regime, followed by (ii) a sudden instability, which resulted in a substantial rapid displacement burst manifested by an instantaneous vertical shearing of the material directly underneath the indenter tip by as much as 30 μm, and (iii) a positively sloped plateau for displacements between 10 and 70 μm. In situ nanomechanical indentation experiments revealed that the shear strain was accommodated by an array of coiled carbon nanotube "microrollers," providing a low-friction path for the vertical displacement. Mechanical response and concurrent deformation morphologies are discussed in the foam-like deformation framework with a particular emphasis on boundary conditions.

I. INTRODUCTION

Considerable efforts have been dedicated to explore the deformation mechanisms of vertically aligned carbon nanotube (VACNT) forests, in part motivated by their wide range of potential applications in areas such as energy dissipation devices, electrical interconnects, thermal interface materials, microelectromechanical systems, and microelectronics.[1–6] To date, instrumented indentation has been a common method for testing the mechanical behavior of VACNT films on substrates. However, due to the limitations of the displacement actuators, most of the existing studies are limited to shallow indentation depths (and strains), varying from a few hundred nanometers to several micrometers. Additionally, while VACNT forest films may have millimeter-sized lateral and vertical dimensions, they are composed of individual nanotubes with diameters in the nanometer range, which drives their mechanical response to be distinct from monolithic materials. Hence, the accurate estimation of the contact area between the VACNT film and the commonly used parabolic[7,8] and pyramidal[7] indenter tip geometries, necessary for indentation data analysis, poses a significant challenge.

In this work, we utilize flat-punch diamond indenter tips, resulting in a constant contact area with the sample, to conduct large displacement indentations into VACNT films grown using atmospheric pressure chemical vapor deposition (APCVD). Using both on-edge in situ and in-bulk ex situ flat-punch indentations, we examine the combined quantitative information (load–displacement) along with the concomitant morphological changes. To explore the effect of lateral boundary constraints, these findings are compared with our previous report[9] on uniaxial compressions of the same APCVD-grown VACNTs patterned into cylindrical bundles.

Mechanical response of VACNTs is a complex phenomenon occurring across multiple length scales due to its hierarchical structure. The collective behavior of these materials is expected to rely heavily on the properties of the individual carbon nanotubes (CNTs), as well as on the variations in the collective intertube interactions and inherent property gradients of the microstructure, which in turn are dictated by their synthesis techniques.[10–12] A wide range of mechanical behavior has been reported in VACNTs as a result of such variations in their microstructure. These include modulus and buckling strengths ranging from sub-MPa[13,14] to tens of MPa[15–17] to GPa,[8,18]

[a]Address all correspondence to this author.
e-mail: pathak@caltech.edu, siddharthapathak@gmail.com
DOI: 10.1557/jmr.2012.366

as well as a complete gamut of recoverability—from nearly 100% recovery even after large deformations[5,9,13,19,20] to permanent distortion even at modest strains.[2,11,17,21,22] Such drastic differences in properties make it impractical to compare VACNTs synthesized by nonidentical growth techniques. In this work, we focus on VACNTs grown by APCVD technique[23] and describe their response under indentation, as compared with our previous work on uniaxial compressions of 30 × 30 μm (diameter × height) cylindrical bundles.[9] These APCVD VACNTs bundles exhibit three distinct regimes in their compressive stress–strain curves: (i) a short initial elastic section, followed by (ii) a sloped plateau with characteristic wavy features corresponding to localized buckle formation, and (iii) a densification characterized by a rapid stress increase—all of which liken their deformation to that of a typical foam.[5,9,11] Unlike foams, however, the compressive strain in VACNTs is accommodated entirely via the formation of localized folds or buckles forming progressively along their lengths.[5,11,16,22,24,25] During compression of our particular APCVD VACNT system, such localized buckles fully recovered upon load release even from relatively large strains of 60–80% (i.e., the onset of densification) under fast displacement rates of 1000 nm/s. In addition, repeated cycling also revealed a distinctive hysteresis behavior for the VACNT bundle in compression, suggesting energy dissipation in every cycle.[9] However, since these properties were mainly documented for short height APCVD VACNTs under uniaxial compression, it is still largely unknown whether they demonstrate similar lucrative mechanical properties under different loading and boundary conditions.

In this work, we focus on the deformation response of 142-μm-tall APCVD-grown VACNT films under large displacement flat-punch indentations and compare it with that of uniaxial compressions of ~30 × 30 μm (height × diameter) cylindrical pillars patterned into the same starting material. Thus, we directly compare the influence of the boundary conditions posed by the presence or absence of the external matrix. We use both an in situ nanoindentation methodology to observe the on-edge deformation in real time using a custom-built in situ nanomechanical deformation instrument, SEMentor,[26] as well as more traditional ex situ indentation methods. Recent work by our group[9,11,23] and others[16,24] showed the efficacy of conducting in situ compressions inside the scanning electron microscope (SEM), which allows for uninterrupted observation of the real-time evolution of deformation morphology while simultaneously recording load versus displacement data. Unlike compression experiments, where the indenter tip applies an axial load to an individual structure readily visible in SEM, in situ indentation experiments have to be conducted on the edge of the sample, as opposed to in bulk, to facilitate uninhibited inspection of the material cross section.[23] Although boundary conditions and constraints associated with such on-edge tests are different from those during in-bulk indentations, they are instrumental in providing useful information on morphological evolution in deforming VACNTs, not easily obtainable by other methods.

II. MATERIALS AND METHODS

A. CNT growth

VACNT films with thicknesses between 25 and 142 μm were grown using APCVD technique in a commercial (CVD) system (Black Magic Pro 4″; Aixtron SE) as described in detail in Ref. 23. A trilayer catalyst of Ti (30 nm)/Al (10 nm)/Fe (3 nm) was deposited by electron beam evaporation on Si substrates to seed the growth of the VACNT films. A gas mixture of 160/100/7500 sccm of $C_2H_2/H_2/N_2$ was used to maintain the chamber pressure at 750 mbar during growth, which occurred at ~750 °C. Multiwall CNTs, with an average diameter of 8.8 ± 2.1 nm (average ± standard deviation) and average mass density (CNT mass divided by volume) of ~80 mg/cm^3, were produced by this process.[23]

B. Ex situ indentation tests

Two different VACNT films with thicknesses of ~142 and 25 μm were selected for large displacement cyclic indentation tests. The indentation experiments were performed using the XP module of Agilent's nanoindenter G200 with adjustable software control methods as described in Ref. 11. Tests were performed in air using a custom-made cylindrical diamond flat punch with ~120 μm diameter and ~80 μm height. For the 142-μm-thick VACNT sample, indentations were performed under a constant displacement control to varying indentation depths up to a maximum penetration depth of around 70 μm (restricted by the height limitations of the diamond flat punch). For the thinner samples, the maximum depth was limited to 90% of the film thickness. Tests were conducted in the interior of the samples (i.e., away from the sample edge) at three different constant displacement rates: 10, 100, and 1000 nm/s. Typically, five unload–reload cycles were performed at each displacement level. No hold time was applied at the maximum loads to maintain the cyclic nature of the tests. Minimum of 10 tests were conducted at each displacement rate. The indents were spaced at least 500 μm apart to eliminate any possible proximity effects.

C. In situ SEM indentation experiments

To visualize the morphological changes in the VACNT samples during indentation and correlate them with the concurrent load–displacement data, in situ tests were conducted in a custom-built mechanical deformation instrument, SEMentor,[26] composed of a nanomechanical dynamic contact module (Agilent Corp.) inside a SEM

AU7 (Quanta 200; FEI). Tests in SEMentor were conducted with a conductive diamond flat punch with a rectangular flat cross section of ~60 × 80 μm. The loading axis in SEMentor is inclined at ~86° with respect to the electron beam, thus allowing continuous observation of the deformation morphology of the VACNT film cross section during the on-edge in situ experiments. Importantly, the outer constraints in on-edge indentations are different from those during in-bulk tests, and therefore, their stress–strain behavior is expected to be different, as well. SEM observations were recorded as a video file at 30 frames/s capture rate and synchronized with the indentation data to provide a real-time correlation between each video frame and the corresponding position on the load–displacement curve (see video files S1 and S2, shown at 15 and 10 times their original speeds, respectively, in the supporting online material). SEMentor tests were conducted to a maximum penetration depth of 30 μm (instrument limit). In addition, while, nominally, the experiments performed in both G200 and SEMentor are identical, one notable difference is that SEMentor tests are conducted in a vacuum environment, while those in G200 are conducted in air. Further, in SEMentor experiments, the samples are constantly exposed to the electron beam, and they are oriented horizontally such that gravity is acting perpendicularly to the compression axis. Due to these subtle differences between the two instruments, the SEMentor-generated results were used only for visualization purposes in this study, while all data analyses were performed on tests conducted in air in the G200 nanoindenter.

D. Data analysis

The applied load, P, and measured displacement, h, were corrected for machine compliance following the procedure outlined in detail in Ref. 11. We assumed negligible friction between the indenter sidewalls and the VACNT matrix—a reasonable approximation based on previous reports.[27,28] The initial loading portion in a typical flat-punch indentation experiment often suffers from misalignment issues between the indenter tip and the sample surface requiring special care in reliable extraction of useful properties. On the other hand, applying the Hertzian contact model to the initial unloading segment of the measured load–displacement curve permits a reasonable estimation of the Young's modulus[29,30]:

$$E_{\text{eff}} = \frac{\sqrt{\pi}}{2}\frac{S}{\sqrt{A}} = \frac{S}{2a}, \qquad \frac{1}{E_{\text{eff}}} = \frac{1-\nu_s^2}{E_s} + \frac{1-\nu_i^2}{E_i} \quad , \tag{1}$$

where E_{eff} denotes the effective modulus of the combined indenter–specimen system, $S(=dP/dh)$ is the stiffness measured from the slope of the initial 30% of the unloading load–displacement curve, ν and E are the Poisson's ratio and the Young's modulus, respectively, and the subscripts s and i refer to the specimen and the indenter, respectively. Following the common nanoindentation protocols, we chose the modulus of 1041 GPa and Poisson's ratio of 0.07 for the diamond indenter tip. Since the APCVD-grown VACNT bundles have been shown to exhibit foam-like deformation with minimal lateral expansion under compressive load,[9] we assume a vanishing Poisson's ratio of $\nu = 0$ for the VACNTs as has also been suggested previously.[31] We note that this choice may be an approximation since the deformation in VACNTs is highly localized. However, the error introduced is not expected to be significant since the accuracy of E_s depends only weakly on ν [see Eq. (1)]; e.g., a change in ν from 0 to 0.3 causes only a 5.3% error in E_s.

We also note that Eq. (1) treats the overall material behavior as that of an isotropic continuum medium, according to the inherent assumptions of the Hertz's theory. VACNTs, on the other hand, demonstrate varying degrees of anisotropy at each level of its hierarchical microstructure (see Fig. 1), rendering our calculations of indentation moduli an approximation rather than an exact value. Nevertheless, isotropic continuum framework has been previously utilized in developing the constitutive relations in VACNTs[11] and foams[31] and appears to have accurately captured the qualitative features of outer deformation profile and the stress–strain curves. Despite the discrete constituents and apparent vertical alignment at low magnification, the continuum foundation was motivated by the nearly isotropic network of CNTs as revealed by images at or above magnifications of 240,000x [Fig. 1(c)] and above.

We define the percentage recovery (R) as the displacement recovered at the end of each cycle with respect to the maximum displacement, i.e., $R = \frac{h_{\max} - h_{\text{unload}}}{h_{\max}}$, where $h_{\max}$ is the maximum displacement at the end of loading and h_{unload} is the displacement after unloading to 10% of the maximum load in each cycle.

The loss coefficient, η (a dimensionless quantity), measures the degree to which a material dissipates energy and is calculated as[32]:

$$\eta = \frac{\Delta U_i}{2\pi U_1},\ U = \int_0^{\sigma_{\max}} \sigma_{\text{ind}} d\varepsilon_{\text{ind}} \approx \frac{1}{2}\frac{\sigma_{\max}^2}{E_s},$$
$$\Delta U = \oint \sigma_{\text{ind}} d\varepsilon_{\text{ind}} \quad , \tag{2}$$

where U_1 is the elastic energy stored in the material when it is loaded elastically to a stress $\sigma_{\max}$ in the 1st cycle and ΔU_i is the energy dissipated in the ith load–unload cycle [see Fig. 5(d)].

To compare the indentation response of VACNTs to its stress–strain behavior under compression, we define the

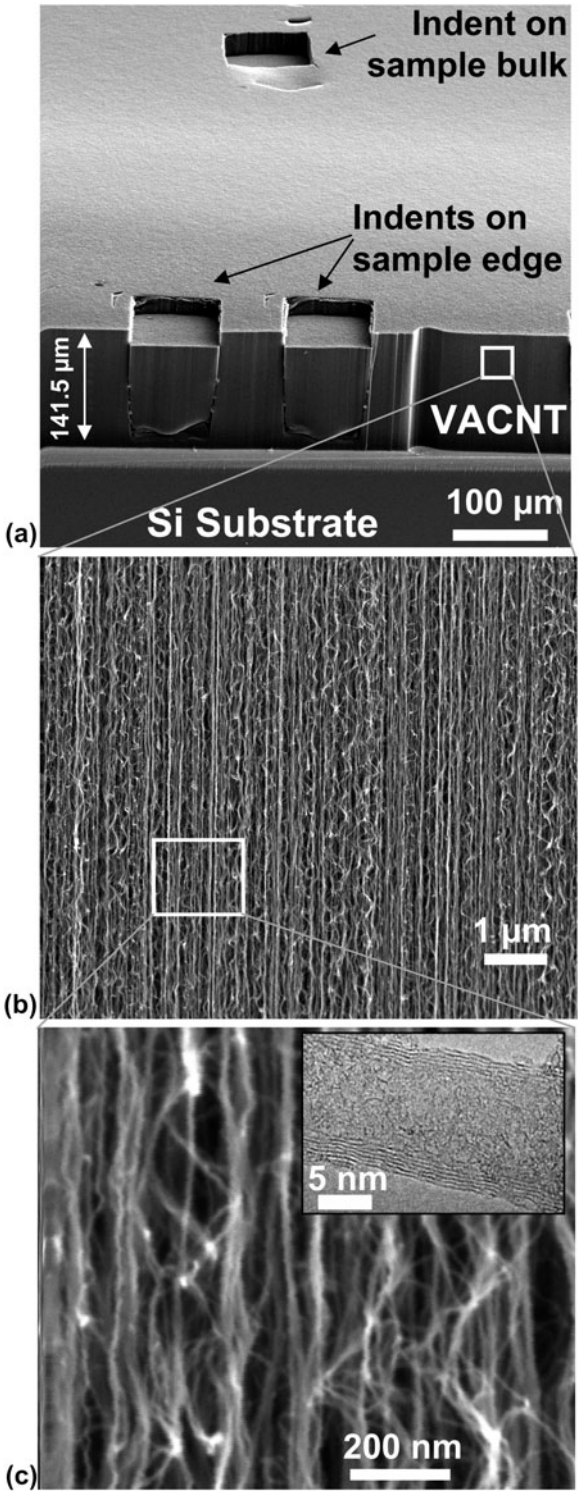

FIG. 1. SEM images reveal the hierarchical morphology of the (a) 141.5-μm-thick VACNT films (magnification 260x), which consist of (b) nominally vertical aligned CNTs visible at a lower magnification of 30kx, and (c) a complex intertwined network seen at higher magnifications of 240kx. SEM pictures are taken at a 60° tilt angle. (c inset) Individual multiwalled CNTs of outer diameter 8.8 ± 2.1 nm (average ± standard deviation) are visible in the TEM image.

average indentation stress (σ_{ind}) and strain (ε_{ind}) under a flat-punch cylindrical indenter of contact diameter $2a$ and contact area A as given below.[33] In Eq. (3), the indentation response is assumed to free of any substrate effects:

$$\sigma_{ind} = \frac{P}{A} = \frac{P}{\pi a^2}, \qquad \varepsilon_{ind} = \frac{h}{2a} \quad . \tag{3}$$

E. Viscoelastic characterization

The viscoelastic properties of the VACNT film were measured following the procedure outlined in Ref. 11. In this method, the indenter is loaded into the sample in air at a constant displacement rate of 100 nm/s up to a specified indentation depth where the indenter head is oscillated at ~8 nm amplitude across a range of frequencies from 1 to 50 Hz. The cutoff frequency of 50 Hz is dictated by the instrumental limit, as detailed in Refs. 11 and 34. The procedure was repeated at seven different constant indentation depths: from 5 to 70 μm.

Viscoelastic materials are commonly characterized by their storage (E') and loss (E'') moduli, where the former represents the stored energy or the elastic response and the latter corresponds to the amount of energy dissipated, or the viscous response, as well as their ratio—tanδ. Assuming linear viscoelastic behavior, these terms can be computed following the calculations described in Refs. 34–37 as follows:

$$\begin{aligned} E' &= k' \frac{\sqrt{\pi}}{2\beta} \frac{1-\nu_s^2}{\sqrt{A}}, \quad k' = \left|\frac{F_0}{u_0}\right| \cos\varphi - \left|\frac{F_0}{u_0}\right|_{air} \cos\varphi_{air}, \\ E'' &= k'' \frac{\sqrt{\pi}}{2\beta} \frac{1-\nu_s^2}{\sqrt{A}}, \quad k'' = \left|\frac{F_0}{u_0}\right| \sin\varphi - \left|\frac{F_0}{u_0}\right|_{air} \sin\varphi_{air} \quad , \\ \tan\delta &= \frac{E''}{E'} \quad . \end{aligned} \tag{4}$$

Here, k' and k'' are the storage and loss stiffnesses of the sample, obtained by finding the real and complex parts, respectively, of the stiffness differences between oscillating the indenter head on the sample at a fixed displacement and in air at the same raw displacement, and β is a constant (=1 for a flat-punch indenter). F_0 and u_0 are the load and displacement oscillation amplitudes, respectively, and φ is the phase angle between the load and displacement oscillations. We note that the accuracy in the values of E' and E'' in Eq. (4) can be affected by several factors: uncertainties in Poisson's ratio, since it may be frequency dependent, and ambiguity in contact area, especially at shallower indentation depths, where full contact may not have been established. On the other hand, calculation of tanδ is independent of the contact area and thus is ideally suited as a measure of the viscoelasticity of the indented material.[8,38]

III. RESULTS AND DISCUSSION

A. VACNT microstructure

Figure 1 shows the SEM and transmission electron microscopy (TEM) images at different magnifications of a ~142-μm-thick VACNT film on a Si substrate grown using the APCVD synthesis technique (see Sec. II). All SEM images [Figs. 1(a)–1(c)] were taken at a 60° tilt to visualize both top and edge surfaces of the sample. These figures show the complex hierarchical nature of the VACNT microstructure with their distinct organizational details across multiple length scales. Thus, while the VACNT appears as a continuous film at lower magnifications of 260x [Fig. 1(a)], the nominally vertical alignment of CNTs growing perpendicularly to the support substrate in the VACNT bundle becomes visible at a higher magnification of 30,000x [Fig. 1(b)]. Increased magnification of 240,000x reveals significant intertwining in the long curved lengths of individual CNTs, revealing the isotropic CNT network.[11,12,31] As a result, in their as-grown states, certain segments of the CNT forest appear to be prebuckled/prebent, and the favorable contact energy between the tubes (van der Waals) is thought to balance the bending strain energy of their arrangement, resulting in a stable low energy configuration.[15] The diameters of the individual multiwalled (3–6 walls) CNTs (8.8 ± 2.1 nm) are visible at the nanometer length scale shown in the TEM image in Fig. 1(c) inset. Such hierarchy in the VACNT microstructure governs its overall mechanical behavior, which is a result of not only the properties of individual CNTs but also of their complex mutual interactions and distribution throughout the array.

Figure 1(a) shows the residual imprints of indentations (indicated by arrows): one ex situ, performed in the interior of the sample away from the edges, and two in situ indentations, performed on a sample edge inside the SEMentor using a rectangular ~60 × 80 μm flat punch (see Sec. II). As can be seen clearly from this image, the indentations left a significant imprint on the surface of the VACNT film, suggesting marginal postmortem elastic recovery. This is in contrast with the nearly full recoverability exhibited by the same VACNTs patterned into micrometer-sized bundles and compressed to the same nominal strain.[9] This permanent shape change underneath the indenter appears to have occurred along the vertical edges via a single shear offset (see also Fig. 3). Notably, although the two indents on the sample edge shown in Fig. 1(a) are only 60 μm apart from one another, we see no evidence of any influence of the earlier (left) indent on the latter (right). This observation suggests that the lateral extent of the plastic zone size in VACNTs under the indenter is much narrower as compared with the rounded continuum indentation stress field contours spanning the regions as far as one indenter diameter away from the flat-punch indenter tip in monolithic materials.[39] This further underlines the importance of understanding the hierarchical nature of VACNT materials as their postindent morphological signature is clearly of nonmonolithic nature, while its stress–strain response is akin to that of an open-cell foam.

B. In situ on-edge flat-punch indentations

To correlate the morphological changes underneath the indenter with the details of the indentation load–displacement curve, a series of in situ indentations were performed in SEMentor using the procedures described in Sec. II. Figure 2(a) shows two representative load–displacement curves, with the respective indentation stress values plotted on the secondary *y* axis. These correspond to two of the three indentations shown in Fig. 1: one on the edge and another in the sample interior. Both tests were performed at a nominal displacement rate of 100 nm/s. This plot indicates that while the curves are similar in shape, the on-edge regions deform at significantly lower loads than in-bulk locations at equivalent indentation depths. This result is not surprising due to the less restrictive boundary conditions in the on-edge setup. In both cases, the load first increases steeply up to an instability manifested by a large displacement burst of ~20 μm, after which the indenter tip is unloaded [Fig. 2(a)]. Video frames from the indent-on-edge setup are provided in supporting online video (file S1), with several representative snapshots shown in Figs. 2(b)–2(d). As revealed by these images, the first buckle marked by double arrows in Fig. 2(c) forms close to the substrate during the initial loading at the load of ~6 mN. This buckle is initially observed only in the region just underneath the indenter tip—the lateral features outside of this region marked with single arrows appear after the displacement burst (see supporting online video S1). Interestingly, the first buckle location was always ~9 μm above the substrate. Other tests on VACNT samples of different film thicknesses have also shown a similar response where the first buckle invariably formed close to the bottom substrate.[23] This indicates that the presence of a stiff substrate results in localized buckle formation under both compression[5,9,11,16,22] and nanoindentation.

Upon further loading the buckle extends laterally [region marked with the single arrows in Fig. 2(c)] until the load of ~7.3 mN, where a sudden and extensive displacement burst of ~20 μm occurs. SEM images obtained immediately after this burst (video capture frame rate was not fast enough to catch the details during the instantaneous burst) reveal that a portion of VACNT film sheared off nearly perfectly vertically along the edges of the indenter tip [Fig. 2(c)], and new buckle lines are visible next to the initial buckles.

Closer inspection of the sheared-off region conveys several noteworthy features. First, the deformation appears to be highly localized, occurring only at the shear offset

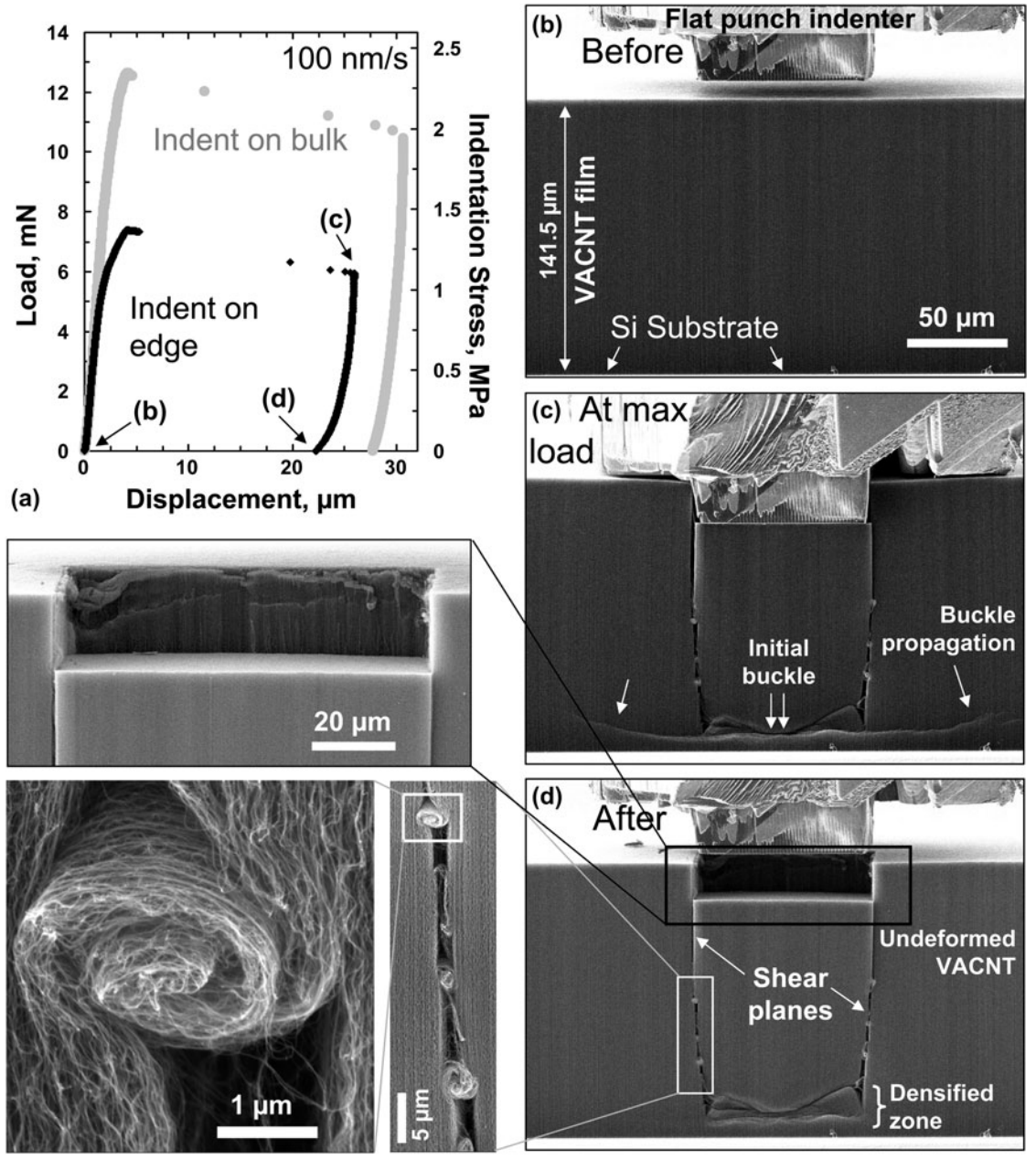

FIG. 2. (a) Comparative indentation load (and stress)–displacement curves at 100 nm/s loading rate of in situ SEM indentation tests conducted on the sample edge versus in the interior of the sample using a 60 × 80 μm rectangular flat-punch indenter. (b, c, and d) For the indent on edge, the indentation process was recorded as a video file from which individual picture frames were extracted corresponding to a particular event during the loading–unloading cycle (as indicated on the load–displacement graph). The double arrows in (c) mark the initiation of the first buckle at a load of around 6 mN. The wide lateral buckles marked by single arrows are formed after the first buckle and increase in size with loading. (d) Upon unloading, these lateral buckles disappear. (d inset top) The large displacement burst results in a vertical shear of the VACNT structure along the indenter edges. Note the clean edge of the shear wall. (d bottom insets) The shear appears to have been carried by a series of CNT "microrollers," which act as effective lubricants protecting the rest of the VACNT structure from further damage. All SEM images except the bottom two insets for (d) were taken at 86° tilt angle. The bottom two insets for (d) were at 60° tilt angle.

regions and the buckles formed at the bottom of the sample. The remaining portions of the VACNT film appear completely unaffected [Fig. 2(d) top inset]. Second, the shear appears to have been carried by a series of tangled CNTs, or "microrollers," seen in the magnified inset images in Fig. 2(d), whereby originally vertical strands of several entangled CNT collectively coiled themselves into helical structures. Three pairs of such coiled strands of CNTs can be seen on either side of the sheared region. We find the length of the coiled CNTs in each microroller

to be ~6 μm, and thus, the total displacement carried by the rollers is ~18 μm. This distance is in reasonable agreement with the displacement burst extent of ~20 μm shown in Fig. 2(a). We hypothesize that these microrollers provide a low-friction path during the shear process.

The shear event and the formation of the CNT microrollers [Figs. 2(c) and 2(d)] are unique characteristics seen only in the intertwined VACNT systems. Neither foams,[40,41] where the deformation is confined only to regions directly beneath the indenter, nor noninteracting VACNTs,[42] where such shear would propagate without any microroller formation, show the unique features seen in Fig. 2. As shown before in Fig. 1, the hierarchical design of these materials results in considerable interlinking between the individual struts. Thus, in spite of their nominally vertical structure, the CNTs along the shear plane of the VACNT film can perform as highly efficient lubricants by collectively coiling themselves and thereby carrying the shear strain in response to axial loading. The effectiveness of this "lubrication process" is evidenced by the very rapid nature of the burst and the resulting shear event under the indenter. Comparing SEM images at maximum load and after unload [Figs. 2(c) and 2(d)] shows that this shear event caused permanent damage to the material structure, as unloading the indenter tip results in minimal recovery. Upon unloading, the CNT microrollers did not uncoil, and the only observed difference in the morphology of the before and after deformation material was that the buckle contours, which extended laterally beyond the sheared block, disappeared upon unloading.

C. Ex situ in-bulk large displacement indentations

To analyze the deformation beyond the initial large burst, ex situ indentation tests were conducted in air in the Agilent G200 nanoindenter (see Sec. II) to larger depths of ~70 μm in the interior of the as-grown VACNT film away from the edges. This maximum indentation depth was chosen based on the height of the cylindrical punch (~80 μm) and to avoid the influence of the rigid Si substrate. Figure 3(a) shows a typical indentation load (stress)–displacement curve for a representative test conducted at the displacement rate of 10 nm/s up to a final displacement of 70 μm on the 142-μm-thick VACNT film. Similar to the compression experiments on the same VACNT system,[9] three distinct regions are apparent: (i) a short elastic regime, followed by a (ii) sudden instability, which results in a 40% load drop at ~4.3-μm displacement with the subsequent and (iii) sloped plateau region with a small positive slope starting at the displacement of ~11 μm, where the load increases more gradually with displacement and contains several undulations. We calculate σ_{ins} at the point of instability to be ~1.6 MPa, a value nearly 40% below the buckling stress of ~2.5 MPa

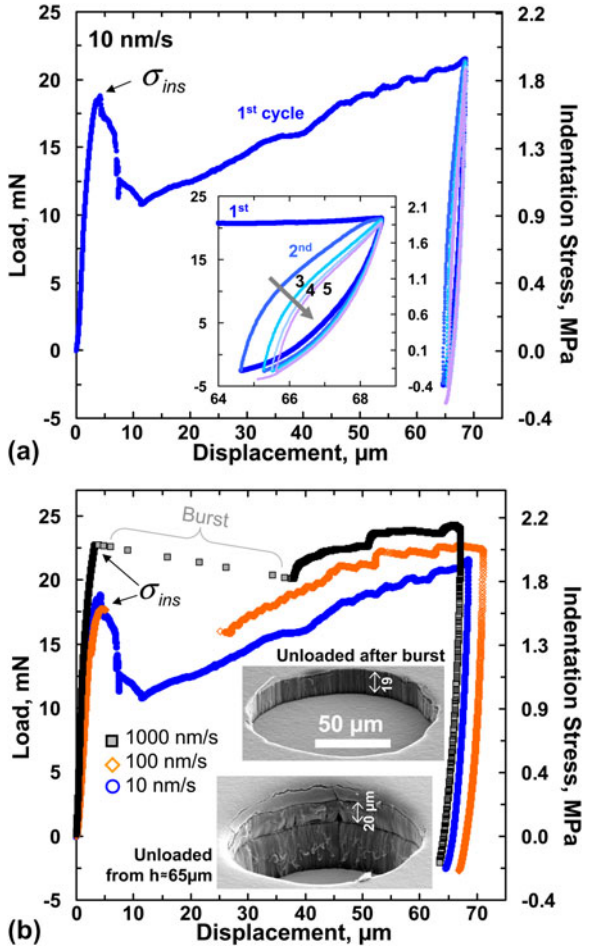

FIG. 3. (a) Five load–unload cycles during indentation on a 141.5-μm-thick VACNT film at 10 nm/s loading rate using a 120-μm-diameter flat-punch indenter showing three distinct regimes; elastic, drop in load at a critical instability stress σ_{ins}, and plateau regime. (a inset) Successive load–unload cycles to the same maximum displacement reveal a gradual drop in recovery in every cycle, suggesting progressive damage accumulation in the material. The corresponding indentation stress values are shown along the secondary *y* axis. (b) Indentations at different displacement rates showing a large displacement burst and more pronounced buckling signatures at the faster rates. The inset images show the residual impressions of two different indentations conducted at a rate of 100 nm/s, one when the indenter is unloaded just after the burst versus when it is unloaded from a maximum displacement of ~65 μm. (color online)

exhibited by this material system when patterned into 30 × 30 μm, height × diameter, bundles under compression in the same instrument.[9] Probable causes for this difference between the indentation and compression tests are detailed in the following sections.

Figure 3(a) also shows the effect of unload–reload cycling and hysteresis[8] demonstrating that the material recovers only slightly after the first cycle, while subsequent cycling results in a substantially higher relative recovery. This renders the first cycle distinctly different from all subsequent loading cycles, as has been widely

observed for CNT foams.[4,5,9] The inset in Fig. 3(a) shows the zoomed-in load–unload segments during cycling and indicates that both the amount of hysteresis, corresponding to the energy dissipated per cycle, and the recovered displacement after unloading diminish with each subsequent cycle. Although each cycle was specified to be unloaded to only 10% of the maximum load from the previous cycle, in some cases, the applied loads were measured as slightly negative, likely due to the adhesion between the VACNT tips and the diamond indenter.[12,15]

Several indentation load (and stress)–displacement curves for three different displacement rates are shown in Fig. 3(b). Although the general behavior across the different rates is similar in appearance, several important distinctions can be made. For example, at the faster loading rates of 100 and 1000 nm/s, there appears to be a rapid extensive displacement burst of ~20 μm or larger immediately upon attaining σ_{ins}, resulting in a temporary loss of contact between the sample and the indenter tip. The burst size appears to increase with loading rate. This is in contrast to the gradual load removal, where contact is maintained at all times, shown in the tests conducted at the slowest rate of 10 nm/s. Based on the in situ indentation tests described in Fig. 2, it appears that the burst may be caused by a rapid vertical shearing of the material directly underneath the indenter tip along the indenter edges. Indeed, when the test was stopped at the moment of the burst [top SEM image in Fig. 3(b) at 100 nm/s], we observe the formation of a large imprint of depth ~19 μm mirroring the shape of the indenter, with the residual depth equivalent to the displacement burst. Closer inspection of the imprints indicates that the material directly underneath the indenter is mostly unperturbed, with all deformation—again—appearing to have been localized in the vertical shear region along the rim of contact between the sample and the indenter tip.

Further loading beyond the first burst is characterized by the reappearance of the sloped plateau. Such sloped plateau regions have been observed previously[9,11] and were attributed to an inherent property gradient in the VACNT microstructure along its height. Current authors reported a similar gradient present in APCVD VACNT films where both—the CNT number and mass densities—were found to vary as a function of the film height.[23] It is, therefore, reasonable to assume that a similar density variation is present in the samples described here, resulting in the indenter punch encountering a denser, and hence stiffer, material in the deeper regions. This requires the application of a higher stress to form each successive buckle, leading to an increasing global slope in the plateau region. While the slopes of the plateau region appear to be similar among all three rates shown in Fig. 3(b), samples deformed at the faster rates sustain higher stresses, a behavior considered typical for viscoelastic solids.[43]

The plateau region is composed of several undulations or kinks for all three loading rates. Such features have been observed previously during in situ compression experiments of 60-μm-tall VACNT bundles[11] and in ex situ tests,[5,11,16,22,24,25] as well as more recently by the present authors for in situ compressions of 30 × 30 μm height × diameter VACNT micropillars made from the same APCVD process.[9] The in situ compression studies of Hutchens et al.[11] revealed that the formation of each undulation corresponded to the formation of localized folds or buckles along the pillar height, with the faster rates showing drops of larger amplitude.[9,11] While—unlike in compression experiments—direct observation of buckle formation is not possible during indentation in the interior of the sample, it is reasonable to assume that a similar deformation mechanism operates during flat-punch indentations. Thus, the series of load drops in the load–displacement curves likely correspond to the coordinated sequential lateral collapse events somewhere below the indenter, with the force required to cause them being much smaller than that of the initial instability.

Unloading from a depth of ~65–70 μm results in very little recovery as shown by the residual imprint in the bottom SEM image of Fig. 3(b) inset. The imprint also shows the remnant of the first large burst, which is seen as a shear line at a depth of ~20 μm along the walls of the crater. The vertical walls of the indent imprint indicate a clear shearing of the VACNTs along the rim of the indenter.

D. Effect of substrate on buckle formation

Figure 3 and video S1 indicate that the buckle formation in the VACNT film is strongly influenced by the constraints imposed by the stiff substrate. In the taller ~142-μm-thick sample shown in Figs. 1 and 2, the location of the initial buckle is always close to the substrate, while the region underneath the indenter tip remains largely unaffected. Further loading is thought to cause additional localized folds to continuously form along the VACNT film height, and the indenter starts probing the folded/collapsed densified region—an effect similar to that observed during compression experiments on these VACNTs patterned into micrometer-sized bundles.[9] It stands to reason that such a response can be observed under indentation by using a shorter sample. This is shown in Fig. 4(a) where the indentation response of a shorter 25-μm-thick VACNT film is compared to a thicker ~142-μm-thick film. Both tests shown in Fig. 4(a) were conducted in the samples' interior. It is evident that while the initial loading portions of both samples are similar, the shorter VACNT film has a significantly higher slope in its plateau up to an indentation depth of ~19 μm, suggesting a higher degree of stiffening in the shorter sample. Moreover, the plateau region of the shorter sample shows

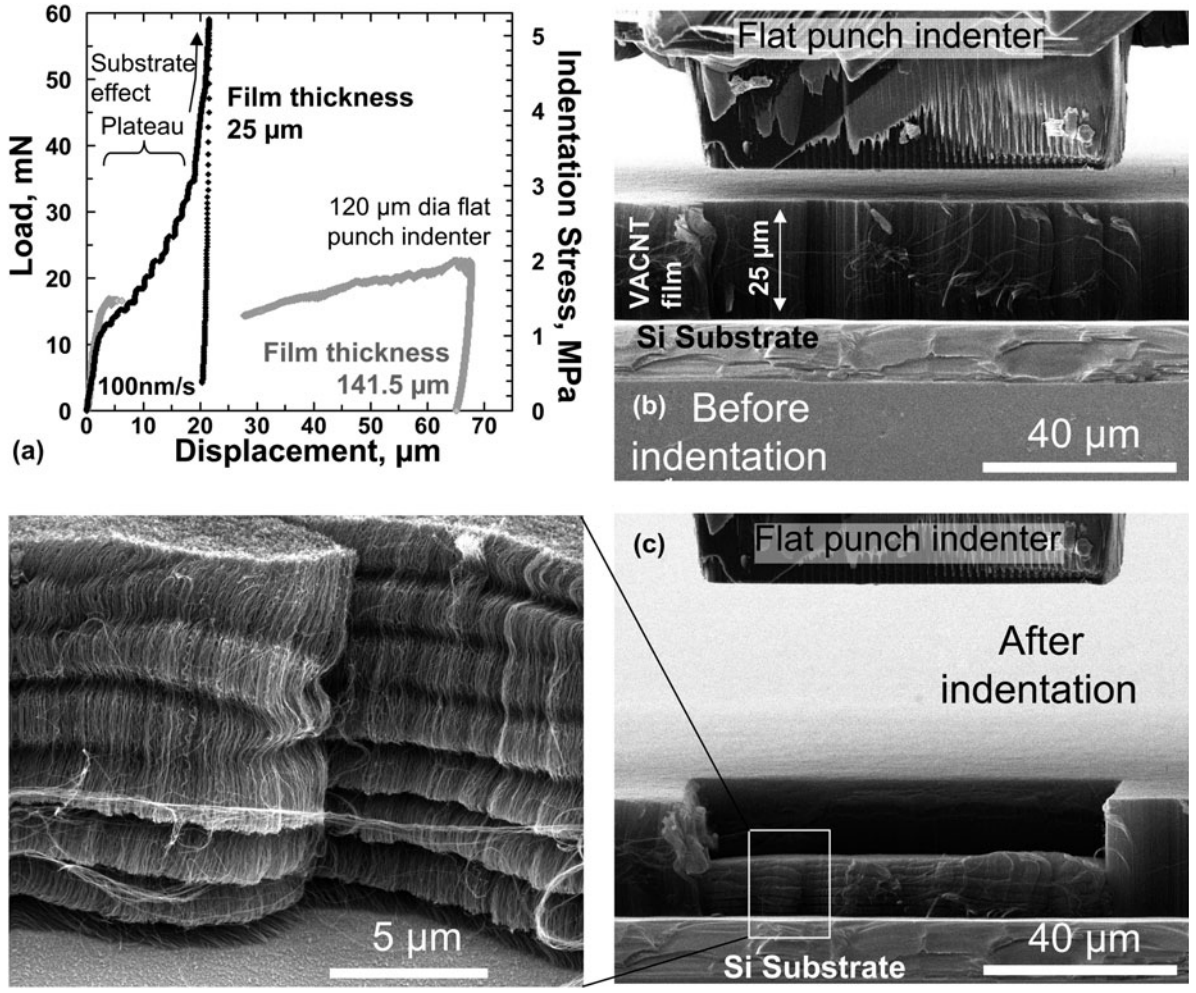

FIG. 4. (a) Comparative load–displacement curves at 100 nm/s loading rate of indentation tests conducted on a thin (25 μm) VACNT film versus a thick (141.5 μm) VACNT film. These indentations were performed on the interior of the sample far away from edge effects using a 120-μm-diameter cylindrical flat-punch indenter. The film morphology (b) before and (c) after in situ SEM indentations using a 60 × 80 μm rectangular flat-punch indenter on the edge of the sample help reveal the (c inset) progressive buckling seen in the shorter (25 μm) VACNT film sample. All SEM images except the bottom (c inset) were taken at 86° tilt angle. The (c inset) image was at 60° tilt angle.

more prominent undulations than during indentation of the thicker sample at the same rate. Beyond the indentation depth of 19 μm, the effect of the stiff Si substrate becomes significant in the shorter sample as displayed by a steep rise in the load–displacement response. Consistent with these observations, stiffnesses calculated from the unloading portions of the load–displacement curves were an order of magnitude higher than those of the thicker film, showing the combined effects of densification and of the substrate influence in the shorter films.

To gain insight into the possible distinctions in morphological features between samples with different thicknesses, we conducted in situ indentation experiments in SEMentor of the shorter 25-μm-thick VACNT film sample. As shown in Figs. 4(b) and 4(c) and supporting online video S2, these tests were conducted on the edge of the VACNT film [unlike the in-bulk tests shown in Fig. 4(a)]. As in the case of the thicker samples (Fig. 2), the deformation extent in the shorter sample is localized to a zone directly underneath the indenter tip [compare Figs. 2 and 4(c)]. However, unlike the thicker samples, clear evidence of densification can be seen in the shorter VACNT film sample [Fig. 4(c) inset]. Figure 4(c) inset also shows that substrate proximity has resulted in multiple folds or buckles in the shorter VACNT film.

E. Analysis of indentation response

Figure 5 shows the results of indentation experiments conducted on the ~142-μm-thick VACNT film sample. Only the data from the sample interior (i.e., no on-edge tests) are shown. Unloading modulus, defined in Eq. (1), is plotted as a function of loading cycle number in Fig. 5(a). This plot reveals that the modulus varies within a range of

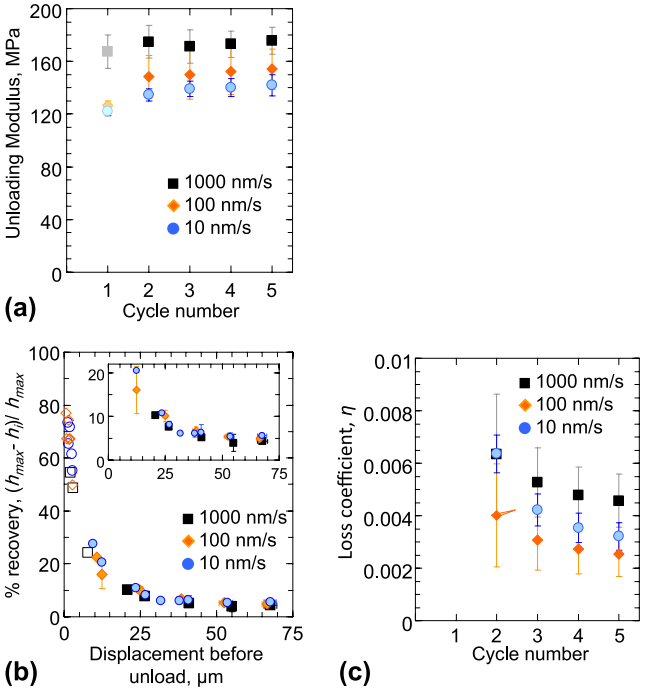

FIG. 5. (a) The unloading modulus (average ± standard deviation) at three different loading rates as a function of the load–unload cycle number. The lighter shade of the modulus values calculated from the first unload cycle reflects the uncertainty in their accuracy due to the approximations inherent in their calculations. (b) % recovery as a function of maximum displacement before unload. Unloading the indenter before the displacement burst (open symbols) shows significantly higher values of % recovery than after the burst (filled symbols). (c) The loss coefficient values as a function of load–unload cycles showing very poor energy dissipation under indentation. (color online)

120–175 MPa as a function of displacement rate and load–unload cycle number. These moduli further demonstrate a strong rate effect, with the fastest rate of 1000 nm/s consistently resulting in the highest moduli for all load–unload cycles. Such a rate dependence of the material stiffness is a known characteristic of viscoelastic solids.[43] In contrast, repeated cycling appears to have only a marginal effect on the sample modulus, although there is a small increase from first to second cycle, remaining nearly constant during subsequent cycles for each displacement rate. We note that the above method of calculation of unloading moduli inherently assumes indentation of an elastic half-space, usually represented well by a monolithic material.[30,44] Therefore, they may not be suitable for VACNT indentation—particularly for the first load–unload cycle where a block of material separates from the outer matrix. In spite of these aspects, Fig. 5(a) helps to underscore the higher degree densification of the VACNT film at faster rates. We also find that the higher modulus at faster rates leads to greater instability stress (Fig. 3), which increases from 1.49 ± 0.2 MPa at 10 nm/s to 1.54 ± 0.2 MPa at 100 nm/s to 1.75 ± 0.3 MPa at 1000 nm/s (average ± standard deviation over 10 or more measurements). Importantly, the indentation moduli shown in Fig. 5(a) match well with those measured during compression of APCVD VACNT micropillar samples (160–180 MPa,[9] see Table I). AU9

Figure 5(b) shows the trend in the % recovery as a function of maximum displacement before final unload across the three loading rates. Two distinct regions can be identified in this figure: (i) a segment of higher recovery between 50–80% when the indentation tests are stopped before the large initial displacement burst [open symbols in Fig. 5(b)], while (ii) loading beyond the burst (filled symbols) results in a very low (<10%) recovery. This indicates that the shear event, manifested by the large displacement burst in the indentation curve, results in permanent damage of the VACNT structure and significantly compromises its recoverability. We note that the virtually nonexistent material recovery from postdisplacement burst during indentation is in stark opposition to the almost full (~100%) recovery seen in these materials under compression experiments[9] (see Table I). We did not observe any significant deformation rate effects on the % recovery.

The loss coefficient η (see Sec. II) is shown in Fig. 5(c) as a function of load–unload cycle number. The data contain only those results for the tests loaded beyond the displacement burst. As a consequence of the marginal recovery [Fig. 5(b)], the loss coefficient associated with nanoindentation into this material is also very low, on the order of 0.003–0.006, a value nearly an order of magnitude lower than those for compression of the same material[9] (Table I).

The viscoelastic indentation response of the VACNT film, in terms of the measured values of their storage modulus (E'), loss modulus (E''), and tanδ values, is shown in Fig. 6. Similar to the % recovery results, two distinct responses are seen in this figure depending on whether the indenter is oscillated before the large initial displacement burst (open symbols in Fig. 6) or after (filled symbols). Both E' and E'' increase by a factor of ~3–4 once the displacement burst has occurred [Figs. 6(a) and 6(b)], while tanδ decreases by 20–30% after the burst [Fig. 6(c)]. Before the burst, these parameters depend more strongly on the applied load during oscillations, as evidenced by the larger spread in the data.

We find the storage modulus to be frequency independent over the range of frequencies probed. On the other hand, the loss modulus (and the tanδ) strongly increases with increasing frequency, although two local minimas exist at 30 and 50 Hz [Figs. 6(b) and 6(c)]. Unfortunately, the cutoff frequency (50 Hz) of our instrument prevents further study of this behavior at higher frequencies.

As shown earlier (Figs. 2 and 3), the large displacement burst occurring in the initial loading stages results in

significant buckling. Thus, the higher E' characteristic of the postburst structure indicates that the material is capable of storing a higher amount of energy in this state, with the excess energy presumably being stored in the buckled regions. The corresponding increase in E''—related to the dissipated energy—is at a lower proportion, thus leading to a less pronounced viscous response (lower values of tanδ) after the burst. The postburst decrease in tanδ is likely caused by the increased adhesion between the individual nanotubes in the buckled regions when they are brought into proximity of one another after buckling. A similar response has been observed in polymeric materials like rubber,[45] where an increase in cross-linking leads to a decrease of the viscoelastic response. We note that the trends reported in Fig. 6 are similar to those reported previously for other VACNT microstructures under indentation.[8] The storage modulus E' shown in Fig. 6(a) matches well with the unloading modulus shown in Fig. 5(a).

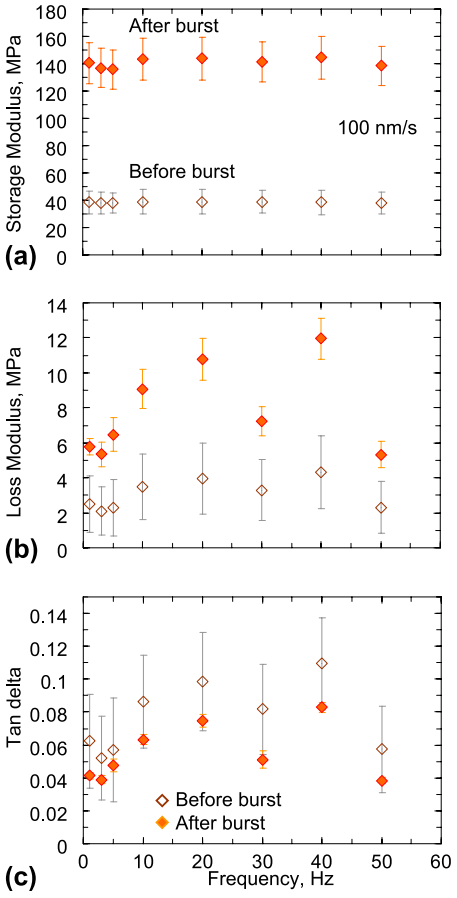

FIG. 6. The viscoelastic indentation response of the VACNT film at a loading rate of 100 nm/s, in terms of the measured values (average ± standard deviation) of their (a) storage modulus, (b) loss modulus, and (c) tanδ values, as a function of frequency. (color online)

F. Comparing indentation and compression

Figure 7(a) displays a comparative analysis between indentations into the ~142-μm-thick APCVD VACNT films in this study and the compressions on 30 × 30 μm (diameter × height) APCVD VACNT micropillars from our previous work.[9] All tests were conducted at the loading rate of 1000 nm/s. The indentation stress (σ_{ind}) and strain (ε_{ind}) values were calculated using Eq. (3). The following observations can be made from this comparison: (i) instability stress in compression is ~1.5 times higher than that in indentation, (ii) indentation is characterized by a significantly larger strain burst of ($\Delta\varepsilon = 0.3$) after the instability as compared to compression ($\Delta\varepsilon = 0.05$). This can be explained by the different deformation mechanisms associated with the bursts. During indentation, a single global shear event is responsible for such a burst, while under compression, a relatively small burst is sometimes observed just after yielding, which has been attributed to a temporary loss in the pillar–indenter contact.[9,11] (iii) After yield, the slope of the plateau region in compression is significantly higher (by a factor of almost 6) than during indentation. Thus, while the compressive stresses rise from ~2.8 MPa at yield to 4.8 MPa at the strain of 0.6 (i.e., before the onset of densification), the stresses at equivalent strains in indentation are relatively constant, in the 2.0–2.1 MPa range. Finally, (iv) after unloading (to 10% of maximum load), the material under

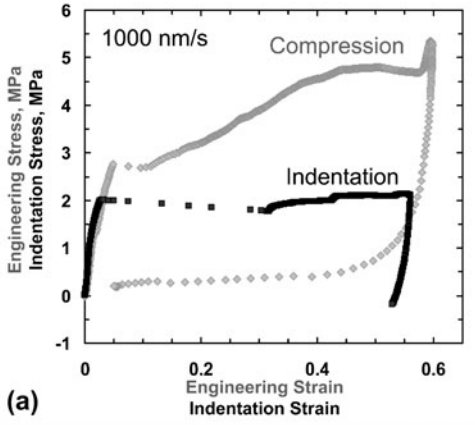

1000nm/s	Indentation	Compression
Instability stress	1.75±0.3 MPa (shear)	2.69±0.1 MPa (buckling)
Recovery @ ε=0.5	4.3±0.3 %	95.7±2.8 %
Loss Coefficient @ ε=0.5	0.005±0.001	0.05±0.01
Modulus @ ε=0.5	173.7±2 MPa	176.9±11 MPa

(b)

FIG. 7. (a) Comparative stress–strain curves of VACNT in indentation and compression. (b) Table comparing the measured values from indentation (this study) versus compression (Ref. 9).

indentation shows negligible (<5%) recovery, while compression leads to an almost complete (>95%) recovery.

While determining the underlying physics of the described observations requires rigorous multiscale modeling, some of these phenomena can be understood in terms of the differences in boundary conditions between the two loading configurations (indentation versus compression), in combination with the overall similarity of the VACNT deformation to that of open-cell foam materials.[46] The characteristics of flat-punch indentations into VACNT films closely resemble those reported for metallic[40,47] and polymeric foams.[41,46] In the spirit of foam-like deformation, the indentation zone for VACNTs is confined to the region directly beneath the indenter, while the surrounding regions are unaffected (see Fig. 2). The lack of lateral spread in the deformed region is typical for foams, whereby it can be attributed to the nonexistent Poisson's ratio.[2,40,46] This is diametrically opposite to monolithic materials, where the plastic zone underneath the indenter tip is typically represented by a continuous hemispherical plastic zone.[39] Another common characteristic between indentation into conventional foams and VACNTs is the appearance of a so-called "tear line"[40,41] along the corner of the flat-punch indenter where the shear force is largest. The depth of this shear line in a foam generally depends on its strength.[40,41] Unlike foams, however, the constituents of the VACNT system—the individual CNTs themselves—are nominally vertically aligned with respect to the indenter tip [Fig. 1(b)], and thus, the vertical plane is expected to be the plane of lowest shear strength in the VACNT matrix. Once the critical shear stress is attained during loading, the shear off proceeds catastrophically along this vertical plane through the thickness of the VACNT film down to the underlying substrate. This results in highly localized deformation along the shear plane, with no notable perturbation in other regions. Subsequent loading initiates folding or buckling of the material close to the substrate but not in the sheared-off block. In the extreme case of indenting a short VACNT film (Fig. 4), subsequent densification of the already folded/buckled CNTs commences.

On the contrary, under uniaxial compression, the shear stresses acting on the VACNT matrix are negligible. Instead, the applied compressive strain is accommodated entirely via the formation of lateral folds or buckles along the length of the bundle, while the remaining portion remains virtually unscathed.[9,11] Thus, the first instability shown in the compression stress–strain response in Fig. 7(a) is related to the onset of the first buckle formation in the VACNT matrix. Further loading beyond yield results in the compression of the collapsed buckles. The resulting densification of the matrix, in combination with a possible property gradient in the VACNT structure,[9,11] results in the strong positive slope of the compression stress–strain curve in the plateau region.

A comparison of the instability stresses between compression (buckling, 2.69 ± 0.1 MPa) and indentation (shear, 1.75 ± 0.3 MPa) on the APCVD VACNT samples indicates that the instability stress in indentation is 40% lower than that of compression [Fig. 7(b)]. Interestingly, this observation is opposite to that of traditional indentation tests into monolithic materials, where yield in indentation typically requires 1–3 times higher stresses than for the uniaxial case for most solid[29] and porous[39] as well as foam[40,46,48] materials. The two distinct modes of deformation in VACNTs—shear under indentation and buckling in compression—are likely responsible for this apparent reversal in their instability stress values, i.e., during indentation, the APCVD VACNT film reaches its critical shear stress before it can buckle.

While our findings may be representative of the overall CNT film deformation, it is important to recognize that both the shear strength and the deformation behavior of the VACNT matrix are strongly affected by its microstructural details such as tube and node density and tortuosity. These parameters govern the entanglement of the individual CNTs within the matrix, and hence, our observations are valid only for the particular APCVD VACNT film studied in this work. Further, even the standard APCVD growth techniques for VACNTs are notoriously difficult to control. For example, despite the growth recipe to create the 30-μm-tall VACNT pillars studied in Ref. 9 and the 142-μm-tall VACNT films investigated in this work being nominally identical (other than the growth time), it is reasonable to expect substantial differences in the VACNT density, alignment, and tortuosity, and, especially, their respective variations along the sample heights. Both of these parameters have proved to be very difficult to quantify experimentally. Similarly, the two VACNT film thicknesses shown in Fig. 4 may also show a similar difference since they were grown in different batches. Our related work on VACNTs produced using other CVD methods[49] as well as that of others in the field[25] have yielded a wide range in instability stresses under both indentation and compression, which are thought to be a consequence of the particular details (e.g., density, degree of entanglement, etc.) of the CNT structure and arrangement in their matrix.

We attribute the large difference in recoverability of the VACNT matrix in indentation (4.3% ± 0.3%) versus compression (95.7% ± 2.8 %) to the different deformation modes and boundary conditions under these two loading modes. The almost complete recovery of the VACNT structure under compression in Ref. 9 is related to the elastic unfolding of the buckles created during loading. This has been explained by the intertube interactions of the CNTs where the zipping and unzipping of CNTs in contact have been proposed as the primary criteria for the superior viscoelasticity and creep recovery of VACNTs.[19,20,25,50] On the contrary, recovery in indentation is inhibited by the

additional constraints of the surrounding VACNT material. Thus, even at lower strains (before the large shear burst), the recovery under indentation is still lower [50–80%, Fig. 5(b)] than that in compression. After the displacement burst, recovery of the VACNTs in indentation is further compromised by the permanent nature of the damage caused by the shearing of a large block of the material from the matrix.

Similarly, the viscoelastic properties of the VACNT matrix are also different in indentation (Fig. 6) versus compression (Ref. 9). While the frequency dependence of tanδ is similar in both cases, the values of tanδ in indentation (as measured after burst) were 20–30% lower than those in compression, suggesting a lower viscous response.

IV. CONCLUSIONS

In summary, we demonstrate that under large displacement indentations, APCVD-grown VACNT films deform by a single vertical catastrophic shear-off event along the rim of the indenter tip, manifested by an extensive ~20–40-μm-long displacement burst in the load–displacement curve. Similarly, to foam materials with negligible Poisson's ratios, the indentation in VACNTs is also exclusively confined to regions directly beneath the indenter. Through in situ nanomechanical indentation experiments, we show that the axial strain during the catastrophic shearing event is accommodated by rolling of several coiled-up CNT sections, or "microrollers." We hypothesize that such coiling provides a low-friction path for deformation, which may explain the lower stresses associated with indentation. Loading beyond the initial shear event causes a 20–30% decrease in the material's viscous response. We also find progressive buckling in the VACNT structure, with the buckles forming primarily near the stiff underlying substrate. Comparison of indentation versus compression experiments indicates that APCVD-grown VACNT films reach their critical shear stress before buckling in indentation, which results in the catastrophic shear formation in their microstructure. As a result, these materials demonstrate negligible recovery in indentation, as compared to their almost perfect recoverability under compression.

ACKNOWLEDGMENTS

The authors acknowledge S. Hutchens and A. Needleman for helpful insights and guidance, E. Lim for data analysis, financial support from the Georgia Institute of Technology Foundation through the Joseph Anderer Faculty Fellowship, and the Institute for Collaborative Biotechnologies (ICB) for financial support through Grant No. W911NF-09-0001 from the U.S. Army Research Office. The content of the information does not necessarily reflect the position or the policy of the Government, and no official endorsement should be inferred. S.P. gratefully acknowledges support from the W.M. Keck Institute for Space Studies Postdoctoral Fellowship program for this work. We gratefully acknowledge critical support and infrastructure provided for this work by the Kavli Nanoscience Institute at Caltech.

REFERENCES

1. C.M. McCarter, R.F. Richards, S.D. Mesarovic, C.D. Richards, D.F. Bahr, D. McClain, and J. Jiao: Mechanical compliance of photolithographically defined vertically aligned carbon nanotube turf. *J. Mater. Sci.* **41**, 7872 (2006).
2. A.A. Zbib, S.D. Mesarovic, E.T. Lilleodden, D. McClain, J. Jiao, and D.F. Bahr: The coordinated buckling of carbon nanotube turfs under uniform compression. *Nanotechnology* **19**, 175704 (2008).
3. B.A. Cola, J. Xu, and T.S. Fisher: Contact mechanics and thermal conductance of carbon nanotube array interfaces. *Int. J. Heat Mass Transfer* **52**, 3490 (2009).
4. A. Misra, J.R. Greer, and C. Daraio: Strain rate effects in the mechanical response of polymer-anchored carbon nanotube foams. *Adv. Mater.* **20**, 1 (2008).
5. A.Y. Cao, P.L. Dickrell, W.G. Sawyer, M.N. Ghasemi-Nejhad, and P.M. Ajayan: Super-compressible foamlike carbon nanotube films. *Science* **310**, 1307 (2005).
6. J. Cho, C. Richards, D. Bahr, J. Jiao, and R. Richards: Evaluation of contacts for a MEMS thermal switch. *J. Micromech. Microeng.* **18**, (2008). AU10
7. J.F. Waters, P.R. Guduru, M. Jouzi, J.M. Xu, T. Hanlon, and S. Suresh: Shell buckling of individual multiwalled carbon nanotubes using nanoindentation. *Appl. Phys. Lett.* **87**, 103109 (2005).
8. S. Pathak, Z.G. Cambaz, S.R. Kalidindi, J.G. Swadener, and Y. Gogotsi: Viscoelasticity and high buckling stress of dense carbon nanotube brushes. *Carbon* **47**, 1969 (2009).
9. S. Pathak, E.J. Lim, P. Pour Shahid Saeed Abadi, S. Graham, B.A. Cola, and J.R. Greer: Higher recovery and better energy dissipation at faster strain rates in carbon nanotube bundles: An in situ study. *ACS Nano* (2012) doi: 10.1021/nn300376j. AU11
10. M. Kumar and Y. Ando: Chemical vapor deposition of carbon nanotubes: A review on growth mechanism and mass production. *J. Nanosci. Nanotechnol.* **10**, 3739 (2010).
11. S.B. Hutchens, L.J. Hall, and J.R. Greer: In situ mechanical testing reveals periodic buckle nucleation and propagation in carbon nanotube bundles. *Adv. Funct. Mater.* **20**, 2338 (2010).
12. S.B. Hutchens, A. Needleman, and J.R. Greer: Analysis of uniaxial compression of vertically aligned carbon nanotubes. *J. Mech. Phys. Solids* **59**, 2227 (2011).
13. J. Suhr, P. Victor, L.C.S. Sreekala, X. Zhang, O. Nalamasu, and P.M. Ajayan: Fatigue resistance of aligned carbon nanotube arrays under cyclic compression. *Nat. Nanotechnol.* **2**, 417 (2007).
14. T. Tong, Y. Zhao, L. Delzeit, A. Kashani, M. Meyyappan, and A. Majumdar: Height independent compressive modulus of vertically aligned carbon nanotube arrays. *Nano Lett.* **8**, 511 (2008).
15. S.D. Mesarovic, C.M. McCarter, D.F. Bahr, H. Radhakrishnan, R.F. Richards, C.D. Richards, D. McClain, and J. Jiao: Mechanical behavior of a carbon nanotube turf. *Scr. Mater.* **56**, 157 (2007).
16. A. Qiu, D.F. Bahr, A.A. Zbib, A. Bellou, S.D. Mesarovic, D. McClain, W. Hudson, J. Jiao, D. Kiener, and M.J. Cordill: Local and non-local behavior and coordinated buckling of CNT turfs. *Carbon* **49**, 1430 (2011).
17. Q. Zhang, Y.C. Lu, F. Du, L. Dai, J. Baur, and D.C. Foster: Viscoelastic creep of vertically aligned carbon nanotubes. *J. Phys. D: Appl. Phys.* **43**, 315401 (2010).

18. C.P. Deck, J. Flowers, G.S.B. McKee, and K. Vecchio: Mechanical behavior of ultralong multiwalled carbon nanotube mats. *J. Appl. Phys.* **101**, 23512 (2007).
19. M. Xu, D.N. Futaba, T. Yamada, M. Yumura, and K. Hata: Carbon nanotubes with temperature-invariant viscoelasticity from-196 degrees to 1000 degrees C. *Science* **330**, 1364 (2010).
20. M. Xu, D.N. Futaba, M. Yumura, and K. Hata: Carbon nanotubes with temperature-invariant creep and creep-recovery from −190 to 970 °C. *Adv. Mater.* **23**, 3686 (2011).
21. C. Cao, A. Reiner, C. Chung, S-H. Chang, I. Kao, R.V. Kukta, and C.S. Korach: Buckling initiation and displacement dependence in compression of vertically aligned carbon nanotube arrays. *Carbon* **49**, 3190 (2011).
22. M.R. Maschmann, Z. Qiuhong, D. Feng, D. Liming, and J. Baur: Length dependent foam-like mechanical response of axially indented vertically oriented carbon nanotube arrays. *Carbon* **49**, 386 (2011).
23. P. Pour Shahid Saeed Abadi, S. Hutchens, J.H. Taphouse, J.R. Greer, B.A. Cola, and S. Graham: The effect of morphology on the micro-compression response of carbon nanotube forests. *Nanoscale* (2012).
24. M.R. Maschmann, Q. Zhang, R. Wheeler, F. Du, L. Dai, and J. Baur: In situ SEM observation of column-like and foam-like CNT array nanoindentation. *ACS Appl. Mater. Interfaces* **3**, 648 (2011).
25. P.D. Bradford, X. Wang, H. Zhao, and Y.T. Zhu: Tuning the compressive mechanical properties of carbon nanotube foam. *Carbon* **49**, 2834 (2011).
26. J-Y. Kim and J.R. Greer: Tensile and compressive behavior of gold and molybdenum single crystals at the nano-scale. *Acta Mater.* **57**, 5245 (2009).
27. J.P. Tu, C.X. Jiang, S.Y. Guo, and M.F. Fu: Micro-friction characteristics of aligned carbon nanotube film on an anodic aluminum oxide template. *Mater. Lett.* **58**, 1646 (2004).
28. J.P. Tu, L.P. Zhu, K. Hou, and S.Y. Guo: Synthesis and frictional properties of array film of amorphous carbon nanofibers on anodic aluminum oxide. *Carbon* **41**, 1257 (2003).
29. K.L. Johnson: *Contact Mechanics* (Cambridge University Press, Cambridge, 1987).
30. W.C. Oliver and G.M. Pharr: Improved technique for determining hardness and elastic modulus using load and displacement sensing indentation experiments. *J. Mater. Res.* **7**, 1564 (1992).
31. V.S. Deshpande and N.A. Fleck: Isotropic constitutive models for metallic foams. *J. Mech. Phys. Solids* **48**, 1253 (2000).
32. M.F. Ashby: *Materials Selection in Mechanical Design*, 3rd ed. (Butterworth-Heinemann, Oxford, 2005).
33. R. Hill: *The Mathematical Theory of Plasticity* (Oxford University Press, Oxford, 1950).
34. E.G. Herbert, W.C. Oliver, and G.M. Pharr: Nanoindentation and the dynamic characterization of viscoelastic solids. *J. Phys. D: Appl. Phys.* **41**, 074021 (2008).
35. E.G. Herbert, W.C. Oliver, A. Lumsdaine, and G.M. Pharr: Measuring the constitutive behavior of viscoelastic solids in the time and frequency domain using flat punch nanoindentation. *J. Mater. Res.* **24**, 626 (2009).
36. W.J. Wright, A.R. Maloney, and W.D. Nix: An improved analysis for viscoelastic damping in dynamic nanoindentation. *Int. J. Surf. Sci. Eng.* **1**, 274 (2007).
37. W.J. Wright and W.D. Nix: Storage and loss stiffnesses and moduli as determined by dynamic nanoindentation. *J. Mater. Res.* **24**(3), 863 (2009).
38. S. Pathak, J. Gregory Swadener, S.R. Kalidindi, H-W. Courtland, K.J. Jepsen, and H.M. Goldman: Measuring the dynamic mechanical response of hydrated mouse bone by nanoindentation. *J. Mech. Behav. Biomed. Mater.* **4**, 34 (2011).
39. N.A. Fleck, H. Otoyo, and A. Needleman: Indentation of porous solids. *Int. J. Solids Struct.* **29**, 1613 (1992).
40. P. Sudheer Kumar, S. Ramchandra, and U. Ramamurty: Effect of displacement-rate on the indentation behavior of an aluminum foam. *Mater. Sci. Eng., A* **347**, 330 (2003).
41. E.A. Flores-Johnson and Q.M. Li: Indentation into polymeric foams. *Int. J. Solids Struct.* **47**, 1987 (2010).
42. A. Pantano, D.M. Parks, and M.C. Boyce: Mechanics of deformation of single- and multi-wall carbon nanotubes. *J. Mech. Phys. Solids* **52**, 789 (2004).
43. R.S. Lakes: *Viscoelastic Solids* (CRC Press, Boca Raton, FL, 1998).
44. M.F. Doerner and W.D. Nix: A method for interpreting the data from depth-sensing indentation instruments. *J. Mater. Res.* **1**, 601 (1986).
45. I.M. Ward and J. Sweeney: *An Introduction to the Mechanical Properties of Solid Polymers*, 2nd ed. (Wiley, West Sussex, UK, 2004).
46. L.J. Gibson and M.F. Ashby: *Cellular Solids: Structure and Properties* (Cambridge, UK, 1999).
47. E.W. Andrews, L.J. Gibson, and M.F. Ashby: The creep of cellular solids. *Acta Mater.* **47**, 2853 (1999).
48. E.W. Andrews, G. Gioux, P. Onck, and L.J. Gibson: Size effects in ductile cellular solids. Part II: Experimental results. *Int. J. Mech. Sci.* **43**, 701 (2001).
49. S. Pathak and J.R. Greer.
50. Y. Gogotsi: High-temperature rubber made from carbon nanotubes. *Science* **330**, 1332 (2010).

Supplementary Material

Supplementary material can be viewed in this issue of the *Journal of Materials Research* by visiting http://journals.cambridge.org/jmr.

Effect of morphology on the strain recovery of vertically aligned carbon nanotube arrays: an *in situ* study.

Siddhartha Pathak [*], Jordan R. Raney, Chiara Daraio

Division of Engineering and Applied Science, California Institute of Technology (Caltech), Pasadena, CA, USA

Abstract

We report on the distinctly different mechanical responses of two vertically aligned carbon nanotube (VACNT) films, subjected to large displacement (up to 70 μm) flat punch indentations. The VACNT films were synthesized using the same chemical vapor deposition (CVD) technique but for varying reaction times, which resulted in their different thicknesses (480 and 160 μm, respectively) and morphologies. *In situ* tests reveal that the shorter, more aligned VACNT film deforms *via* an instantaneous vertical shearing of the material directly underneath the indenter tip, which is manifested as a rapid displacement burst in the load-displacement response when tested at rates of 100 nm/s and above. The resultant buckles were of a more permanent nature leading to their low recoverability (22-40%). In contrast, we find the thicker, more tortuous VACNT film to show a higher (~80%) recovery and a more compliant response. These differences in the mechanical response of the VACNTs are discussed in the framework of foam-like deformation with a particular emphasis on their different morphological features, namely density and tortuosity.

Keywords

Vertically aligned carbon nanotubes, indentation, mechanical properties, energy storage, recovery

[*] Contact author: - Materials Science, California Institute of Technology (Caltech), 1200 E. California Blvd., MC 309-81, Pasadena, CA 91125-8100, Phone: +1 (626) 395-8165, Fax: +1 (626) 395-8868, E-mail: pathak@caltech.edu, siddharthapathak@gmail.com

1. Introduction

Among the wide variety of macroscopic carbon nanotube (CNT) architectures, vertically aligned carbon nanotube (VACNT) arrays have attracted special attention due to their possible applications ranging from micro-electro-mechanical systems (MEMS) to energy dissipative systems, such as viscoelastic rubbers and foams [1-6]. VACNT arrays can be readily synthesized by different techniques [7, 8], and the choice of synthesis approach affects the morphology and the properties of the resulting arrays. A popular technique for production of large quantities of VACNTs is chemical vapor deposition (CVD) [7, 9]. However, different CVD synthesis methods can lead to different resulting properties of the VACNTs. For example, the use of 'floating' [10, 11] vs. 'fixed' catalysts [12, 13] can lead to changes in both the structure of the individual CNTs, as well as differences in the complex hierarchical morphology of the VACNT arrays, their collective inter-tube interactions, and inherent property gradients [14]. This variability is reflected in the range of mechanical properties reported for VACNTs, such as elastic modulus and buckling strength that range anywhere from sub-MPa [6, 15] to tens of MPa [16-18] to GPa [19, 20] levels.

Another marked difference among different VACNT arrays is the ability (or lack thereof) to recover from large deformations; with some exhibiting superior creep recovery [1, 5, 6, 21, 22], while others deform permanently even at modest strains [12, 18, 23-25]. The recoverability of VACNTs is known to depend both on the experimental loading and boundary conditions as well as the VACNT morphology. For example, in recent work, Pathak et al. [22] found that under uniaxial compression the recoverability and energy dissipation of certain VACNTs is strain-rate dependent, with the values increasing at faster strain rates. For other VACNT types, however, the energy dissipation has been found to be rate independent [26]. Flat-punch indentation experiments on VACNT films of larger thicknesses (grown by the same technique as in [22]) have shown negligible – almost zero – recovery [27, 28]. Various authors have suggested that the different boundary conditions present in indentation experiments result in significant shear stresses in the material. This often causes the VACNT films to deform by an instantaneous vertical shearing of the material directly underneath the indenter tip, and the permanent nature of the damage caused by shearing severely compromises the recoverability of the VACNTs [28, 29]. The recoverability of VACNTs has also been shown to depend on the VACNT microstructure and morphology. In general, researchers growing CVD-VACNTs made using the 'floating' catalyst route have reported substantial (>90%) recovery in their samples [1, 11, 14, 30], while the recoverability of majority of VACNTs made using the 'fixed' catalyst technique [18, 23-25] has been poor (note: Ref [22] is a notable exception). In general, VACNTs made using the floating catalyst route have much thicker (>40 nm) diameter tubes, and a correspondingly higher density. This effect was studied systematically by Bradford et al. [31], who showed that VACNTs grown using a fixed catalyst technique and exhibiting low resilience changed to an almost complete recovery after a post growth CVD treatment. This was attributed to an increase in the individual CNT wall thickness, which also caused increased surface roughness of the CNTs, resulting in a decrease of the van der Waals interactions.

Other aspects of the VACNT microstructure are also known to influence their mechanical properties, such as their tortuosity (or waviness) and the number of inter-tube junctions in the matrix. A few studies have attempted to explore these effects

experimentally [32-35], but no strong correlations were observed. Some key insights into these parameters can be gained from the theoretical studies involving random network of stiff fibers. For example, Astrom et al. [36] have applied their modified semi-theoretical version of the Cox shear-lag model [37] to CNT mats and fibers, while taking into account the statistical number of bundle–bundle contacts. Their study suggests a linear relationship between the number of contact points and the modulus of the CNT network. A similar result was also obtained by Berhan and coworkers [38], who also found that an increase in the waviness of the nanotube ropes results in a significant decrease in their effective modulus [39].

The lateral interaction of the nominally aligned CNTs is also an important parameter for determining the mechanical behavior of the VACNT array (such as compressive modulus [34]), and it has been observed to vary with total array height, with taller arrays often showing more lateral entanglement [40]. Arrays as short as 50 nm [41] and as long as several mm [19] have previously been examined. The mechanical responses of these extreme cases have been very different, with the short sample being made up of non-interacting parallel CNTs and the long sample consisting of highly entangled CNTs.

Such drastic changes in the VACNT properties make it impractical to compare the performance of VACNTs synthesized by non-identical growth techniques. In this work, we focus on VACNT films of two different heights of 160 and 480 μm respectively, which were grown by the same floating catalyst CVD technique [10, 11] and exhibit a highly entangled morphology. We perform large displacement instrumented indentation experiments to characterize the mechanical behavior of the two VACNT films. We utilize flat punch diamond indenter tip geometries for the indentation tests. Compared to other indenter tip geometries, the contact area for a flat punch indenter does not change with displacement. This is especially advantageous for the unique microstructural hierarchy of VACNT films, where the micrometer-to-millimeter sized film is composed of millions of individual nanotubes with diameters in the nanometer range. Such an arrangement not only renders the mechanical response of VACNTs to be distinct from monolithic materials, but also poses a challenge in the accurate estimation of the contact area between the VACNT film and the commonly used parabolic [20, 42] and pyramidal [42] indenter tip geometries. The constant contact area between the flat punch indenter and the VACNT sample is also of advantage in measuring the viscoelastic response of the VACNT assembly.

We utilize both an *in situ* nanoindentation methodology to observe the on-edge deformation in real time using a custom-built *in situ* nano-mechanical deformation instrument, SEMentor [43], as well as more traditional in-bulk *ex situ* indentation methods in this work. The *in situ* tests conducted inside the scanning electron microscope (SEM) have the advantage of allowing uninterrupted observation of the real-time evolution of deformation while simultaneously recording load vs. displacement data, thus providing a one-to-one correlation between the morphological changes and the mechanical response [23, 27, 44]. However, in order to facilitate an uninhibited view of the material cross-section, *in situ* indentation experiments need to be conducted on the edge of the sample [27]. While such a set-up causes the boundary conditions and constraints to differ from those during in-bulk indentations, they provide important information on morphological evolution during deformation of VACNTs, not easily obtainable by other methods.

2. Materials and Methods

2.1 CNT Growth

Aligned CNTs were synthesized on thermally oxidized Si wafers using vapor phase (or "floating catalyst") thermal CVD techniques that have been in wide use for more than a decade [10]. Synthesis took place at atmospheric pressure in an inert Ar atmosphere at 827 °C. A precursor solution of ferrocene (which pyrolyzes to release atomic Fe to act as a catalyst for CNT growth) and toluene (which acts as a carbon source) was created at a concentration of 0.02 g ml^{-1} and injected at approximately 1 ml min^{-1} into the heating zone of the furnace in a flow of 800 sccm of Ar. The quartz furnace tube had a diameter of approximately 4 cm and the heating zone was about 20 cm long. VACNT samples of different heights were generated by varying the amount of precursor solution used (and hence the total reaction time). Two VACNT samples, of film thicknesses 480 and 160 μm and named samples A and B, respectively, were selected for further study. The longer sample corresponded to 10 ml of precursor solution and the shorter sample to 7 ml of precursor solution (about 10 and 7 minutes total reaction time, respectively). All other synthesis parameters between the samples were unchanged. Large portions of the samples (~ 10 mm^2) were removed from the substrate with a razor blade, and their masses were obtained with a microbalance. Sample densities were obtained by dividing these measured values of mass by the respective volumes of the sample portions (with film thickness determined by scanning electron microscope (SEM) and areal dimensions directly obtained with calipers). Table 1 lists the major differences between samples A and B. The samples were studied using both SEM (FEI Nova 200 and 600, FEI Quanta 200) and transmission electron microscopy (TEM, FEI TF30UT) machines as shown in Fig. 1. Note the localized regions of lower density, visible as horizontal bands along the height of the VACNT structure in sample B in this figure.

Although both samples were synthesized under very similar conditions, we noted significant differences in their morphological features, and therefore in their mechanical behavior. These differences arise due to subtle effects related to the injection of our precursor solution. For example, modest increases in carbon concentration in the reactor can lead to increased entanglement of the individual CNTs [45]. Similarly, because CNT diameter depends on injection rate of the precursor solution [46], fluctuations in this rate can lead to localized regions of lower density, visible as horizontal bands along the height of the final VACNT structure [47]. We have observed in the past that these regions can result in strain localization during compression [47]. Fluctuations in both of these quantities are especially likely at the beginning of our growth process due to variability that occurs during the sudden injection of a precursor solution. Because of the bottom-up growth process by which our VACNTs are synthesized [48, 49], these fluctuations at the beginning of the growth process are reflected in morphological differences near the top of the VACNT array (i.e., where the oldest growth is present). Note that under indentation the majority of the indentation stresses are also localized at the top portions of the VACNT array.

In order to test the repeatability of the samples, we synthesized a third set of VACNT samples with the lower reaction time of 7 min. While this sample set was similar in thickness (~170 μm) to sample B, it did not contain any bands of lower VACNT

density as seen in sample B. The detailed results for this third sample set are not shown in this paper.

2.2 *Ex situ* indentations

We tested the two different VACNT films with thicknesses of 480 and 160 μm (samples A and B) under large displacement cyclic indentation tests. The indentation experiments were performed using the XP module of Agilent's nanoindenter G200 with adjustable software control methods, as described in Ref [23]. Tests were performed in air using a custom made cylindrical diamond flat punch with ~120 μm diameter and ~80 μm height. Indentations were performed under a constant displacement control varying indentation depths up to a maximum of around 70 μm (restricted by the height limitations of the diamond flat punch). Tests were conducted in the interior of the samples (in-bulk tests, i.e., away from the sample edge) at three different constant displacement rates: 10 nm/s, 100 nm/s and 1000 nm/s. Typically 5 load-unload cycles were performed at each displacement level. No hold time was applied at the maximum loads, and each cycle was unloaded to only 10% of the max load in the previous cycle, in order to maintain the cyclic nature of the tests. A minimum of 10 tests were conducted at each displacement rate. The indents were spaced at least 500 microns apart in order to eliminate any possible proximity effects.

2.3 *In situ* SEM indentations

In situ tests were conducted in a custom-built indentation instrument [43], composed of a nano-mechanical dynamic contact module (Agilent Corp.) inside a SEM (Quanta 200, FEI). Tests were conducted on the sample edge ('on-edge' [28] experiments, to facilitate viewing) with a conductive diamond flat punch with a rectangular flat cross-section of ~60 μm × 80 μm. The loading axis in the instrument is inclined at ~86^{o} with respect to the electron beam, thus allowing continuous observation of the deformation morphology of the VACNT film cross-section during the on-edge *in situ* experiments. As described earlier, the outer constraints in on-edge indentations are different from those during in-bulk tests, and therefore the measured mechanical behavior is expected to be different. SEM observations were recorded as a video file at 30 frames per second and synchronized with the indentation data to provide a real-time correlation between each video frame and the corresponding position on the load-displacement curve. Three video files are provided as supporting online material – video file S1 shows the on-edge indentation on sample A conducted at a 100 nm/s displacement rate, files S2 (at 100 nm/s displacement rate) and S3 (at a slower 10 nm/s displacement rate) show the same for sample B. These three video files are shown at 30, 25, and 250 times their original speeds, respectively. These tests were conducted to a maximum penetration depth of 30 μm (instrument limit).

While both the *ex situ* and the *in situ* experiments are nominally identical, some differences exist. First, the *in situ* tests are conducted in a vacuum environment vs. the *ex situ* tests, which are conducted in air. Moreover, in the *in situ* case the samples are constantly exposed to the electron beam, and they are oriented horizontally such that gravity is acting perpendicular to the compression axis. Although the effect of these differences is expected to be minor, the *in situ* results are used here for visualization

purposes only. All data analyses were performed on tests conducted in air in the *ex situ* nanoindenter.

2.4 Data Analysis

The applied load, P, and measured displacement, h, were corrected for machine compliance following the procedure outlined in detail in Ref [23]. The unloading modulus was calculated from the initial unloading segment of the measured load-displacement curve using Hertzian contact mechanics [50, 51] and assuming negligible friction between the indenter sidewalls and the VACNT matrix [52-54] as:

$$E_{eff} = \frac{\sqrt{\pi}}{2}\frac{S}{\sqrt{A}} = \frac{S}{2a}, \qquad \frac{1}{E_{eff}} = \frac{1-\nu_s^2}{E_s} + \frac{1-\nu_i^2}{E_i} \tag{1}$$

where E_{eff} denotes the effective modulus of the combined indenter-specimen system; $S(=dP/dh)$ is the stiffness measured from the slope of the initial 30% of the unloading load-displacement curve; ν and E are the Poisson's ratio and the Young's modulus, respectively; and the subscripts *s* and *i* refer to the specimen and the indenter, respectively, with E_i = 1041 GPa and ν_i = 0.07. A vanishing Poisson's ratio of $\nu = 0$ was assumed for the VACNTs [55]. Unfortunately, due to misalignment issues between the indenter tip and the sample surface Eq. (1) cannot be applied to the initial loading portion of the test. Eq. (1) is also limited by the inherent assumptions of Hertz' theory, which assumes an isotropic, elastic, continuum material behavior. VACNTs, on the other hand, demonstrate varying degrees of anisotropy at each level of its hierarchical microstructure (see Fig. 1). Thus, our measurements of VACNT indentation moduli should instead be treated as their equivalent continuum isotropic values. We also point out that this isotropic continuum framework has been previously utilized in developing the constitutive relations in VACNTs [23] and foams [56], and appears to have accurately captured the qualitative features of their outer deformation profiles and the stress-strain responses. The continuum foundation is also motivated by the nearly isotropic network of CNTs as revealed by images at or above magnifications of 30,000X (Fig. 1c and e).

We define the percentage recovery (*R*) as the displacement recovered at the end of each cycle with respect to the maximum displacement, i.e. $R = \dfrac{h_{\max} - h_{unload}}{h_{\max}}$ (2)

where $h_{\max}$ is the maximum displacement at the end of loading and h_{unload} is the displacement after unloading to 10% of the max load in each cycle.

The loss coefficient, η, (a dimensionless quantity) measures the degree to which a material dissipates energy and is calculated as [57]

$$\eta = \frac{\Delta U_i}{2\pi U_1}\ ,\ U = \int_0^{\sigma_{\max}} \sigma_{ind}\, d\varepsilon_{ind} \approx \frac{1}{2}\frac{\sigma_{\max}^2}{E_s}\ ,\ \Delta U = \oint \sigma_{ind}\, d\varepsilon_{ind} \tag{3}$$

where U_1 is the elastic energy stored in the material when it is loaded elastically to a stress $\sigma_{\max}$ in the 1st cycle, ΔU_i is the energy dissipated in the ith load-unload cycle, and ε indicates the sample's strain.

2.5 Viscoelastic Characterization

The viscoelastic properties of the VACNT films were measured following the procedure outlined in Ref [23]. In this method, the indenter is loaded into the sample in air at a constant displacement rate of 100 nm/s up to a specified indentation depth, at which point the indenter head is oscillated at ~8 nm amplitude across a range of frequencies from 1 to 50 Hz. The cut-off frequency of 50 Hz is dictated by the instrument limit, as detailed in Refs [23, 58]. The procedure was repeated at six different constant indentation depths for sample A: 15, 26, 36, 47, 58 and 68 μm, respectively. In sample B, however, the viscoelastic properties could be measured for only the three deeper indentation depths of 47, 58 and 68 μm. As described in the next sections, there is a large ~30 μm displacement burst in sample B during loading, which masks the viscoelastic measurements at the lesser depths.

Viscoelastic materials are commonly characterized by their storage (E') and loss (E'') moduli, as well as the ratio of the two – $\tan\delta$. E' represents the stored energy or the elastic response, and E'' corresponds to the amount of energy dissipated, or the viscous response. Assuming linear viscoelastic behavior, these terms can be computed following the calculations described in Refs [58-61] as follows:

$$E' = k'\frac{\sqrt{\pi}}{2\beta}\frac{1-\nu_s^{\,2}}{\sqrt{A}},\ k' = \left|\frac{F_0}{u_0}\right|\cos\varphi - \left|\frac{F_0}{u_0}\right|_{air}\cos\varphi_{air},$$

$$E'' = k''\frac{\sqrt{\pi}}{2\beta}\frac{1-\nu_s^{\,2}}{\sqrt{A}},\ k'' = \left|\frac{F_0}{u_0}\right|\sin\varphi - \left|\frac{F_0}{u_0}\right|_{air}\sin\varphi_{air},$$

$$\tan\delta = \frac{E''}{E'} \quad . \tag{4}$$

Here k' and k'' are the storage and loss stiffnesses of the sample, obtained by finding the real and complex parts, respectively, of the stiffness differences between oscillating the indenter head on the sample at a fixed displacement and in air at the same raw displacement, β is a constant (=1 for a flat punch indenter). F_0 and u_0 are the load and displacement oscillation amplitudes, respectively, and φ is the phase angle between the load and displacement oscillations. We note that the accuracy in the values of E' and E'' in Eq. (4) can be affected by several factors: uncertainties in Poisson's ratio, since it may be frequency dependent, and ambiguity in contact area, especially at shallower indentation depths, where full contact may not have been established. On the other hand, calculation of $\tan\delta$ is independent of the contact area, and thus is ideally suited as a measure of the viscoelasticity of the indented material [20, 62].

3. Results and Discussion

3.1 VACNT morphology

Figure 1 shows the SEM and TEM images at different magnifications of the two VACNT samples A and B grown on Si substrates using the CVD synthesis technique with a floating catalyst (see Materials and Methods). The complex hierarchical nature of the VACNT microstructure, with distinct organizational details across multiple length scales, is shown in Figures 1a-c (sample A) and Figs. 1d-e (sample B). Thus, while

VACNTs appear as continuous films at lower magnifications, the nominally vertical alignment of CNT bundles growing perpendicularly to the support substrate is apparent at a higher magnification of 500X and above (Figs. 1a and 1d). Still higher magnifications of 30,000X reveal significant intertwining in the long, curved lengths of individual CNTs along the VACNT height, and at this length scale the CNT network appears more isotropic [23, 56, 63] (Figs. 1c and 1e). A representative image, obtained via TEM, of the internal structure of an individual multiwall (typically 20-60 walls) CNT is shown in Fig. 1f. As a result of this complex hierarchical structure, the mechanical behavior of the VACNT matrix depends both on the properties of individual CNTs, as well as their mutual interactions and distribution throughout the array.

Figure 1 and Table 1 also highlight some of the important morphological differences between samples A and B. The cross-sectional view of Sample A in Fig. 1a indicates that the CNTs in the top 290 μm height of this sample are highly tortuous. The expanded views of this region in Figs. 1b and c show that the tortuous CNT bands have a uniform chord length (straight line distance between the ends of two neighboring tortuous regions) of around 7.5-8 μm throughout this height.

The CNTs seen in the shorter (~160 μm tall) sample B have negligible tortuosity and follow relatively straighter paths (Figs. 1d and e). Note that the bottom ~180 μm of sample A also does not show any major tortuosity. As described in the Materials and Methods section, both VACNT samples were synthesized using the same nominal CVD growth conditions, but for different reaction times. The top portions of the samples thus reflect the regions of oldest growth in each case (CVD is essentially a bottom-up growth process). Since tortuosity is present only in the taller sample, it would seem to indicate that the alignment of individual CNTs in VACNT arrays is related to the CVD growth time (and hence the VACNT height) [49]. Such tortuous paths along a CNT are capable of storing more elastic energy than straight paths.

Sample B also shows the presence of two dark bands in its cross-section. The first of these bands is seen at a distance of ~32 μm from the top surface, while the second one is at ~50 μm (Fig. 1d). As described earlier, these bands develop due to fluctuations in the input rate of the precursor solution [47]. The density of the CNTs in these banded regions is known to be lower than the average [64], and hence these regions are expected to have a softening effect on the overall microstructure [47].

A closer inspection of the top regions of samples A and B also indicate that the CNTs are of much larger diameter in sample A as compared to B (compare Figs. 1c vs. 1e). This effect has been described in detail in Ref [65] where the CNT wall thickness increases as a function of the growth time. The average and standard deviation values of the CNT diameters provided in Table 1 indicate that the tubes in the upper region of sample A (CNT diameter 68.1±10.6 nm) are twice as thick as that of sample B (diameter 31.1±7.5 nm). Also note that as an obvious consequence of the difference in their tube diameters, sample A has larger density than sample B (Table 1).

3.2 *In situ* on-edge flat punch indentations

The different microstructures of the two VACNT samples A and B also result in distinct mechanical responses under indentation. This can be seen in the *in situ* SEM indentations described in Fig. 2. Figure 2c compares the load-displacement responses of the two on-edge tests between samples A and B. The following points are immediately

evident from this figure: (i) The slope of the initial loading segment of the load-displacement curve is significantly larger for sample B, indicating a much stiffer response for sample B than for sample A. (ii) In sample B the initial loading is followed by a sudden instability at a load level of 6.2 mN, manifested by a large displacement burst of length ~22 μm. No such burst is seen in sample A. (iii) Upon unloading, sample A shows almost full recovery, while sample B shows a much lower (~49%) recovery (compare Figs. 2a-b (sample A) vs. Fig 2d (sample B)).

The video files for these two on-edge indentation tests, which correlate the morphological changes happening in the samples under the indenter with their respective load-displacement responses, are provided as supporting online materials (video files S1 and S2), with several representative snapshots shown in Figs. 2a, b and d. For sample A (video file S1), the sequence of events occurring during the *in situ* indentations show that at the onset of indentation CNTs in the topmost ~14 μm of the VACNT film start to bend. As the indenter tip pushes forward, shear lines appear at the corners of the flat punch indenter. Further penetration of the indenter results in the formation of a buckling zone 60 μm directly below the indenter (see Fig. 2a inset). Note that the deformation of the VACNTs under indentation appears to be highly localized. Similar to foam deformation, the indentation zone for VACNTs is confined to the region directly beneath the indenter, while the surrounding regions are unaffected. This has generally been attributed to the non-existent Poisson's ratio in structures such as open-cell foams and VACNTs [24, 56, 66, 67], and is very different from the hemispherical indentation plastic zone reported under monolithic materials [68]. Unloading of the indenter tip reveals a remarkable resilience in the VACNTs in sample A, and hardly any after-effects of the indentation pressure can be seen on the surface of the VACNT film after full unload (compare Figs. 2a vs. 2b).

In contrast, the initial loading in sample B (video file S2) is followed by a small drop in indentation load (from 7.1 to 6.2 mN), after which a sudden and extensive displacement burst occurs. SEM images obtained immediately after this burst (SEM scanning rate was not fast enough to catch the details during the instantaneous burst) reveal that the top portion of the VACNT film has sheared off vertically below the edges of the indenter tip (Fig. 2d). The shear appears to be the result of a single buckle formed at a height of ~32 μm from the top of the VACNT film. The shear burst causes the indenter head to momentarily lose contact with the VACNT film, presumably since the VACNT film is collapsing at a faster rate than the prescribed motion of the indenter head (gravity cannot be responsible for the burst since gravity is acting perpendicular to the indentation axis). Interestingly, the 32 μm distance also corresponds to the location of the zone of dark bands seen in the cross-sections of these films (see Fig. 1d). As described earlier, these dark regions are known be zones of lower density in the VACNT matrix, and thus are predicted to be the first regions to buckle.

We find that the occurrence of the displacement burst in sample B depends strongly on the applied displacement rate. Indentation tests at slower displacement rates of 10 nm/s (video file S3) did not show any discrete behavior such as bursts, etc. Instead, we observe a gradual drop in the load from 6.2 to 3.2 mN after the onset of buckling. This would seem to indicate that at the lower displacement rates the individual CNT struts have enough time to realign themselves so as to avoid a catastrophic burst phenomenon [22]. As in the case of the faster tests, the buckling zone for the slower tests

also coincides with the zone of lower density VACNTs at ~32 μm from the top of the VACNT film. Further loading beyond the load drop at the slow displacement rate results in a flat plateau region where the displacement increases at a constant load. The SEM recordings of this stage indicate that the indenter is now pushing down on a rectangular region of width equal to the indenter tip and bounded at the bottom by the buckled zone (of height ~32 μm).

The buckles formed in sample B (for both the slow and fast indentation rates) are of a more permanent nature, and unloading of the indenter tip results in a much lower recovery for sample B than what was seen for sample A (Fig. 2d).

While the general pattern of deformation seen in the *in situ* videos (Fig. 2) is similar to those of typical open-cell foams, the shear events and the recoverability are unique characteristics seen only in intertwined VACNT systems. In VACNTs the plastic strain under the indenter is accommodated entirely by the formation of the lateral folds or buckles, which are highly localized. This is in contrast to traditional foams, where cell-edge bending and cell collapse are primarily responsible for the elastic-plastic foam response [67, 69]. Similarly, a shear event in non-interacting VACNTs [70] would propagate through the entire thickness, thus severely limiting its recoverability. The two examples shown in Fig. 2 demonstrate how the different degrees of alignment and intertwinement between the individual CNTs affect the ability of the VACNT array to recover from large indentation strains.

3.3 *Ex situ* in-bulk large-displacement indentations

In order to analyze the VACNT deformation beyond the displacement limit of the *in situ* tests, *ex situ* indentation tests were conducted in air in the Agilent G200 nanoindenter to larger depths of ~70 μm in the interior of the as-grown VACNT film away from the edges ('in-bulk' tests, see Materials and Methods). This maximum indentation depth is limited by the height of the cylindrical indentation punch (~80 μm). Figure 3a shows a comparison of the indentation load (stress)-displacement responses of two representative in-bulk tests between samples A and B, conducted at a displacement rate of 10 nm/s. For both samples, three distinct regions are apparent from Fig. 3a: (i) a short elastic regime, followed by (ii) an instability with an accompanied load drop suggesting the onset of buckling, and (iii) a subsequent plateau region. The plateau region can be further subdivided into two separate sections: an initial relatively flat section (where the load is more-or-less constant with increasing displacement) followed by a positively sloped section, where the load increases more rapidly with displacement and contains several undulations. As expected, the in-bulk tests show significantly higher loads than those of the on-edge tests (compare Figs. 2c and 3a) due to the more restrictive boundary conditions in the in-bulk setup.

Figure 3a also shows the effect of unload-reload cycling and hysteresis [20] in the VANCTs. We show 5 load-unload cycles for each sample. As seen from this figure, the first cycle is distinctly different from all subsequent loading cycles [1, 2, 44]. Subsequent cycling also results in a substantially higher relative recovery as compared to the first. In some cases during unloading we also measured the applied loads to be slightly negative, likely due to the adhesive interactions between the VACNTs and the diamond indenter tip [16, 63].

A comparison of the load-displacement curves in Fig. 3a reveals some important differences between the indentation response of VACNT samples A and B. As in the case of the *in situ* on-edge tests, the in-bulk tests also show a much stiffer response for the VACNT sample B as compared to sample A. This is reflected in the higher slope of the initial loading segment, and in the higher resistance to buckling for sample B. In general the indentation loads (and stresses) are seen to be significantly higher for sample B than for sample A at equivalent indentation depths. We calculate the indentation stress at the point of instability (σ_{ins}) to be ~0.9 MPa for sample B, which is twice as high as that for sample A (σ_{ins} = 0.44±0.04 MPa). There is a steep drop in indentation load immediately following the instability. The load drop is larger for sample B (from 10.4 mN to 6.7 mN) than for sample A (from 5.3 mN to 4.9 mN). As seen earlier from the *in situ* tests (video file S3) the load drop signifies the onset of buckling of the VACNTs under the indenter. Particularly in the case of sample B, the *in situ* tests revealed the buckling to originate at the zone of lower density (seen as a dark band in Fig. 1d) which is located at ~ 32 μm below the top surface.

Sample B also shows a pronounced flat plateau region of constant stress following the load drop. As in the *in situ* tests (see video file S3), this flat plateau is a likely result of the continuous buckling of the VACNTs under the indenter within a height of ~ 32 μm (*i.e.* up to the first VACNT band of low density). As expected, the flat plateau ends after around 30 μm of displacement, and is followed by a steep increase in the indentation load as the indenter experiences the denser VACNTs underneath.

Such sloped plateau regions have been observed previously in VACNTs [1, 11, 22], and an inherent property gradient in the VACNT microstructure along its height has been generally suggested as the cause. The particular constraints and boundary conditions under indentation loading, where the indenter continuously samples an increasing material volume, as well as a progressive densification of the VACNT matrix with increasing indentation depth, could also cause such a sloped region [20, 28]. A combination of all of these effects is thought to be responsible for the features seen in Fig 3a, where the indenter encounters a denser, and hence stiffer, material in the deeper regions leading to an increasing global slope in the plateau region.

The later section of the plateau region for sample B also shows a large undulation or kink at around ~50 μm of indentation depth (Fig. 3a). This distance matches well with the location of the second band of lower density in sample B (see Fig. 1d). No such instabilities are observed in sample A.

Unloading from a depth of ~65-70 μm results in a much higher recovery for sample A than for sample B, as shown by the images of the residual imprints (Figs. 3b and 3c respectively). The imprint for the VACNT sample B (Fig. 3c) also shows the remnant of the zone of low VACNT density, which is seen as a shear line at a depth of ~ 32 μm along the walls of the crater. The vertical walls of the indent imprint above this depth indicate a clear shearing of the VACNTs in this height and thus possibly a lower degree of entanglement among the VACNTs for sample B. These images also help to show the highly localized nature of the VACNT deformation, where all of the deformation is limited to the vertical shear region along the rim of contact between the sample and the indenter tip.

We note that at loading rates faster than 10 nm/s the plateau region is obscured by a large displacement burst, particularly for VACNT sample B (a similar effect was noted

earlier in the *in situ* tests as well in Fig. 2c). In these cases a rapid, extensive displacement burst of ~30 μm was noticed immediately after attaining σ_{ins} at the faster loading rates of 100 and 1000 nm/s. Unlike the gradual drop in load seen in Fig. 3a, such a burst indicates a temporary loss of contact between the sample and the indenter tip. Based on the *in situ* indentation tests described in Fig. 2, it appears that the burst may be caused by a rapid vertical shearing of the material directly underneath the indenter tip along the indenter edges up to a depth of ~32 μm (*i.e.* up to the location of the first low density zone). This was verified by stopping the test at the moment of the burst, which resulted in an imprint mirroring the shape of the indenter and of depth ~32 μm.

3.4 Analysis of indentation response

Figure 4 shows a summary of the results from the in-bulk tests on VACNT samples A and B (*in situ* on-edge tests are not included in this summary). The unloading modulus, defined in Eq. 1, is plotted as a function of the maximum displacement before unload in Fig. 4a. Results are shown for three different loading rates – 10, 100 and 1000 nm/s. For sample B, the results are also segregated by whether they are measured before (open symbols) or after (filled symbols) the first instability.

Figure 4a shows that in sample B, the changes in the unloading moduli clearly reflect the softening effects of the zones of lower density present along the height of the VACNT film. As shown in Fig. 1d, two such zones were visible in the cross-sectional view of VACNT sample B: at ~32 and ~50 μm below the top surface, respectively. The unloading moduli for sample B also show two sharp drops just before these displacement levels, as shown by the trend line for the 1000 nm/s tests. The first stiffness drop ($\Delta E_s \approx$ 170 MPa at around 20 μm displacement) is much larger than the second ($\Delta E_s \approx 35$ MPa at around 41 μm displacement), suggesting that the lower density zone closer to the surface has a greater deleterious effect on the mechanical behavior of the sample. After the second drop the moduli are seen to be increasing again (from 129 to 190 MPa) with increasing displacement for sample B.

Sample B also shows an almost three-fold increase in unloading modulus values before the first burst (open symbols, from $E_s = 92$ MPa to 346 MPa). We suspect this large increase to be partly an artifact of the misalignment between the sample surface and the flat punch indenter at the initial stages of loading.

The unloading moduli for sample A show order of magnitude lower values at similar displacement levels. The moduli in this sample range from ~ 7 MPa, at shallow displacement levels (~ 6 μm maximum displacement), to ~ 33 MPa, at the largest indentation depth of 66 μm. This steady increase in the unloading moduli for this sample (as well as the increase seen in sample B after the second instability) is a likely effect of the increase in density due to compaction of the VACNT matrix under the indenter. Both VACNT samples A and B also show slightly higher values of stiffness at the faster rates, consistent with the typical behavior for viscoelastic solids [71].

We note a particular limitation of our method in calculating the unloading moduli from Eq. (1) as reported in Fig. 4a: Eq. (1) inherently assumes indentation of an elastic half-space, as generally found in monolithic materials [51, 72]. This may not be suitable for VACNTs, which are inherently hierarchical in their structure. Moreover, as shown in Fig. 2d for sample B, the VACNT foam can also fracture, further altering the boundary

constraints. In spite of these aspects, Fig. 4a helps to underscore the large difference in stiffnesses between the two VACNT samples.

Such differences in unloading moduli between the two samples can be directly attributed to the differences in tortuosity or waviness in their structures. As shown earlier in Fig. 1, the VACNTs in sample B have a more vertically aligned structure than that of sample A. The longer growth time for sample A results in the distinctive tortuous nature, and the SEM images of this sample show a characteristic waviness with chord lengths of around 7.5-8 μm in their upper cross-section (Fig. 1b). Thus the VACNT network in sample A can be viewed as being already pre-buckled/pre-bent, where the favorable contact energy between the tubes (van der Waals) is balanced by the bending strain energy of their arrangement, resulting in a stable low energy configuration [16]. This structure has a lower mechanical stiffness than the more aligned tubes of sample B. This justification is supported by prior theoretical studies on CNT networks, which have also reported the effective moduli of such networks to be strongly affected by the waviness of the CNT members [38, 39]. These studies have shown that an increase in the tortuosity of the fibers (*i.e.,* either a decrease in the chord length, or an increase in the amplitude) can cause a significant decrease in the modulus of the CNT network. The effect was also found to be magnified at lower densities [39]. Our results from Fig. 4a and Table 1 suggest that both these factors – a stronger waviness in sample A and the lower density of sample B – are responsible for the large differences in the moduli of these two samples.

Figure 4b shows the trends in the % recovery (R, Eq. 2) and Fig. 4c the loss coefficient (η, Eq. 3) as a function of the load-unload cycle number across the three loading rates. The data for both these figures contain results only for the tests loaded beyond the first instability (or burst). The distinctly higher recovery for sample A ($R \approx$ 80% for the first cycle) as compared to sample B ($R \approx$ 22-40%) is evident in Fig. 4b. The loss coefficient η, or fractional energy dissipated during the load-unload cycling process (Fig. 4c), also shows a very similar trend, with sample A demonstrating 2-3 times higher values than sample B.

Interestingly, the two samples show opposite trends with respect to the indentation loading rate. Thus, while in sample A the tests conducted at the slowest 10 nm/s rate are the most permanently deformed (*i.e.* least recovered), the reverse is true for sample B where the fastest 1000 nm/s tests show the lowest values of R and η, especially in the first cycle (Figs. 4b and c). For VACNT networks showing high resilience, such as sample A, the reduced recovery at slower rates is explained by the greater time allowed for the individual CNTs to come in close contact with one another. These inter-tube interactions are inherently adhesive, due to van der Waals attractions [73]. At the slower indentation rates these attractive forces supersede the elastic recovery process and thus decrease the reversibility of the VACNT structure under the imposed strain, resulting in lower values of R and η. Repeated cycling further acerbates the process, and the values are seen to drop even more with increasing cycle number. In contrast, at the faster rates there is insufficient interaction time between the CNTs in sample A, and hence much lower adhesion and higher recovery [22].

For sample B, the deformation is dominated by the zone of lower VACNT density present below the surface. Here, the individual CNT struts are also more vertically aligned than in sample A (Fig. 1), making the shear strength in the vertical plane of this sample much lower than that of sample A. Under the high shear forces generated during

indentation, sample B experiences a catastrophic shearing-off process where the shear proceeds vertically through the VACNT thickness down to the zone of lower VACNT density. This effect is more drastic along the indenter edges where the indentation shear forces are the largest. In contrast, the slower indentation rates allow more time for the CNTs to reconfigure themselves, and thus help prevent the catastrophic nature of the burst. Hence, in sample B the recovery is higher at slower rates due to the lack of the sudden displacement burst during the loading cycle. The same effect is also seen at faster rates during repeated cycling in sample B (Fig. 4b); at 1000 nm/s the large displacement burst in the first cycle results in very low values of recovery (R = 22.6±2 %). The burst is absent in the subsequent cycles and the recovery improves to ~ 30% from the 2nd cycle onwards.

We note that the very high recovery ($R \approx 80\%$) of sample A is quite unique for VACNTs under large displacement indentation boundary conditions. Most VACNT systems exhibiting high recoverability have been tested under uniaxial compression, where shear stresses are negligible [1, 5, 6, 21, 22]. However, when tested under indentation, some of these same systems have shown very poor recovery (R<10%) [27, 28, 74, 75], much lower than that of VACNT sample A in this study.

Some prior indentation studies have also noted the catastrophic shear process in the VACNT network. In these reports, the shear proceeds through the entire VACNT thickness, and leads to their virtually-nonexistent material recovery [27, 28]. Instead, while sample B in our study suffers from the same shear phenomenon, the presence of the zone of low density in this sample helps to arrest the shear process to only the top section of the VACNT film. As a result, the recoverability of sample B ($R \approx$ 22-40%) still compares favorably to others reported in literature under indentation.

The viscoelastic indentation responses of the two VACNT films, in terms of the measured values of their storage modulus (E'), loss modulus (E''), and $\tan\delta$, are shown in Fig. 5. In this figure, both the storage and loss moduli for sample A are seen to increase as the indentation depth is increased from 15, 26, 36, 47, 58 to 68 μm. No such increase was noted for sample B. Note that the data for sample B contain values for only the three deeper depths of 47, 58 and 68 μm (see Materials and Methods, Section 2.5).

We find the storage moduli to be frequency independent over the range of frequencies probed for both samples, indicating that the VACNT's elastic deformation is likely due to the same mechanism (probable tube bending) over the range of timescales tested. On the other hand, the loss moduli (and $\tan\delta$) values for sample A show an almost step increase at 10 Hz; above 10 Hz a doubling in the values of these parameters can be seen in Figs. 5b and 5c. Unfortunately the cut-off frequency (50 Hz) of our instrument prevents further study of this behavior at higher frequencies. Similar to the trends of R and η, such frequency dependence can also be explained by the lower interaction time available at higher frequencies. The additional time available at the lower frequencies increases the adhesive interactions between the CNTs, causing a decrease in its ability to dissipate energy.

No such frequency dependence was noticed for the three deeper depths of 47, 58 and 68 μm in sample B. For both samples, the storage moduli E' shown in Fig. 5 match well with the unloading modulus values described earlier in Fig. 4.

3.5 Morphology and recoverability of VACNT systems

The high recoverability in VACNTs and the lack of morphological damage after deformation has significant implications for their use as protective materials and in energy dissipation devices. We have observed that an increased density and tortuosity correlates with a significantly higher resilience of the VACNT sample.

In order to understand the factors contributing to the recoverability of VACNTs, we first investigate the density gradient(s) present along the film height. The results from Figs. 1, 2 and 4 appear to indicate that the ability of VACNT sample B to recover under indentation can be strongly affected by the presence of a zone of lower VACNT density ~32 μm below the top surface. While such low density zones have an obvious softening effect on the mechanical properties of this sample, it is still unsure whether this in itself is the sole cause for its lower recoverability. In order to test this effect further, a third VACNT sample was synthesized with a similar reaction time of 7 min resulting in a similar film thickness (~179 μm) as sample B. Care was taken to keep the input rate of the precursor solution constant during synthesis of this third sample, and thus (unlike sample B) no lower density bands were present in this case. The recoverability of this sample (after buckling) was calculated to be R = 54%. Although this value is somewhat higher than that of sample B, it is still significantly lower than the R~80% seen for sample A. Hence, we can conclude that the presence of the low density bands is not the prime cause for the lower recovery of sample B.

We hypothesize that the lower recovery for VACNT sample B is caused by the more vertical alignment of the constituent CNTs in its matrix, as shown in Fig. 1 [21, 76]. Once such an aligned network is buckled, it results in significant lateral entanglement of the tubes in its matrix. The lateral interconnections between the adjacent CNTs inevitably lead to a strong bundling of the tubes. These interactions are inherently adhesive, due to van der Waals forces, and hence detrimental to the VACNT recovery. In sample A the more tortuous nature of the VACNTs helps to prevent such an increase in the side contacts between the tubes. The tubes in sample A also have twice the thickness of the CNTs in sample B (see Table 1), and hence the resultant increase in the bending stiffness of the tubes would also aid their elastic recovery process. This matches well with a number of observations in the literature, where reversible VACNT deformation was reported to be more common for thicker tubes (of ≥40 nm diameter) [1, 11, 30].

The above hypothesis is also supported by the results of the viscoelastic measurements of the two samples. In sample A (Fig. 5), we find the storage and loss moduli to increase with increasing indentation depth. Both of these increases can be explained by proportional increase in the number of inter-tube contacts happening at these depths. Theoretical studies have shown that the effective elastic modulus (represented by the storage modulus E') of a stiff fiber network is directly proportional to the number of inter-tube contacts [36, 38, 39]. Similarly the viscoelastic behavior of VACNTs is thought to be due to the zipping and unzipping of the CNTs upon contact [5, 20], and hence an increasing number of interconnections between the tubes should result in a greater viscoelastic response (and a resultant increase in the loss modulus E''). However, since these interactions are also inherently adhesive, it stands to reason that the recovery in this sample should follow the reverse trend, i.e., R should decrease with increasing depth. This can be seen in Fig. 5c (inset) where the recovery gradually decreases from a near complete recovery, R~100%, at the indentation depth of h_{max} ~ 10

μm to R~78% at h_{max} ~ 65 μm, indicating the detrimental effects of increased VACNT interconnections on their recovery.

The large displacement burst seen in sample B also causes a sudden sharp increase in the CNT lateral connections. We theorize that the catastrophic nature of this shear-off process results in a strong bundling of the contacting CNTs. Thus any further increase in the indentation depth beyond the critical shear-off depth causes very little change in the VACNT viscoelastic properties (see data for sample B in Fig. 5). Beyond this critical indentation depth the bundled VACNTs in sample B also lose any frequency dependence in their behavior.

We note that while these results were found to be repeatable over different sample sets (including the third sample set described above), they are however valid only for the particular growth technique used in this work. The CVD technique for synthesizing VACNTs can be notoriously difficult to control. Changes in the synthesis routines – such as the use of a variable precursor input rate instead of a constant one – can substantially change the resultant VACNT density, alignment, and tortuosity, including their respective variations along the film heights, which affects their recovery [47]. This is reflected in the wide range of recoverability values reported for CVD-VACNTs synthesized using the CVD method [1, 5, 6, 12, 18, 21-25]. Experimentally quantifying these parameters continues to be a challenging task.

4. Conclusions

In summary, we report a correlation between certain morphological features of VACNT films, such as the tortuosity of the individual CNTs, and the recoverability of the systems after indentation. We find that the taller VACNT films synthesized for a longer growth time show a higher resilience under indentation. We hypothesize that the higher recovery in the taller films is caused by the increased tortuosity of the constituent CNTs in their network, as well as their higher densities. This combination enables the taller VACNT films to avoid a catastrophic shear failure under the indenter, hence enhancing their recoverability.

Supporting Online Material

Three video recording of the SEM observations of indentations on the two VACNT samples A and B, synchronized with their respective indentation load-displacement curves, are provided as supporting online material as described below:
Video file S1: Sample A, 100 nm/s displacement rate, shown at 30 times its original speed
Video file S2: Sample B, 100 nm/s displacement rate, shown at 25 times its original speed
Video file S3: Sample B, at a slower 10 nm/s displacement rate, shown at 250 times its original speed

Acknowledgments

We acknowledge Prof. Julia R. Greer for helpful discussions and for providing access to testing facilities. SP gratefully acknowledges support from the W.M. Keck Institute for Space Studies Postdoctoral Fellowship program for this work. JRR

acknowledges the Army Research Office and the Department of Defense for funding via a National Defense Science & Engineering Graduate fellowship during the course of this work. CD acknowledges support from the Institute for Collaborative Biotechnologies under contract W911NF-09-D-0001 with the Army Research Office. We acknowledge critical support and infrastructure provided for this work by the Kavli Nanoscience Institute at Caltech.

[1] A. Y. Cao, P. L. Dickrell, W. G. Sawyer, M. N. Ghasemi-Nejhad, P. M. Ajayan, Science 2005, 310, 1307.
[2] A. Misra, J. R. Greer, C. Daraio, Advanced Materials 2008, 20, 1.
[3] J. Cho, C. Richards, D. Bahr, J. Jiao, R. Richards, J. Micromech. Microeng. 2008, 18.
[4] B. A. Cola, J. Xu, T. S. Fisher, International Journal of Heat and Mass Transfer 2009, 52, 3490.
[5] M. Xu, D. N. Futaba, T. Yamada, M. Yumura, K. Hata, Science 2010, 330, 1364.
[6] J. Suhr, P. Victor, L. C. S. Sreekala, X. Zhang, O. Nalamasu, P. M. Ajayan, Nature Nanotechnology 2007, 2, 417.
[7] M. Kumar, Y. Ando, Journal of Nanoscience and Nanotechnology 2010, 10, 3739.
[8] V. Presser, M. Heon, Y. Gogotsi, Advanced Functional Materials 2011, 21, 810.
[9] A.-C. Dupuis, Progress in Materials Science 2005, 50, 929.
[10] R. Andrews, D. Jacques, A. M. Rao, F. Derbyshire, D. Qian, X. Fan, E. C. Dickey, J. Chen, Chemical Physics Letters 1999, 303, 467.
[11] J. R. Raney, A. Misra, C. Daraio, Carbon 2011, 49, 3631.
[12] O. Yaglioglu, in *Dept. of Mechanical Engineering*, Vol. PhD, Massachusetts Institute of Technology, 2007.
[13] M. Bedewy, E. R. Meshot, H. Guo, E. A. Verploegen, W. Lu, A. J. Hart, Journal of Physical Chemistry C 2009, 113, 20576.
[14] O. Yaglioglu, A. Cao, A. J. Hart, R. Martens, A. H. Slocum, Advanced Functional Materials 2012, DOI: 10.1002/adfm.201200852.
[15] T. Tong, Y. Zhao, L. Delzeit, A. Kashani, M. Meyyappan, A. Majumdar, Nano Letters 2008, 8, 511.
[16] S. D. Mesarovic, C. M. McCarter, D. F. Bahr, H. Radhakrishnan, R. F. Richards, C. D. Richards, D. McClain, J. Jiao, Scr. Mater. 2007, 56, 157.
[17] A. Qiu, D. F. Bahr, A. A. Zbib, A. Bellou, S. D. Mesarovic, D. McClain, W. Hudson, J. Jiao, D. Kiener, M. J. Cordill, Carbon 2011, 49, 1430.
[18] Q. Zhang, Y. C. Lu, F. Du, L. Dai, J. Baur, D. C. Foster, Journal of Physics D-Applied Physics 2010, 43, 315401.
[19] C. P. Deck, J. Flowers, G. S. B. McKee, K. Vecchio, Journal of Applied Physics 2007, 101, 23512.
[20] S. Pathak, Z. G. Cambaz, S. R. Kalidindi, J. G. Swadener, Y. Gogotsi, Carbon 2009, 47, 1969.
[21] M. Xu, D. N. Futaba, M. Yumura, K. Hata, Advanced Materials 2011, 23, 3686.
[22] S. Pathak, E. J. Lim, P. Pour Shahid Saeed Abadi, S. Graham, B. A. Cola, J. R. Greer, ACS Nano 2012, 6, 2189.
[23] S. B. Hutchens, L. J. Hall, J. R. Greer, Advanced Functional Materials 2010, 20, 2338.
[24] A. A. Zbib, S. D. Mesarovic, E. T. Lilleodden, D. McClain, J. Jiao, D. F. Bahr, Nanotechnology 2008, 19, 175704.
[25] C. Cao, A. Reiner, C. Chung, S.-H. Chang, I. Kao, R. V. Kukta, C. S. Korach, Carbon 2011, 49, 3190.
[26] J. R. Raney, F. Fraternali, C. Daraio, In preparation

[27] P. Pour Shahid Saeed Abadi, S. Hutchens, J. H. Taphouse, J. R. Greer, B. A. Cola, S. Graham, Nanoscale 2012, 4, 3373.
[28] S. Pathak, N. Mohan, P. Pour Shahid Saeed Abadi, S. Graham, B. A. Cola, J. R. Greer, Journal of Materials Research 2012 (submitted).
[29] Y. C. Lu, J. Joseph, Q. Zhang, M. R. Maschmann, L. Dai, J. Baur, Experimental Mechanics 2012, in press. DOI 10.1007/s11340.
[30] J. R. Raney, F. Fraternali, A. Amendola, C. Daraio, Composite Structures 2011, 93, 3013.
[31] P. D. Bradford, X. Wang, H. Zhao, Y. T. Zhu, Carbon 2011, 49, 2834.
[32] M. A. Al-Khedher, C. Pezeshki, J. L. McHale, F. J. Knorr, Nanotechnology 2007, 18.
[33] H. Malik, K. J. Stephenson, D. F. Bahr, D. P. Field, Journal of Materials Science 2011, 46, 3119.
[34] C. M. McCarter, R. F. Richards, S. D. Mesarovic, C. D. Richards, D. F. Bahr, D. McClain, J. Jiao, Journal of Materials Science 2006, 41, 7872.
[35] Y. Gao, T. Kodama, Y. Won, S. Dogbe, L. Pan, K. E. Goodson, Carbon 2012, 50, 3789.
[36] J. A. Astrom, A. V. Krasheninnikov, K. Nordlund, Phys. Rev. Lett. 2004, 93, 215503.
[37] H. L. Cox, British Journal of Applied Physics 1952, 3, 72.
[38] L. Berhan, Y. B. Yi, A. M. Sastry, E. Munoz, M. Selvidge, R. Baughman, Journal of Applied Physics 2004, 95, 4335.
[39] L. Berhan, Y. B. Yi, A. M. Sastry, Journal of Applied Physics 2004, 95, 5027.
[40] M. R. Maschmann, Q. Zhang, R. Wheeler, F. Du, L. Dai, J. Baur, ACS Applied Materials & Interfaces 2011, 3, 648.
[41] J. F. Waters, L. Riester, M. Jouzi, P. R. Guduru, J. M. Xu, Applied Physics Letters 2004, 85, 1787.
[42] J. F. Waters, P. R. Guduru, M. Jouzi, J. M. Xu, T. Hanlon, S. Suresh, Appl. Phys. Lett. 2005, 87, 103109.
[43] J.-Y. Kim, J. R. Greer, Acta Materialia 2009, 57, 5245.
[44] S. Pathak, E. J. Lim, P. Pour Shahid Saeed Abadi, S. Graham, B. A. Cola, J. R. Greer, ACS Nano 2012, DOI: 10.1021/nn300376j.
[45] R. M. Malek Abbaslou, J. Soltan, A. K. Dalai, Applied Catalysis A: General 2010, 372, 147.
[46] M. Maghrebi, A. A. Khodadadi, Y. Mortazavi, M. Rahimi, A. Sane, Z. Tsakadze, S. Mhaisalkar, Materials Chemistry and Physics 2010, 124, 1139.
[47] J. R. Raney, R. Y. Wang, C. Daraio, Carbon 2012 (in review).
[48] X. Li, A. Cao, Y. J. Jung, R. Vajtai, P. M. Ajayan, Nano Letters 2005, 5, 1997.
[49] M. Pinault, V. Pichot, H. Khodja, P. Launois, C. Reynaud, M. Mayne-L'Hermite, Nano Letters 2005, 5, 2394.
[50] K. L. Johnson, *Contact Mechanics*, Cambridge University Press, Cambridge, 1987.
[51] W. C. Oliver, G. M. Pharr, Journal of Materials Research 1992, 7, 1564.
[52] J. P. Tu, C. X. Jiang, S. Y. Guo, M. F. Fu, Materials Letters 2004, 58, 1646.
[53] J. P. Tu, L. P. Zhu, K. Hou, S. Y. Guo, Carbon 2003, 41, 1257.

[54] B. Bhushan, L. Xing, A. Jungen, C. Hierold, Physical Review B (Condensed Matter and Materials Physics) 2008, 77, 165428.
[55] L. Lattanzi, J. R. Raney, L. De Nardo, A. Misra, C. Daraio, Journal of Applied Physics 2012, 111.
[56] V. S. Deshpande, N. A. Fleck, Journal of the Mechanics and Physics of Solids 2000, 48, 1253.
[57] M. F. Ashby, *Materials Selection in Mechanical Design*, Butterworth-Heinemann; , 2005 (3 ed.).
[58] E. G. Herbert, W. C. Oliver, G. M. Pharr, Journal of Physics D: Applied Physics 2008, 41, 074021.
[59] E. G. Herbert, W. C. Oliver, A. Lumsdaine, G. M. Pharr, Journal of Materials Research 2009, 24, 626.
[60] W. J. Wright, A. R. Maloney, W. D. Nix, International Journal of Surface Science and Engineering 2007, 1, 274.
[61] W. J. Wright, W. D. Nix, "Storage and loss stiffnesses and moduli as determined by dynamic nanoindentation", 506 Keystone Drive, Warrendale, PA 15086, United States, 2009.
[62] S. Pathak, J. Gregory Swadener, S. R. Kalidindi, H.-W. Courtland, K. J. Jepsen, H. M. Goldman, Journal of the Mechanical Behavior of Biomedical Materials 2011, 4, 34.
[63] S. B. Hutchens, A. Needleman, J. R. Greer, Journal of the Mechanics and Physics of Solids 2011, 59, 2227.
[64] J. J. Jackson, A. A. Puretzky, K. L. More, C. M. Rouleau, G. Eres, D. B. Geohegan, ACS Nano 2010, 4, 7573.
[65] X. Li, L. Ci, S. Kar, C. Soldano, S. J. Kilpatrick, P. M. Ajayan, Carbon 2007, 45, 847.
[66] P. Sudheer Kumar, S. Ramchandra, U. Ramamurty, Materials Science and Engineering A 2003, 347, 330.
[67] L. J. Gibson, M. F. Ashby, *Cellular Solids: Structure and Properties* 1999.
[68] N. A. Fleck, H. Otoyo, A. Needleman, International Journal of Solids and Structures 1992, 29, 1613.
[69] L. J. Gibson, Annual Review of Materials Science 2000, 30, 191.
[70] A. Pantano, D. M. Parks, M. C. Boyce, Journal of the Mechanics and Physics of Solids 2004, 52, 789.
[71] R. S. Lakes, *Viscoelastic Solids*, CRC Press, 1998.
[72] M. F. Doerner, W. D. Nix, Journal of Materials Research 1986, 1, 601.
[73] R. S. Ruoff, J. Tersoff, D. C. Lorents, S. Subramoney, B. Chan, Nature 1993, 364, 514.
[74] M. R. Maschmann, Z. Qiuhong, D. Feng, D. Liming, J. Baur, Carbon 2011, 49, 386.
[75] Y. C. Lu, J. Joseph, Q. Zhang, M. R. Maschmann, L. Dai, J. Baur, Experimental Mechanics 2012, in press. DOI 10.1007/s11340.
[76] L. Ge, L. Ci, A. Goyal, R. Shi, L. Mahadevan, P. M. Ajayan, A. Dhinojwala, Nano Letters 2010, 10, 4509.

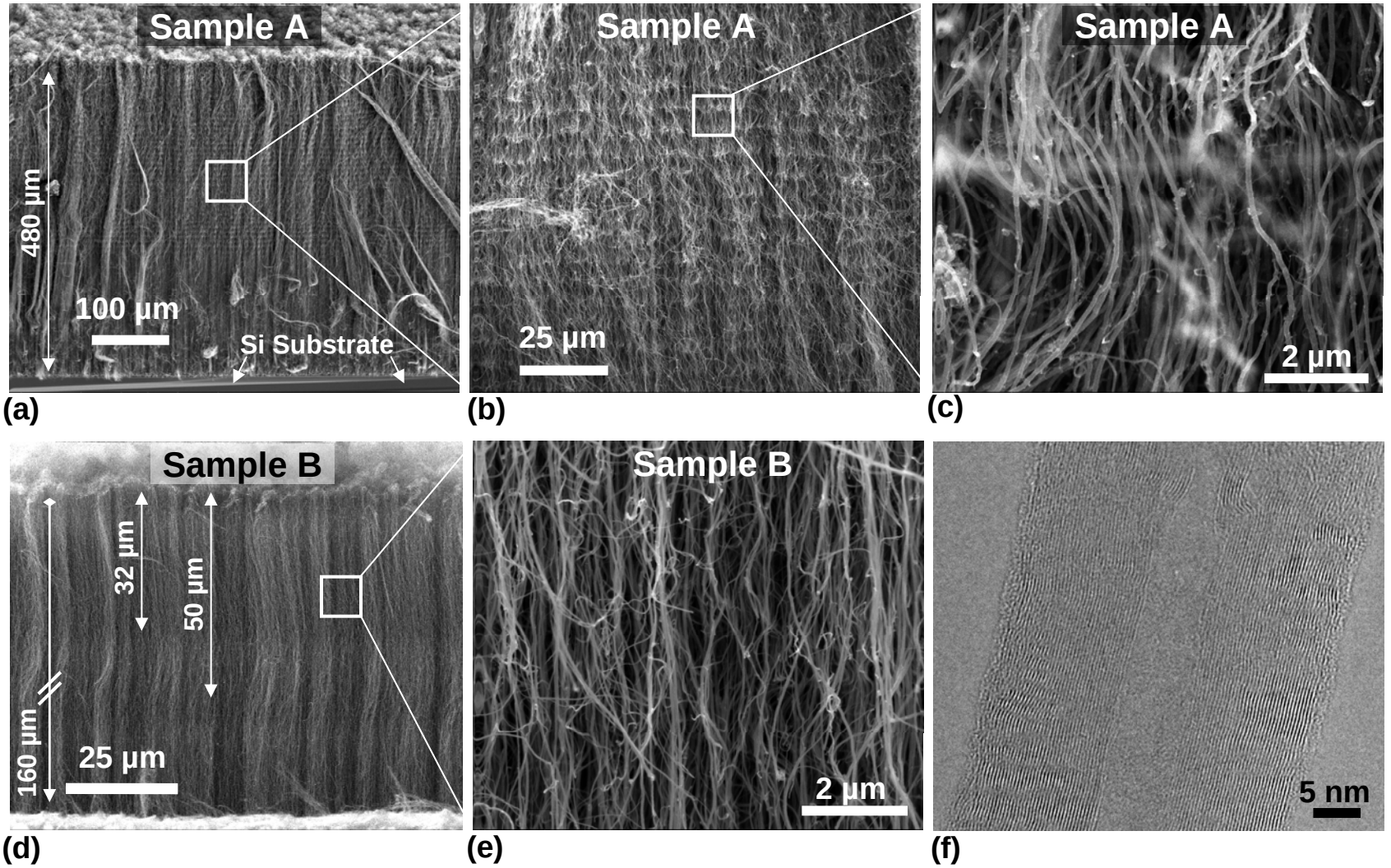

Figure 1. SEM images reveal the hierarchical morphology of the (a) 480 µm thick VACNT films (Sample A), which consist of (b) horizontal layers of high tortuosity, and (c) a complex intertwined network of nominally vertical CNTs at higher mag. (d) On the other hand, a lower thickness VACNT film (Sample B, only top portion of the 160 µm film is shown) shows (e) a more aligned CNT structure at high mag. Note the dark bands starting at ~32 µm from the top in Sample B suggesting regions of lower density in (d), as well as the lower wall thickness of the CNTs in Sample B (compare (c) and (e)).

SEM pictures (a), (b), (c) and (e) are taken at a 60 deg tilt angle while (d) is at 86 deg tilt. (f) Individual multiwalled CNTs are visible in the TEM image.

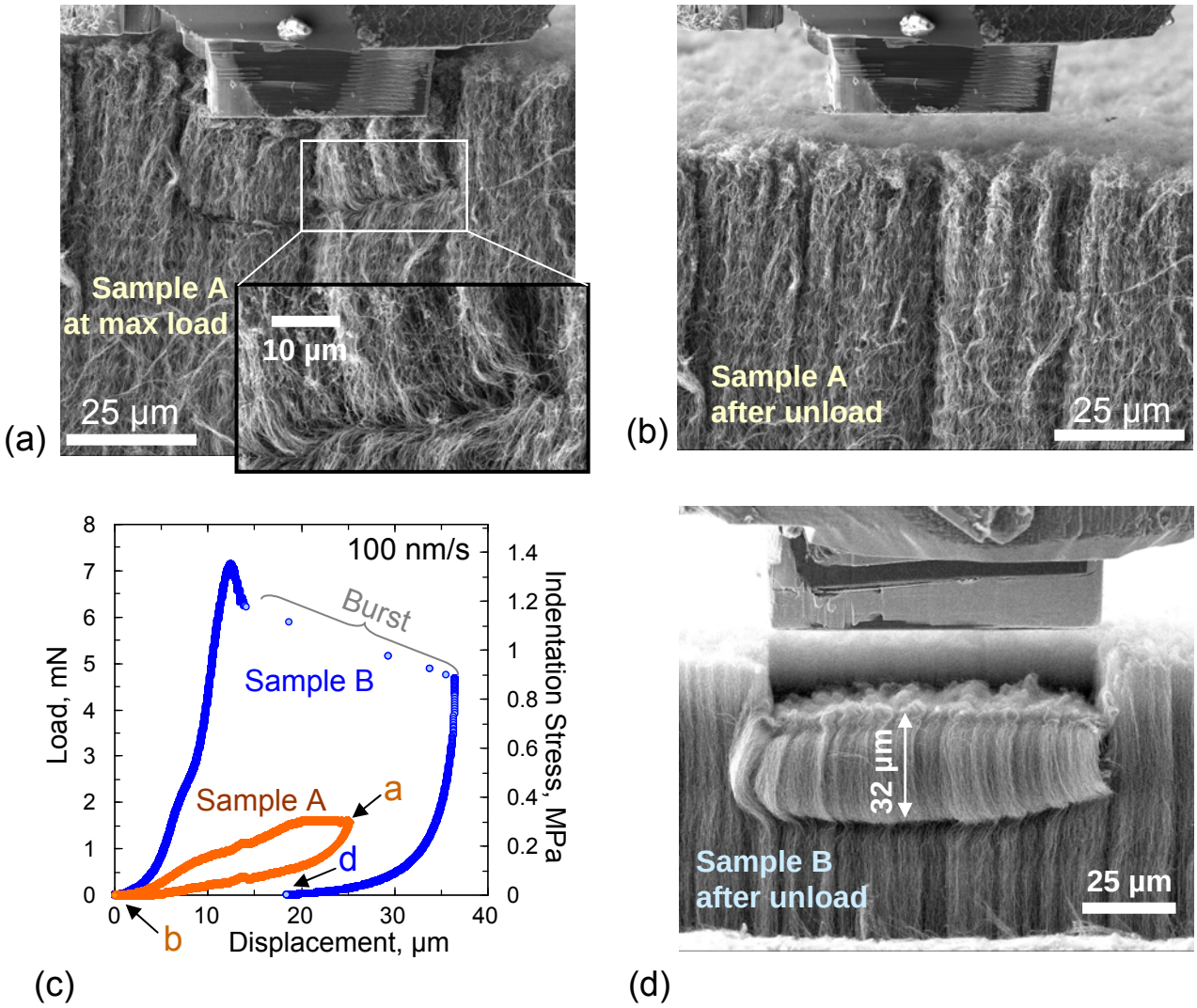

Figure 2. *In-situ* SEMentor observations of on-edge indentations on (a) Sample A at maximum load, (b) Sample A after unload, and (d) Sample B after unload. Their corresponding locations on the load-unload cycles at 100 nm/s loading rate is shown in (c). All SEM images were taken at 86 deg tilt angle. These snapshots were captured from video files S1, S2 and S3.

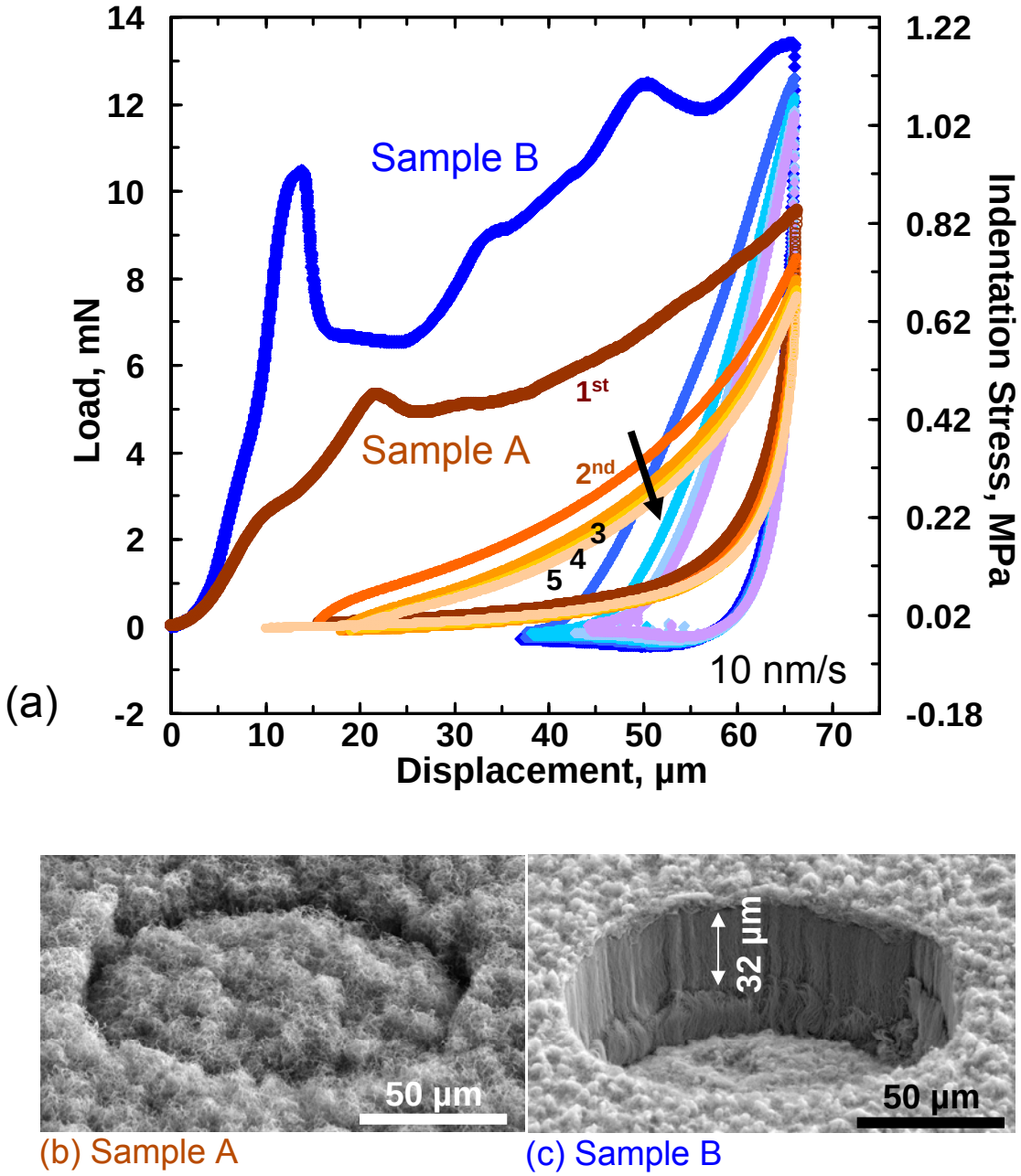

Figure 3. Indentations in the bulk of the sample, away from edge effects. (a) Comparative indentation load (stress) – displacement cycles (5 cycles each) for VACNT samples A and B. Loading at 10 nm/s loading rate shows 3 distinct regimes; elastic, a drop in load at a critical instability stress and plateau regime. Successive load-unload cycles to the same maximum displacement reveal a gradual drop in recovery in every cycle, suggesting progressive damage accumulation in the material. The corresponding indentation stress values are shown along the secondary y axis.

Residual imprints of flat punch indentation are shown for (b) Sample A and (c) Sample B.

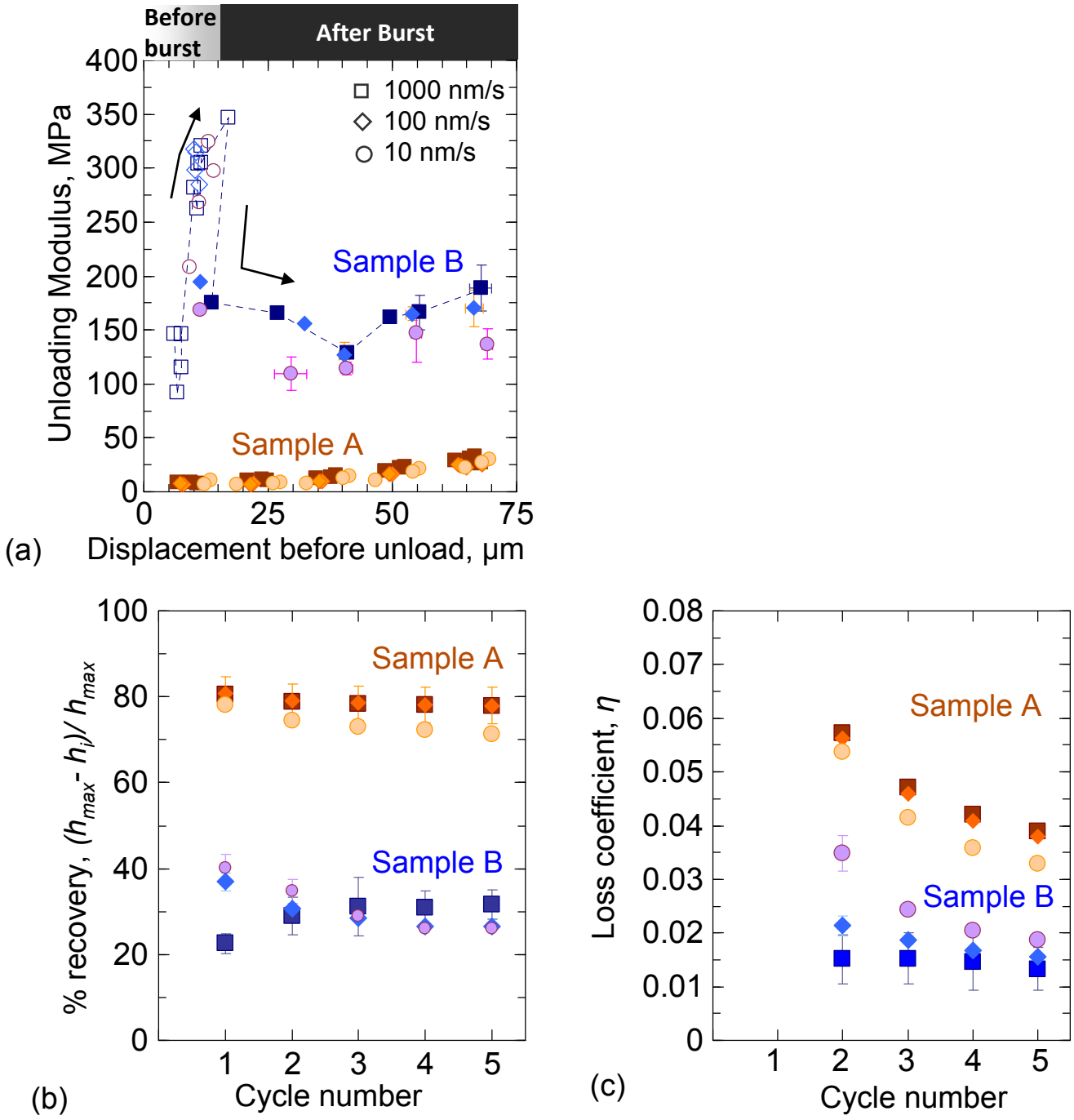

Figure 4. (a) Unloading modulus as a function of max displacement before unload for three different loading rates. For sample B the open symbols represent values before the first instability (burst) during indentation loading of this sample, while the filled symbols are for the values after the instability.

(b) % recovery and (c) loss coefficient – both calculated at large indentation depths (*i.e.* after the first instability) – as a function of cycle number for samples A and B.

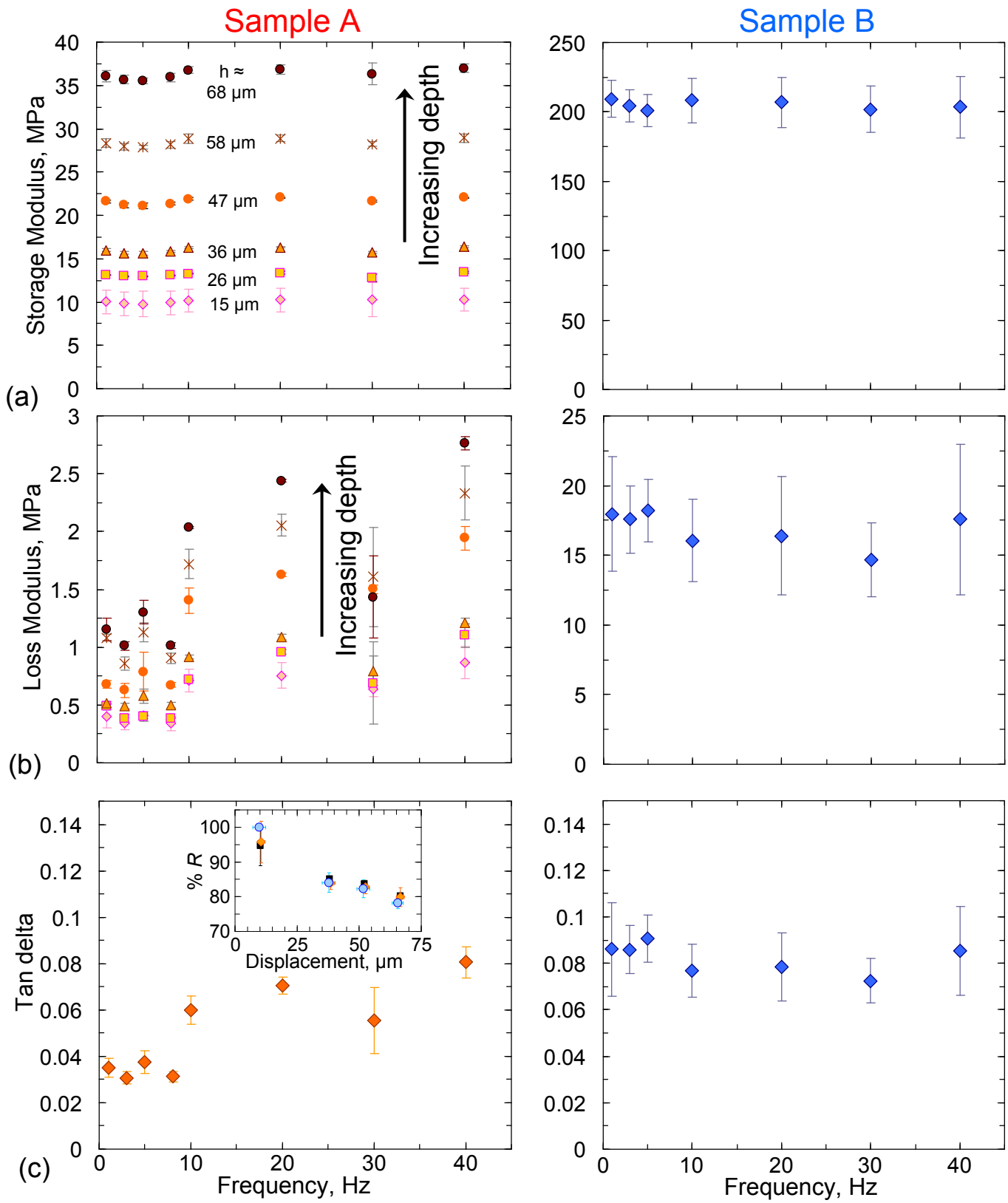

Figure 5. Viscoelastic indentation response of the VACNT films at a loading rate of 100 nm/s, in terms of the measured values (average ±standard deviation) of their (a) storage modulus, (b) loss modulus and (c) tan δ values, as a function of frequency. Note the difference in the y-axis scales between samples A and B for (a) and (b). (c inset) % recovery as a function of max displacement before unload for sample A at three different rates, 1000 nm/s (squares), 100 nm/s (diamond) and 10 nm/s (circles).

Table 1. Comparison between Samples A and B. The uncertainty in the density values is around 10%. The CNT diameters are average ± standard deviation values from the top portions of the VACNT films.

	Sample A	**Sample B**
Synthesis time	10 min	7 min
Height	480 μm	160 μm
Density	0.13 gm/cm^3	0.06 gm/cm^3
CNT dia	68.1±10.6 nm	31.1±7.5 nm